Mass Measurement of Right-Handed Scalar Quarks and Time Measurement of Hadronic Showers for the Compact Linear Collider

Lars Weuste

SIGILL. UNIVERSITAT. LUDOVIC. MAXIM.

München 2013

Mass Measurement of Right-Handed Scalar Quarks and Time Measurement of Hadronic Showers for the Compact Linear Collider

Lars Weuste

Dissertation
an der Fakultät für Physik
der Ludwig–Maximilians–Universität
München

vorgelegt von
Lars Weuste
aus Fürstenfeldbruck

München, den 8. Mai 2013

Erstgutachter: Prof. Dr. Christian Kiesling
Zweitgutachter: Prof. Dr. Otmar Biebel
Tag der mündlichen Prüfung: 12. Juni 2013

Zusammenfassung

Der *Compact Linear Collider* (CLIC) ist ein Konzept eines 48.3 km langen $e^+ \, e^-$ Beschleunigers mit einer Schwerpunktsenergie von 3 TeV. Sein Ziel ist sowohl die Präzisionsvermessung bereits bekannter, als auch die Entdeckung bislang unbekannter Teilchen. Der *International Large Detector* (ILD) ist eines der Detektorkonzepte, die speziell für die Anwendung des *Particle Flow Algorithmus* entworfen wurde. Der Inhalt dieser Arbeit gliedert sich in zwei Teilbereiche, die beide im Kontext von CLIC stehen.

Im ersten Teil dieser Arbeit wird die Messung der Zeitstruktur hadronischer Schauer in Kalorimetern mit Wolframabsorber, wie es auch im ILD Konzept für CLIC benutzt wird, präsentiert. Das beinhaltet die Entwicklung und Konstruktion eines kleinen Testbeam-Experimentes namens *Tungsten Timing Testbeam* (T3B), welches aus lediglich 15 Szintillator Kacheln der Dimension $30 \times 30 \times 5\,\mathrm{mm}^3$ besteht. Diese werden mit Silicon Photomultipliern ausgelesen, welche wiederum mit USB Oszilloskopen verbunden sind. T3B wurde während der Testreihen am CERN in den Jahren 2010 und 2011 hinter dem Prototypen des analogen hadronischen Kalorimeters (W-AHCal) der CALICE Kollaboration platziert. Die gewonnenen Daten wurden mit Simulationsergebnissen verglichen, die mit den drei verschiedenen Modellen hadronischer Schauer der GEANT4 Simulation gewonnen wurden: `QGSP_BERT`, `QGSP_BERT_HP` und `QBBC`. Die Ergebnisse der 60 GeV Datennahme sind zumeist mit `QBBC` und `QGSP_BERT_HP` konsistent. Hingegen überschätzt `QGSP_BERT` wegen der fehlenden Präzisionsverfolgung von Neutronen die Häufigkeit später Energiedepositionen.

Im zweiten Teil wird einer der sechs Benchmark-Prozesse gezeigt, die im Rahmen des CLIC *Conceptual Design Report* die Detektor Leistungsfähigkeit am CLIC Beschleuniger gezeigt haben. Der vorgestellte Benchmark Prozess behandelt die Messung der Masse und des Wirkungsquerschnitts der Paarerzeugung von supersymmetrischen rechtshändigen skalaren Quarks (squarks). Im zugrundeliegenden SUSY Modell zerfallen diese fast ausschließlich in das leichteste Neutralino (fehlende Energie) und das zugehörige Standardmodell Quark (Jet). In der Analyse wird der Beam-generierte pile-up Untergrund von $\gamma\gamma \rightarrow$ *Hadronen* durch die Anwendung der Hadronen Variante des k_t-Algorithmus der FASTJET-Bibliothek unterdrückt. Standardmodell Prozesse, die der Ereignisstopologie entsprechen, werden durch die Anwendung von *Boosted Decision Trees*, implementiert im *Toolkit for Multivariate Analysis* (TMVA), zurückgewiesen. Die Squark-Masse wird durch die Konstruktion der M_C-Verteilung und dem folgenden Fit an die mit verschiedenen Squark-Massen generierten Templates extrahiert. Die Ergebnisse sind konsistent mit ihren Eingangswerten und zeigen, dass Massenmessungen von schweren, stark wechselwirkenden Teilchen bei CLIC mit Genauigkeiten von unter 1% möglich sind.

Abstract

The Compact Linear Collider (CLIC) is a concept for a 48.3 km long e^+ e^- accelerator with a center-of-mass energy of 3 TeV. Its purpose is the precise measurement of particles discovered by the LHC as well as the discovery of yet unknown particles. The International Large Detector (ILD) is one of its detector concepts which was specifically designed for the usage of the Particle Flow Algorithm. This thesis is divided into two parts, both within the context of CLIC.

In the first part of this thesis the unprecedented measurement on time structure of hadronic showers in calorimeters with tungsten absorber material, which is used in the ILD concept for CLIC, will be presented. It shows the development and the construction of a small testbeam experiment called Tungsten Timing Testbeam (T3B) which consists of only 15 scintillator tiles of $30 \times 30 \times 5\,\mathrm{mm}^3$, read out with Silicon Photomultipliers which in turn were connected to USB oscilloscopes. T3B was placed downstream of the CALICE tungsten analog hadron calorimeter (W-AHCal) during beam tests performed at CERN in 2010 and 2011. The resulting data is compared to simulation obtained with three different hadronic shower physics models of the GEANT4 simulation toolkit: `QGSP_BERT`, `QGSP_BERT_HP` and `QBBC`. The results from 60 GeV high statistics run show that `QBBC` and `QGSP_BERT_HP` are mostly consistent with the testbeam data, while `QGSP_BERT`, which is lacking a sophisticated treatment of neutrons, overestimates the late energy depositions.

The second part of this thesis presents one out of the six benchmark processes that were part of the CLIC Conceptual Design Report (CDR) to verify the detector performance at CLIC. This benchmark process is the measurement of the mass and cross-section of two supersymmetric right-handed scalar quarks. In the underlying SUSY model these almost exclusively decay into the lightest neutralino (missing energy) and the corresponding standard model quark (jet). Within this analysis pile-up from beam induced background of $\gamma\gamma \to$ hadrons is rejected by choosing the hadron variant of the k_t-algorithm as it is implemented in the FASTJET library. Standard Model processes mimicking the signal event topography are rejected with a forest of Boosted Decision Trees using the Toolkit for Multivariate Analysis (TMVA). The squark mass is extracted by constructing the M_C distribution and fitting it to templates generated with different squark masses. The results for the mass and cross-section are consistent with the input generator values and show that sub-percent accuracy for the masses of heavy strongly interacting particles can be reached with CLIC.

Contents

Chapter 1

Motivation

“Where do we come from?” “Why is everything the way it is?”

Such questions have been asked many times by many humans, not least by curious children. These questions, despite their intriguing simplicity are very hard to answer due to their fundamental nature. There are entire fields of a philosophical or religious nature trying to give a satisfying answer.

The field of physics, historically originating from philosophy, tries to find answers from a scientific point of view, by breaking the questions down into smaller pieces for which individual theories can be constructed which in turn can be eventually probed by experiments. This breakdown of questions leads us along the chain of “What are we made of?” over “What is matter made of?” to “What are the rules describing the behaviour of matter?”.

Throughout history many different theories evolved to answer these questions. One popular, well known example is the atomism, developed by Leucippus and Democritus in ancient Greece. It postulates that every piece of matter is ultimately made of small, undividable pieces, the atoms (from atomos - uncuttable). This theory was overruled by the experimental discovery of electrons, which were called corpuscles by Thomson in 1897 [1]. Based on this discovery, Thomson created a model describing the structure of the atom to be a sphere of positive charge which was filled with smaller (negative charged) electrons [2]. As the electrons were distributed uniformly like plums in a pudding, this model is known as plum-pudding model. However, this theory, too, was overruled by an experiment, this time conducted by Rutherford in 1911 [3]. By shooting α-particles on a thin gold foil, he was able to conclude that most of the space within an atom is empty with the exception of a small, very massive object - the nucleus. Based on this observation Rutherford invented his own theory, the Rutherford model, with an atom consisting of a massive yet small nucleus surrounded by the lighter electrons. The latest theory is based on atomic orbitals, which describe by quantum mechanical considerations the probability density function of electrons surrounding a nucleus. This example describes pretty well the evolution of theories based on the interplay between theory and experiment over the years. The first observations of nature and fundamental considerations lead to a simple model, which is subsequently replaced by more advanced and detailed theories, which take latest experimental results into account.

As of today it is known that the atom is a compound object of electrons, protons and neutrons, of which the latter two are a compound of yet further subatomic particles called partons. These are only a few examples of the number of different particles that are known to exist, and Particle Physics is the field of fundamental research that deals with these particles as well as their interactions. It contains the latest theory that tries to answer our question of "What are the rules describing the behaviour of matter?", which is called the Standard Model of Particle Physics.

The Standard Model, of which a detailed introduction will follow in chapter 2, is often claimed to be the most successful theory throughout the history of Particle Physics. With the exception for the gravitational force it describes all of the known interactions of matter and was even able to unify the electromagnetic and the weak force [4–6] in the 1960s. Since then it successfully predicted the existence of further particles, such as the weak gauge bosons or the top quark.

However, some experimental results indicate that the Standard Model cannot be ultimate answer to our question above. Among them is the observation of neutrino oscillation. These experiments conclude that neutrinos do have a small albeit not negligible mass, whereas within the Standard Model they are completely massless. Another issue is that although observations implicate the existence of dark matter, the Standard Model lacks candidates for dark matter particles. So to successfully extend or overrule the theory of the Standard Model and give a better answer to our question above, more experiments are necessary.

Thomson and Rutherford were still able to use small sized experimental setups, capable to be run on a table in their laboratory. However, the insight gained by these setups is limited by their maximum achievable energy, just as the highest magnification of a microscope is limited by the wavelength of the used light as described by the Abbe diffraction limit. To increase the resolution in a microscope light of smaller wavelength is needed, which is the equivalent of increasing the energy of the electromagnetic wave.

Therefore in modern physics particles are accelerated to high energies by very large accelerator structures before they are brought to collision. Such a machine is the Large Hadron Collider operated by CERN [7] where protons are accelerated up to a collision energy of 14 TeV[1]. At every single of these collisions the partons within the protons perform an interaction, forming new particles which are identified by particle detectors. The Standard Model predicts which particles can be created, how they decay and how they behave. By repeatedly comparing the Standard Model predictions with the experimental data, the Standard Model is probed with great accuracy.

As a first result the two general purpose LHC experiments ATLAS [8] and CMS [9] already saw strong hints on the existence of the predicted Higgs Boson. However, only a precise measurement of its properties can confirm its exact nature, e.g. if its properties are fully consistent with the Standard Model, or if there are small deviations.

While the LHC is an excellent tool for this task of discovering new particles and hence will continue to take data, its final accuracy is limited by the usage of protons as colliding particles. Thus a complementary particle accelerator is needed which uses leptons instead of protons. A concept for such an accelerator is the Compact LInear

---

[1] Here and throughout this thesis we use the notation of $\hbar = c = 1$

Collider (CLIC). While being still in the research and development phase, the concept is already rather sophisticated and detailed. Its key features are the usage of electrons and positrons as colliding particles, with a collision energy of 3 TeV. To get the necessary amount of statistics, the time between two bunch crossings, i.e. two possible collisions, is as short as 0.5 ns, which in itself is already very challenging.

The particles created by the collision are detected by particle detectors surrounding the interaction point. One concept of such a detector is a variant of the International Large Detector which was optimized for the environment at CLIC (CLIC_ILD). Following the typical onion shell principle the CLIC_ILD has a series of subdetectors. These consists of tracking detectors, to follow the path of charged particles, and calorimeters, to measure the energy of the particles. A detailed description of the accelerator and the detector along with the underlying detector physics will be given in chapter 3.

However, although the overall concept is rather evolved, there are still a few open questions that need to be addressed, one of which is the focus of the first part of this thesis.

For the measurement of the particle energy the CLIC_ILD concept uses calorimeter, which rely on the development of electromagnetic and hadronic showers. These are a cascade of particles, created by the original particle through interaction with the dense absorber material, which in case of the CLIC_ILD is tungsten. In hadronic showers the atomic nuclei of the absorber material can be excited. The de-excitation of the nuclei, however, is not an instantaneous process and can lead to particles being created and thus detected several ns or even μs after the arrival of the initial particle that is supposed to be measured in the calorimeter. As the repetition rate at CLIC is as low as 0.5 ns, this could lead to a potential problem and thus was studied in simulations. However, the time structure of hadronic showers specific to tungsten was not measured before, and thus the simulations need to be verified. For that purpose a small experiment was designed and conducted in the context of this thesis. Its setup, the results as well as the comparison to simulation are the subjects of chapter 4.

To show that the concept of CLIC and CLIC_ILD are fully capable of detecting and measuring physics beyond the Standard Model, six benchmark processes were studied using realistic detector simulations. These are part of the Conceptual Design Report (CDR, [10]), which gives details on the machine and its concept. One of these benchmarks was the measurement of the mass and cross-section of (hypothetical) right-handed scalar quarks. These are supersymmetric particles, i.e. particles beyond the Standard Model, and in the present case decay almost exclusively to two high energetic jets and as such are a performance stress test on the energy and particle reconstruction capability of the detector in the environment of CLIC. The benchmark study is discussed in detail in chapter 5.

Chapter 2

The Standard Model and Beyond

This chapter introduces the fundamental theories in particle physics.

First a short introduction to the Standard Model (SM) will be presented in section 2.1, which is the latest and most accurate theory as of today. After that a famous extension to the Standard Model known as Supersymmetry (SUSY) will be is discussed in section 2.2. It addresses some of the inconsistencies of the SM and is used in the CLIC CDR benchmark analysis presented in chapter 5.

The introduction is mainly based on [11] and [12].

2.1 The Standard Model of Particle Physics

The Standard Model of Particle Physics is a quantum field theory developed in the mid to late 20th century. It started with the unification of two of the four known forces in nature, the electromagnetic and the weak force. Since then it was gradually extended by the interplay of many theoretical and experimental physicists. It has very successfully predicted the existence of particles, such as the weak gauge bosons which were discovered by experiments at the Super Proton Synchrotron at CERN [7]. As of today it is the most tested and accurate theory describing the fundamental forces and interactions of particles.

2.1.1 Introduction

Within the Standard Model there are several types of particles. An overview is given in Figure 2.1, where the size of the particles indicates their respective relative mass. These particles can be sorted according to their properties, one of which is their spin.

Bosons in general are particles with integer spin and gauge bosons in particular carry spin 1. The known gauge bosons are the Photon γ, the charged $\mathrm{W}^{\pm}$ vector bosons, the neutral Z^0 vector boson and a set of eight gluons g. In addition there is the Higgs boson H with spin 0.

Fermions on the other hand are particles with spin $\frac{1}{2}$. Their corresponding anti-particles carry opposite quantum numbers. Fermions are divided into quarks (top platform in Figure 2.1) and leptons (the two central platforms).

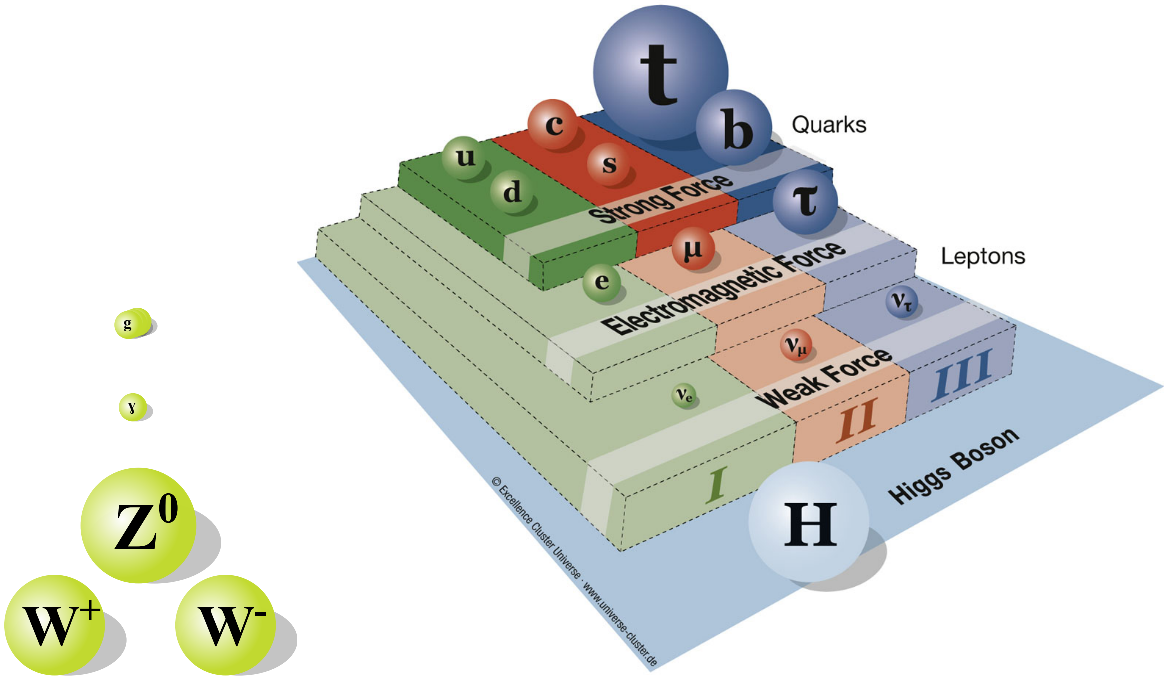

© Excellence Cluster Universe · www.universe-cluster.de

(a) Gauge Bosons (b) Fermions and Higgs Boson

Figure 2.1: An overview over all known fundamental particles ordered by their respective coupling to the different forces. The size corresponds to the particle's mass.

The quarks are further subdivided into their respective flavours of up u, charm c and top t, which carry an electric charge of +2/3, and down d, strange s and bottom b, which carry an electric charge of −1/3. Leptons, too, have subgroups: On the one hand are the electrically charged leptons of electron e^-, muon μ^- and tau τ^-. On the other hand are the electrically neutral leptons called neutrinos, all of which have a charged lepton as partner: electron neutrino ν_e, muon neutrino ν_μ and tau neutrino ν_τ.

All these fermions can be put into families, indicated by the color and the roman numerals of the platforms in Figure 2.1

Any interaction between two particles is mediated via forces. As of today's knowledge there are four different ones:

- The gravitational force, which is the attractive force between two objects with mass. This force is not included in the Standard Model.
- The electromagnetic (EM) force. It describes the electromagnetic waves and is responsible for the chemical binding of molecules as well as the electrons to the nucleus. It couples to the electric charge.
- The strong nuclear force. Using "color" as its charge it is responsible for the nuclei being stable.

- The weak nuclear force. It is responsible for certain decays of e.g. the neutron to the proton, and is the only force coupling to neutrinos. Its charge is the weak charge.

The Standard Model (SM) is a gauge theory describing the electromagnetic, the strong and the weak nuclear force, but not gravity, as interactions between two particles via an exchange of gauge bosons coupling to the respective charges. The mediators of the forces are the photon for the electromagnetic force, the charged and neutral vector bosons for the weak force and the gluons for the strong force.

As quarks carry electrical, weak and color charge they can interact through all three types of interactions. Leptons on the other hand do not carry color charge and hence cannot interact with gluons, but only through the weak force. In addition the charged leptons can interact through the electromagnetic force, as well.

The foundation of the Standard Model was layed by Glashow [4], Salam [5] and Weinberg [6] when they introduced the electroweak theory, unifying the electromagnetic and the weak nuclear force. The four corresponding gauge bosons γ, $\mathrm{W}^{\pm}$ and Z^0 are generated by the spontaneous symmetry breaking as described in the Higgs mechanism, of which the Higgs Boson is a direct consequence. The Higgs boson couples to the mass of a particle (like the photon to the electric charge) and hence it couples to all of the above particles with the exception of the massless photon and the gluons.

Note that most of the particles discussed here cannot be observed directly in nature as they either have a very short lifetime or they form a bound state. The latter is true especially for quarks which will always form a colorless compound of either two (quark-antiquark $q\overline{q}$, called meson) or three (anti-) quarks (qqq or $\overline{q}\overline{q}\overline{q}$, called baryon), such as the proton (uud). This is due to an effect called confinement and originates from the unintuitive behaviour of the strong force increasing in strength with distance. Thus when trying to create a free quark by “pulling” it from a compound an infinite amount of energy would be necessary. However, with enough energy a new quark-antiquark pair is created, of which one will replace the old quark in the compound, and the other together with the “free” quark will form a new colorless state. Thus any try in creating a free quark will instead result in the creation of new mesons or baryons.

2.1.2 The Electroweak Unification and the Higgs Mechanism

The underlying symmetry group

The Standard Model is based on the gauge principle, stating the invariance of the forces under certain local symmetry transformations. The overall symmetry group is

$$SU_C(3) \otimes SU_L(2) \otimes U_Y(1), \tag{2.1}$$

in which Y is the weak hyper-charge and L indicates that the $SU_L(2)$ group only applies to left handed fermions. The $SU_C(3)$ is the symmetry underlying Quantum Chromo Dynamics (QCD), which describes the strong nuclear force. The C stands for color, which is the charge of QCD.

$$\begin{array}{cccccc}
\begin{pmatrix}\mathrm{u}\\ \mathrm{d}'\end{pmatrix}_L & \begin{pmatrix}\mathrm{c}\\ \mathrm{s}'\end{pmatrix}_L & \begin{pmatrix}\mathrm{t}\\ \mathrm{b}'\end{pmatrix}_L & \begin{array}{c}\mathrm{u}_R\\ \mathrm{d}_R\end{array} & \begin{array}{c}\mathrm{c}_R\\ \mathrm{s}_R\end{array} & \begin{array}{c}\mathrm{t}_R\\ \mathrm{b}_R\end{array} \\
\begin{pmatrix}\nu_\mathrm{e}\\ \mathrm{e}\end{pmatrix}_L & \begin{pmatrix}\nu_\mu\\ \mu\end{pmatrix}_L & \begin{pmatrix}\nu_\tau\\ \tau\end{pmatrix}_L & \begin{array}{c}-\\ \mathrm{e}_R\end{array} & \begin{array}{c}-\\ \mu_R\end{array} & \begin{array}{c}-\\ \tau_R\end{array}
\end{array}$$

Table 2.1: The fermions in the SM form left handed doublets, but right handed singlets. The SM does not contain right handed neutrinos.

The weak and the electromagnetic force is united to the representation of $SU_L(2) \otimes U_Y(1)$ as in the second part of Equation 2.1. Here, the $SU_L(2)$ couples only to left (L) handed fermions which in the Standard Model, as opposed to right handed particles (R) which remain singlets, form doublets and have different quantum numbers (cf. Table 2.1). As a consequence three weak bosons $\mathrm{W}^0, \mathrm{W}^1$ and W^2 together with the abelian boson B are created. All these four bosons are massless.

The Higgs mechanism

The particles in the SM are known to have mass. The theory described above, however, contains only massless particles. The Higgs mechanism [13] describes how these particles gain mass through spontaneous symmetry braking.

Assuming a single isospin doublet of complex scalar fields with hypercharge $Y = 1$

$$\Phi(x) = \begin{pmatrix} \phi^+(x) \\ \phi^0(x) \end{pmatrix} = \begin{pmatrix} \phi_1 + i\phi_2 \\ \phi_3 + i\phi_4 \end{pmatrix}, \tag{2.2}$$

the Lagrangian density of the Higgs field can be written as

$$\mathcal{L} = T - V = (D_\mu \Phi)^\dagger (D^\mu \Phi) - V(\Phi) \tag{2.3}$$

$$V(\Phi) = -\mu^2 \Phi^\dagger \Phi + \lambda (\Phi^\dagger \Phi)^2, \tag{2.4}$$

where D_μ denotes the covariant derivative. The illustration of a one dimensional, non complex version of this potential $V(\phi)$ can be seen in Figure 2.2. The important fact of this potential is that it is symmetric and is minimal for $\phi_1^2 + \phi_2^2 = \frac{\mu^2}{2\lambda}$, leading to a non vanishing vacuum expectation value (VEV):

$$\langle \Phi \rangle = \frac{1}{\sqrt{2}} \begin{pmatrix} 0 \\ v \end{pmatrix} \qquad \text{with} \qquad v = \sqrt{\frac{\mu^2}{\lambda}} \tag{2.5}$$

Note that although the potential has the symmetry of $SU_L(2) \otimes U_Y(1)$, the VEV only includes the $U_{em}(1)$ symmetry: the symmetry is spontaneously broken. In order to be able to expand around the ground state, one of the VEVs has to be chosen. In the unitary gauge this is done by redefining the field to

$$\Phi(x) = \frac{1}{\sqrt{2}} \begin{pmatrix} 0 \\ v + H(X) \end{pmatrix}, \tag{2.6}$$

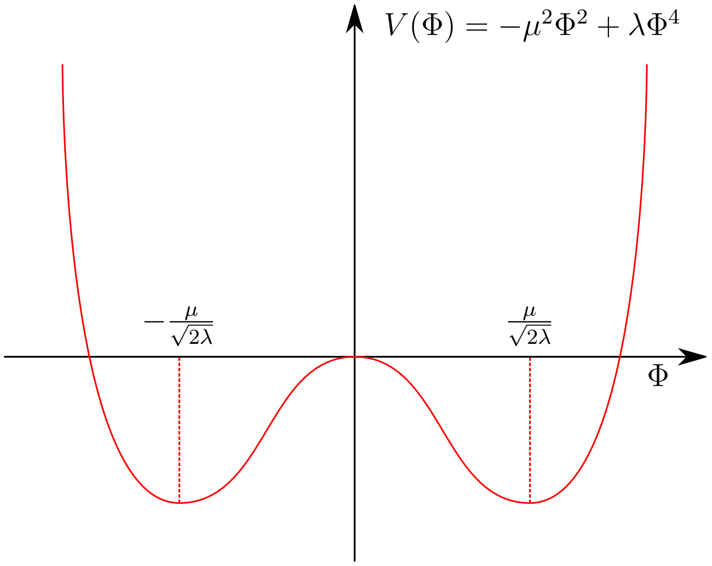

Figure 2.2: Example of the Higgs potential in one dimension.

with the real field $H(x)$ describing physical neutral scalar particles, which are the Higgs bosons with mass $m_H^2 = 2\mu^2 = 2\lambda v^2$.

The Higgs field introduces additional mass terms into the Lagrangian density, leading to a mixing of the three weak bosons $\mathrm{W}^0, \mathrm{W}^1$ and W^2 together with the abelian boson B. Through this mixing three of the four bosons gain mass and create the four electroweak bosons of the SM ($\gamma, \mathrm{W}^\pm$ and Z^0):

$$\mathrm{W}^\pm = \frac{\mathrm{W}^1 \mp i\mathrm{W}^2}{\sqrt{2}}, \quad \mathrm{Z}^0 = -\sin\theta_W \mathrm{B} + \cos\theta_W \mathrm{W}^3, \quad \gamma = \cos\theta_W \mathrm{B} + \sin\theta_W \mathrm{W}^3, \tag{2.7}$$

where $\cos\theta_W = \frac{m_\mathrm{W}}{m_\mathrm{Z}}$ is the Weinberg angle.

2.1.3 Shortcomings of the Standard Model

The Standard Model is the most successful theory in particle physics. Among its predictions are the existence of the top quark and the tau-neutrino, which were successfully confirmed by experimental data. Even the existence of the Higgs boson, which for a long time was the sole missing piece, seems to be confirmed as recent discoveries of CMS [9] and ATLAS [8] at the Large Hadron Collider at CERN [7] suggest.

Despite its successes the Standard Model cannot be the ultimate theory, as:

- It does not incorporate Dark Matter or any explanation of Dark Energy.
- The neutrinos do not have mass in the SM, although experimental data tells us otherwise.
- The CP violation of the SM is not enough to explain the matter-antimatter asymmetry of the universe.

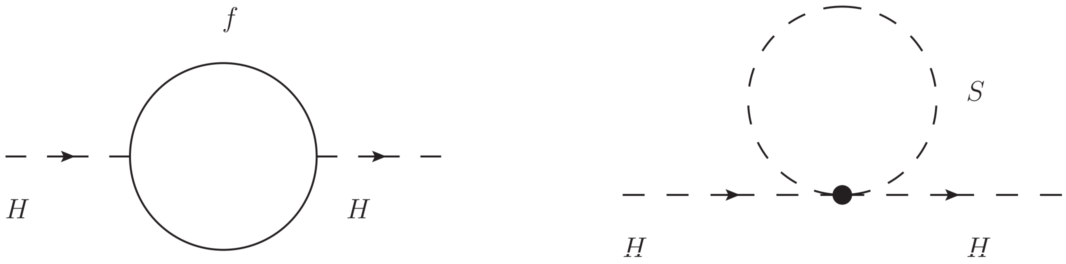

(a) Fermion (b) Scalar

Figure 2.3: Feynman Diagrams of loops contributing to corrections of the Higgs mass due to fermions (left) and scalar particles (right).

- It does not incorporate gravitation.
- Having 19 free parameters, including most of the particle masses and their hierarchy, can considered to be unsatisfactory.
- The hierarchy problem and the necessary fine tuning, which we will now discuss in more detail.

The Hierarchy Problem

Experimental measurements set the non vanishing vacuum expectation value of the Higgs field (cf. Equation 2.5) to be $v \approx 246\,\mathrm{GeV}$, while $m_H \approx 100\,\mathrm{GeV}$ [14].

The problem is, however, that μ^2 receives large corrections from all particles coupling to the Higgs field.

Fermions f with mass m_f, for example, can create a loop diagram as shown in Figure 2.3(a). If the fermions have a term of $-\lambda_f \Phi f \bar{f}$ in the Lagrangian, this leads to a correction of:

$$\Delta\mu^2 = -\frac{|\lambda_f|^2}{8\pi}\Lambda_{UV}^2 + \ldots, \tag{2.8}$$

where Λ_{UV} is a ultraviolet momentum cutoff and should be interpreted as the energy scale up to which the Standard Model is valid. This introduces a quadratic term into the correction factor. Assuming that Λ_{UV} would be near the Planck scale M_P, the top alone, which has a Yukawa coupling of $\lambda_t \approx 1$, will lead to a correction which is 30 orders of magnitude higher than the current experimental value of μ^2 [12].

There are several approaches to compensate this quadratic correction factors. Without any extensions to the Standard Model this quadratic divergence is compensated by careful renormalization. This requires substantial fine tuning and is directly dependent on the correct value of Λ_{UV}, artificially setting the correct value of the vacuum expectation value to the experimental value without any physical motivation [15].

The introduction of an additional symmetry, called Supersymmetry [16], provides an elegant solution to this problem, also offering potential solutions for other open issues of the SM, as discussed in the following.

2.2 Supersymmetry

2.2.1 Motivation: A Solution to the Hierarchy Problem

Assume a scalar particle S of mass m_S. This would introduce a term of $-\lambda_S|\Phi|^2|S|^2$ into the Lagrangian and could interact with the Higgs via a loop diagram as shown in Figure 2.3(b). This loop yields a correction factor of:

$$\Delta\mu^2 = +\frac{\lambda_S}{16\pi}\Lambda_{UV}^2 + \dots \tag{2.9}$$

By comparing the corrections of Equation 2.8 with Equation 2.9, one can see that they are of similar magnitude, but with opposite sign.

By introducing an overlying particle symmetry, i.e. a super symmetry, this can be used to tackle the Hierarchy problem. Assuming that for each fermion there is a pair of two bosonic partners (one for the right-handed fermion and one for the left-handed fermion), each of them with a Yukawa coupling of

$$|\lambda_f|^2 = \lambda_S \equiv \lambda, \tag{2.10}$$

the corresponding loop corrections would cancel:

$$\Delta\mu^2 = -\frac{\lambda}{8\pi}\Lambda_{UV}^2 + 2\frac{\lambda}{16\pi}\Lambda_{UV}^2 + \dots \tag{2.11}$$

Due to this supersymmetry, or SUSY, of fermions and bosons all higher corrections which were not written in the above equations do cancel, as well, presenting a valid solution to the Hierarchy problem.

2.2.2 SUSY Algebra

The underlying operator of this supersymmetry is called Q. It acts as a generator by adding or subtracting a spin of 1/2, turning a boson in a fermion and vice versa:

$$Q\,|\text{Boson}\rangle = |\text{Fermion}\rangle \qquad\qquad Q\,|\text{Fermion}\rangle = |\text{Boson}\rangle \tag{2.12}$$

Q and its hermitian conjugate $Q^\dagger$ both are fermionic operators, carrying a angular momentum spin of 1/2. They are two-component spinors (Weyl-Spinors) and fulfill the following algebraic commutation relations:

$$\{Q_\alpha, Q^\dagger_{\dot\alpha}\} = -2\sigma^\mu_{\alpha\dot\alpha}P^\mu, \tag{2.13}$$

$$\{Q_\alpha, Q_\beta\} = \{Q^\dagger_{\dot\alpha}, Q^\dagger_{\dot\beta}\} = 0, \tag{2.14}$$

$$[P^\mu, Q_\alpha] = \left[P^\mu, Q^\dagger_{\dot\alpha}\right] = 0, \tag{2.15}$$

where P^μ is the four-momentum generator of spacetime translations, and σ are the Pauli-Matrices. In addition Q commutes with the generators of the gauge transformations.

As a consequence the quantum numbers of the state are not changed by Q. In particular the transformed and the original state have the same mass.

The irreducible representation of single particle states in this algebra are supermultipletts, which consist of an equal number of bosons and fermions. These bosons and fermions are superpartners of each other. In the naming scheme of supersymmetry all superpartners to fermions, which are scalars, get an s in front of their name (sfermions, squarks, sleptons, ...), while the superpartners of bosons get an additional -ino at the end (e.g. wino, higgsino, ...).

2.2.3 The Minimal Supersymmetric Extension of the Standard Model (MSSM)

There are several types of supermultipletts. The usage of the two simplest ones to represent the particles of the Standard Model (together with their respective superpartners) is called the Minimal Supersymmetric extension of the Standard Model (MSSM).

The first supermultiplett is called the *chiral* or *scalar* supermultiplett. It has a fermionic two component Weyl spinor (corresponding to two fermions) and two complex scalar bosons (spin 0). Most notable is that the chiral supermultiplett is the only one that can contain fermions where the left and the right-handed states transform differently under the gauge group transformation. As this is the case for all SM fermions, they are part of chiral supermultipletts.

The *gauge* or *vector* supermultiplett on the other hand has a single boson with two helicity states (spin 1) with a massless spin 1/2 Weyl spinor as superpartner, again with two helicity states. These are used for the SM gauge bosons.

The Higgs boson, as it is a spin 0 particle, would be part of a chiral supermultiplett. However, having only a single supermultiplett would lead to a gauge anomaly. Instead the Higgs is represented using two chiral supermultipletts, where the Higgs scalar is divided into an up type Higgs $\mathrm{H_u} = (\mathrm{H_u^+}\ \mathrm{H_u^0})$ coupling to u,c,t and one down type $\mathrm{H_d} = (\mathrm{H_d^0}\ \mathrm{H_d^-})$ coupling to d,s,b. The Standard Model Higgs is represented through a mixing of $\mathrm{H_u^0}$ and $\mathrm{H_d^0}$.

A list of all supermultipletts is shown in Table 2.2. The l and r indices denote the helicity in case of the Standard Model fermions. However, their superpartners are scalars and hence have no helicity. In that case the index denotes the helicity state of the corresponding superpartner.

2.2.4 R-Parity

The most general form of a supersymmetric Lagrangian would include terms that allow for both Baryon number B and Lepton number L violation. Such a violation has never been observed in nature. A prominent example is the decay of the proton, which is experimentally known to have a half-life greater than 10^{32} years [17]. Baryon number violation, however, introduces decay chains which can lead to a lifetime in the order of fractions of a second. Hence in the MSSM the R-parity is introduced. It is defined as

$$P_R = (-1)^{3(B-L)+2s}, \tag{2.16}$$

name	spin 0	spin 1/2
squarks, quarks (× 3 families)	$(\widetilde{\mathrm{u}}_\mathrm{l}\ \widetilde{\mathrm{d}}_\mathrm{l})$ $\widetilde{\mathrm{u}}_\mathrm{r}$ $\widetilde{\mathrm{d}}_\mathrm{l}$	$(\mathrm{u}_\mathrm{l}\ \mathrm{d}_\mathrm{l})$ u_r d_l
sleptons, leptons (× 3 families)	$(\widetilde{\nu}_\mathrm{l}\ \widetilde{\mathrm{e}}_\mathrm{l})$ $\widetilde{\nu}_\mathrm{r}$ $\widetilde{\mathrm{e}}_\mathrm{r}$	$(\nu_\mathrm{l}\ \mathrm{e}_\mathrm{l})$ ν_r $\widetilde{\mathrm{e}}_\mathrm{r}$
Higgs, higgsinos	$(\mathrm{H}_\mathrm{u}^+\ \mathrm{H}_\mathrm{u}^0)$ $(\mathrm{H}_\mathrm{d}^0\ \mathrm{H}_\mathrm{d}^-)$	$(\widetilde{\mathrm{H}}_\mathrm{u}^+\ \widetilde{\mathrm{H}}_\mathrm{u}^0)$ $(\widetilde{\mathrm{H}}_\mathrm{d}^0\ \widetilde{\mathrm{H}}_\mathrm{d}^-)$

name	spin 1/2	spin 1
gluino, gluon	$\widetilde{\mathrm{g}}$	g
wino, W-boson	$\widetilde{\mathrm{W}}^\pm\ \widetilde{\mathrm{W}}^0$	$\mathrm{W}^\pm\ \mathrm{W}^0$
bino, B-boson	$\widetilde{\mathrm{B}}$	B

Table 2.2: The supermultipletts. Left table contains the chiral supermultipletts with spin-0 complex scalars and spin-1/2 left-handed two-component Weyl fermions. The right table shows the gauge supermultipletts.

reinstating baryon B and lepton L number conservation. Note that s denotes the spin of the particle. As the two superpartners of a supermultiplett differ by spin 1/2, they do have opposite R-parity. Standard Model particles and the Higgs bosons have even R-parity ($P_R = +1$), while the new supersymmetric particles have odd R-parity ($P_R = -1$).

As a direct consequence of the R-parity the lightest supersymmetric particle (LSP) must be stable, and every heavier supersymmetric particle must finally decay into an odd number of LSPs (usually only one). In addition if the LSP is electrically neutral, it only interacts through the weak force, making it a potential Dark Matter candidate.

2.2.5 Mass Eigenstates

Note that the supermultipletts only represent the gauge eigenstates. The mass eigenstates on the other hand can be the result of mixing of the gauge eigenstates. This affects all supersymmetric particles with the exception of the gluino as it is a color octet fermion and thus cannot mix with other MSSM particles. Due to the large Yukawa-couplings the mixing is most prominent for third family squarks and sleptons, while the first and second family have only negligible mixing angles. For example, the left and the right handed stop $\widetilde{\mathrm{t}}_\mathrm{l}, \widetilde{\mathrm{t}}_\mathrm{r}$ often mix to the mass eigenstates $\widetilde{\mathrm{t}}_1$ and $\widetilde{\mathrm{t}}_2$. The same applies for the sbottom.

A more prominent example, however, is the mixing of the gauginos (without the gluino) and the higgsinos, building a set of neutral (neutralinos) or charged (charginos) fermions. These are denoted with $\widetilde{\chi}^0_{1,2,3,4}$ and $\widetilde{\chi}^\mp_{1,2}$ respectively, and are numbered based on their increasing mass. Especially the lightest neutralino $\widetilde{\chi}^0_1$ is of interest, as in most SUSY models it is the lightest supersymmetric particle (LSP). The exact mixing relations are subject to the different SUSY models and their respective parameters.

2.2.6 Soft SUSY Breaking

In Supersymmetry, as we have seen in the previous section, the quantum numbers (with the exception of the spin) and the mass of two superpartners are identical. Hence these new supersymmetric particles should have been discovered at various experiments, which is not the case. One way out of this dilemma is the assumption that Supersymmetry is a broken symmetry. Just as the spontaneous symmetry breaking at the weak scale gives mass to the gauge bosons in the Standard Model via the Higgs mechanism, the superpartners could gain their increased mass in a similar way.

However, such a breaking of the supersymmetry has to be soft, as otherwise the assumed relation in Equation 2.10 between the bosonic and fermionic Yukawa couplings might not hold, leaving us the divergent loop corrections to the Higgs mass and reintroducing the hierarchy problem:

$$\Delta\mu^2 = \frac{1}{8\pi}\left(\lambda_S - |\lambda_f|^2\right)\Lambda_{UV}^2 + \dots \tag{2.17}$$

Mathematically this soft breaking is introduced by an additional term in the Lagrangian:

$$\mathcal{L} = \mathcal{L}_{\text{SUSY}} + \mathcal{L}_{\text{soft}}, \tag{2.18}$$

where $\mathcal{L}_{\text{SUSY}}$ is the unbroken SUSY Lagrangian including all gauge and Yukawa interactions and $\mathcal{L}_{\text{soft}}$ breaks SUSY, but only contains positive mass contributions. If the largest of these masses is m_{soft}, this leads to a correction to the Higgs mass of the form of

$$\Delta\mu^2 = m_{\text{soft}}^2\left[\frac{\lambda}{8\pi^2}\ln\left(\frac{\Lambda_{UV}}{m_{\text{soft}}}\right), + \dots\right] \tag{2.19}$$

where λ denotes various dimensionless couplings. The Higgs mass is thus only logarithmically dependent on Λ_{UV}, which is significantly lower compared to the quadratic dependence before. Therefore, if SUSY is to provide a solution to the hierarchy problem, this small dependence implies that the mass splitting between m_{soft} and the Standard Model particles cannot be too large, with expected SUSY masses at around the 1 TeV scale.

Supergravity

A phenomenological motivation for an additional term of $\mathcal{L}_{\text{soft}}$ in the Lagrangian is not obvious. In general it is attributed to a "hidden sector", which contains many different particles which do not at all or only extremely weak couple directly to the "visible" particles which are the known chiral supermultipletts. The symmetry breaking is mediated to the visible sector via flavour-blind interactions (cf. Figure 2.4).

There are several models describing these mediating interactions. Amongst the more popular ones is the Planck-Scale-mediated SUSY breaking (PMSB), in which SUSY is broken by new physics, including gravity, at the Planck scale M_P. Hence it is sometimes called supergravity, or SUGRA.

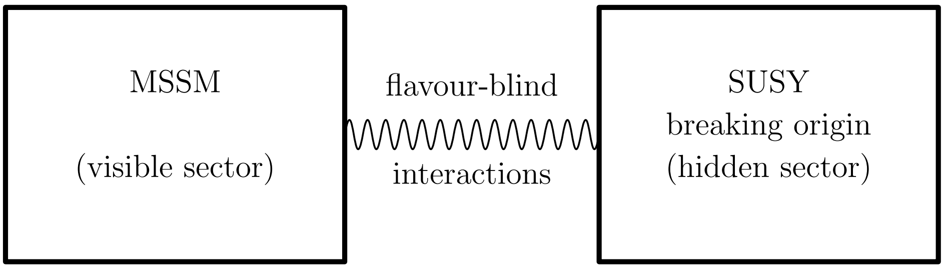

Figure 2.4: Schematic on the presumed process of breaking Supersymmetry via a flavour-blind interaction with a hidden sector.

The resulting terms for $\mathcal{L}_{\text{soft}}$ in the case of the MSSM require additional parameters such as mass terms for the bino M_1, wino M_2, the gluino M_3, and the remaining quarks, leptons and the higgs as well as their Yukawa coupling strength, their phases and mass mixing parameters. In total these add up to 105 [18].

The Constrained Minimal Supersymmetric Model

In the case of the constrained Minimal Supersymmetric Model (cMSSM), sometimes called mSUGRA for minimal supergravity, this high number of parameters is artificially reduced by sorting the parameters in five different groups [12]. All parameters within a group share a single common value valid at the renormalisation scale of $Q = M_P$, thus reducing the total number of parameters to five.

One example is the grouping of the mass parameters for the bino M_1, the wino M_2 and the gluino M_3, and setting them all to the same value, called the gaugino mass $m_{1/2}$:

$$m_{1/2} \equiv M_1 = M_2 = M_3 \qquad \text{(cMSSM)} \tag{2.20}$$

The remaining four parameters are the Higgs field mixing parameter μ, the ratio of the VEVs of the two Higgs fields $\tan\beta$, the parameter A_0 and the scalar mass m_0.

Note that even though through this grouping many of the original mass parameters share the same value, they only do so at the renormalisation scale. Through the soft SUSY breaking the mass hierarchy of the cMSSM still allows for different masses of all particles, and they might differ significantly from their corresponding renormalisation scale values.

There are some simple extensions to the cMSSM where the gauge mass $m_{1/2}$ is not used. Instead the three gauge mass parameters for the bino M_1, wino M_2 and gluino M_3 are set individually, as in the non cMSSM case, and thus the relation in Equation 2.20 does not hold anymore. Such a model is used for the CLIC CDR benchmark process in chapter 5.

SUSY Search Status

Both of the two general purpose experiments ATLAS and CMS operating at CERN at the Large Hadron Collider pursue the search for new physics, including supersymmetric particles. The latest results published by CMS[19] which were based on the data collected 2012, corresponding to an integrated luminosity of $\int \mathrm{d}t\mathcal{L} = 10.5\,\mathrm{fb}^{-1}$ at 8 TeV, indicate no excess above the expected Standard Model background. Instead it was possible to impose lower mass limits on the particles. For example for the assumption on the decays of stops, sbottoms and lightest chargino as $\widetilde{\mathrm{t}}_1 \to \mathrm{t}\widetilde{\chi}^0_1$, $\widetilde{\mathrm{b}}_1 \to \mathrm{t}\widetilde{\chi}^-_1$ and $\widetilde{\chi}^-_1 \to \mathrm{W}^-\widetilde{\chi}^0_1$, the limit for gluinos is about 1 TeV and about 450 GeV for sbottom.

Chapter 3

Future Lepton Colliders and their Detector Systems

As it was discussed in detail in section 2.1, the Standard Model, although it describes three of the four known forces with high precision, cannot be the ultimate theory. Hence further investigations on the fundamental forces of nature are necessary, for which particle accelerators are used.

This chapter will first give a short motivation on why a lepton collider is necessary for these measurements (cf. section 3.1), before introducing the concept of the Compact Linear Collider in section 3.2. At these colliders particle detectors are used for the measurement of the physics processes. In section 3.3 their underlying physical principles are introduced, before a detector concept for CLIC based on the International Large Detector (ILD) is discussed in section 3.4. One of the prototypes of a hadronic calorimeter, which was built in the context of the Calorimeter for a Linear Collider Experiment (CALICE) collaboration, will be introduced in section 3.5. Finally the simulation of events at detectors will be discussed in section 3.6.

3.1 Lepton Collider: A Complementary Accelerator to the LHC

The search for the Higgs Boson along with possible extensions to the Standard Model were among the driving arguments behind the construction of the Large Hadron Collider (LHC). The LHC was built in a tunnel at CERN with a circumference of 27 km and was designed to collide two proton beams with a center-of-mass energy of up to 14 TeV.

There are different types of colliders which are distinguished based on the particles used: lepton colliders and hadron colliders. As the colliding particles are protons, the LHC is a hadron collider. One of their big advantages is that it is easier to increase the center-of-mass energy at hadron colliders than at lepton colliders due to reasons that will be discussed later on. Furthermore the production processes available at leptons colliders are limited to the electroweak force, whereas the quarks and the gluons in the hadrons carry color charge and thus allow QCD processes in addition. Depending on the desired final state particles, this can increase the production cross-section dramatically. Thus as hadron colliders have typically a higher center-of-mass energy and can have higher production cross-sections than lepton colliders, they are the ideal tool for the discovery of yet unknown high energetic particles.

However, hadrons and thus protons have a substructure consisting of many partons. The amount of the total proton momentum shared amongst the partons is described by Parton Distribution Functions. These partons are the particles that undergo the actual hard process of the collision. As the amount of momentum carried by the colliding partons is a priori not known, there is no way to predict the total energy sum available for the hard process. Instead it can be anywhere in between no collision at all and the maximum collision energy, which is 14 TeV in the case of the LHC. Additionally, the remaining partons of the protons which do not contribute to the event, i.e. the proton remnants, lead to the creation of additional background particles in an "underlying event". As leptons have no (known) substructure, underlying events are not possible and the available center-of-mass energy prior to the collision is known at lepton colliders, thus giving additional information on the event.

Furthermore the high cross-section for QCD processes applies to signal and background. On the one hand there are technical limitations. An accelerator is not using single protons for the collisions but bunches of protons. Thus more than one collision can occur per proton bunch crossing, leading to "pile-up" of events. For the period of 2011 and 2012 where the LHC ran with a reduced center-of-mass energy and luminosity, the average number of p p collisions per bunch crossing was already between 9 and 19 [9]. In addition the time between two bunch crossings is only 25 ns at the LHC. Some of the detector systems are not fast enough to perform their readout in this short time frame, and thus events from the subsequent collision overlay over the previous one. This effect contributes to the pile-up and is not an exclusive feature of hadron accelerators, but can happen at leptons colliders, as well. While it is possible to identify the individual underlying and pile-up events using advanced techniques such as vertexing and time stamping, the event reconstruction is still a challenging task. However, in addition events originating from the signal process can be hard to distinguish from physics background events. Starting with soft QCD processes up to processes mimicking the desired event topology, the cross-section of the signal process is typically several orders of magnitude smaller when being compared to the total cross section of all processes. Therefore a very sophisticated background rejection is necessary.

Thus for precision measurements a lepton collider is preferred, as it provides a much cleaner environment without any of the contributions from underlying events and only limited event pile-up. Moreover the difference between the signal and the total cross-section is typically not as high as at hadron colliders. Most importantly, however, leptons have no (known) substructure. Hence the initial state is known with much higher precision and this information can be used during the analysis, for example when searching for events with missing energy. This can even be used to perform a threshold scan, i.e. the collision energy is slowly increased around a certain threshold of a process, such as for example the top-pair-production around 350 GeV, to gain an even higher precision on measurements such as the particle mass.

The usage of a lepton collider as a tool for precision measurements in contrast to the usage of hadron colliders for the discovery of new particles is historically well established. The weak gauge bosons for example were detected at the Super Proton Synchrotron (SPS) [20][21], while their properties have been measured at the Large-Electron-Positron (LEP) collider [22]. This, however, does not mean that they are exclusively used for precision measurements. Electro-weak processes are difficult to measure at a hadron collider, due to the high QCD background. In contrast lepton colliders exclusively use electro-weak processes for the production, and thus can be used not only for precision measurements, but for the discovery (or exclusion) of particles coupling strongly or even exclusively to the electro-weak force, as well. One example is the discovery of the J/ψ particle and with it the c quark by Burton Richter at the $e^+ e^-$ SPEAR accelerator [23].

Recently the two general-purpose experiments ATLAS and CMS at the LHC have discovered the existence of the Higgs boson when both collaborations found evidence for a particle with spin 0 within the expected mass range at approximately 125 GeV [8][9]. The precise measurements of it's properties such as mass, cross-section, decay modes and couplings to fermions, bosons and self-coupling can yield more insight in the consistency of the SM and can give hints on possible extensions. Hadron colliders such as the LHC do contribute to these measurements. However, for the reasons mentioned above experiments at lepton colliders yield typically in a higher precision or can even perform measurements that are not accessible to hadron colliders. Thus for high precision measurements of, among others, the properties of the Higgs the LHC, too, needs a complementary lepton collider in the TeV energy range.

3.2 The Compact Linear Collider

The Compact LInear Collider (CLIC), as the International Linear Collider (ILC) is a concept of a linear $e^+ e^-$-accelerator. Although these two concepts differ in their acceleration technology and their center-of-mass energy, they do share a lot of common development, especially on the detector side. This section will explain why a linear collider is necessary before focusing on the CLIC concept.

3.2.1 Requirements

Depending on the actual measurements that are planned to be done at a new lepton collider, the center-of-mass energy and the luminosity must be high enough.

Higgs coupling to Z and branching ratios can be measured for energies at or above approximately 250 GeV. A top threshold scan on the other hand needs an energy around 350 GeV, whereas measurements on the coupling between Higgs and top or the Higgs self coupling needs at least 500 GeV. Physics beyond the Standard Model might be found already at 500 GeV in the weak sector. However, chances for discovering new particles increase with an center-of-mass energy in the multi-TeV range. As most of the measurements above can not only be done at higher energies, as well, but actually gain from the increase in energy, the goal should be an multi-TeV accelerator.

The cross-section of s-channel processes drops with $\sqrt{s}$ at lepton colliders in general. In addition some of the expected processes such as the creation of new particles are very rare. Thus the instantaneous luminosity must be in the order of several $10^{34}\,\mathrm{cm}^{-2}\mathrm{s}^{-1}$ in order to generate enough data for precision measurements.

Lastly in the order for the new lepton collider to be feasible, the overall size of the machine should be in the same order as the one of LHC which had a circumference of 27 km.

3.2.2 Reasons for a Linear Collider

Particles in circular accelerators, such as at the LHC or LEP, suffer from synchrotron radiation. It is a special form of Bremsstrahlung coming from the constant acceleration of the particles towards the center of the ring which is necessary to keep the particles on their circular path. For particles of charge e at energy E, the power P that is lost and has to be permanently added to the beam just to keep the momentum of the particles constant, is inversely proportional to the square of the colliders radius R, and increases with the 4-th power to the particle energy:

$$P = \frac{\mathrm{d}E}{\mathrm{d}t} \approx \frac{2ce^2}{3}\frac{\gamma^4}{R^2} = \frac{2ce^2}{3R^2}\left(\frac{E}{m_0c^2}\right)^4 \tag{3.1}$$

At LEP, which was the biggest lepton collider so far with an energy per beam of about 100 GeV at a circumference of 27 km, the synchrotron radiation was already the limiting factor. A lepton collider that is complementary to the LHC needs to be able to reach a center-of-mass energy of between a few hundred GeV and a few TeV, depending on its exact purpose. Assuming a center-of-mass energy of 1 TeV, the LEP beam energy must be increased to 500 GeV per beam, which is a factor of 5. If one wants to maintain the level of energy loss originating from synchrotron radiation from LEP ($P_{\mathrm{new}} = P_{\mathrm{LEP}}$), the new accelerator would need to have a radius of

$$R_{\mathrm{new}} = \left(\frac{5E_{\mathrm{LEP}}}{E_{\mathrm{LEP}}}\right)^2 \cdot R_{\mathrm{LEP}} = 5^2 \cdot 4.3\,\mathrm{km} = 107.4\,\mathrm{km}. \tag{3.2}$$

This corresponds to a circumference of 675 km, which is clearly infeasible to build.

One way to reduce the synchrotron radiation and thus keeping the radius within feasible limits is to use heavier particles. As the mass m contributes with the inverse of the 4-th power to the synchrotron radiation power loss, this compensates the increase in energy. Hence at the LHC protons are used which are a factor of 2000 heavier than electrons. Consequently the LHC can reach energies of up to 7 TeV per beam without being limited by the synchrotron radiation. Instead the limiting factor in case of the LHC is the maximum achievable magnetic field which holds the protons on their circular path. Compared to LEP, LHC reaches a center-of-mass energy that is a factor of 70 higher although both accelerators use the same tunnel.

In the charged lepton sector the next heaviest particle after the electron is the muon. Its mass is over 200 times larger than the one of the electron and hence would be a perfect candidate to build a new lepton collider [24]. However, within the charged lepton domain only the electron is stable. Muons on the other hand decay within a few μs. Hence, the time to collect and accelerate the muons is very limited, and requires a sophisticated method of "cooling" the muon beam before its acceleration, which is not yet in a state to be used at an accelerator.

Instead the concept that will be discussed here avoids synchrotron radiation altogether by using a linear as opposed to a circular accelerator. This, too, places stringent requirements on the technology to provide a feasible solution. Especially the overall size of the accelerator complex has to be in the same order as the circumference of the LEP/LHC tunnel. However, unlike at a storage ring particle bunches cannot be reused at a linear accelerator. Thus, the bunches need to reach their final energy in a single acceleration stage. Depending on the desired collision energies and the maximal tunnel length this translates into a requirement on the acceleration gradient of 30 to 100 MeV/m and above.

3.2.3 A new Acceleration Technology: CLIC

The Compact LInear Collider (CLIC, [25][26]) is a concept of a new electron-positron collider which can act as a complementary machine to the LHC. Its key features are:

- A center-of-mass energy of 3 TeV. The exact value is subject to yet to be made results from the LHC and as such the choice of 3 TeV is arbitrary.
- An instantaneous luminosity in the order of several $10^{34}\,\mathrm{cm}^{-2}\mathrm{s}^{-1}$. This is achieved by a strong focusing of the beam combined with a low beam emittance and a large number of electrons (positrons) per bunch of more than $10^9\,\mathrm{e}^{\pm}$/bunch.
- To keep the overall length of the accelerator in a feasible region of about 50 km, the acceleration gradient has to be greater than 100 MeV/m.

Classically at colliders bunches of charged particles are accelerated using cavity resonators. These generate resonances of strong electrical fields when a high powered radio frequency (RF) is coupled in. This field in turn is used for the acceleration of the particles, during which energy is extracted from the field and transferred to the particles. Thus in order to maintain the desired field strength and thus acceleration gradient, the RF has to be of high intensity. In addition at CLIC the RF needs to be in the order of 12 GHz to prevent sparks or strong surface heating in the cavities which leads to a breakdown of the electrical field and can damage the cavities.

Such high powered radio frequencies can only be created by klystrons. Still, the power output of a single klystron is limited, and even through combination the power necessary for the acceleration $10^9\,\mathrm{e}^{\pm}$/bunch is not feasible. Instead CLIC uses a different approach: While the klystrons can continuously generate the RF, the duty cycle of the main accelerator is very low, i.e. it is not active for most of the time. Thus a viable solution would be to temporarily "store" the energy generated by the klystrons and wait until enough energy has built up such that compressing it would be enough for the peak power output to reach the desired threshold necessary for the acceleration. At CLIC this is achieved by storing the energy in a secondary beam which is then compressed.

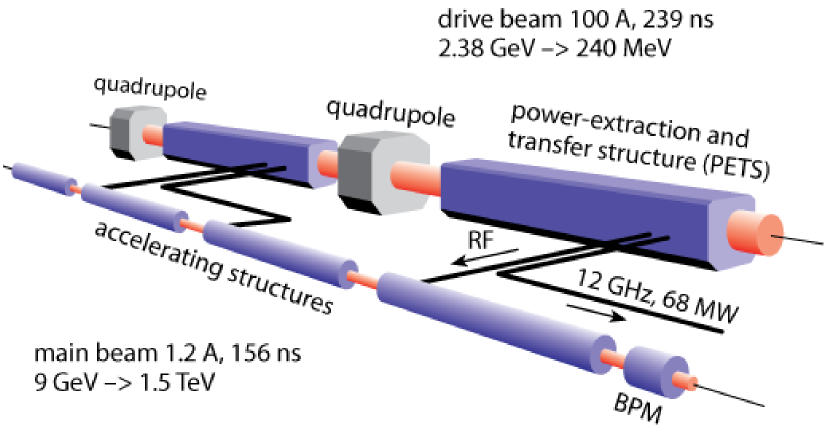

Figure 3.1: The two beam acceleration scheme used at CLIC.

As this requires two beams instead of one, this scheme is called Two-Beam-Acceleration (TBA) scheme.

Two-Beam-Acceleration (TBA) scheme

The secondary beam is called drive beam as opposed to the main beam. It is first generated with a bunch spacing frequency of 0.5 GHz. The compression of the drive beam is performed by a sophisticated series of delay loops and combiner rings, such that 24 original bunches are combined into a single one and the bunch spacing frequency is multiplied by another factor of 24 to 12 GHz. Thus the peak intensity is $24 \times 24 = 576$ times higher than the one from the uncompressed drive beam and reaches values of over 100 A with a relatively low energy of 2.38 GeV.

The drive beam is lead through power-extraction and transfer structures (PETS), where it induces electrical fields and thus the desired radio frequency. As shown in Figure 3.1 this RF can be transferred to the main beam line where it is used to accelerate the electron (positron) bunches.

The layout of the CLIC concept for 3 TeV is shown in Figure 3.2. It has a total length of 48.3 km including beam delivery systems. The complete set of parameters is shown in Table 3.1.

As a consequence of this complicated drive beam generation and in order not to damage the main beam acceleration cavities by too long exposure to the high intensity electric field, only a total of 312 bunches are able to be accelerated within a bunch train of 156 ns. Thus the bunch crossing rate is at 2 GHz (0.5 ns). With a bunch train repetition rate of 50 Hz an instantaneous luminosity $\mathcal{L}$ of $5.9 \times 10^{34}\,\mathrm{cm}^{-2}\mathrm{s}^{-1}$ is achieved. However, due to beamstrahlung individual particles lose energy causing the beam energy spectrum not to have a single peak at the expected 1.5 TeV, but instead being a distribution. Only 35% of the collisions have an energy above $0.99\sqrt{s}$, reducing the instantaneous luminosity to $\mathcal{L}_{0.01} = 2.0 \times 10^{34}\,\mathrm{cm}^{-2}\mathrm{s}^{-1}$. In total a CLIC based accelerator including detectors would have a an estimated power consumption of

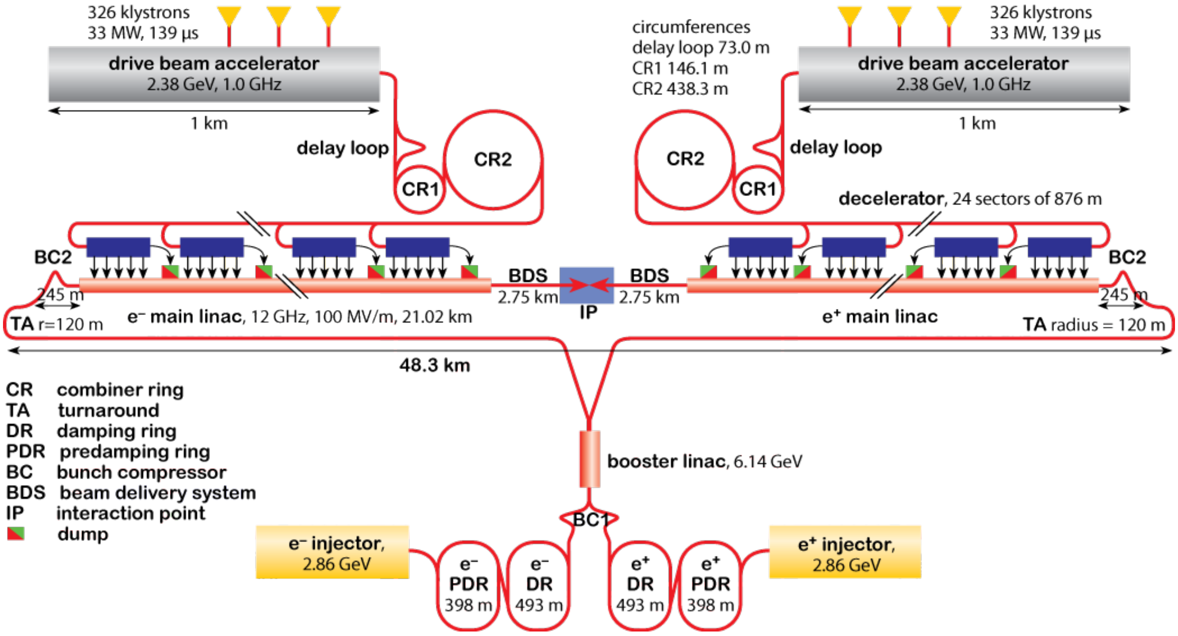

Figure 3.2: The Layout of the Compact Linear Collider.

Parameter	Symbol	Unit	Value
Center-of-mass energy	$\sqrt{s}$	GeV	3000
Repetition frequency	f_{rep}	Hz	50
Number of bunches per train	n_b		312
Bunch separation	Δ_t	ns	0.5
Accelerating gradient	G	MV/m	100
Total luminosity	$\mathcal{L}$	$10^{34}\,\mathrm{cm}^{-2}\mathrm{s}^{-1}$	5.9
Luminosity above 99% of $\sqrt{s}$	$\mathcal{L}_{0.01}$	$10^{34}\,\mathrm{cm}^{-2}\mathrm{s}^{-1}$	2
Main tunnel length		km	48.3
Charge per bunch	N	10^9	3.7
Bunch length	σ_z	μm	44
IP beam size	σ_x/σ_y	nm	$\approx 40/1$
Normalized emittance	ϵ_x/ϵ_y	nm	660/20
Estimated power consumption	P_{wall}	MW	589

Table 3.1: The parameters of the CLIC accelerator [26].

589 MW.

Beam induced Background

There are different sources for beam related background at CLIC. One of these processes is the production of coherent and incoherent pairs of e^+ e^- through interaction of beamstrahlung induced photons with either the collective field (coherent) or individual particles (incoherent) of the opposing beam. Another is the creation of hadrons via the interaction of virtual or real photons of the colliding beams: $\gamma\gamma \rightarrow$ hadrons.

Particles produced by either of these processes tend to have low angles. Hence many of these leave the detector volume without being detected. Others, however, are added to the particles of the physics event and have to be rejected. Details on these background and their influence on the analysis will be discussed in subsection 3.4.4 and subsection 5.2.3.

3.3 Detectors at Colliders: Interaction of Particles with Matter

The goal of a collider is to measure fundamental physics processes. As there is no way of observing the actual process, the processes can only be identified by their initial and final state particles and their corresponding properties. At lepton colliders the properties of the initial state particles are mostly defined by the accelerator. However, the final state can only be identified by measuring the resulting particles using a detector.

Therefore a detector tries to measure the type, mass, flight path, momentum and energy of all created particles. Any kind of measurement requires some kind of interaction between the detector and the measuring object. In particle physics all known particles passing through matter will eventually perform some kind of ionization, i.e. deposit energy which in turn can be picked up by the detector. However, the exact type of interaction between the (detector) matter and the particle is subject to the particle type, its properties such as its energy, and the type of matter.

Therefore subdetectors specialize on the measurement of only specific properties (e.g. the energy) of a class of particles by focusing on certain interaction types. Through combination of these subdetectors most of the particles and their properties can be measured. A concrete example of such a detector will be given in the subsequent section. This section, however, will first give an overview on the different kind of interactions of particles with matter used by these detectors.

3.3.1 Neutrinos

Neutrinos ν are light-weight, point-like particles with no electrical charge. As their cross-section for the interaction with (detector) matter is negligible low, they are responsible for the missing (i.e. undetected) energy in Standard Model events.

3.3.2 Minimum Ionizing Particles

Fast moving electrically charged particles lose energy through ionization when passing through matter. The ionization comes from many single collisions with the bound atomic electrons, each collision with an energy loss E which is typically very small ($< 100\,\mathrm{eV}$). The total amount of deposited energy is dependent on many parameters, but first of all on the distance the particle travelles through the matter. Hence we will focus here on the mean energy loss per distance travelled $-\left\langle \frac{dE}{dx} \right\rangle$, which is called stopping power.

For particles in the range of $0.1 \lesssim \beta\gamma \lesssim 1000$ the relativistic Bethe equation[27] predicts the stopping power of a particle with charge $z \cdot e$ and speed βc when passing through an absorber material with atomic number A and atomic mass Z with an accuracy of a few per cent:

$$-\left\langle \frac{dE}{dx} \right\rangle = K \frac{Z}{A} \frac{z^2}{\beta^2} \left[\frac{1}{2} \ln \frac{2 m_e c^2 \beta^2 \gamma^2 T_{\max}}{I^2} - \beta^2 - \frac{\delta(\beta\gamma)}{2} \right] \tag{3.3}$$

$$K = 4\pi N_A r_e^2 m_e c^2 = 4.919883 \times 10^{-18}\,\mathrm{m^4 s^{-2} kg} \tag{3.4}$$

Here, I gives the mean excitation energy and $\delta(\beta\gamma)$ applies a density correction to the ionization loss. $T_{\max}$ denotes the maximum kinetic energy that can be transferred onto an electron in a single collision, and introduces a slight dependency on the mass of the particle. Apart from this small effect, the stopping power is only dependent on the momentum of the particle for a given absorber. Its distribution can be seen in Figure 3.3, which shows the stopping power for μ^+ in copper over a large momentum range, including the range in which the Bethe formula is valid.

The energy loss is minimal for particles with $\beta\gamma \approx 3 - 4$. As the increase of the stopping power up to $\beta\gamma \approx 1000$ is very moderate, all particles in this range are considered to be minimal ionizing and consequently are called *minimum ionizing particles* (MIP).

The Bethe equation is not valid for electrons as their collision with the atomic electrons requires that the spin and the identity of the two particles is accounted for. Furthermore it violates the assumption underlying to the Bethe formula that the mass of the incident particle is large, such that it is not deflected by the collisions with the atomic electrons. Nevertheless a formula similar to Equation 3.3 can be derived for electrons [28].

Thin absorbers: Landau Distribution

While the Bethe formula provides a good approximation of the mean value, the actual amount of energy deposited in the absorber material varies from event to event. In thin absorbers the number of collisions is limited and in 90% of these collisions only less than 100 eV is deposited. However, in the remaining 10% of the collisions, which are mainly delta electrons, the energy deposition can exceed this value by far. Thus, the total amount of energy deposited changes from event to event, depending on the types of the collisions, resulting in an asymmetric distribution. This distribution was calculated by Landau [29] and can be seen in Figure 3.4. The mean energy deposition

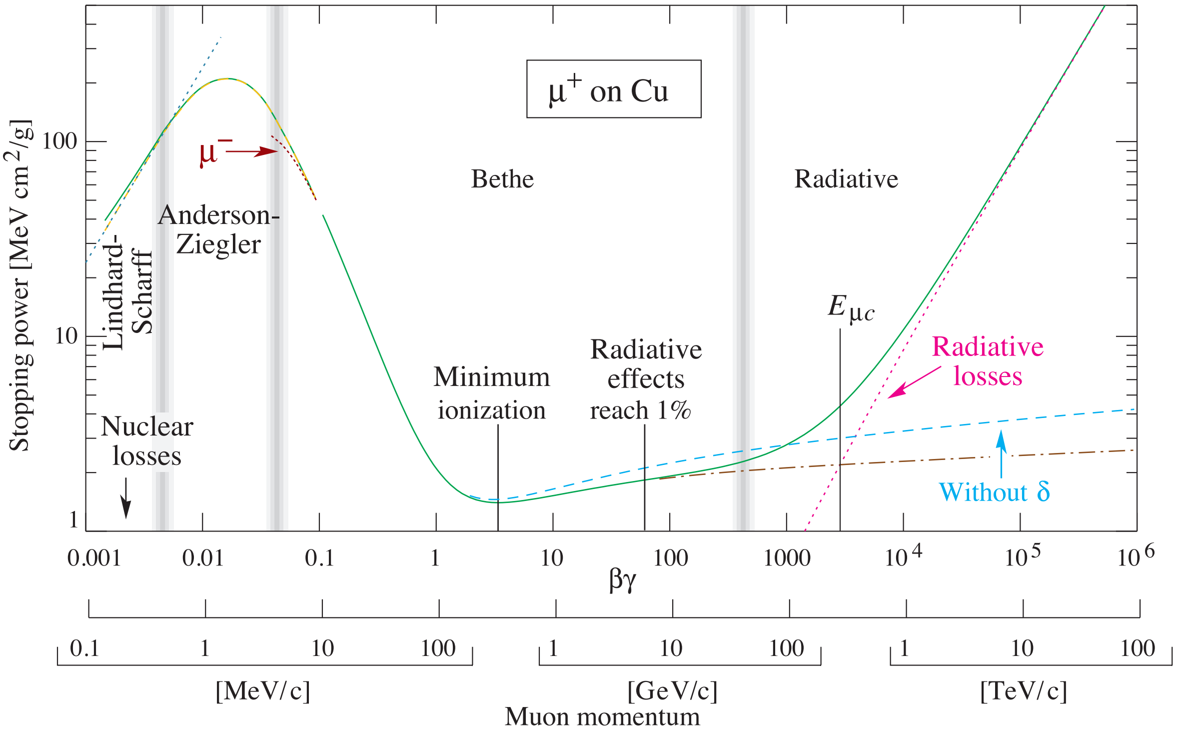

Figure 3.3: Mean energy loss per unit path ($-\left\langle\frac{dE}{dx}\right\rangle$) of μ^+ passing through copper in dependence of their momentum[14].

of minimum ionizing particles changes only in the order of a few per cent over the relevant momentum range. However, the most probable energy deposition, i.e. the peak of the landau distribution, changes even less. Consequently, it provides an excellent tool for the energy calibration of detectors. As the peak is created by the passage of a minimum ionizing particle, the energy unit is often called MIP and is defined as the most probable value (MPV) of the landau distribution. This definition of the energy scale is almost independent of the type and the momentum of the particle used for the calibration.

Note that the landau distribution is only describing the energy deposition of minimum ionizing particles in thin absorbers. However, all detectors used throughout this thesis can be considered thin.

Effect of Limited Detector Resolution on the Landau Distribution

The accuracy of the measurement of the deposited energy is limited by the detector's resolution. The resolution is often a result of many different effects, such as electronic noise, and is therefore characterized with a Gaussian, affecting every single measurement.

In the above case of the passage of charged particles through thin matter this is taken into account by convoluting the Landau distribution L with a Gaussian G. The resulting distribution of $L \otimes G$ is sometimes referred to as "Langau" and is the response of thin detectors towards passing charged particles.

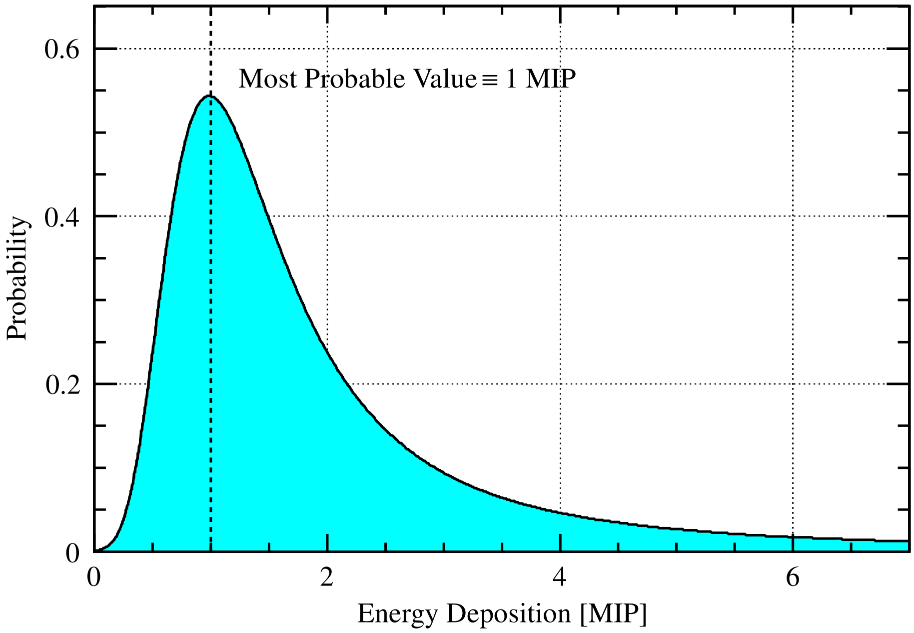

Figure 3.4: The Landau distribution, describing the amount of energy deposited by particles passing through thin detectors. Here the energy is given in units of MIP, which is defined as the most probable energy deposition which is marked by the dashed line.

3.3.3 Electromagnetic Showers

In addition to the energy deposition through ionization as described in the previous section, high energy electrons and positrons passing through matter emit photons. These come mainly from Bremsstrahlung due to the interaction with the atomic electrical field. These high energy photons undergo pair production, i.e. creating a pair of high energy electrons and positrons. In combination these two interactions result in a cascade of electrons, positrons and photons as illustrated in Figure 3.5. Such a cascade is called an electromagnetic shower.

At each step of the cascade the energy is distributed mainly among the newly created particles. Thus the cascade ends once photons have insufficient energy to perform pair production or the electrons (positrons) will not create additional high energy photons. The remaining energy is lost through multiple scattering until the particle is finally absorbed. Note that the number of particles created throughout the shower evolution is approximately proportional to the energy of the incident particle $N \propto E$.

The typical length of a step of the cascade is called radiation length X_0. It is defined as both the mean distance in which a high energy electron (positron) loses $1 - 1/e$ of its energy via Bremsstrahlung and as $7/9$ of the mean free path for pair production of high energy photons. The radiation length is dependent on the type and especially on the density of the absorber material. For dense materials such as steel it is in the order of a few cm and ca be as short as 3 mm for tungsten.

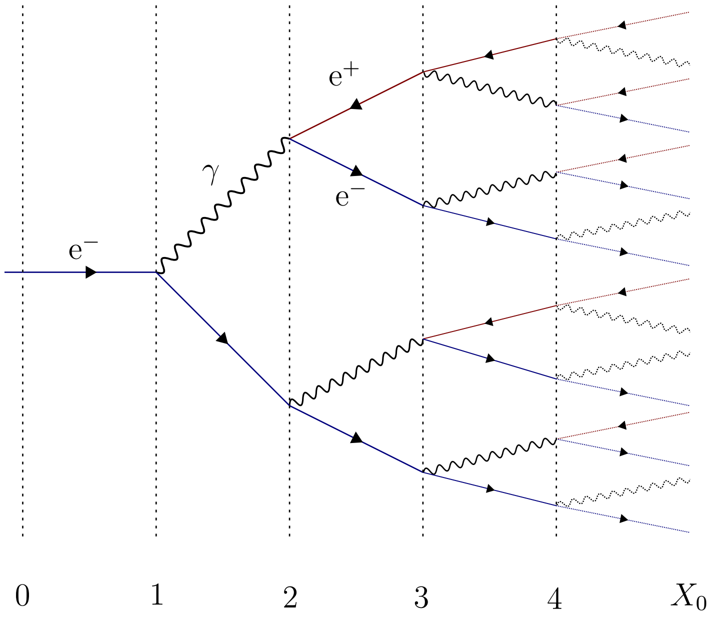

Figure 3.5: Schematics of the development of an electromagnetic shower starting with an electron.

3.3.4 Hadronic Showers

Highly energetic hadrons also create a particle cascade when passing through absorber material. These hadron showers are substantially more complex than the electromagnetic ones which were discussed in the last section.

Due to the higher mass of charged hadrons their energy loss due to Bremsstrahlung is irrelevant, and thus they do not directly induce electromagnetic cascades. Instead hadrons are capable of interacting with the absorber nuclei via the strong force. This is especially true for neutral particles for which, apart from seldom weak interactions, the strong force presents the only way of ionization.

The strong interaction between the hadronic projectile and the absorber nucleus enables a big set of different processes, most of which will lead to some kind of break up of the absorber nucleus. Such a break-up is called nuclear spallation[30].

Nuclear Spallation

Nuclear spallation can be divided into two phases.

In the first phase, sometimes called cascade phase, the incident hadron undergoes a series of quasi-free collisions with the nucleons, transferring part of its energy. The struck nucleons themselves collide with other nucleons, causing an intra-nuclear cascade.

At each of these collision the transferred energy can be used to create new hadronic particles if the projectile's energy is sufficient (pion production threshold is at $\mathcal{O}\,(1\,\mathrm{GeV})$). Most of these particles are light mesons such as π or K, but baryons such as p, n or Λ can be created as well, especially if the projectile is a baryon, too (baryon number conservation).

These particles are created in partonic interactions, i.e. only a parton of the projectile interacts with one parton of the nucleus, filling up the missing quarks to built the new particles by taking them from the "sea". As the remaining quarks are not participating, they are called spectator quarks. The spectator quarks of the projectile carry a significant part of its momentum and thus the new particle consisting of these spectator quarks does, too. Therefore this high energetic particle it is called leading particle.

The newly created particles and the nucleons with sufficient energy escape the nucleus in the same general direction as the projectile. Their energy is typically in the order of a few GeV and above. The intra-nuclear cascade is a pure QCD process and thus very fast ($\mathcal{O}\left(10^{-22}\,\mathrm{s}\right)$[31]).

In the second step of the nuclear spallation, which is called evaporation phase, the intermediate nucleus de-excites by emitting free nucleons (n, p), photons (γ) and sometimes heavier nucleons aggregates (α-particles, ...). Unlike the intra-nuclear cascade, the emissions are independent on the direction of the incident hadron and are distributed isotropically. These de-excitation emissions are only possible if the available energy of the nucleus is large enough to overcome the nucleons binding energy. Note that as protons have to overcome the Coulomb-Barrier on top, the number of created neutrons is typically higher than the number of protons. This is especially true for materials with a large atomic number Z, where the Coulomb-Barrier is larger. The escaping neutrons and protons have a typical energy of $1 - 10\,\mathrm{MeV}$. The nuclear de-excitation is considerably slower than the intra-nuclear cascade and takes about $\mathcal{O}\left(10^{-13} - 10^{-18}\,\mathrm{s}\right)$[31].

Note that for the release of nucleons in both phases energy is necessary to overcome the binding energy barrier. This energy is thus lost for ionization of the target material and hence is sometimes called invisible energy. It can make up of up to 30% of the entire non-EM component of the shower.

The Hadronic Cascade

The cascade is formed mainly by the secondary hadrons created during the intra-nuclear cascade, as they carry enough energy to induce further reactions.

One of these reactions is the induction of further spallation processes, creating additional secondary particles. Similar to the radiation length in electromagnetic cascades, the nuclear interaction length λ_I denotes the typical distance these hadron fly before the interaction. It is defined as the path x after which the number N of particles without interaction drops to the $1/e$ part of the number of incident particles N_0.

$$N(x) = N_0 \cdot e^{-\frac{x}{\lambda_I}} \tag{3.5}$$

As the cross section, i.e. the probability for such an interaction, is different for protons and pions, the nuclear interaction length has different values for pions. Hence a special pion interaction length λ_π is introduced. An example scheme of such a cascade is shown in Figure 3.6.

Another possible reaction is the decay of the hadron. Charged pions for example can decay via the weak process $\pi^\pm \to \mathrm{W}^\pm \to \mu^\pm\nu$, creating an undetectable neutrino

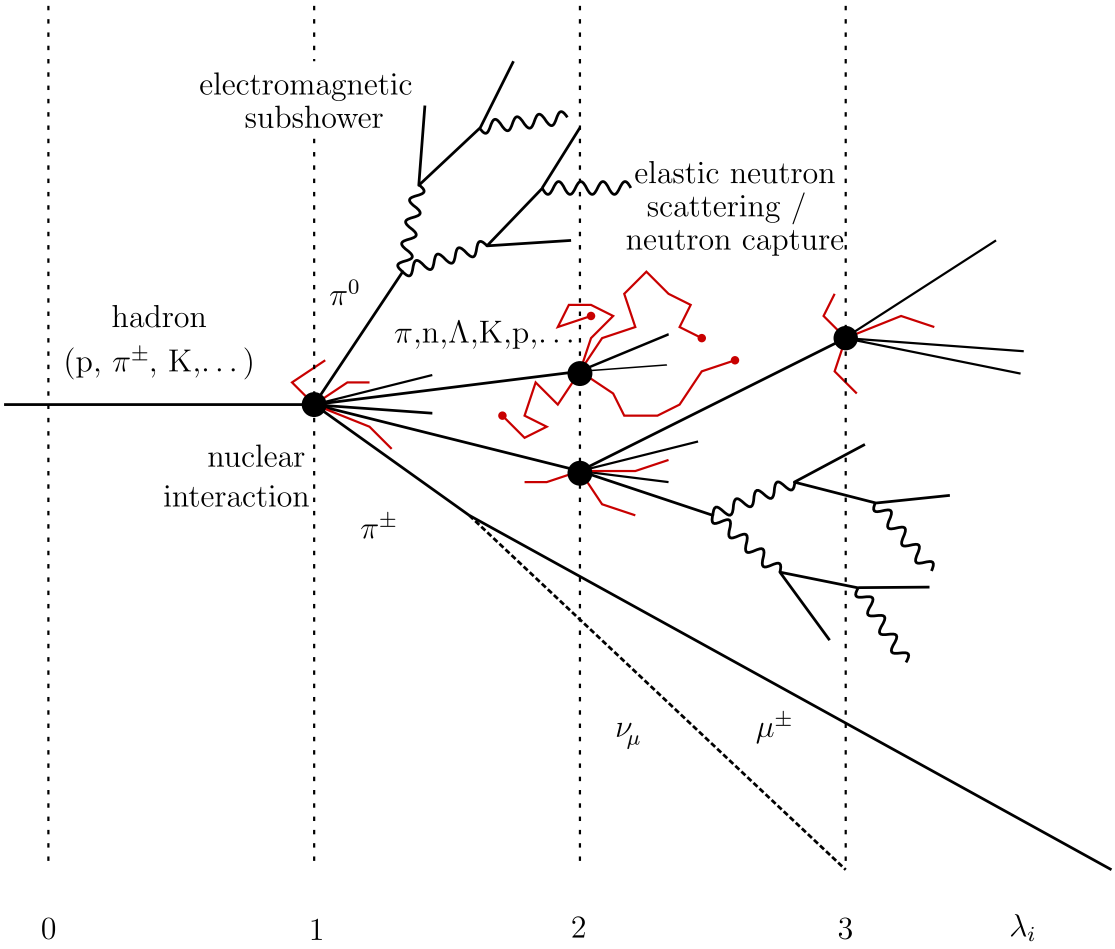

Figure 3.6: Example scheme of the development of a hadronic shower starting with a hadron. The high energetic fast spallation processes are marked by black dots, while the slower neutron capture and scattering is shown in red. For the sake of visibility not all particles are drawn. Especially the neutron capture is only shown at one of the spallation processes.

and a muon which performs MIP-like ionization before escaping the absorber material (lower part in Figure 3.6) without contributing any further to the development of the hadronic cascade.

Electromagnetic Subshower

A special case of decay processes within a shower is the decay of neutral pions π^0. Their average life time is extremely short ($8.52 \times 10^{-17}\,\mathrm{s}$ [14]), such that their mean path before decay of $c\tau = 25.5\,\mathrm{nm}$ is too short for inducing new spallation processes. Instead, it decays into a pair of electron and positron, which then starts an electromagnetic subshower. This is indicated in the top part of the first interaction shown in Figure 3.6. These showers mark the electromagnetic component of hadronic showers.

In most materials the radiation length is much smaller than the nuclear interaction length. Thus electromagnetic cascades are much denser compared to the sparse nuclear interactions.

As the particles involved in an EM shower cannot induce further spallation processes, their creation is in this sense a one-way street. At each nuclear interaction there is a non-zero probability to produce a π^0. Thus, with a rising number of nuclear interactions the overall probability to create π^0 rises and with it the electromagnetic fraction. The number of hadronic interactions rises with the energy of the primary particle, and thus the electromagnetic fraction of the cascade rises, too.

Note that the creation of π^0 is a statistical process. It might happen at every nuclear interaction or even not at all. Hence the electromagnetic fraction varies heavily from event to event. In combination with the large number of possible processes that can happen within a hadronic cascade in general, not two hadronic showers look alike, thus making predictions on individual shower development impossible.

Time Development: Late Neutron Component

Both the intra-nuclear cascade and the particle de-excitation are depositing the energy almost instantaneously.

However, the evaporating neutrons of the de-excitation phase undergo different kind of interactions with the nuclei of the absorber material and thus introduce a significant delay in the ionization. The interactions of these “late neutrons”, which have an energy of a few MeV, are:

- Inelastic scattering. This is the low energy variant of spallation without the creation of additional hadrons via the intra-nuclear cascade. Instead the excited nucleus emits photons or, depending on the type of material, even nucleons or α-particles. This process is valid for neutron energies above 1 MeV.

- Elastic scattering. For neutron energies in the region of keV to MeV the elastic scattering of the neutron on the absorber nuclei is the dominating process. At each collision the neutron loses a part of its energy. As the scattering is elastic, the average amount of energy lost per collision is dependent on the mass difference of the two particles. While it is small for collisions of neutrons with heavy nuclei, the average transferred energy is maximal for collisions with hydrogen (on average 50% energy loss per collision). At each collision the neutron loses energy and gets slower. However, at the same time the cross-section for elastic scattering rises, decreasing the mean free path length. Hence, the time between two collisions is approximately constant. All collisions together sum up to a typical time length of 10 ns.

- Neutron capture. If the energy of the neutron is insufficient for performing elastic scattering, it can be captured by a nucleus. The time scale for this process is in the order of μs, which is far above the typical integration time of detectors at a collider experiment. Note that during this process the binding energy of the neutron is released ($\mathcal{O}\,(\mathrm{MeV})$), reclaiming the invisible energy component

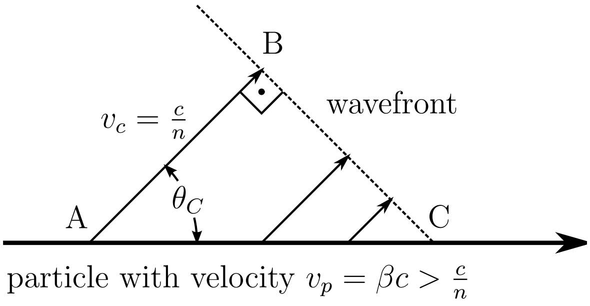

Figure 3.7: Creation of a wavefront of cherenkov radiation by a charged particle passing through material with a speed v_p greater than the speed of light in the same material v_c.

from above. But as the time constant of neutron capture is way beyond typical recording times at particle detectors, this energy is still invisible.

The amount of late energy contributions thus increases in hadronic cascades with a large number of evaporation neutrons. This number is dependent on the absorber material and increases for elements with a large atomic number Z.

3.3.5 Cherenkov Radiation

When a charged particle of speed $v_p = \beta c$ travels through matter with the refractive index n, Cherenkov radiation occurs if the particle travels faster than the speed of light in this same medium $v_c = \frac{c}{n}$ [32].

This radiation originates from the fact that charged particles induce polarization in the matter around them. For $v_p < v_c$, this polarization is symmetric around the particles path and no Cherenkov radiation is emitted. However, for $v_p > v_c$ the symmetry is broken and the time variation of the dipol field adds up to the emission of Cherenkov radiation. The angle θ_C under which the radiation is emitted can be derived from the triangle in Figure 3.7. It gives the distance that both the Cherenkov photons (AB) and the particle (AC) travel within the same time. This leads to the relation

$$\cos\theta_C = \frac{v_c}{v_p} = \frac{c}{n\beta c} = \frac{1}{n\beta}. \tag{3.6}$$

As the particle passes through the matter constantly emitting Cherenkov radiation, a wavefront is created.

This effect can be used for particle identification (PID) of particles with the same momentum. Two types of particles have different masses and thus have different velocities v_1 and v_2 for a fixed momentum. By choosing a medium with an refractive index n such that its speed of light v_c lies between the two particle velocities $v_1 < v_c < v_2$, only one of the particle types will create Cherenkov radiation, which in turn can be collected by a photon detector.

3.4 Particle Detectors: The CLIC_ILD Detector

Particle detectors are the heart of any high energy physics collider experiment. They perform the detection of the particles within the events, which is the basis of the measurement of the underlying fundamental physics process.

For that it is important to gather as much information on the final state particles as possible. This includes the measurement of the particle's momentum and energy, along with an identification of the particle. Moreover with the measurement of the particle's impact parameter its vertex, that is its point of origin, can be estimated.

Therefore modern general purpose detector systems for a collider experiment consist of several layers of subdetectors which are all built for the measurement of specific properties or specific particles. These subdetectors are situated in an onion-shell arrangement in different layers around the interaction point where the particles are brought to collision. Each of this layers is designed to cover as much space around the interaction point as possible (4π detectors), leaving only necessary gaps for the incoming beam-pipe, cables and other required support structures.

The subdetectors are ordered as follows: Close to the beam-pipe tracking detectors to measure the particle's flight path are installed. Further out there is the calorimetric system, starting with first the electromagnetic calorimeters which is followed by hadronic calorimeters. At least a part of the detector systems are placed inside a large magnetic coil. Thus charged particles will have a curved path due to the Lorentz force which in turn is used to measure their momentum. The coil is typically placed between the electromagnetic and hadronic calorimeters or outside of the hadronic calorimeters.

This section will describe the working principle of the different subdetector components at the example of the general purpose CLIC_ILD detector. It is based on the International Large Detector (ILD [33]), which was designed for the International Linear Collider (ILC [34]). Modification to the design were made in order to adjust the detector to the different environment and requirements of the Compact Linear Collider.

The CLIC_ILD is optimized for the usage of Particle Flow Algorithms for the event reconstruction. Their principle is to measure each particle individually, using the best available information from the various subdetector systems. This requires that the particle can be followed through all subdetectors with minimal loss of information. Therefore the hadronic calorimeter along with all other subdetectors is placed within the coil.

Part of this introduction follows closely [35].

3.4.1 Tracking Detectors

A tracking detector measures the flight path of charged particles. It makes use of the ionization of matter through energy deposition as described in subsection 3.3.2. The coil surrounding the entire CLIC_ILD detector induces a magnetic field B parallel to the beam axis. Due to this magnetic field the particle's path will be curved due to the Lorentz force F_L and the radial force F_r. The radius r of the curve is dependent on the particle's transverse momentum p_t, its charge q and the intensity of the magnetic field

B.

$$F_L = F_r \qquad \Rightarrow \qquad \frac{p_t}{r} = qB \tag{3.7}$$

Hence a tracking detector can be used to measure the transverse momentum of charged particles. Note, however, that the relative resolution $\frac{\sigma(p_t)}{p_t}$ increases for higher p_t.

By extrapolating the identified tracks towards the interaction point it is possible to calculate their impact parameter. Especially through the combination of several tracks it is possible to identify the particles' common vertex. This information is very useful for the characterization of the underlying physics process event. However, the vertices of a single process are usually very close with respect to each other. Thus the tracking system must provide tracks with a very good resolution.

In order to increase particle separation the CLIC_ILD detector favours a tracking system with a large radius. Therefore a gas filled time projection chamber (TPC, [33][28]) is used as main tracking device. It has the big advantage that it is cheaper than a pure silicon based tracker of the same size. Furthermore as the number of measured spatial points is very large (up to 226 real 3D points per track) the TPC provides excellent pattern recognition capabilities, which is important for the track identification. However, the resolution of the individual points is limited to about $\sigma_{\text{point}} = 100\,\mu\text{m}$ in the $r\phi$-plane and especially to only $\sigma_{\text{point}} = 0.5\,\text{mm}$ in the rz-plane [33].

Therefore the CLIC_ILD concept foresees additional layers of tracking detectors to improve the vertex finding. Such detectors are in general called vertex detectors and are layers of silicon with integrated sensitive strips or pixels. At CLIC_ILD several layers are used, both in the forward and in the barrel region. The ones in the barrel region are divided into two types of inner trackers (VXB, Vertex Barrel and SIT, Silicon Internal Tracker) and one outer layer (SET, Silicon External Tracker). The SITs are placed next to the beampipe at a radius of 165 mm and 309 mm and are thus located inside the TPC, while the SET layer is placed outside of the TPC. Both the SIT and the SET consist of "false double-sided" silicon micro-strip detectors, resulting in a $r\phi$ resolution of $7\,\mu$m and an rz resolution of $50\,\mu$m[33].

3.4.2 Calorimetry

Particle Energy: Measurement Principle

For the measurement of a particle's energy a detector called calorimeter is used. Calorimeters rely on the principle of electromagnetic and hadronic cascades which were introduced in subsection 3.3.3 and subsection 3.3.4.

During such cascades many secondary particles are created using the energy of the incident particle. These secondaries deposit their energy, and thus the energy of the projectile, in the surrounding material through ionization. Thus by measuring the amount of ionization, the energy of the incident particle can be determined.

The number of particles created in such a cascade is roughly linear to the energy of the original particle $N \propto E$. Assuming that each of these particles deposit roughly the same amount of energy, calorimeters count the number of secondary particles that were created during the cascade. Thus they are historically called shower counters.

Calorimeter Types

Depending on the material the nuclear interaction length is usually much larger than the radiation length ($\lambda_I \gg X_0$). Thus there are calorimeters specialized in measuring electromagnetic or hadronic (with electromagnetic subshowers) showers. The electromagnetic calorimeter (ECal) of CLIC_ILD has a depth of $23\,\mathrm{X_0}$ (and $1\,\lambda_\mathrm{I}$) while the hadronic calorimeter (HCal) has a depth of $7.5\,\lambda_\mathrm{I}$.

Both are sandwich calorimeters, i.e. they consist of interleaving layers of dense absorber material and sensitive detector readout material. Most of the reactions causing particle multiplication take place in the absorber, which is tungsten for both detectors in the barrel region.

The sensitive layers typically only see ionization from minimum ionizing particles. In the case of the ECal they are made of silicon pads, whereas the HCal uses scintillators which are readout with small photo sensors called Silicon Photomultipliers.

Detector Resolution

As the development of electromagnetic and especially hadronic cascades is subject to statistical fluctuations, the amount of energy deposited in the sensitive area of the calorimeters fluctuates, too. The resulting relative energy resolution of the measurement σ_E/E is influenced by:

- a Stochastic fluctuations. In principle the calorimeter counts the number of secondary particles of a shower to measure the initial particle's energy. Counting is a stochastic process and its width σ_a increases with $\sqrt{N}$. But as $N \propto E$ this corresponds to $\sqrt{E}$. The absolute width would therefore increase with the energy $\sigma_a \propto \sqrt{E}$, but the relative width $\frac{\sigma_a}{E} = \frac{a}{\sqrt{E}}$ decreases.
- b Noise. Every channel of the calorimeter will produce signal created from electrical noise. This signal does not represent energy deposited from a passing particle. Hence it happens independently of the particles energy and the width σ_b is constant. Therefore the relative width decreases for higher energies: $\frac{\sigma_b}{E} = \frac{b}{E}$.
- c Constant term. This value increases through miscalibration and uninstrumented areas or other sources for leakage. It will yield in an additional relative width $\frac{\sigma_c}{E} = c$

The total energy resolution $\frac{\sigma_E}{E}$ is than the quadratic sum of these terms [36]:

$$\begin{aligned}\frac{\sigma_E}{E} &= \frac{a}{\sqrt{E}} \oplus \frac{b}{E} \oplus c \\ &= \sqrt{\left(\frac{a}{\sqrt{E}}\right)^2 + \left(\frac{b}{E}\right)^2 + c^2}\end{aligned} \tag{3.8}$$

Note that the relative detector resolution improves for higher energetic particles in calorimeters due to the stochastic term. This is the exact opposite behaviour to the relative momentum resolution of tracking detectors, where the resolution deteriorates for higher energetic particle tracks.

3.4.3 Particle Flow Algorithm

Using the different detector system described above it is possible to extract a lot of information, such as momentum and energy on the final state particles of a process of an event. However, through a sophisticated combination of the available information it is possible to follow individual particles on their way through the detector and improve the overall measurement. For example the statistical fluctuations in calorimeters limit their resolution, especially for low energetic particles. With a particle hypothesis and thus known mass, the energy can be determined with a significant greater precision using the momentum measurement of the tracking detector. This is the basis of the Particle Flow Algorithms to improve the overall jet energy resolution of the detector.

Final State Fragmentation: Particle Jets

The purpose of a collider such as CLIC is the measurement of fundamental processes of nature. Such a process could be the creation of Higgs via Higgs-Strahlung, with the Higgs decaying to a pair of photons and the Z decaying to a pair of quarks:

$$\mathrm{e^+e^-} \to \mathrm{Z}^* \to \mathrm{ZH} \to q\overline{q} + \gamma\gamma$$

Processes like this one are identified via their final state particles. These particles, however, are not necessarily the ones that are registered by the detector. Especially quarks have the property that they are not observed as standalone particle, but instead form either a meson of quark-antiquark, or a baryon of quark-quark-quark. This property is called confinement. Hence the final state quarks will undergo a series of (mainly) QCD reactions and create a set of (semi-)stable particles, a process which is called fragmentation or hadronization. The newly created particles share the same general direction of the final state quark and thus create a significant signature within the detector. This set of particles is called a jet. A simple example limited to the production of pions out of a $q\overline{q}$-pair is shown in Figure 3.8. Note that the pions are colorless mesons, while single quarks always carry color. Hence during the fragmentation process of a single quark a color-exchanging connection to a second quark is necessary. However, the momentum transfer of this color connection is typically small. Thus despite this connection, the overall momentum and direction of a jet matches closely its originating quark. Because of this modern particle detectors are optimized for their jet energy resolution.

CLIC Jet Energy Resolution Requirements

At CLIC most of the interesting physics processes will result in multi-jet final states. These may be accompanied by leptons or missing energy, especially if Supersymmetry

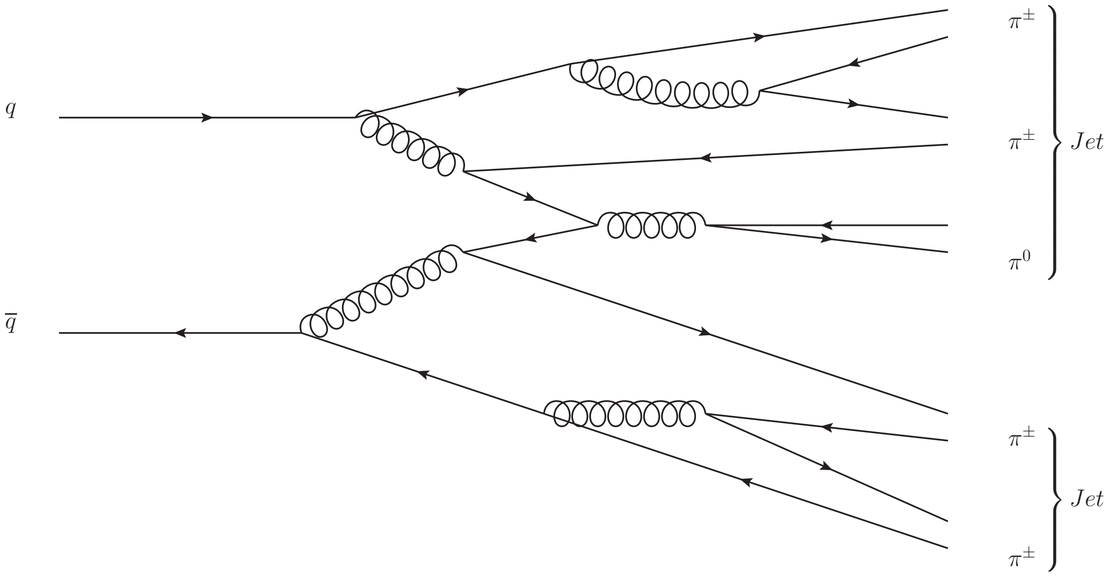

Figure 3.8: Example fragmentation of a $q\overline{q}$ pair to two jets.

is within the energy reach of CLIC. Two examples of such SUSY processes are

$$\mathrm{e}^+\mathrm{e}^- \rightarrow \widetilde{\chi}_2^0\widetilde{\chi}_2^0 \rightarrow \overbrace{\widetilde{\chi}_1^0\widetilde{\chi}_1^0}^{\mathrm{E_{miss}}} + \overbrace{\mathrm{Z}^0\mathrm{Z}^0}^{\mathrm{jets}} \tag{3.9}$$

$$\mathrm{e}^+\mathrm{e}^- \rightarrow \widetilde{\chi}_1^+\widetilde{\chi}_1^- \rightarrow \underbrace{\widetilde{\chi}_1^0\widetilde{\chi}_1^0}_{\mathrm{E_{miss}}} + \underbrace{\mathrm{W}^+\mathrm{W}^-}_{\mathrm{jets}}. \tag{3.10}$$

The Z and W in the final state of these processes predominantly decay into quarks, creating jets. Thus these are intrinsically difficult to distinguish, as in both cases the missing energy limits the use of initial state information, and both processes create four high energetic jets (two per Z/W$^\pm$). The only way to tell those processes apart is the energy of the jets. Calculating the invariant mass of that pair of jets originating from the same Z (W$^\pm$) will result in the corresponding mass which is known to be 91.2 GeV (80.4 GeV). However, the Z and the W$^\pm$ have a very similar mass. Thus already a jet energy resolution of 5% makes the two particles almost indistinguishable, as one can see in Figure 3.9. To reach a separation between the two particles of about 2.5 σ, a jet energy resolution of 3.5% is necessary. Other processes, too, would benefit from such a good jet energy resolution and thus for CLIC requires such an jet energy resolution for all jets in the energy range from 50 GeV to 1 TeV [10]. This goal is reached by using the Particle Flow Algorithms and detectors specialized for this kind of event reconstruction.

Particle Flow Principle

Historically the energy of a jet was measured by the calorimetric system and thus the jet energy resolution was defined solely by the calorimetric resolution. Thus due to

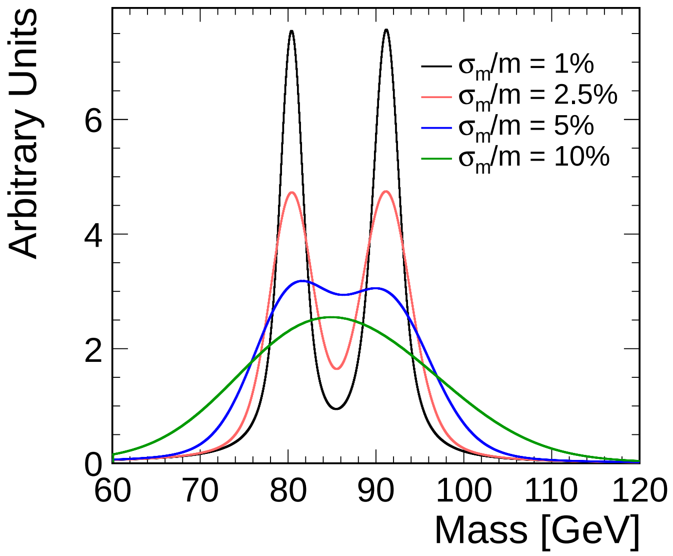

Figure 3.9: The invariant masses from jets originating from either $W^{\pm}$ or Z^0, showing their possible separation for different jet energy resolutions $\frac{\sigma_m}{m}$ [10].

the inherent statistical fluctuations of electromagnetic and especially hadronic cascades improvements on the energy resolution are limited.

In contrast to this the Particle Flow Algorithm (PFA, [37]) achieves the required jet energy resolution by measuring the energy of each jet particle individually, using measurements of all subdetector systems. Especially the energy of charged particles can be estimated with high precision from the momentum measurement of the tracking detector if the particle mass is known.

To better understand the exact working principle, the detector response to the different kind of particle classes is indicated in Figure 3.10. It shows the Interaction Point (IP) from which all particles originate, the tracking detector (Tracker), the electromagnetic calorimeter (ECal) and the hadronic calorimeter (HCal). Dashed lines indicate the flight path of the particle, while full lines indicate the measurement of the tracking detector. Hits, i.e. measured energy depositions in the electromagnetic and hadronic calorimeters are indicated by small rectangles.

The individual particle classes are [35]:

$e^{\pm}$ Electrons or positrons are charged particles and thus create visible tracks in the tracking system. Their energy is deposited in the electromagnetic calorimeter (ECal) through an electromagnetic shower.

$\mu^{\pm}$ Muons can pass through almost any material in the detector without getting stopped. Their momentum can be measured by the tracking system. They get identified with the muon system and their tracks in the calorimeters.

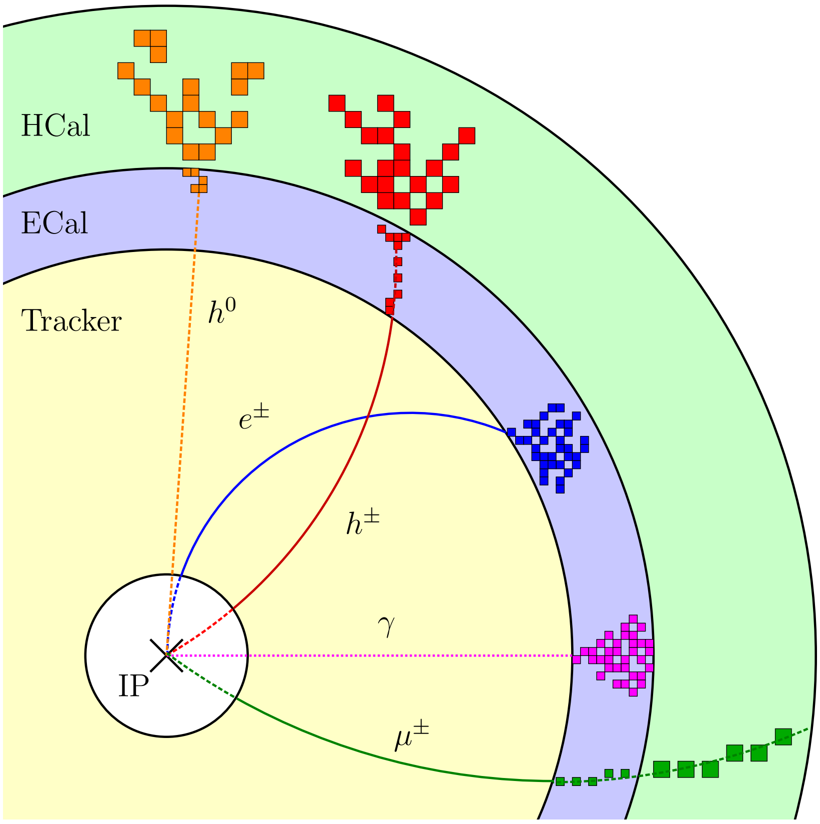

Figure 3.10: Detector response to different types of particles. It includes neutral hadrons h^0, charged hadrons $h^\pm$, electron (positron) $e^\pm$, photons γ and muons $\mu^\pm$.

- $h^\pm$ Charged hadrons, too, create a visible track. They are stopped finally in the hadronic calorimeter (HCal) with a hadronic shower.
- γ^0 Photons are invisible in the tracking devices and usually pass through them until they start a shower in the ECal.
- h^0 Neutral hadrons as photons won't create a trace in the tracking chamber but just as charged hadrons will be stopped in the hadronic calorimeter, depositing their energy.

Thus the response of the detector can be classified into two general parts.

On the one hand there are charged particles. Their momentum is accurately measured within the tracking chamber, as the magnetic field will force those particles on a curve. The radius of this curve is a precise measurement of its momentum p with a resolution $\frac{\sigma_p}{p}$ proportional to the momentum: $\frac{\sigma_p}{p} \propto p$. Given a hypothesis on the type and thus the mass of the particle, the energy can be determined with a precision that is in most cases significantly better than the one from the calorimetric system. However, for high momentum tracks the momentum resolution degrades, such that in extreme cases calorimeters can still provide a more accurate measurement.

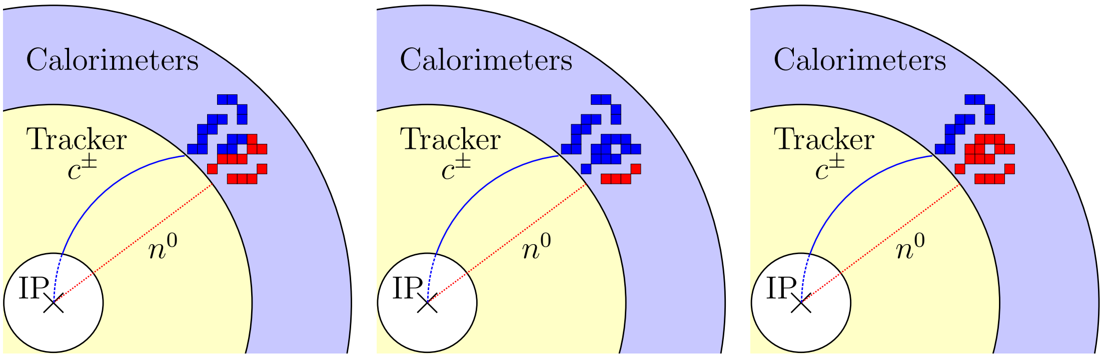

(a) Real cluster distribution. (b) Too much charged energy contribution. (c) Too much neutral energy contribution.

Figure 3.11: Example of Particle Flow confusion caused by the clusters of a charged particle $c^{\pm}$ close to the one of a neutral particle n^0. The left figure shows the true situation. In the central figure one part of the neutral cluster is counted towards the charged cluster, while in the right figure one part of the charged cluster is counted towards the neutral one.

Neutral particles on the other hand will only be measurable with the calorimetric system. Just like most charged particles, neutral particles, too, will create a shower - a cluster of hits - in the calorimeters.

The fundamental idea of Particle Flow is to geometrically follow the charged particle starting from their generation at the interaction point down to their absorption in the calorimeters. Thus the cluster in the calorimeters corresponding to charged particle's track can be identified by geometrical means, providing two energy measurements of the same particle and thus improving its resolution.

This technique relies heavily on the possibility to distinguish individual clusters in the calorimetric system. Hence, highly granular calorimeters are necessary. In addition all subdetectors need to be within the magnetic coil, as the coil represents dead material providing no information on the particle and thus stops the "flow" of following the particle.

Particle Flow Limitations: Confusion

Particle Flow relies heavily on the ability to geometrically separate individual contributions of particles. However, clusters of two close particles can overlap.

As hadronic showers can be very sparse they can easily create multiple clusters of hits in the calorimeter. This is especially true when considering high energetic neutral particles which can travel undetected for several λ_I before the next cluster is created.

Thus if a charged and a neutral particle enter the calorimetric system with only a small distance, the Particle Flow Algorithm might assign the wrong hits to a cluster of particles, thus either over- or underestimating the neutral energy component of an event. This effect is called confusion and has a negative influence on the jet energy

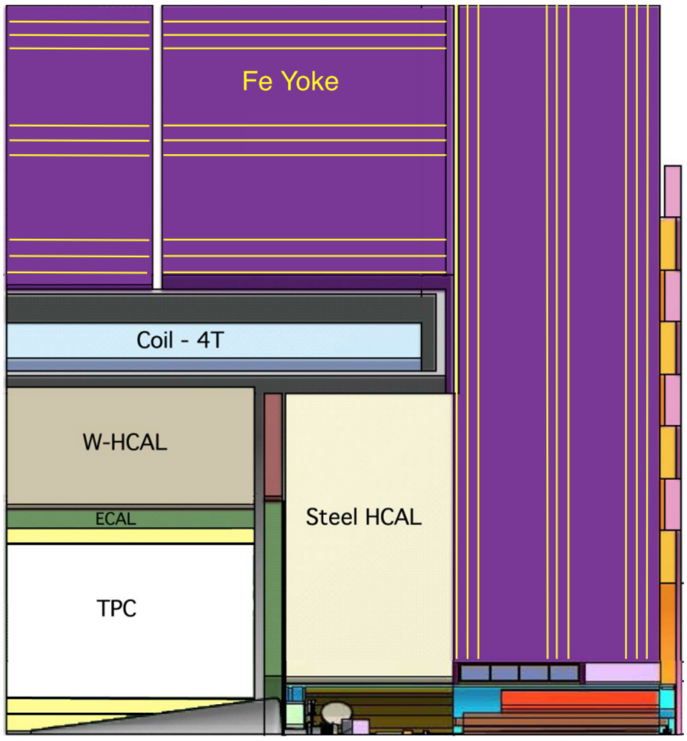

Figure 3.12: The CLIC_ILD detector [10].

resolution. An example is shown in Figure 3.11.

Confusion is not limited to the example given. Other geometrical particle constellations contribute to confusion, as well, such as a minimum ionizing particle (muon) passing through a cluster.

Part of the confusion can be resolved by performing a reclustering where the expected amount of energy, known from the tracking detector, is taken into account.

3.4.4 The CLIC_ILD Detector

For CLIC several adjustments were made to the original ILD concept [33], such as increasing the inner radius of the vertex detector to compensate for the increased beam-related background. Moreover, the depth of the calorimetric system was increased to 7.5 λ_I by exchanging the original steel absorber with tungsten, to compensate for the higher center-of-mass energy of 3 TeV.

The components of the CLIC_ILD follow the typical onion shell principle of general purpose detectors. The subdetectors are ordered from interaction point outwards (cf. Figure 3.12):

- As vertex detector a multi-layer pixel-vertex-detector placed in a pure barrel geometry is used (VXB, Vertex Barrel). It contains three super-layers consisting out of two layers each. Its purpose is mainly to measure the impact parameter of tracks, which is needed for the vertex identification.

- Two layers of Si-Strip detectors at the barrel (SIT) and for low angle coverage a system of Si-Pixel and Si-Strip detectors in the forward region (FTD, Foward Tracking Disc).
- A Time Projection Chamber (TPC) with up to 226 real 3D points per track. This high number of points allow for a good pattern recognition when searching for particle tracks. At CLIC the two-track separation performance in an environment of 312 overlayed bunches of a single bunch-train is crucial for the overall performance.
- A second set of Si-Strip detectors outside the TPC (SET, Silicon External Tracker). It is necessary for improving the space resolution of the tracks from the TPC.
- A highly granular electromagnetic calorimeter (ECal) using tungsten absorber plates and silicon plates as read-out. It has a total absorber depth of $23\,\mathrm{X}_0$ and $1\,\lambda_\mathrm{I}$.
- A highly granular hadronic calorimeter (HCal) which is read out using scintillator tiles with cell sizes of $3 \times 3\,\mathrm{cm}^2$. The overall thickness of $7.5\,\lambda_\mathrm{I}$ is achieved by using steel absorber in the endcap part. In the barrel, however, the steel absorber is replaced by a much denser tungsten absorber to minimize the outer detector radius, which is limited by the coil.
- A large superconducting coil surrounding all calorimeters. It creates an axial B-field up to 4 T.
- An iron yoke returning the magnetic flux of the solenoid. It is instrumented with scintillator strips to be used as Tailcatcher/Muontracker.

Most of these specifications are identical to the ILD concept which is used for the ILC. However, due to the increased beam induced background, the different timing structure and the higher energy at CLIC, some adaptions have been made to the CLIC_ILD concept. Among the most important are:

- Due to the increased beam induced background of incoherent pairs, the inner radius of the vertex detector is increased by 15 mm.
- New readout technology for the vertex tracker is used which has a time stamping capability of $\mathcal{O}\,(10\,\mathrm{ns})$.
- Increase of the magnetic field from 3.5 T to 4 T.
- Increase the time stamping capability in the HCal to $\mathcal{O}\,(1\,\mathrm{ns})$.
- Increase the absorber depth of the HCal to $7.5\,\lambda_\mathrm{I}$ ($8.5\,\lambda_\mathrm{I}$ ECal and HCal) in order to compensate for the higher energy at CLIC. As the outer radius of the HCal is fixed by the size of the magnetic coil, the only option to achieve this absorber depth is to replace the steel absorber with tungsten in the barrel.

As the bunch crossing frequency at CLIC is only 0.5 ns, the usage of tungsten as HCal absorber material could potentially introduce some challenges. Tungsten has a high atomic number Z. Thus the number of created low energetic neutrons is considerably larger than for steel and thus carry a higher fraction of the shower energy. Therefore the structure of the shower is more sparse in tungsten than in steel, potentially increasing the confusion term of PFA. But as most of these neutrons originate from the evaporation process they take time until they deposit their energy either via elastic scattering ($\mathcal{O}(10\,\mathrm{ns})$) or via neutron capture (up to $\mathcal{O}(1\,\mu\mathrm{s})$). In order not to deteriorate the calorimetric energy resolution, the signal collection time (sometimes called integration time) has to be large enough to capture a significant fraction of the deposited energy.

However, these times are considerable larger than the bunch crossing repetition rate at CLIC of 0.5 ns. Especially as neutrons do not create tracks, their clusters of energy depositions within the calorimeter cannot be assigned to a certain bunch crossing with certainty. Therefore naively a value 0.5 ns denotes the maximum integration time of the detectors in order not to create pile-up from different bunch crossings. However, at CLIC the probability for an e^+ e^--physics interaction within a single bunch crossing is relatively small. Therefore longer signal recording times necessary to capture a large fraction of the energy depositions will usually not lead to pile-up of additional physics events. However, pile-up from beam induced background will increase and thus a too long integration time will deteriorate the energy resolution, too.

Consequently the exact length of the time recording window has to be carefully tuned to minimize the obtained energy resolution. This procedure relies heavily on simulations. However, simulation of hadronic showers is complex and often not very accurate, especially in the low energy, non-perturbative regime where the asymptotic freedom needed to calculate QCD results from Feynman-diagrams is not applicable any more. Therefore, to validate the simulation of hadronic showers in tungsten absorber structures, the T3B experiment was constructed. Its design and the results will be discussed in detail in chapter 4.

3.5 CALICE: Calorimeter for a future Linear Collider Experiment

Particle Flow, as presented in the previous section, is based on the possibility to separate individual clusters in the calorimeters. Hence it needs very granular calorimeters with very small individual cells in the order of a few cm^3. Such types of calorimeters are sometimes called imaging calorimeters.

The CALICE collaboration (Calorimeter for a future Linear Collider Experiment) is an international collaboration with the focus on the development and testing of different technologies for the electromagnetic and the hadronic calorimeter with high granularity optimized for PFA. Within this context several prototypes where constructed, one of which is the Analog Hadron Calorimeter (AHCal) [38].

The sensitive part of the AHCal consists of small tiles of scintillators (cf. subsec-

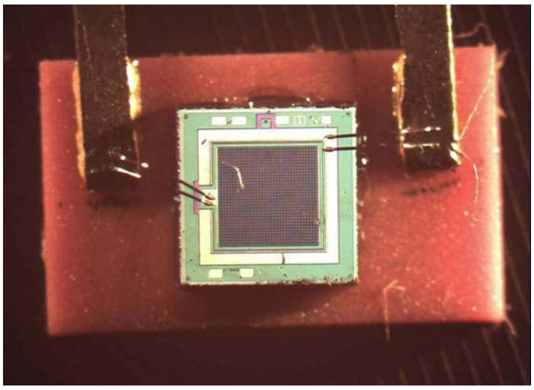

Figure 3.13: A picture of a Silicon Photomultiplier.

tion 3.5.2) which are read out with Silicon Photomultipliers (SiPM, cf. subsection 3.5.1), a novel silicon-based single photon detector. With the SiPMs attached to plastic scintillator tiles, in total 38 active layers were constructed, each consisting of up to 216 tiles (cf. subsection 3.5.3). In the AHCal the active layers were interleaved with absorber material. Two different options as absorber materials where explored during various campaigns of beam-tests using a secondary high energetic particle beam at the Fermilab Meson Testbeam Facility (MTBF), the CERN Proton Synchrotron East Hall and the CERN Super Proton Synchrotron North Hall (cf. subsection 3.5.4). The first absorber option was steel (Fe-AHCal), which is the absorber used in the ILD detector for the ILC. As second material option tungsten was studied (W-AHCal), which is used in the CLIC_ILD at CLIC.

This section will give some details on the used technology and thereby follows [35].

3.5.1 SiPM: Silicon Photomultipliers

The Silicon Photomultiplier (SiPM, [39][40]) is a multi-pixel Geiger mode Avalanche photo diode. It consists of an array of photo sensitive diodes. A picture of such a device is shown in Figure 3.13.

Working Principle of a Single Pixel

The diodes/pixels are photo diodes which are used in the so called "Geiger Mode", i.e. the applied bias voltage is above the device specific breakdown voltage ($U_{\text{bias}} \geq U_{\text{break}}$). At these high voltages the electric field within the device is strong enough such that free electrons, which could be created by ionizing photons, knock out additional electrons and thus starting an avalanche. The avalanche reaches saturation and hence its charge is always the same and not dependent on the charge set free by the incident photon(s). Thus, a single diode/pixel acts as a binary device, capable of detecting single photons, but not their amount.

The avalanche is self-sustaining, constantly creating new electron-hole pairs. In order to stop the avalanche a quenching resistor is attached to the pixel. Thus, once

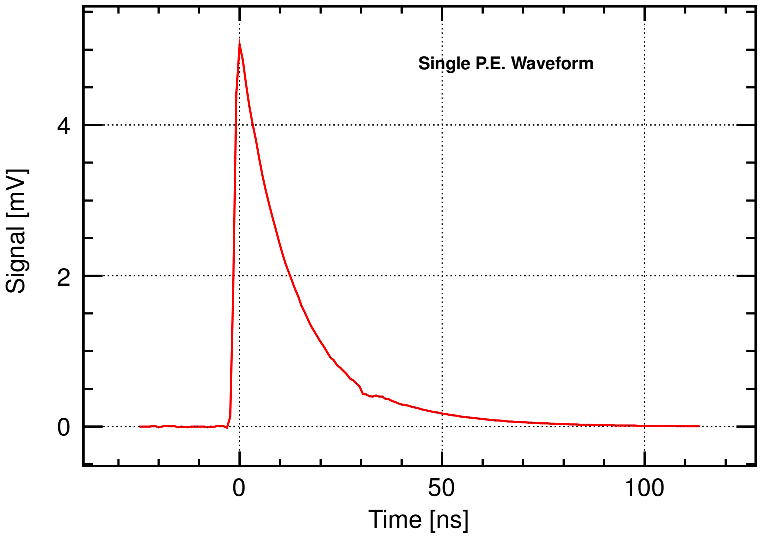

Figure 3.14: The signal generated by a photon equivalent (p.e.), i.e. by a single fired pixel of a Hamamatsu MPPC 50P SiPM. Obtained by averaging over 10000 waveforms of Dark Pulses recorded with the T3B experiment (cf. chapter 4) including an amplification stage of factor 8.9.

current flows due to the avalanche, the applied voltage drops below the breakdown voltage, stopping the avalanche. The time until the avalanche is terminated and the pixel is in the same state as prior to the incident photon is called recovery time. The recovery time is specific to the device and is in the order of a few ns up to several thousand ns. An example waveform of a single pixel is shown in Figure 3.14. One can clearly see how the single photon causes a fast rising peak before the signal slowly drops back due to the quenching of the avalanche. Such a signal of a single pixel is usually caused by a photon and thus called photon equivalent (p.e.).

The avalanche acts as a charge multiplication stage. The multiplication factor, called Gain G, is in the order of 10^6. The exact value, however, depends on the device and the applied overvoltage $U_{over} = U_{bias} - U_{break}$. The breakdown voltage is temperature dependent, and thus the Gain G varies with temperature T. Details can be found in [41]. Thus for detectors using SiPMs a temperature monitoring system or a way of constantly monitoring the gain is important.

Array of Pixels for a Linear Response

In order to get an analog signal scaling linearly with the intensity of the incident light, an array of these diodes with a typical size of 1000 pixels per SiPM is used. The array is connected in series, such that the total response is the sum of all individual pixels and thus linear to the light intensity, as the signal that is generated by single pixel is approximately the same for all pixels.

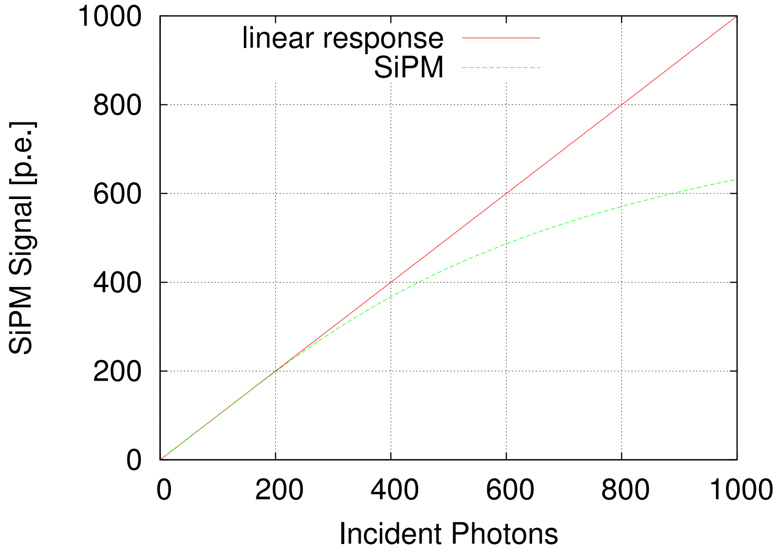

Figure 3.15: Mean response in photon equivalents of a SiPM with 1000 pixel to incident photons. To illustrate the SiPM saturation effect the ideal linear response is shown, too.

The fact that an already fired pixel is incapable of measuring a second photon leads to a saturation effect[42]. Figure 3.15 shows the mean response of a SiPM with 1000 pixels for a given number of detectable photons. For low photon intensities the mean response is approximately linear. However, when the number of incident photons is comparable to the number of pixels, the probability of a photon hitting an already fired pixel increases and thus reduces the mean SiPM response. In the CALICE AHCal the average signal per MIP is at approximately 15 p.e.[36]. Therefore we can call the measurement linear for most cases.

Darkrate, Afterpulses and Crosstalk

SiPMs, like most detectors, suffer from noise and other unwanted side effects. Among the most important ones are:

- Dark Rate or Dark Count:
  If a pixel was not fired by an incident photon but by other means, the event is called a Dark Count. Usually the avalanche of a Dark Count is caused by temperature induced lattice excitations (phonons) of the silicon. The rate at which these Dark Pulses occur is thus temperature dependent. For some SiPM devices the Dark Rate at room temperature can reach up to several 100 kHz at the single p.e. level.

- Afterpulse:
  During the quenching of the avalanche a hole or an electron might get captured in a potential caused by lattice defects of the silicon. The electron is bound within

the defect, but once it escapes it can initiate yet another avalanche, faking a signal equivalent to a photon. These afterpulses happen most often within a few ns after the actual pulse, but can even occur up to μs after the initial pulse.

- Optical cross-talk:
  During the avalanche electrons and holes constantly recombine. Such a recombination emits photons which in turn might hit neighbouring pixel, possibly inducing further avalanches and triggering the pixels to fire. As the traveling time of a photon from a pixel to its neighbour is negligible, the signal of both pixels is almost instantaneous. Thus through a single incident photon multiple pixels might be triggered to fire, creating a signal equivalent to multiple photons.

For details see [42] and [41]. The SiPMs used in the AHCal were produced by the MEPhI/PULSAR group. They consist of an area of $1\,\mathrm{mm}^2$ covered by 34×34 pixels, each with a recovery time between 100 ns and 1000 ns [36].

General Remarks

The necessary bias voltage is typically well below 100 V and thus easier to handle compared to the several kV that are necessary for PMTs. The major advantages, however, are that this device is insensitive to magnetic fields and thanks to the silicon technology can be produced in sizes of several cm^3 including a protective packaging, both of which are essential for the devices to be usable in the ILD detector, where the calorimetric system is placed inside the magnetic coil.

An example of a SiPM waveform caused by a particle passing through an attached scintillator is shown in Figure 3.16. One can clearly see the peak of the incident scintillation photons created from the passing particle. The signal quickly drops back to the baseline. After the main peak some single p.e. depositions occur after several 100 ns. These can be due to afterpulsing or darkrate.

3.5.2 The Scintillator Tiles

The AHCal uses plastic scintillator based on Polystyrene as active material. The scintillating material is cut into quadratic tiles which converts the energy deposited through ionization from the passing particle into several thousand photons of which a part will be measured by SiPMs.

The tiles come in a size of $3 \times 3\,\mathrm{cm}^2$, $6 \times 6\,\mathrm{cm}^2$ and $12 \times 12\,\mathrm{cm}^2$ with the smaller tiles are placed in the middle of the layer where the beam is set to hit the detector. They all have a thickness of 5 mm. A photo of one layer is shown in Figure 3.17(a).

The tiles have an integrated wavelength shifting fiber (WLS) that collects the created photons in the scintillator and carries them to the SiPM at the side via total reflection (Figure 3.17(b)). This has two reasons:

1. The first-generation SiPM used in the CALICE AHCal is not sensitive to the blue light produced by the scintillator material. The fiber shifts the wavelength to green, a region where the SiPM is sensitive.

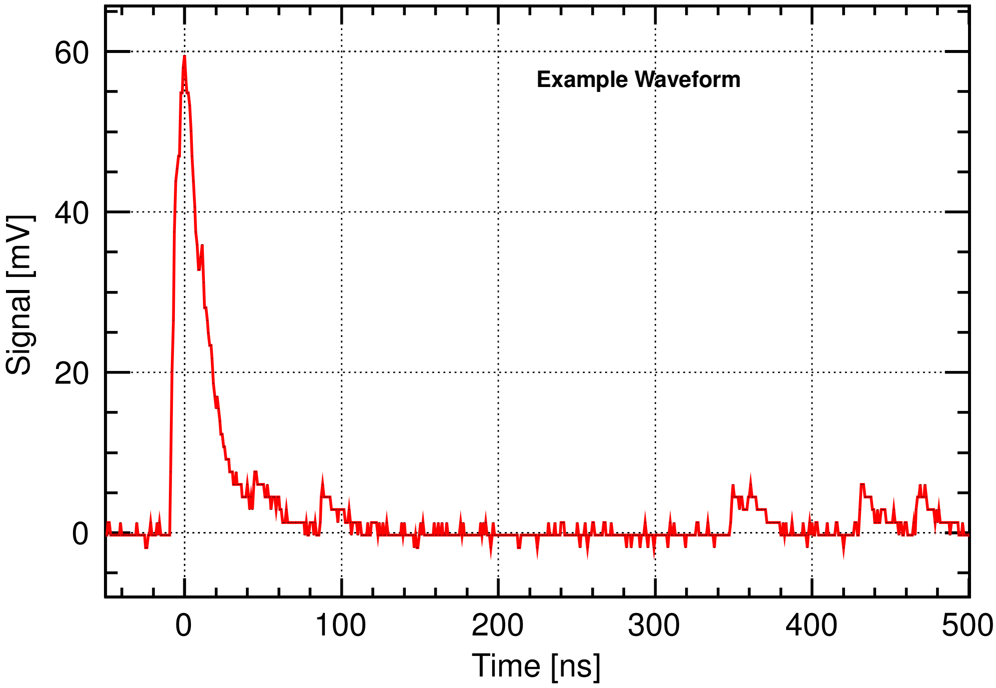

Figure 3.16: A real waveform of a Hamamatsu MPPC 50P SiPM after a particle passed through the attached scintillator. Recorded with the T3B experiment (cf. chapter 4) with a preamplification stage which has an amplification factor of 8.9.

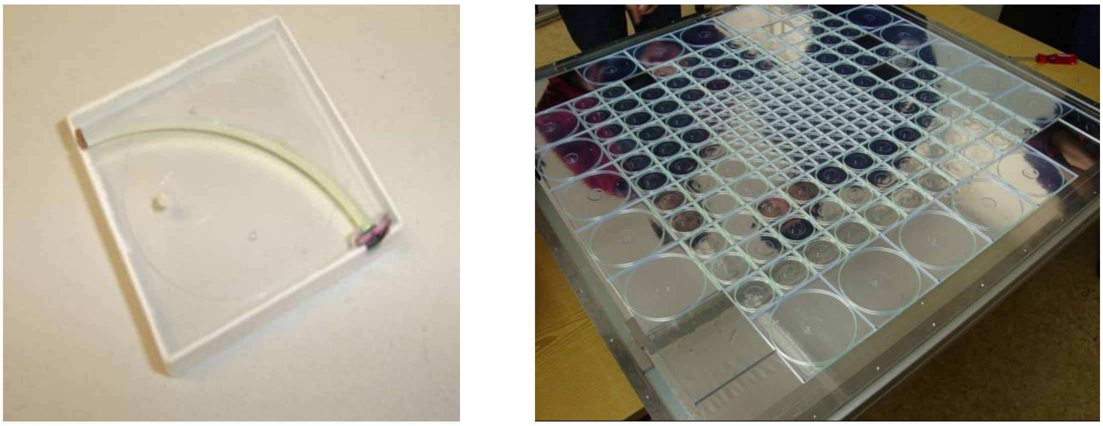

(a) A scintillator tile with wavelength shifting fibre (WLS) with a SiPM at the end.

(b) Picture of a layer of scintillator tiles with wavelength shifting fibers and embedded SiPMs.

Figure 3.17: Pictures of a single plastic scintillator tile with Wavelength Shifting Fiber and embedded SiPM (left) and a complete detector layer out of these scintillator tiles (right).

2. As the fiber collects the photons from the whole tile, it ensures the uniformity of the response. For studies of the impact on a non uniform distributed response, see [43].

The WLS collecting the photons and the SiPM have to be aligned very carefully with respect to each other. Otherwise the photons from the WLS won't be able to hit all of the SiPM's pixels and thus effectively reduce its pixel count. In turn this leads to an increased saturation effect and a reduced signal.

Therefore a version without the Wavelength Shifting Fiber was developed [43][44]. This is possible with the development of blue sensitive SiPMs which do not require a conversion of the scintillation light and thus these devices can be directly coupled to the scintillator tile. In order to maintain a uniform response, the tile needed to be modified. Such tiles are used for the T3B experiment, which will be described in detail in chapter 4.

3.5.3 The AHCal Layers

The calorimeter consists out of 38 sensitive layers with a thickness of 5 mm. The SiPMs are mounted on an electronic boards (1 mm). A gap containing fibres for a LED light calibration system takes an additional 1 mm. Each layer is encased in a steel cassette adding 4 mm of steel [38].

Each layer has five temperature sensors centered on the x-axis and additional ones in the electronics. Their position can be seen in Figure 3.19. A layer is not equipped with $3 \times 3\,\mathrm{cm}^2$ tiles everywhere, but it has a finer structure in the center. The layers are subdivided into two areas.

Layers 31 to 38, placed at the back of the AHCal, contain the "coarse" layer structure. It consists mainly of $6 \times 6\,\mathrm{cm}^2$ sized tiles and a frame of $12 \times 12\,\mathrm{cm}^2$ tiles. It is shown in the right picture of Figure 3.18.

Layers 1 to 30, placed at the AHCal front, contain the "fine" layer structure. Its design is similar to the coarse structure, but in the center it uses 100 smaller sized tiles of $3 \times 3\,\mathrm{cm}^2$. It is shown in the left picture of Figure 3.18.

Every cell in the layer has an cell index (i, j, k):

i, j The distance in cm of the bottom left corner of the tile to the bottom left corner of the detector layer, starting with 1.

k The layers are numbered starting at 1 for the front layer and stopping at 38 for the last layer. Sometimes called layer index.

3.5.4 The Absorber Stack at CERN

The absorber structure was a set of plates placed in between two active layers and before the first layer.

During the beamtests from 2006 to 2009 at CERN and Fermilab, a steel absorber stack was used (Fe-AHCal). The steel plates (density: $\rho_{Fe} = 7.86\,\mathrm{g/cm}^3$) had an average

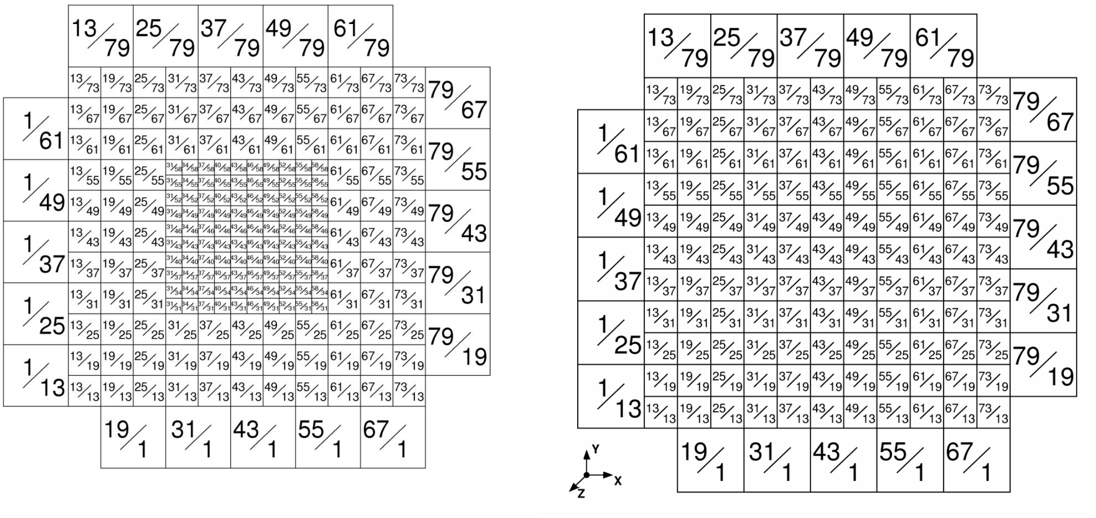

Figure 3.18: The different layer geometries of the AHCal. On the left side the fine structure for layers 1-30, on the right side the coarse structure for layers 31-38. Each cell is given by its index i/j.

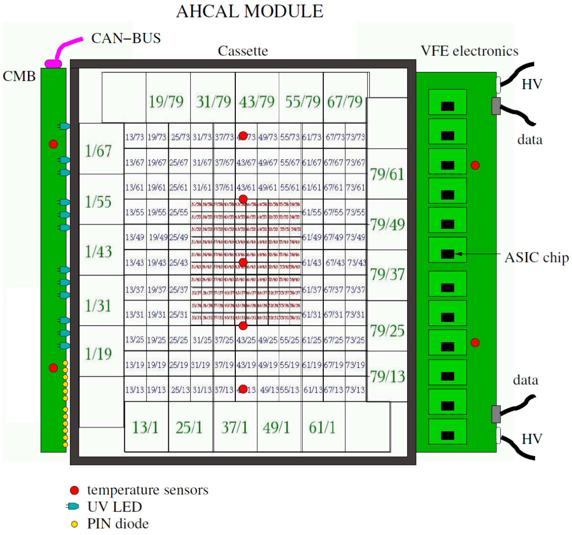

Figure 3.19: Module of the AHCal. The temperature sensors are marked as red dots. [38]

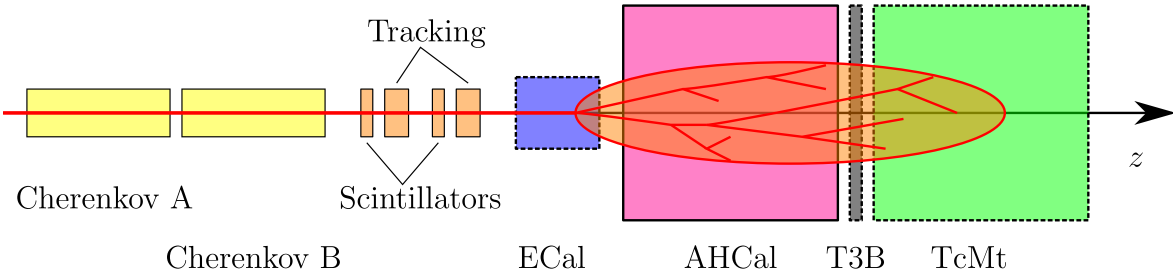

Figure 3.20: The testbeam setup. The secondary particle beam arrives from the left side along the z-axis. The subdetectors that were not part of all testbeam campaigns are marked with a dashed line.

thickness of 17.4 mm, thus resulting together with the steel cassette enclosing of a total absorber thickness of 21.4 mm per layer and a layer-to-layer distance of about 31.6 mm. The total absorber depth of the calorimeter sums up to 5.3 λ_I [38].

The second absorber stack, which was used in the years 2010 and 2011, was made of a tungsten alloy (density: $\rho_W = 17.8\,\mathrm{g/cm^3}$) with a thickness of 10 mm per layer. For cost reduction reasons only an octagonal shaped central part of the absorber plates was made from tungsten. The plates were glued onto a 0.5 mm strong steel support layer. The layer-to-layer distance of this W-AHCal was 24.7 mm, resulting in a total absorber depth of 4.9 λ_I for all 38 layers [45].

The big advantage of tungsten over steel absorbers is that due to its higher density, tungsten calorimeters of the same dimensions have a shorter total nuclear interaction length than steel absorbers, which is important for high energy collider experiments such as CLIC. The downside, however, is that hadronic cascades in tungsten produce a higher amount of low energetic neutrons, which in turn lead to a more complex time structure of the energy deposition. Thus a precise measurement on the time structure of the energy depositions was performed by the Tungsten Timing Testbeam experiment, which was parasitic to the W-AHCal and will be discussed in detail in chapter 4.

3.5.5 The Beam Test Setup

The beam tests of the AHCal calorimeter prototype were performed in dedicated testbeam facilities. The details of the setup varied between the individual testbeam campaigns. An general overview is shown in Figure 3.20, with the subdetectors which were not present at all times marked with dashed lines. Note that the focus lies on beam tests with the participation of the AHCal prototype.

The individual components are, following the direction of the beam:

Beam The beam is a secondary particle beam, generated from high energy protons hitting a dedicated beryllium target. The secondary particles undergo a momentum selection before they are focused towards the front of the detector setup. A secondary particle beam consists of a variety of particles which are created from interactions in the target block. The main components are charged pions $\pi^{\pm}$, (anti-)protons p,$\overline{\mathrm{p}}$, muons $\mu^{\pm}$ and electrons $\mathrm{e}^{\pm}$. Other particles such as $\mathrm{K}^{\pm}$ are generated, as well, but their contribution is small and often negligible. The momentum selector can be switched to either positive or negative polarity, thus selecting particles of a specific charge. As the primary beam consists of protons, they occur more often in the secondary beam than anti-protons which have to be explicitly created. Thus secondary beams at positive polarity can contain a large fraction of protons, while at negative polarity the amount of anti-protons is considerably smaller and most often negligible.

At the beginning of each data taking period muon data was taken for energy calibration of the detectors.

Cherenkov At secondary particle beams the type of the incident particle is not known. Therefore a particle identification system is needed. Here two gaseous Cherenkov detectors are used. They rely on the creation of Cherenkov light (cf. subsection 3.3.5) of particles travelling faster than the speed of light in a medium. Through selection of the gas and its pressure, only particles below a certain mass threshold create Cherenkov light. Typically one Cherenkov detector is set to the threshold between electron an pion, and the other between pion and proton. The Cherenkov light is readout via Photo Multiplier Tubes and is saved in the data acquisition system for offline analysis.

Scintillator Coincidence as Trigger A Trigger system is an electronic system that based on information obtained from specific detectors decides to record an event. In CALICE the Trigger system was connected to two $10 \times 10\,\mathrm{cm}^2$ scintillators which were placed before the calorimeters. If a particle passes through both of them, the coincidence of the attached PMT signals causes the trigger system to trigger the event recording. There were other combinations of scintillators, too. For example for muon calibration two $80 \times 80\,\mathrm{cm}^2$ scintillators were used, instead.

Tracking In order to determine the exact position of the incoming particle, a tracking system was installed before the calorimeters. Usually drift chambers were used. These use a strong electric field to force the ions and the corresponding electrons, which are created in the gas by the passing particle through ionization, to move to a side where they could be measured. The time the electrons take to drift to the sides of the chambers was taken to calculate the position where the particle passed through the chamber.

ECal In the beam test campaigns between 2006 and 2009 in most cases a prototype of an electromagnetic calorimeter (ECal) was installed. There were two versions tested so far: The SiW-ECal [46–48] which uses silicon as active material, and the SciW-ECal [49] which uses scintillators with SiPM readout. Both use tungsten as absorber material.

In all beam periods the ECal was removed from the beamline for dedicated runs in order to measure the response of the hadronic calorimeter prototype to electrons. For the testbeam campaign in 2010 and 2011, no ECal was installed.

HCal The prototype of the analog hadronic calorimeter, which was discussed in detail in the previous sections.

T3B During the testbeam campaign in 2010 and 2011, a single strip of 15 scintillator tiles was placed at the back of the AHCal. These were readout with oscilloscopes to get a measurement of the time development of hadronic showers. Details of the setup and the results will be discussed in chapter 4.

TcMt The Tailcatcher/Muon-Tracker uses the same readout technology as the AHCal: Scintillator with attached SiPMs. However, its structure is more coarse, using scintillator stripes with a size of $1000 \times 50 \times 5\,\mathrm{mm}^3$ [50]. It is used to measure the part of the hadronic showers that leaked out of the back of the AHCal, which happens especially at higher beam energies. It was installed in most, but not all testbeam periods.

3.5.6 Shower Start Identification: The Primary Track Finder

The high granularity of the imaging calorimeters allows a detailed view into the start and development and of hadronic showers. Therefore within the CALICE collaboration an algorithm was developed that is capable of identifying the shower starting position on an event-by-event basis for the prototype of the analog hadron calorimeter (AHCal). As it was originally developed for the identification of the track of the incident particle, the algorithm is called Primary Track Finder.

It is based on the comparison of the amount of deposited energy in consecutive layers. If the sum of these is beyond a certain threshold, the corresponding layer is defined to be the starting position. For more details the reader is referred to [51]. Tests on Monte Carlo Simulation, where the exact shower starting position is known, show an accuracy of ±1 layer for 78% of the events, and an accuracy of ±2 layers for 90% of the events [52].

3.6 Monte Carlo Simulation

General purpose detectors such as the ILD are very large and expensive. Therefore it is crucial to validate whether their performance meets the requirements prior to their construction. Part of this can be done by the construction of prototypes of important subcomponents, such as the calorimeter prototypes of the CALICE collaboration. The change of key parameters, however, is easier done in a computer model. Therefore large parts of the detector optimization studies are done in computer simulations. However, simulations are very complicated and thus still need to be validated by a comparison to the results of the testbeam experiments.

In general such simulations of events at a detector, like the ILD, are divided into three major steps.

1. A detector independent simulation of the collision of particles towards a certain set of final state particles via specified processes. This step is called Event Generation.

2. The interaction of the generated particles with the (detector) material. This step includes the development of electromagnetic and hadronic cascades and their energy deposition within the detector material.

3. Simulation of the reaction of the different subdetectors and their corresponding electronics towards the energy deposition. At the end of this step which is called Digitization, the simulated data should ideally not be distinguishable from a real detector signal.

For steps 1 and 2 typically Monte Carlo based simulations are used. The Monte Carlo method is based on repeated random sampling of a phase space. With it, it is possible to perform numerical integrations, which is important for the cross section calculation of certain processes in the first step. The random sampling, however, is used in the actual event generation, as well, when the energy and momentum of the particles need to be determined.

Monte Carlo methods only give an approximation on the real result, but they have the advantage that they can be used in cases where analytical methods fail.

Keep in mind that the simulation is based on theoretical models and parametrizations to data. Thus the results obtained from simulation might differ from real world measurements. Especially in the case of the models for the hadronic cascades validation of the simulation is important.

3.6.1 Event Generation

Event generation is the simulation of a specific high energy process such as $\mathrm{e^+e^-} \to q\bar{q}$ down to the resulting particles including their momenta. In principle it is a calculation of the corresponding Feynman-diagram with a subsequent fragmentation step, independent of any surrounding material and thus detectors.

There are many different Monte Carlo programs available to do the simulation, one of which is WHIZARD [53, 54]. To generate single events, WHIZARD first takes a generic process such as $\mathrm{e^+e^-} \to q\bar{q}$ and calculates the actual processes that contribute to this final state. In this example q stands for any of the six different quarks, giving a total of six different processes:

$$
\begin{array}{lll}
\mathrm{e^+e^- \to u\bar{u}} & \mathrm{e^+e^- \to c\bar{c}} & \mathrm{e^+e^- \to t\bar{t}} \\
\mathrm{e^+e^- \to d\bar{d}} & \mathrm{e^+e^- \to s\bar{s}} & \mathrm{e^+e^- \to b\bar{b}}
\end{array}
$$

For each of these subprocesses the matrix elements are generated and subsequently integrated, thus retrieving the corresponding cross sections.

With this information the actual event generation is performed. One of the subprocesses is randomly chosen based on their corresponding cross sections. Then the momenta of the final state particles are randomly chosen, while taking their momentum distribution and energy conservation obtained from the numerical integration into account.

The Monte Carlo method is used twice within this step. First for the integration of the matrix elements, and second when randomly choosing a specific set of final state particles and momenta.

Note that the integration of the matrix elements is dependent on the energy available at the collision, and thus is dependent on the beam energy spectra of the two incident beams. Initial state radiation (ISR), i.e. the emission of photons by the incident electron/positron prior to the collision, has the same effect on the available collision energy and is included in the event generation. In addition the photons created by ISR can leave a signature in the detector and hence are included in the event.

After all these steps the simulated event contains the requested final state particles of (one of) the processes, plus the ISR photons.

As quarks and gluons are not able to exist standalone due to confinement, in a last step every quark and gluon in the final state is passed to a fragmentation algorithm and turned into a jet of particles. The most often used library for this purpose is PYTHIA 6 [55], implementing the Lund-String model.

3.6.2 Interaction of Particles with Matter: GEANT4

For the simulation of the interactions of the particles created during the collision with the detector matter, GEANT4 is used. GEANT4 (Geometry and Tracking, [56, 57]) is a library that is widely used even outside of particle physics.

It provides the ability to implement the geometry of a detector as well as many different processes for the interaction of particles with matter. These include ionization by MIP-like particles as well as electromagnetic and hadronic cascades.

The simulation itself is performed by tracking the individual particles from one step to another throughout the detector material. At each step a list of possible interactions with the matter is generated and one of them is randomly chosen based on their respective cross sections. If daughter particles are created, they in turn are added to the list of tracked particles. In order to avoid infrared divergences and limit the computing time to a feasible amount, all particles are only tracked down until their energy drops below a certain threshold. Particles below this threshold will deposit their energy in an instant at their current position and hence will not be tracked any longer. In GEANT4 these cuts are implemented as a minimal range cut the particles have to be able to travel in that material. Thus by adjusting this cut the accuracy of the simulation can be exchanged for computing time, as during most steps secondary mostly low energetic particles are created. After all tracked particles dropped below the range cut threshold or have left the considered volume, the simulation of the single event is stopped. At this point GEANT4 provides information of how much energy was deposited in which detector volume.

While the simulation of electromagnetic processes is well understood and can reach accuracies on the sub-percent level, hadronic cascades are more challenging as they involve QCD processes and nuclear reactions. Due to the running of the strong coupling constant α_s, only high energy QCD processes can be calculated (asymptotic freedom). At lower energies, however, the underlying perturbation theory collapses.

Therefore, various theoretical and data parametrized models are used instead. These are only valid for certain energy ranges and types of particles and cover only specific subsets of processes during the collision. These range from energy exchange, including the creation of new particles, de-excitation and evaporation of excited nuclei over to the tracking of low energy neutrons.

The most important models are [58–60]:

Parametrized Models The low energy parametrized (LEP) respectively high energy parametrized (HEP) data set. These are the only data driven models in GEANT4 and are essentially an adaptation of the GEISHA model [61] used in GEANT3.

Parton String Models These models are valid for higher energies ($E > 10\,\mathrm{GeV}$), where the interaction is mainly between the incoming particle and the partons of one of the nucleons of the struck nucleus. These models build a string between two quarks, one of the struck nucleon and one from the incident particle. While enough energy is left, new quark-antiquark pairs are created from the string. In GEANT4 two different models are available which differ in the way of string formation and splitting. One is the Quark-Gluon-String (QGS, [62]) model, which uses Pomerons to mediate the scattering process. The other one is the Fritiof (FTF, [63]) model, which describes the diffractive hadronic interactions of the projectile with a nucleon via momentum exchange.

Intra-nuclear Cascade Models These models are valid for collisions at lower energy ($E < 10\,\mathrm{GeV}$), where the substructure of the nucleons is neglected and the interaction forms an intra-nuclear cascade. Within the GEANT4 models the nucleus is treated as a Fermi gas of nucleons, where all nucleons fill all possible energy states under the consideration of the Pauli exclusion principle. Collisions lead to excitations, which are handled by the specific models. In GEANT4 two different models exist: The Bertini cascade (BERT, [64]) differs from the binary cascade (BIC, [65]) in their modeling of the Fermi-gas and thus the creation of the particles. The Bertini cascade includes a complete de-excitation description, whereas the Binary cascade leaves the de-excitation step to an external model.

Precompound A model for the de-excitation of the nucleus. Used for the residual excited nuclei of models such as FTF and BIC.

High Precision Neutron Tracking At low energies ($E < 20\,\mathrm{MeV}$) the thermal motion becomes relevant for the cross-section and angular distribution calculations. The high precision (HP) neutron tracking model is based on experimental data and simulates the neutron capture. This model is very CPU intensive and thus only used if the low energy neutron part is relevant.

As the different models are only valid for specific energy regions, several models are combined to a physics list covering a larger energy range. At the overlapping regions a linear interpolation between the two lists in question is performed by randomly choosing one of the two models on an event-by-event basis.

LHEP A combination of the LEP and the HEP models, with a transition region from 25 GeV to 50 GeV. It is known to be less accurate than newer models, but is included here to provide an indication of the progress achieved with more recent codes.

QGSP_BERT Uses the QGS model followed by the Precompound (P) and evaporation model for the de-excitation of nuclei for energies above 12 GeV. The Bertini cascade is used for energies below 9.9 GeV. In the intermediate region between those two models in the range from 9.5 GeV to 25 GeV the LEP model is used.

FTFP_BERT Uses the FTF model followed by a Reggeon cascade and the Precompound evaporation (P) model for energies higher than 4 GeV. Below 5 GeV the Bertini cascade is used. This physics list uses the same cross section model as the QGSP_BERT list.

QGS_BIC This list is identical to QGSP_BERT for energies above 12 GeV. However, for lower energies the Bertini cascade is replaced by a combination of the LEP model and the binary cascade (BIC), with a transition between 1.2 GeV and 1.3 GeV.

QGSP_BERT_HP Same list as QGSP_BERT, but uses the high precision neutron tracking in addition.

QBBC A combination of various models depending on the energy and particle type. For pions BERT is used below 5 GeV, FTFP is used in the range of $4 - 25$ GeV and finally QGSP is used above 12.5 GeV. It has its own implementation of low energy neutron tracking which is similar to the high precision model (HP), but significantly faster.

The simulation of hadronic showers based on the physics lists above is in reasonable agreement with data acquired during beam tests. Most of the shower observables such as energy deposition, density, transversal and longitudinal size are often within 15% [59] or better, depending on the observable, the process and the physics list. However, further validation is still necessary to improve the various models. The prototypes of imaging calorimeters of the CALICE collaboration with their so far unmet fine granularity are therefore a rich source of information.

3.6.3 Modelling Detector Effects: Digitization

In the last step of the full detector simulation, the response of the detectors and the electronics is simulated. This “digitization” step is based on the information provided by the GEANT4 simulation of particles traversing the detector and the resulting ionization energies in the various materials.

This includes:

- The conversion of the deposited energy into a detector signal.

- Detector thresholds and noise, such as darkpulses in SiPMs.
- Dependence of the detector response on changes in temperature, applied voltage and other environmental conditions.
- Detector and read-out specific features or shortcomings such as Afterpulsing or saturation in the case of SiPMs.

The goal is to convert the knowledge of the deposited energy into a signal as it would have been recorded at a real experiment. As this is highly specific to the detector and the used read-out, no generic software is available. Instead for each detector the corresponding digitization software has to be written anew, using very detailed knowledge of the detector behaviour.

Chapter 4

Measurement of the Time Development of Hadronic Showers in Tungsten

One of the challenges to perform precision measurements at CLIC is the high bunch crossing frequency of 2 GHz (0.5 ns) which makes it more difficult to correctly correlate a measurement of one of the subdetectors to a certain event. This is especially true for energy depositions of hadronic showers in the calorimetric system, as hadronic showers, unlike electromagnetic ones, have a non-instantaneous component (cf. section 3.3). These "late energy depositions", albeit small, can occur tens of ns up to several microseconds after the actual interaction and thus can be wrongly assigned to one of the succeeding bunch crossings during reconstruction. This is especially true for the CLIC_ILD detector concept where the calorimetric system uses tungsten as absorber, in which the amount of evaporating neutrons causing these late energy depositions is relatively high.

There are several techniques to ensure a correct assignment between bunch crossing and detected energy deposition. One of them is searching for clusters in the calorimeters over a larger time frame and then using a single timestamp for the entire cluster of hit cells, assuming they all originate from the same event. This technique was tested amongst others against a full detector simulation based on Geant4 (cf. subsection 3.6.2) plus a sophisticated digitization simulating detector effects based on experiences obtained from testbeam data like the one from the CALICE collaboration (cf. section 3.5). Obviously such a comparison relies on the accuracy of the simulation. Therefore a small experiment was designed to actually measure the timing structure of hadronic showers and compare them to the predictions of the simulation. As the absorber used in the calorimetric system of the ILD detector for CLIC is tungsten, this testbeam experiment was called "Tungsten Timing Testbeam" (T3B).

This chapter will show the details of this experiment, starting with the experimental setup in section 4.1. In section 4.2 the calibration and reconstruction of the data will be discussed, while section 4.3 gives details on the simulation. Finally, the results including a comparison between data and Monte Carlo are shown in section 4.4.

4.1 T3B: The Tungsten Timing Testbeam Experiment

The measurement of the time structure of hadronic showers is quite challenging. Depending on the spatial resolution, a prototype of a hadronic calorimeter already needs several hundred or thousand read out channels. For example, the CALICE Fe-AHCal with a depth of about $5.3\,\lambda_{\mathrm{I}}$ has already about 7800 channels, using varying cell sizes with the smallest being $3 \times 3\,\mathrm{cm}^2$ [38]. To measure the timing of hadronic showers each read out channel has to be monitored with a very good accuracy in the order of one nanosecond over a period of several microseconds. This does not only lead to a huge amount of data, but is on the other hand very expensive to construct. Consequently the number of channels that can actually be monitored with this high timing precision is limited.

One way to get a comparable lateral resolution by using only a limited number of channels is to place all tiles in a straight line, starting perpendicular from the shower axis. Given enough recorded events such a detector can measure the average development of hadronic showers by using the radial symmetry around the showers axis. As the dimensions of the used tungsten absorber plates were $80 \times 80\,\mathrm{cm}^2$, a strip of 15 tiles, each with dimensions of $3 \times 3\,\mathrm{cm}^2$ and thus covering a radius of 45 cm, is sufficient for the measurement of hadronic showers.

As it was discussed in subsection 3.3.4, hadronic showers are statistical processes. Especially the shower starting point, which we shall define as the first hard interaction with the creation of secondary particles, differs on an event-by-event basis and its distribution is defined by a falling exponential (cf. Equation 3.5). Thus a single detector layer placed after a sufficient depth of absorber material sees every single development stage of hadronic showers, starting from no hadronic interaction of punch-through and thus MIP-like particles, over the central part of the cascade down to the tails of hadronic showers starting at the front of the calorimeter. If the distance between the detector layer and the shower starting position is known by exterior means on an event-by-event basis, the measurements of these 15 channels are sufficient to describe the average response of hadronic showers.

During the testbeam campaigns T3B was always parasitic to a fully functional prototype of the Tungsten Analog Hadronic Calorimeter (W-AHCal) of the CALICE collaboration, which is able to determine the shower starting position and provide it to the T3B experiment for offline analysis. Hence, some effort was made in order to synchronize the data streams and thus the event recordings of the two independent experiments.

4.1.1 The Experimental Setup

The CALICE W-AHCal Testbeam Campaign

The CALICE collaboration performed beam tests at the CERN Proton Synchrotron (PS) at the end of 2010 and the Super Proton Synchrotron (SPS) several times during

2011. The aim of this testbeam campaign was to test tungsten as an absorber for a hadronic sampling calorimeter, reusing the existing active layers of the steel analog hadron calorimeter (Fe-AHCal) prototype which is based on scintillators read out via SiPMs (cf. section 3.3, [38]). A mechanical stack was constructed holding layers of the tungsten absorber material in place while allowing to easily slide in the read out layers of the CALICE AHCal in between. The stack was designed to hold up to 40 layers of active material, while during the testbeam campaign not more than the first 38 layers were equipped. Hence the remaining slots were used to hold parasitic experiments like the T3B layer.

The first testbeam campaign with hadrons took place for two weeks in November 2010. The T9 beam line of the CERN Proton Synchrotron (PS) at the East Hall provided a mix of electrons, pions, muons and protons with a momentum range of 1 to 10 GeV. During this period the mechanical frame of the W-AHCal contained only 30 active and tungsten absorber layers. The remaining 8 layers were added for the beam tests performed at the SPS, which took place for a total of three weeks in June, July and September 2011 at the H8 beam line in the North Hall which was used to provide particles with a momentum between 10 and 180 GeV.

More details on the beam tests by the W-AHCal can be found in [45].

The T3B Layer with Scintillator Tile Readout

As it was described in section 3.5, the hadron calorimeter of the ILD as well as its prototype, the AHCal of the CALICE collaboration, both use scintillator as active medium which in turn is read out using Silicon Photomultipliers. As the focus of the T3B experiment lies on the measurement of the time structure of hadronic showers in the context of an ILD detector at CLIC, the same read-out technology was used. However, as already pointed out at the end of subsection 3.5.2, a few adaptations were made with respect to the CALICE prototype.

This includes the usage of blue sensitive Hamamatsu MPPCs [66] which are capable of directly recording the scintillation light. Thus it is now possible to use tiles which are directly coupled to the SiPM, in contrast to the coupling via a Wavelength Shifting Fiber (WLS) for the tiles of the CALICE AHCal. This modification was necessary, as the WLS introduces an additional time delay as well as an unwanted broadening of the signal over time, caused by the conversion of the blue scintillation light to green. To ensure a uniform response regardless on the position of a passing charged particle, a small hole (a “dimple”) was drilled into the scintillator tile [44]. The tile dimensions stayed the same with respect to the ones used in the CALICE AHCal prototype ($30 \times 30 \times 5\,\mathrm{mm}^3$).

Apart from a small hole for the SiPM, the scintillator tile was covered by a layer of reflective 3M foil [67] to maximize light collection. The SiPMs were mounted on a small PCB which contained a preamplifier and the necessary connectors. The size and form of the PCB was chosen to cover the attached scintillator tile, such that the tile, the SiPM and the PCB were one dedicated unit (Figure 4.1). Black plastic foil, normally used to cover photo multiplier tubes, was wrapped around the tiles including the SiPM to minimize noise from ambient light.

15 of these preamplifier boards with tiles and attached SiPMs were mounted on an

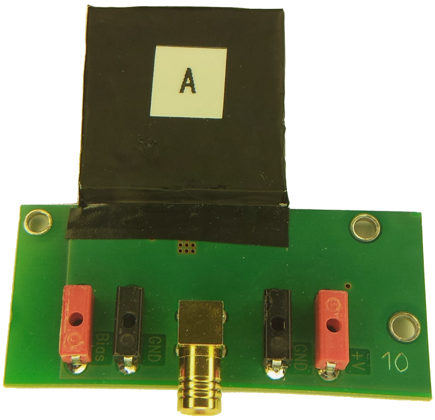

Figure 4.1: A T3B tile directly coupled to the SiPM on the preamplifier board. The tile is wrapped in black, light tight foil. The connections on the preamplifier board are (from left to right): bias voltage for the SiPM (+/-), signal, 5V for preamplifier (-/+).

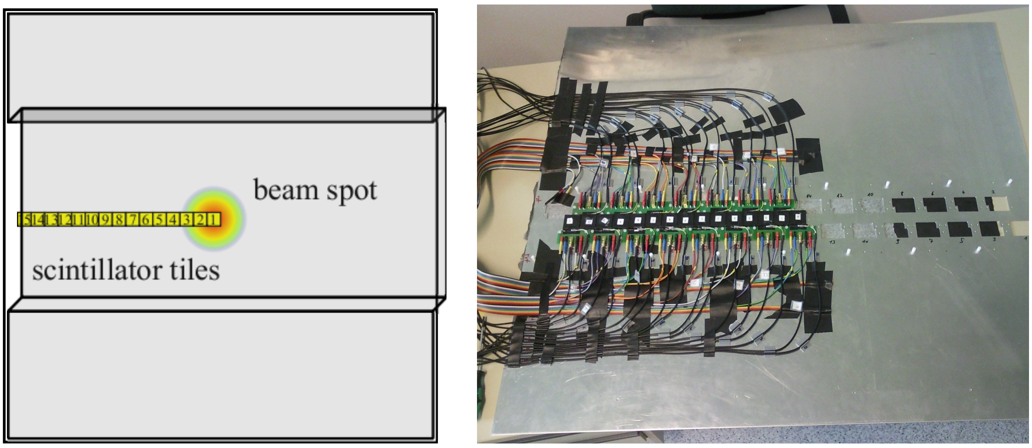

(a) Sketch of the T3B layer

(b) Foto of the opened T3B layer

Figure 4.2: The T3B layer. The left plot shows a sketch with the positions of the scintillator tiles shown in yellow. The expected position of the particle beam is marked as well. The right figure shows the opened T3B layer including the cables to the preamplifier boards.

1 mm thick aluminium layer (see Figure 4.2(b)). The size of $1.0 \times 1.0\,\mathrm{m}^2$ was chosen to easily fit into one of the slots of the CALICE absorber structure stack with the central tile being at the foreseen beam center. A second aluminium plate was mounted on top to convert the layer into a cassette and protect the preamplifier boards both from damage and ambient light. A sketch of the layer can be seen in Figure 4.2(a).

The Readout

The T3B experiment is designed to record its data at a beam line at a testbeam facility which uses secondary particles created by shooting protons on a target. As there are many users of such a facility, the time is divided among them and each user gets assigned a "spill window". Only inside this spill window particles are delivered. This window had a length of about 350 ms with a varying repetition rate of 5-15 s at the CERN PS, and about 10 s with a repetition rate of 45 s at the CERN SPS. Within the spill window between 10^2 and 10^4 and more particles were delivered.

Most of these particles are hadrons which will almost always create a hadronic shower in the absorber of the CALICE hadronic calorimeter which is located upstream with respect to T3B. Each of these hadronic showers has to be recorded over a few microseconds with nanosecond precision. This requires fast digitizers with a recording speed of at least one giga sample per second per T3B channel. However, the particles are randomly distributed within the spill window and arrive with a rate of up to 1 kHz on average. It is difficult to transfer this amount of data directly onto a PC's harddisk. Consequently the digitizers used for the T3B read out need to be able to trigger significantly faster and store each waveform in an internal buffer which is big enough to record all events within a spill window.

During the design phase of the T3B experiment different digitizers were tested. One option which fulfilled all the requirements is the PicoScope 6403 (Figure 4.3(b)) of the PS 6000 series created by Pico Technology [68], a digital oscilloscope operated via USB from a standard PC. In addition to the official manufacturer's software it is possible to directly access the oscilloscopes via a software development kit (SDK) giving full control to a custom made C/C++ program working as a data acquisition (DAQ). The latter option was chosen and the created DAQ will be described in more detail in subsection 4.1.2. The PS 6403 has four channels with a sampling rate of 1.25 GS/s each and with a vertical resolution of 8 bit. It has a shared internal buffer of 1 GS which is large enough to store several ten thousand events with each waveform being recorded over $2 - 3\,\mu$s with the maximum resolution of 800 ps. The connection to the PC is done via a USB 2.0 interface which proved fast enough to transfer up to 10000 events recorded by four different oscilloscopes attached to the same PC in the time between two spill windows at the SPS (≈ 35 s).

The data acquisition has to be started at the beginning of the spill window, and stopped at its end. Hence it is necessary to monitor the current status of the spill window. At CERN each beam line provides the necessary signal for the start and the stop of the particle extraction. These signals come at a maximum rate of around 1 Hz and can be recorded by the much cheaper PicoScope 2203 (Figure 4.3(a)) with a maximum sampling rate of 40 MS/s and a buffer which is only large enough to save a single waveform. Like the PS 6000 series it is a USB oscilloscope and is controlled and read out via the official manufacturer's software or the SDK.

(a) Picoscope PS 2203 (b) Picoscope PS 6403

Figure 4.3: Picture of the PicoScope PS2203 (left) and the PS6403 (right) oscilloscopes used in the T3B experiment [68].

Temperature Monitoring

SiPMs are very sensitive towards temperature changes (cf. subsection 3.5.1). Thus each sensor was monitored individually by a PT-1000 platinum resistance, read out via a 4-wire connection using a custom made temperature monitoring board that is attached to the data acquisition PC via USB. Each sensor was read out about once per minute with a relative accuracy which is expected to be in the mK region.

Testbeam Setup

T3B was placed in one of the last layers of the W-AHCal absorber structure, acting as a parasitic experiment. The exact position changed during the different campaigns. At the PS beamlines T7 and T9, T3B was installed in slot 33, with slot 32 being empty, slot 31 containing a prototype of the MicroMegas layer [69], and slots 30 to including 1 were equipped with the AHCal sensitive scintillator layers. Only slots 1 to 30 were equipped with tungsten absorbers, while for slots 31 and up no absorber was used.

At the SPS beamline H8 T3B was installed in layer 40, with layer 39 being empty and layer 38 to 1 were equipped with the AHCal sensitive layers and tungsten absorber. Again layer 39 and 40 had no absorber plates installed.

As it was mentioned earlier it is essential to be able to synchronize the two data streams of the W-AHCal and the T3B experiment if one wants to use the information of the shower starting position from the AHCal. Therefore the T3B experiment was triggered by the W-AHCal, such that they both recorded the same events. A complete sketch of the experimental setup which was used both at the T9 and the H8 beamlines is shown in Figure 4.4.

The data acquisition (DAQ) of the W-AHCal monitors two $10 \times 10\,\mathrm{cm}^2$ scintillators placed upstream with respect to the calorimeter. If both see a signal from a passing

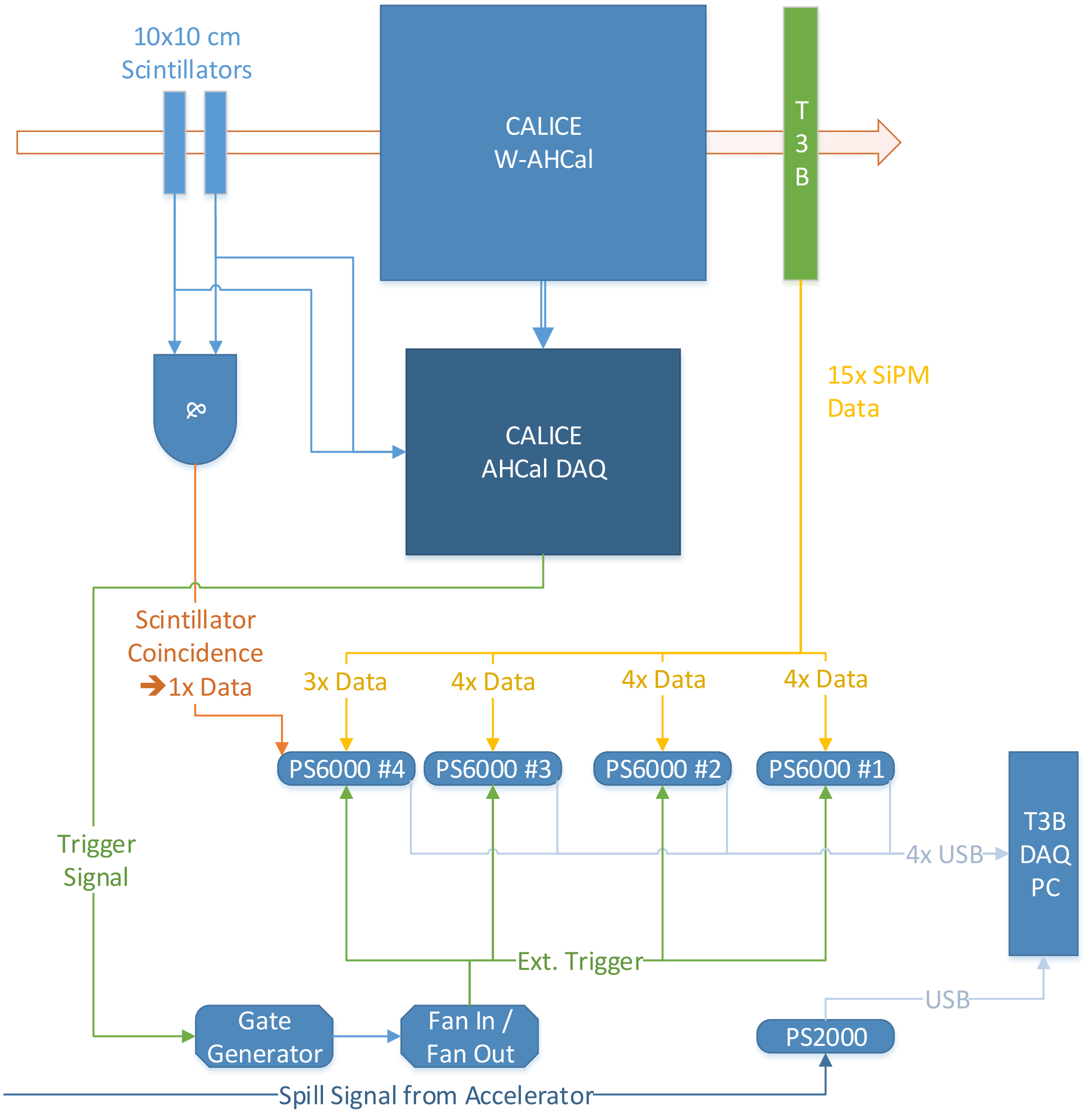

Figure 4.4: A sketch of the T3B experimental setup as part of the CALICE testbeam campaign at CERN.

particle in coincidence, the CALICE DAQ records the event and gives a signal to the T3B DAQ via the green trigger line. This signal is distributed to the external trigger input (EXT) of the four PS6000 PicoScopes by using a linear Fan-In/Fan-Out NIM module of type LeCroy model 428F. On arrival of the trigger signal at the EXT input, each PS6000 records the waveform with a total length of $2.4\,\mu$s of each of its four channels and stores it in its internal buffer. These channels are connected to the 15 SiPMs (orange lines in Figure 4.4) of the T3B layer.

The PS2000 oscilloscope is attached to the spill signal which is provided by the beam line, in order to start and stop the data acquisition.

All PicoScopes are connected to the central DAQ PC via USB (cyan lines in Figure 4.4). The PC runs a self written data acquisition software which controls the oscilloscopes and will be described in detail in subsection 4.1.2.

Independent of the coincidence generated internally by the CALICE DAQ from the signal of the two scintillators, a NIM coincidence unit (Type LeCroy model 365AL) creates a similar signal which is fed into the last remaining channel of the four PS6000. This is used in the offline analysis to check that exactly one particle hit the detector setup and is needed for two reasons:

- Rejecting events with multiple particles within the recording time window.
- Rejecting calibration events generated internally by the CALICE W-AHCal DAQ without passing particles.

Another way of data taking is the usage of the NIM generated coincidence as trigger input instead of the one from the CALICE W-AHCal. This circumvents the long dead time of the CALICE DAQ after the recording of one event and allows a significant higher data acquisition rate. To ensure that the T3B experiment can cope with this high rate, the trigger is fed through a gate generator which is a NIM module of type LeCroy Model 222. This module ensures that once a trigger arrives, there is a minimum time span of $3\,\mu$s before the next trigger signal is delivered to the four PicoScopes. This prevents the four oscilloscopes to run out of sync, as the time to recover from a recording (dead time) is not the same for all, which can lead to one oscilloscope recording an event, while another is still busy. This was useful to increase the statistics on the one hand and was used for beam tests together with the CALICE SDHCal, which uses steel instead of tungsten as absorber on the other. Details of this setup and the analysis which includes a comparison of steel to tungsten absorber is available in [70]. However, when running in this standalone mode no information on the shower starting point is available from the CALICE W-AHCal. Hence, in the analysis presented here only events which could successfully be synchronized to the W-AHCal were used.

4.1.2 The T3B Data Acquisition Software

The spill structure of the testbeam as well as the need to use several oscilloscopes to read out all SiPM channels, the scintillator coincidence and the spill signal in parallel places unique requirements on the data acquisition (DAQ) software. Especially the fact that the DAQ software needs to manage all connected oscilloscopes at once is an untypical use case and was not foreseen by the vendor's software. Hence the DAQ software was designed and created anew for this experiment, using the available software development kit (SDK).

This SDK was available in C for Visual Studio on Windows and gives full control of the PicoScopes. It is available on the website of the vendor [68]. However, during the preparation phase some shortcomings of the driver available at that time were identified. This included certain race conditions within the PS6000 that lead to measurement of wrong values. These were fixed by a custom made version of the driver and SDK by the vendor. Although these changes were later included in the succeeding official releases by the vendor, only the custom made version was available in time and was therefore used for the first and for the sake of consistency subsequently for the entire testbeam campaign.

As the SDK is based in C, it was a natural choice to create the software DAQ using C/C++. Prior to the actual programming a list of required features was specified. The software had to provide:

- Control of all PicoScopes according to the data acquisition / read out cycle at the testbeam.
- Several customizable sets of oscilloscope settings.
- Support for the live monitoring the SiPM gain by monitoring their dark pulses.
- A fast data transfer from all oscilloscopes to the PC.
- A fast way of saving the data to the disk without blocking the acquisition.
- A graphical user interface usable by both experts and non-expert shift personnel.
- Support for creating log files for debugging.

The DAQ Software Core

The DAQ software had to be working reliably without crashes over a time of several weeks without interruption, as a downtime caused by crashes or slow execution due to non optimal implementation would cause losing acquisition time and hence valuable data. Therefore its major tasks were divided into several classes.

The core components are:

DataReadOut The central manager and control class. The functions exposed to the public give the necessary control of the data acquisition and can be used by a user interface of any kind.

OscilloscopeRunManager This class is responsible for initializing and controlling the oscilloscopes according to the data acquisition / read out cycle and can be considered as the actual working horse.

RunMode The `RunMode` contains the actual values of the settings to program the oscilloscopes and determine the end of the data acquisition.

A full UML diagram can be found in appendix A.

Oscilloscope Settings: The Run Mode

Before data can actually be recorded the DAQ has to be configured for the run. These settings include:

- Definition of the end of a single acquisition (typical: Spill) cycle, i.e. the number and type of oscilloscopes that need to be finished with their data acquisition task.
- Oscilloscope specific settings:
    - Maximum number of recorded waveforms.
    - Time resolution and acquisition duration.
    - Channel specific settings such as vertical resolution.
    - Trigger configuration.

All these settings form a set which is called Run Mode. A Run Mode is specific to a way of taking data, e.g. one can be used for the acquisition of testbeam data, while another one is used for the acquisition of random noise without the usage of any kind of spill information. Within the software DAQ different RunModes are represented by instances of the class `RunMode`.

Apart from the oscilloscope settings, a Run Mode contains settings which decide when the DAQ has to stop the data acquisition and start with the transfer of the data to the PC. This can be done via setting the maximum number of events recorded by each oscilloscope and defining how many oscilloscopes have to be finished. At the testbeam usually the end of the acquisition is defined by requiring the PS2000 to have recorded the spill end event. In addition the Run Mode has a setting allowing to start the acquisition only after the PS2000 has recorded an event with inverted trigger direction, which marks the start of the spill window.

Each of these settings has to be restored from a file when (re-)starting the DAQ software. For that purpose a configuration file was used. It had the format of an INI file which is a widely used, text based configuration file storing settings in the form of a simple `SettingsName=Value`. The access to the different settings was simplified by having an instance per setting of the class `Setting`. Its access functions provide easy access to the desired value as well as a sensible default value if the settings is not yet part of the configuration file. Access to the `Setting` instances is managed by a single instance of the class `SettingsManager`.

Monitoring the Gain of the SiPM via Intermediate Run Modes

SiPMs are very sensitive to environmental changes. Especially the gain of the sensors changes with temperature, thus altering the height of the recorded signals. In order to correct these changes during the calibration, the gain has to be known for any given time of the experiment. Of course one could use the temperature measurements and extrapolate the gain to any given point in time, but it is easier and less error prone to constantly monitor the gain throughout the experiment.

As the gain influences the entire waveform, it can be extracted from SiPM dark rate by comparing the integral of 1 and 2 p.e. waveforms, which occur at a rate of several kHz for each device. These should be monitored as close to the actual data acquisition as possible. As at the testbeam the beam arrives in spills, the time in between two spills can be used for the dark rate recording. For that purpose intermediate Run Modes were introduced.

Through class inheritance an intermediate Run Modes contains the same settings as a normal Run Mode and can be configured in the same way. The main difference lies in the fact that an intermediate Run Mode is attached to a normal Run Mode and thus the data recorded in both are stored within the same spill structure. The intermediate Run Mode has full access on all oscilloscopes and could use the PS2000 to wait for the next spill signal. However, by convention the intermediate Run Mode is disabling the PS2000 and configures the PS6000 to trigger on SiPM dark rate to record a predefined number of dark pulses. As the time between two spills was lower at the PS, only 500 events were required for the gain determination, while at the SPS this value was set to 1500 events. Note that for each given event only one of the attached SiPMs recorded a dark pulse, while the other three attached SiPMs typically saw nothing. Assuming that the dark pulse probability is approximately equal for all devices, the intermediate Run Mode records approximately 125 (PS) respectively 375 (SPS) events per spill and SiPM.

The intermediate Run Mode is activated directly after the normal Run Mode finished the transfer to the PC and would start with a new acquisition cycle.

Transfer and Storage of the Acquired Data to the PC Harddisk

The large buffer of the PS6000 series oscilloscopes of 1 GB allows to record more than 10000 events per spill. Given that typically each waveform of the four channels is recorded with 3000 samples with a vertical resolution of 8 Bit, these 10000 events need 960 MBit per oscilloscope, resulting in a total of 3.84 GBit or 480 MByte per spill. This data needs to be transferred via USB 2.0 to the PC within less than 30 s, such that the oscilloscopes are ready for acquisition at the beginning of the next spill window after 35 s for the SPS.

Considering only the gross transfer rate of USB 2.0, which is 480 MBit/s or 60 MB/s, a single USB controller would need a minimum of 8 s for a complete transfer of the acquired data. As there is significant overhead slowing down the net transfer speed, only one oscilloscope should be attached to the same USB controller. If this is the case, the transfer of the four attached oscilloscopes can be done in parallel, as the full rate of 480 MBit/s are available for a single oscilloscope, significantly lowering the necessary time.

In the software this was implemented by running each transfer of the oscilloscope in its own thread, while the main thread in `OscilloscopeRunManager` is waiting for the transfer to finish.

Once the data transfer to the PC is done the recorded waveforms need to be saved to the harddisk. This part is taken care of by the `DataWrite` class in an asynchronous, non blocking implementation. For this it first gets all waveforms and the information on the run mode by the `OscilloscopeRunManager` in the main thread. These are added to a queue, which has a maximum length for storing 10 Spills. After the transfer to the `DataWrite` class the control is immediately returned, such that the DAQ can be prepared for the next spill without having to wait for the harddisk. An additional thread in `DataWrite` takes care of the actual disk access.

The T3B Data Acquisition Workflow

The workflow of the T3B data acquisition for the recording of a single run is shown in Figure 4.5. It was designed for the acquisition and the readout of an entire spill before starting over.

The main thread is starting in the upper left and is responsible for the main workflow, shown here in gray. It incorporates the optional setting of waiting for the spill start signal from the accelerator via the PS2000 in the upper right in light blue. This assumes that the PS2000 is set to trigger on the spill end signal, and that the spill start signal is the same, but with an inverted flank.

As already mentioned before, the transfer of the acquired waveforms from the oscilloscopes to the PC is done in several parallel threads in order to speed up the process. For the sake of readability only a single transfer thread is included in the diagram in dark blue, as their workflow is identical for all. The DAQ, however, uses one thread per active oscilloscope which are all started for each spill by the main thread. During the transfer the main thread is idle and waiting for all transfer threads to finish their jobs. In addition to the control flow indicated by the black arrows, the data flow is included in Figure 4.5 by red arrows.

Once the data transfer is finished, the main thread adds the data of the current spill to a queue. As the queue is accessed from multiple threads, the access is regulated by a mutex. A data write thread constantly monitors the queue, dequeuing available data and storing it on the disk. The thread is running constantly and is started together with the DAQ. This ensures that the disk speed doesn't negatively influence the time necessary for a complete readout cycle. Note that the size of the queue is limited to a maximum of 10 spills. If the queue grows larger, the main thread execution is blocked until the data of one spill is successfully written to disk and removed from the queue, freeing a slot.

After the data is handed over to the data write thread, the main thread checks if an intermediate Run Mode is available. If it is, it exchanges the active Run Mode with the intermediate one, and marking the actual Run Mode as the “intermediate Run Mode of the intermediate Run Mode”, such that it will be changed back in the next cycle.

This acquisition/read-out cycle is repeated until the run is marked to stop by the user. For this reason the (graphical) user interface is running in yet another thread.

As unforeseen events can happen, the user is given the opportunity to force quit the current acquisition cycle. In order not to leave the threads in an undefined and thus potentially blocking state, between each of the steps described above the threads are

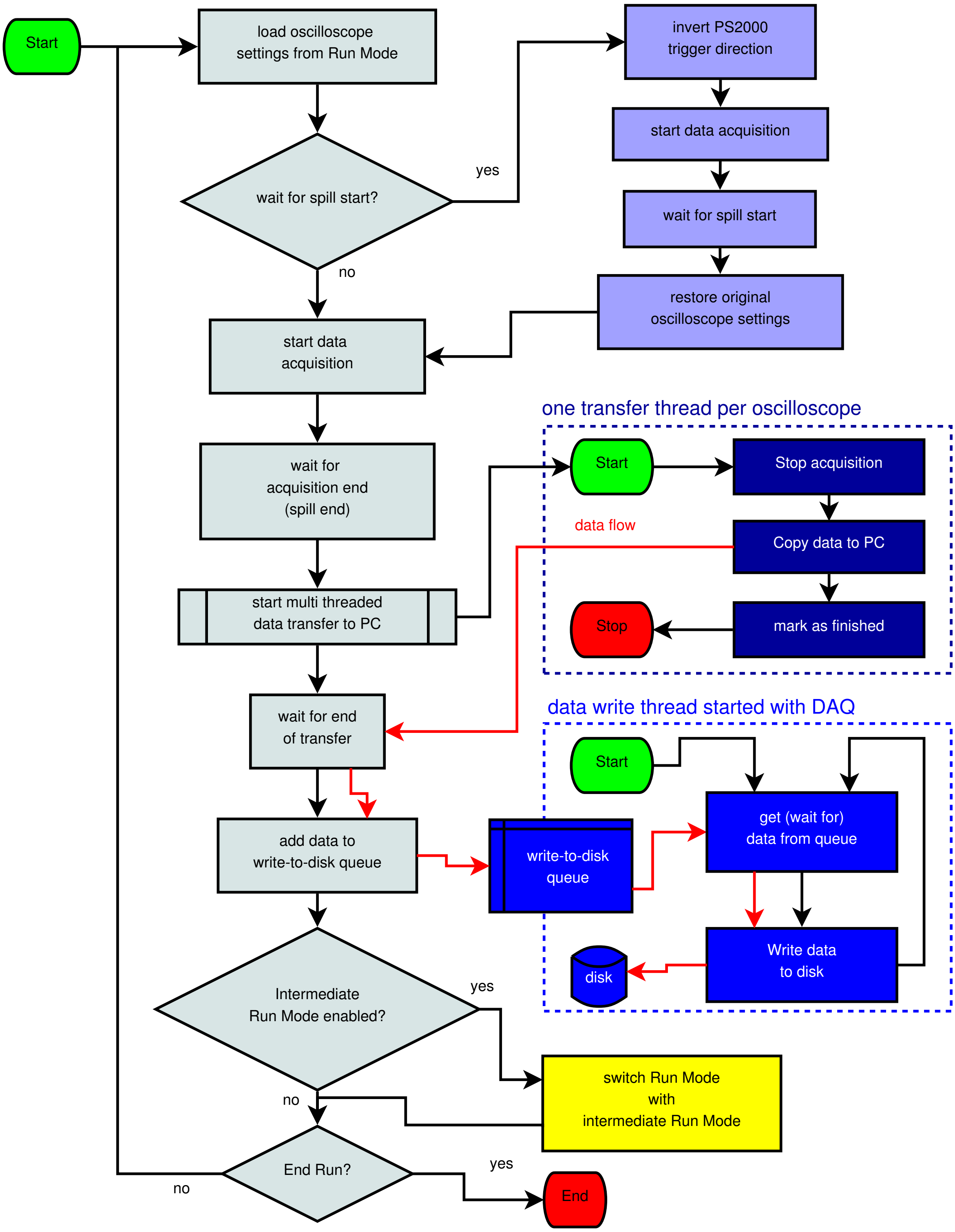

Figure 4.5: Flow chart of data acquisition. Refer to text for explanations.

monitoring an externally set variable which notifies them if the user desires to force quit the acquisition. If set to true, each of the threads immediately stops their respective actions, i.e. resetting the oscilloscopes, deleting unsaved data, etc. and then returning control such that the program is in idle state, waiting for the user to start a run.

4.1.3 Event Synchronisation with the CALICE W-AHCal

In order to extend the T3B measurement along the shower axis into the z direction, the information on the shower starting position provided by the W-AHCal can be used. Therefore the data acquisition systems of T3B and the CALICE W-AHCal shared the same trigger (cf. subsection 4.1.1).

However, both experiments use different data acquisition systems and data streams. Hence, it is necessary to perform a matching for each event between these two independent data streams. Ideally this synchronisation of events would have taken place in situ by simply recording information on the event status of the respective other data acquisition into the own data stream. However, this was not possible as both experiments use an internal buffer before writing the events to disk at the end of the spill. During the acquisition of the spill no or not enough information could be provided. On top, such information would have been needed to be transferred within a few hundred μs to the respective other data acquisition system, which itself is already a challenging task. As a consequence the event matching was performed offline.

The event synchronisation needs data which is available in both data streams. An ideal candidate would be the time of the individual events. This information, however, was not available for the events recorded with the T3B data acquisition. Instead, only the start and ending times of the spill in which the events were taken could be recorded, together with the number of events within that spill. The same information can be extracted for the W-AHCal. By assuming that the order of the events within each spill is consistent between both data acquisition systems, the synchronisation is thus performed first on the spill-by-spill level. In a second step the matching of the events within the spill can be checked by using the external NIM-generated scintillator coincidence, which is monitored by both acquisition systems.

The Spill-by-Spill Synchronization Step

The spill-by-spill synchronisation is performed by creating a list of all spills for a single T3B run, ordered by their end time. The same list is created for the corresponding CALICE W-AHCal runs. For each spill in T3B a corresponding one is searched for in the W-AHCal list by looking at a similar ending time, i.e. spills that end up to 5 s later than T3B spills. If both spills contain the same number of events, the correlation is added to a list of successfully matches spills.

However, when creating this list one has to keep in mind that the clocks used in the two data acquisition systems were not synchronized. Thus, there is an unknown offset between the spill ending times in the two data streams, which varies through the different testbeam periods. As the offset is unknown, the list of successfully matches spills is created multiple times, each time with a different assumed offset in the range

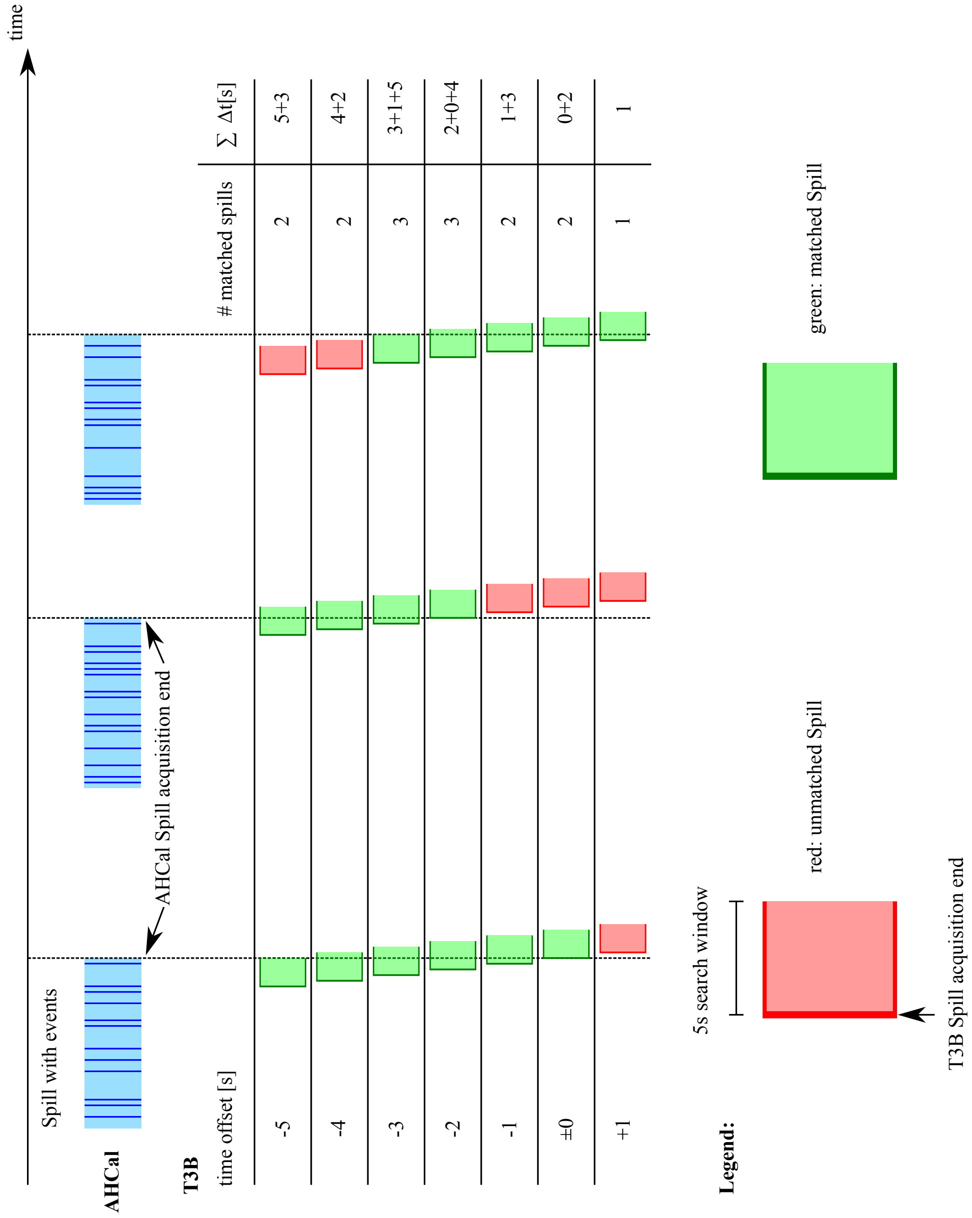

Figure 4.6: Example of the spill-wise synchronization between the CALICE AHCal and T3B based on the time of the ending of the data acquisition of a spill of the independent data streams. An AHCal spill is matched with a T3B spill if the T3B spill starts up to 5 s earlier than the AHCal spill, including a global time offset within the T3B data stream. Here the matching status for different offsets is displayed.

from −60 s to +60 s. An example is given in Figure 4.6, which shows the time structure of the spills of the CALICE W-AHCal (blue, upper part) and the ending times of T3B including a few assumed time offsets (lower part). The color of the T3B spills indicates if a matching AHCal spill was found (green) or not (red). In the right table, the number of successfully matched spills are given together with the total time difference of these spills.

Out of these the list(s) with the highest number of entries, i.e. with the highest number of successfully matched spills is chosen. In the example of Figure 4.6, these would be the ones with offsets of −3 and −2 s. If there is more than one list the one with the lowest quadratic sum of the difference of number of events per spill for all spill pairs is taken:

$$\sum_{\text{spills}} \left(N_{\text{T3B}} - N_{\text{AHCal}}\right)^2$$

Note that during the preparation of the list of successfully synced spills, only unique correlations are allowed. Lists in which a CALICE spill can be correlated with two or more T3B spills (or vice versa) are discarded.

Checking the Trigger Line History

The CALICE DAQ used during the beam tests of the W-AHCal has several trigger inputs, called trigger lines. They are mostly used to monitor the status of various external scintillators, the signal of the two Cerenkov detectors for particle identification and the status of the spill signal. Within a single event the history of these trigger lines is recorded over a time of $6.4\,\mu$s divided in 256 bins of each 25 ns width.

Here we will only consider the trigger line which was monitoring the same NIM generated coincidence of the two $10 \times 10\,\text{cm}^2$ scintillators as the T3B DAQ. Most, but not all events recorded by the CALICE DAQ (and thus the T3B DAQ as well) are caused by an incoming particle. In some cases, however, the recording is triggered by an oscillator with a frequency of at least one event per second. In these oscillator events the $10 \times 10\,\text{xm}^2$ scintillator coincidence line will mostly be empty, except for rare cases where oscillator and incoming particle coincide by chance. As the scintillator coincidence was monitored by both DAQ systems and is thus available in the T3B and in the W-AHCal data stream, it is used to check the correlation on an event-by-event level. If the coincidence trigger is visible in one data stream but not in the other, the synchronisation of this spill was not successful and the spill is removed from the list of successfully mapped spills.

All events of the remaining spills are entered into a lookup table, which gives a unique relation of a pair of T3B run and event number to a pair of CALICE W-AHCal run and event number. This lookup table is used during the analysis of T3B events to quickly get the corresponding fully reconstructed and calibrated CALICE AHCal event information.

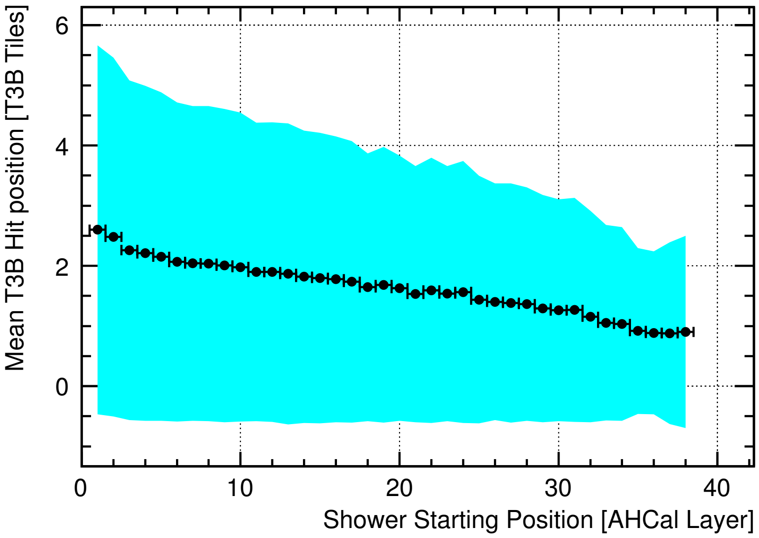

Figure 4.7: The mean T3B hit position with their respective standard deviation drawn as error for events with different shower starting position.

Energy	60 GeV	80 GeV	180 GeV
Event Eff.	0.84	0.75	0.76
Spill Eff.	0.76	0.70	0.67

Table 4.1: Mean synchronization efficiency for all runs at the same energy. Efficiency once calculated on the number of successfully synchronized events, and once on the number of successfully synchronized spills.

Crosscheck and Efficiency

To crosscheck if the events in the two independent data streams were successfully synchronized the average hit position within the T3B layer was calculated independently for all events for a certain shower start layer. The underlying assumption is that if the shower starts directly in front of the T3B layer, only the central tiles with index 0 or 1 are hit. Only if the shower starts closer to the calorimeter front, the outer T3B tiles are hit more often, as the shower has a limited angle of propagation.

Thus if the event synchronization was successful, there should be a dependence of the mean hit tile position of T3B on the shower starting layer. This is shown for all 60 GeV runs in Figure 4.7. The graph shows the mean hit tile position while the cyan colored background denotes the standard deviation of the hit tile position. Clearly mainly the central T3B tiles were hit if the shower starts close to the T3B layer, i.e. in W-AHCal layer 38. However, if the shower started earlier, the mean and the standard deviation of hit T3B cells increases, which is exactly the expected behaviour for a successfully synchronized run.

During the synchronization process some events or spills were not successfully synchronized. The efficiency once calculated from the number of successfully synchronized events and once for the number of successfully synchronized spills is shown in Table 4.1.

4.2 Data Reconstruction and Calibration

Prior to the analysis the data needs to be reconstructed and calibrated by correcting for changes in the amplitude of the recorded waveforms due to variations of the gain of the SiPMs. This is done by a sophisticated decomposition of the waveforms into their contributions of individual photon equivalents and a subsequent search for the first actual energy deposition per tile and its corresponding time (the *time of first hit*), alongside with corrections to their amplitude due to SiPM effects. Here only an overview is given. For more details please refer to [70].

4.2.1 Waveform Decomposition

The gain of a SiPM is the amplification factor by which the initial photo electrons are multiplied before they are actually measured (cf. subsection 3.5.1) and thus has direct influence on the amplitude of the recorded waveform of the SiPM signal. However, the gain is sensitive to the environmental conditions, especially changes in the temperature. Thus the gain was constantly monitored by recording dark pulses in the intermediate run mode (cf. section 4.1.2). The DAQ was configured to record around 500 pulses/min per device.

With this data the average waveform of a single photon equivalent can be generated for any given point during the run period. An example is shown in Figure 3.14.

A minimal ionizing particle traversing the scintillator creates a few thousand photons of which only a few are hitting the SiPM. Typically around 18 pixels or photon equivalents (p.e.) per MIP are detected within a few ns. The resulting waveform of such an event is formed by the sum of the individual photon equivalent waveforms. A typical example is shown in Figure 3.16.

With the knowledge on the shape of the waveform of a single p.e., each waveform can be decomposed into their individual contributions. This is done by repeatedly subtracting the averaged 1 p.e. waveform from the highest (remaining) peaks of the waveform at hand until no peaks remain. At each subtraction the position in time of the peak is filled into a 1 p.e. hit histogram. An example is shown in Figure 4.8, with the original waveform shown in blue and the 1 p.e. hit histogram shown in red.

After the decomposition the 1 p.e. hit histogram contains only the pure contributions of the SiPM fired pixels in time. Specifically the varying amplitudes due to changes of the gain are automatically corrected by this procedure.

To ensure the correctness of the waveform decomposition, the waveform is reconstructed from the 1 p.e. hit histogram and compared with the original waveform. This is done by filling the averaged 1 p.e. waveform for each entry in the 1 p.e. hit histogram with the correct time into a histogram. This histogram is shown in black in Figure 4.8.

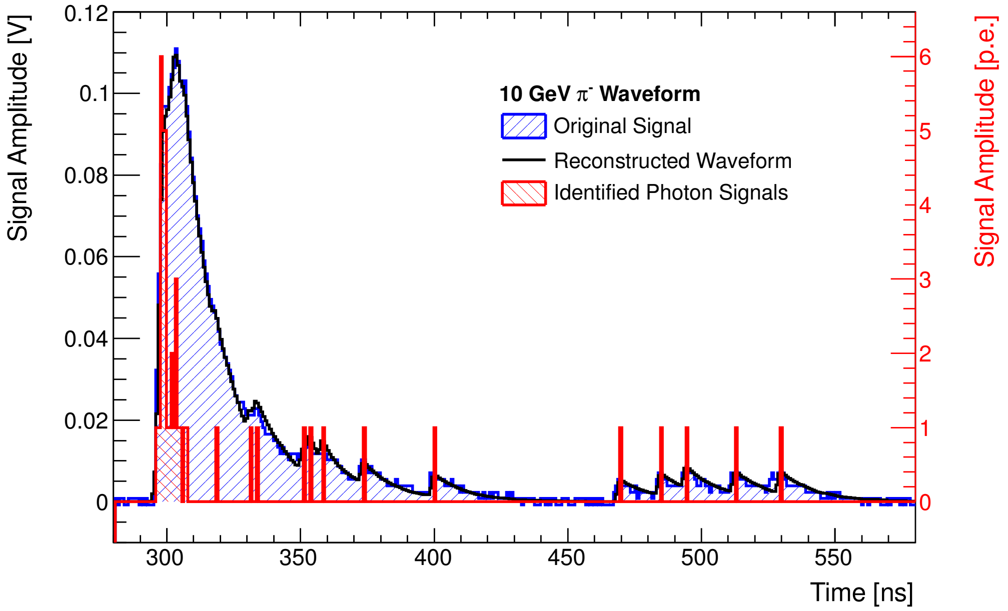

Figure 4.8: The waveform of typical hadron event (blue) is decomposed into its individual contributions from single pixels (red). As a crosscheck, the original waveform is reconstructed using only the decomposed data and the waveform of a single photon equivalent (black).

The reconstructed histogram is then compared with the original waveform by a standard χ^2 test. If the resulting value is too large, the waveform is rejected.

This technique provides several advantages:

- Automatic correction and thus implicit calibration of SiPM gain variations.
- Any additional picked up noise such as white noise from the oscilloscope or the electronics cannot be decomposed to a single p.e. and is thus filtered out. Additionally high noise contribution has a negative impact on the χ^2 check, and thus can easily be identified and the corresponding event can be rejected.
- The hit histogram provides an intuitive overview of the individual photon arrival times.
- The amount of data that needs to be stored is significantly reduced. This allows for faster access and analysis.

However, for the waveform decomposition to work, the waveform has to be recorded at sufficient precision. In the case of the T3B experiment oscilloscopes with a vertical resolution of 8 bit were used. In order to correctly identify contributions of single pixels, the resolution has to be chosen such that these contributions use around 2 bits. In the present case a typical 1 p.e. waveform has an amplitude of 5 mV and was recorded with a vertical range of 400 mV, limiting the maximum amplitude to around 80 p.e. (1.7 bit per single p.e.), which corresponds to 20 % of the number of pixels of the SiPM.

4.2.2 Hit Reconstruction: The Time of first Hit

The 1 p.e. hit histogram contains contributions both from SiPM effects like dark rate and after pulsing (cf. subsection 3.5.1) and from actual photons generated by energy depositions in the scintillator. As only the latter contain meaningful information on the shower development, an algorithm searches for real energy deposition hits within the hit histogram. As very small energy depositions are indistinguishable from dark noise, the algorithm is designed to search for hits with a minimal energy deposition of $\mathcal{O}(0.5\,\mathrm{MIP})$.

Energy depositions of a minimum ionizing particle lead to hits of $\mathcal{O}(20\,\mathrm{p.e.})$ in the SiPM. As the scintillator has a time coefficient for the conversion, not all photons are created at the same time. In addition some of the photons hit the SiPM directly, while others are reflected several times within the tile and thus travel a significant amount of time. Therefore the length of the time window in which the SiPM registers photons from a single energy deposition can be up to several 10 ns, and should be large enough in order not to lose information.

Dark pulses, on the other hand, occur randomly in time. Thus a longer time window increases the probability for including them. The same is true for after pulses. These are triggered by a previously fired pixel, such as the ones fired by the photons from the actual energy deposition. However, a feature of the after pulses is that they have a minimum time after the initial pulse before they can occur. Thus choosing a smaller time window rejects unwanted contributions both from after pulses and from dark pulses.

However, this is only true for the first real energy deposition within a tile. If the tile is hit a second time, after pulses of the first hit will be overlayed over the second hit. Therefore only the first energy deposition in each tile is reconstructed in the present analysis.

To identify hits originating from energy depositions in the scintillator, a minimum of 8 p.e. within a time window of 9.6 ns is required. The threshold of 8 p.e. (corresponding to 0.45 MIP, cf. subsection 4.2.3) has proven to reject dark pulses with a very high efficiency, while in such a short time window the contribution of after pulses to the overall signal is small. In addition as the probability for after pulsing scales with the initial amplitude, the signal of the after pulses can be considered part of the actual energy deposition, if the time of the after pulses do not contribute to the measurement.

Due to the photon time distribution of a real energy deposition and the after pulse contribution, the actual *Time of the first Hit* (TofH) is thus defined by the start of the pulse, taken as the second photon within the time window. The second photon is chosen over the first one to prevent single p.e. dark pulses near the actual energy deposition to smear the Time of first Hit.

Data shows that the probability of identifying at least a second hit after the initial one, i.e. at least one time window of 9.6 ns after the previous TofH has less than 8 p.e., lies below 12%. Note that the definition of 8 p.e. in 9.6 ns is not sufficient to reject the significant amount of afterpulsing, which increases the probability for the identification of a second hit drastically. Hence, the given 12% denote only an upper limit for the probability of encountering second (or third, ...) hits within the same tile.

Note that only the arrival time of the second photon equivalent acts as time definition of the Time of first Hit. Thus all subsequent registered photons are artificially shifted towards earlier times and thus are always earlier as the mean of all photon equivalents contributing to the Time of first Hit. This is supposed to act as a compensation of the photon traveling time and the time constant of the scintillator. In addition it mimics the expected behaviour of the actual calorimeter read out electronics as it will be used in the CLIC_ILD concept, which saves the time when a cell was hit while continuing to integrate the signal over a longer time window of up to 100 ns and more.

Finally the absolute time scale is calibrated. This is done by using the information of the central T3B tile, which can be hit by punch-through, muon-like particles. When filling all identified Time of first Hits of this central tile of a single run into a histogram, these punch-through particles will thus create a peak which is smeared by the detector resolution. This peak is the earliest time a particle can hit the T3B detector, and is thus used to define $t = 0$ ns.

The position of the peak is extracted from the above histogram in several steps. First the bin of the histogram with the most entries is identified, which gives a rough position of the peak. Then a Gaussian is fitted around this peak in the range of -3 ns to $+2$ ns to get a rough estimate on the sigma σ and the mean μ of the peak. In order to be less sensitive to statistical fluctuations of the peak position and thus limit the influence of the tail of the Time of first Hit distribution which is not caused by the punch-through particles but by the development of the hadronic cascade, a second Gaussian is fitted to the peak. The second Gaussian uses the mean μ from the previous fit as input, and is limited around this mean in the range of -2.5σ to $+1.5\sigma$. The mean μ of the second fit is then used to define $t = 0$ ns.

Examples of the Time of first Hit distribution for all tiles of T3B are given in Figure 4.9. All presented data sets were taken at the SPS at 180 GeV and are normalized to the number of events. Muons (shown in green) were recorded in dedicated runs. Protons (blue) and pions (red) were identified from the same hadron run by using the Cerenkov particle identification information, which was available through the synchronized CALICE W-AHCal event data stream. One can clearly see the tail caused by late energy depositions in the hadron data sets while the tail is less pronounced in the muon data. This proofs the sensitivity of the setup to late hadronic energy depositions, which are absent in muon data.

4.2.3 Calibration to the MIP Scale

In order be able to compare the energy deposition information of the Time of first Hit to simulation or data taken with the CALICE W-AHCal, it needs to be converted into the MIP scale, where 1 MIP is defined as the most probable energy deposited by a minimum ionizing particle (MIP) passing a single T3B tile.

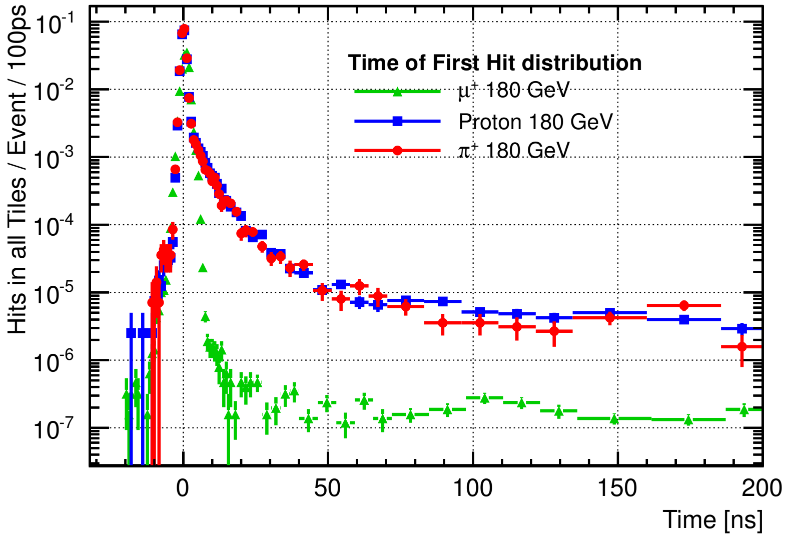

Figure 4.9: The Time of first Hit distribution for all tiles of T3B. Late energy depositions are predominant in hadron data (pion in red, proton in blue) in comparison to muon data (green).

Details on the procedure for the T3B experiment can be found in [70], whereas here only a short overview is given.

The calibration information was extracted from temperature controlled laboratory measurements, where the minimum ionizing particles were electrons of 2.28 MeV endpoint energy obtained from a ^{90}Sr radioactive source. The electrons of this β source are not real MIPs. Instead the most probable value of the energy deposition of electrons passing the scintillator tile is about 22% higher than for muons at the testbeam. When building the distribution of the deposited energy, this factor was taken into account, such that the resulting distribution is similar to the one of real minimum ionizing particles. The distribution was then fitted with a convolution of a Landau and a Gaussian, where the peak at 17.8 p.e. of the resulting distribution was defined as 1 MIP. Thus the threshold of the Time of first Hit of 8 p.e. is equivalent to 0.45 MIP.

The most probable value of the energy distribution and thus the MIP definition is dependent on the environmental temperature. This originates from changes in the dark rate and after pulse probability as well as in the gain variation of the SiPM [41]. During the reconstruction this effect was taken into account.

4.2.4 Overshoot Correction

The vertical range of the used Picoscopes is limited to 400 mV in the present case. Assuming the typical 5 mV/p.e. and 17.8 p.e./MIP, this limits the resolution to instantaneous energy depositions of 80 p.e. = 4.5 MIP. Higher energy depositions will lead to an overshooting of the waveform outside of the vertical range.

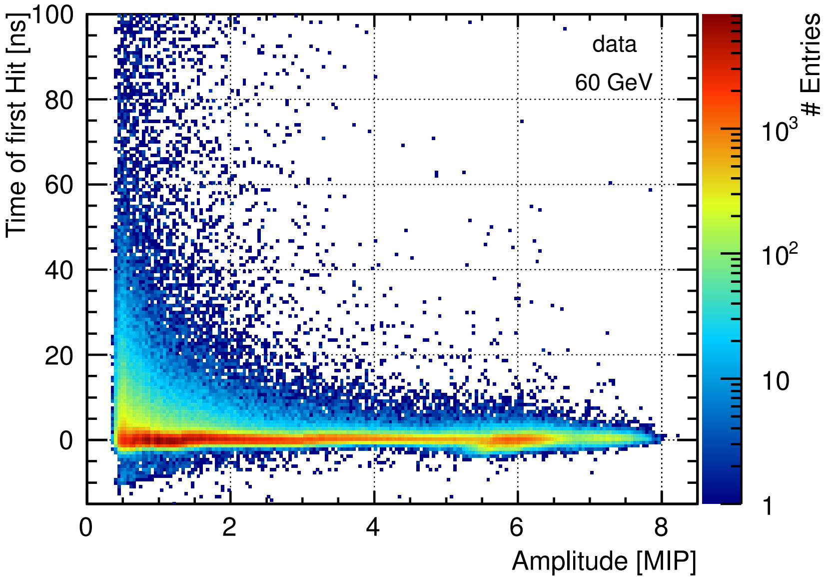

(a) Energy vs Time of first Hit

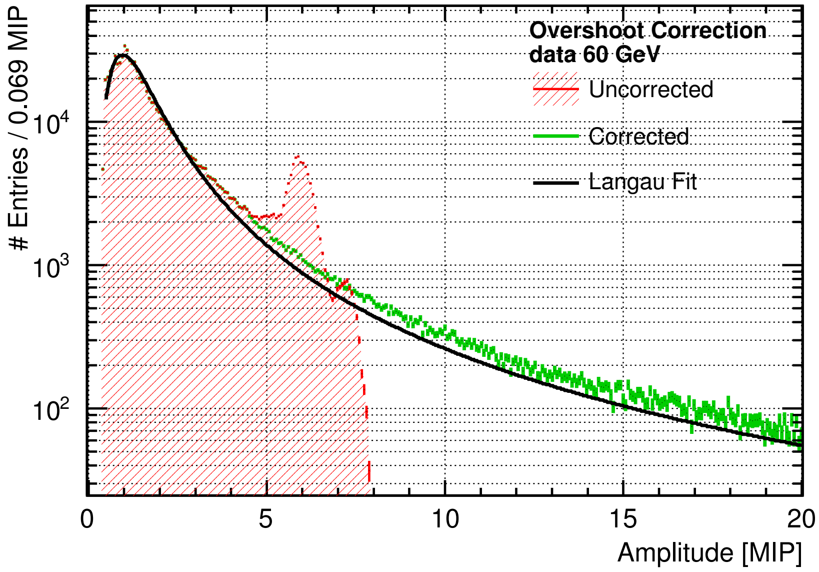

(b) Energy Deposition with and without Correction

Figure 4.10: The upper plot shows the Time of first Hits plotted against their respective amplitude. The region around 6 MIP comes from the limitations of the oscilloscopes vertical resolution. The lower plot is a projection of the upper, and shows the Amplitude distribution of all Time of first Hits, once before and once after the Overshoot correction.

In reality it is not a hard threshold, as the photons are not registered at the same time at the SiPM, giving some pixels time to recover and thus reduce the waveforms accumulated signal to below the upper bound again. The red curve in Figure 4.10(b) shows the distribution of the amplitudes of the Time of first Hits for a 60 GeV pion run. The peak around 6 MIP originates from this limitation.

This barrier limits large energy depositions, reducing the total amount of deposited energy. Thus when calculating the fraction of the total deposited energy for a hit, the contribution of all hits below this threshold is overestimated. Therefore an amplitude correction is applied in order to restore the original energy deposition distribution.

Assuming only minimum ionizing particles, one would expect the distribution to be Landau-shaped (cf. subsection 3.3.2), convoluted with a Gaussian due to electronic noise. Fitting this function to the distribution in the region of $0 - 4.5\,\mathrm{MIP}$, the tail of the distribution can be successfully extrapolated. The fit including the extrapolated region is shown as black line in Figure 4.10(b).

In order to re-establish a realistic distribution of the amplitude and thus correct the overshooting events, the amplitude of all Time of first Hits above 4.5 MIP were randomly chosen from the fit result. This is possible as almost all Time of first Hits with more than 4 MIP occur at the same time. This can be seen in Figure 4.10(a), showing the Amplitudes for all Time of first Hits prior to the correction. Hence the effect of the redistribution on the accuracy of the Time of first Hit is small.

The resulting amplitude distribution after the Overshoot correction is shown in green in Figure 4.10(b), successfully restoring the expected energy deposition distribution.

4.2.5 Geometric Amplitude Correction

For comparisons based on the total energy deposition in the T3B layer one has to keep in mind that T3B consists of only a sensitive strip, starting from the calorimeter center to higher shower radii. Thus the sensitive area is not equally distributed along the radius: While the central tile covers an entire 360° angle, the outermost tile covers only a tiny fraction of the shower at that radius. Thus when considering the shower shape or the fraction of deposited energy over time, the amplitude needs to be scaled accordingly to their transverse section covered by the corresponding tile.

Here we follow the approach of an effective area that should be covered by the tile, and compare it to the actual coverage of $3 \times 3\,\mathrm{cm}^2$.

The lower part of Figure 4.11 shows the 15 scintillator tiles of the T3B detector. They are arranged in such a way, that the central tile is hit at the center, and from there outgoing all tiles are placed with a gap of 1 mm in between. With a tile size of 30 mm, the total sensitive radius is the sum of 14 tiles with adjacent gaps, plus half of the central tile: $14(30\mathrm{mm} + 1\,\mathrm{mm}) + 15\,\mathrm{mm} = 449\,\mathrm{mm}$. The two red lines on top of the T3B tiles mark the arc that we shall consider to be the effective sensitive area. It is limited by the size of the outermost scintillator tile. To calculate the effective area per tile, the upper part of Figure 4.11 shows a sketch of one of the tiles together with the upper half of the arc. In order to be able to calculate the effective area per tile, it is divided into an upper triangle area $A_{\triangle}$ and an lower rectangular area $A_{\square}$. They

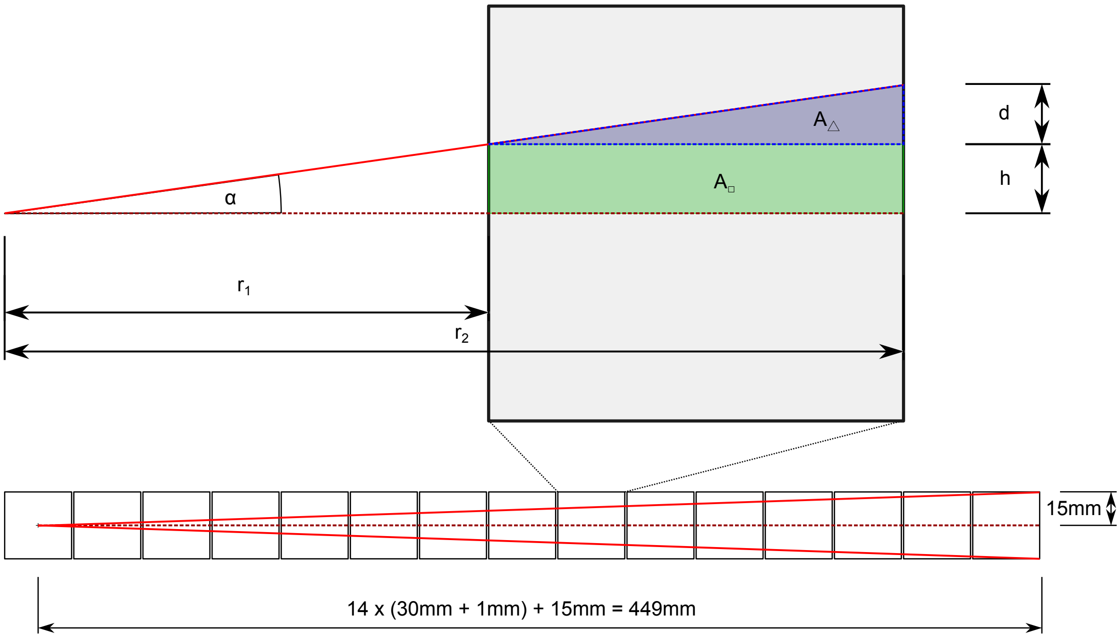

Figure 4.11: Construction of the effective area per tile for the correction of the amplitude of Time of first Hits.

tile position	1	2	3	4	5	6	7	8
weight	0.786	6.5	13	19.5	26	32.5	39	45.5
tile position	9	10	11	12	13	14	15	
weight	52	58.5	65	71.4	77.9	84.4	90.9	

Table 4.2: Weighting factors for the different tile positions.

depend on the opening angle α of the arc, which can be calculated from $\tan\alpha = \frac{15\,\mathrm{mm}}{449\,\mathrm{mm}}$. From the sketch one can deduce:

$$\begin{aligned} d &= (r_2 - r_1)\tan\alpha \\ h &= r_1 \tan\alpha \\ A_\triangle &= \frac{1}{2}(r_2 - r_1)d = 15.03\,\mathrm{mm}^2 \\ A_\square &= h(r_2 - r_1) = r_1 \frac{450}{449}\mathrm{mm} \end{aligned}$$

The sum of the triangle $A_\triangle$ and the rectangular area $A_\square$ results in half of the effective area per tile. For the central tile, however, there is an exception, as the arc starts in its center. Thus $A_{\square,\mathrm{center}} = 0\,\mathrm{mm}^2$, and the triangle sides are both only half as long, resulting in only a quarter of the original area: $A_{\triangle,\mathrm{center}} = A_\triangle/4$.

The resulting weighting factors, which are the effective area divided by the real area of the tiles and scaled to a complete circle of 360° are displayed in Table 4.2.

4.2.6 Time Resolution

The time resolution defines how well the Time of first Hit can be determined from the measurement. It has many contributions, of which the most notable are:

- Time jitter of the trigger setup, caused by time jitter of the triggering scintillators and their coincidence.
- Photon travel time within the T3B scintillator tiles.
- The time constant of the scintillator. The data sheet of the scintillator[1] in use gives a FWHM of 1.3 ns.
- False identification of single photon equivalents during the waveform decomposition.
- The oscilloscopes time resolution of $800\,\text{ps}/\sqrt{12} = 231\,\text{ns}$.
- Dark rate near the actual energy deposition.
- Time slewing due to the hit amplitude. This will be discussed in detail in the following.

Amplitude Dependence

The Time of first Hit is defined as the time of the second photon equivalent within a time window of 9.6 ns containing a minimal amplitude of 8 p.e. = 0.45 MIP. The window is necessary because the detection of the created photons is spread in time and assures that even these low energy depositions can be identified. However, the usage of the second photon regardless on the total amplitude of the hit introduces a dependence on the amplitude. Hits with higher energy, i.e. more photons will on average have their second photon earlier than hits with a lower total number of photons.

To study the influence on the Time of first Hit one has to know the distribution and the width of the time resolution of the recorded photon equivalents. This resolution is independent on the time jitter of the trigger setup, as the trigger jitter shifts the recording time and thus all incident photons within an event by the same value. Unfortunately the contributions of the remaining individual components are not known except for the intrinsic resolution of the oscilloscope of $\sigma_{\text{osci}} = \frac{800\,\text{ps}}{\sqrt{12}} = 231\,\text{ps}$. Therefore different time resolutions σ_{tot} are considered for this study, motivated by these assumptions:

1. The intrinsic oscilloscope resolution is the dominant contribution. This leads to a time resolution of $\sigma_{\text{tot}} = 231\,\text{ps}$.
2. All five contributions are of equal size of approximate $\sigma_{\text{cont}} \approx 230\,\text{ps}$. This leads to a total time resolution of $\sigma_{\text{tot}} = \sqrt{5\sigma_{\text{cont}}^2} \approx 500\,\text{ps}$.

---

[1] Saint-Gobain, Premium Plastic Scintillator BC-420, `http://www.detectors.saint-gobain.com`

3. At least one of the components has a significant higher contribution resulting in an total time resolution of $\sigma_{\text{tot}} \approx 1\,\text{ns}$. Given the fact that the scintillator alone claims to have a decay time in the order of 1 ns, this scenario seems to be most likely.
4. Fitting a Gaussian to the peak of the raw hit histogram of all events in a run yields in a time resolution of $\sigma_{\text{tot}} \approx 1.3\,\text{ns}$. Note that this includes jitter from the triggering system, which does not contribute to the time slew effect. Instead this value merely describes the upper bound for σ_{tot}.

It is expected that the shape of the distribution is Gaussian, as it is the result of many single contributions. Muon data on the other hand shows a time of 1 p.e. hit distribution with a tail to long times. This tail is likely caused by afterpulsing or other detector effects, and hence is irrelevant for the present study. In addition the tail does contribute very little to the Time of first Hit determination. Nevertheless it is included in the present analysis by using a Landau distribution, which provides a reasonably good description for the first few nanoseconds of the distribution.

In a toy Monte Carlo experiment photon equivalents with amplitudes in the range of 8 to 100 p.e. are distributed according to a Landau and a Gaussian distribution. Both distributions are centered at 0 ns with a width of $\sigma_{\text{tot}} = 231\,\text{ps}, 500\,\text{ps}$, 1.0 ns and 1.3 ns. Then the Time of first Hit is identified. This experiment is repeated 500 times and the mean of the Time of first Hit is plotted against the amplitude in Figure 4.12. This result shows clearly the time slewing effect and its dependence on the T3B detector resolution. For a realistic resolution of $\sigma_{\text{tot}} = 1.0\,\text{ns}$, the mean Time of first Hit for high energy depositions of 80 p.e. = 4.45 MIP is up to 1.5 ns earlier than low energy depositions of 8 p.e. = 0.45 MIP.

This time slew dependency on the amplitude was corrected by building the mean Time of first Hit from muon data for different Time of first Hit amplitudes. Amplitudes of 1 MIP were defined to have no correction. The resulting distribution was described with $f(x) = \frac{a}{x} + bx + c$. Using this function each Time of first Hit was corrected during the reconstruction. For a more detailed description the reader is once more referred to [70].

Overall Time Resolution of the Time of first Hit

By creating the Time of first Hit distribution of the central tile of an entire run and fitting its peak in a range of ±3 ns using a Gaussian, one can extract the total time resolution σ_{TofH} directly from data. This assumes that the peak of the distribution is dominated by instantaneous contributions from particles passing the calorimeter without hard interactions, and hence any late contributions from shower activity lead to an overestimation of the time resolution. The result is $\sigma_{\text{TofH}} = 0.8\,\text{ns}$ for hadron data. Muon data was recorded with a different trigger setup which had higher time jitter on the used scintillators for the coincidence, resulting in a total time resolution of the Time of first Hit of $\sigma_{\text{TofH},\mu} = 1.4\,\text{ns}$.

Note that the time jitter of the trigger setup only contributes when comparing multiple events. During the determination of the time of first hit on the single event

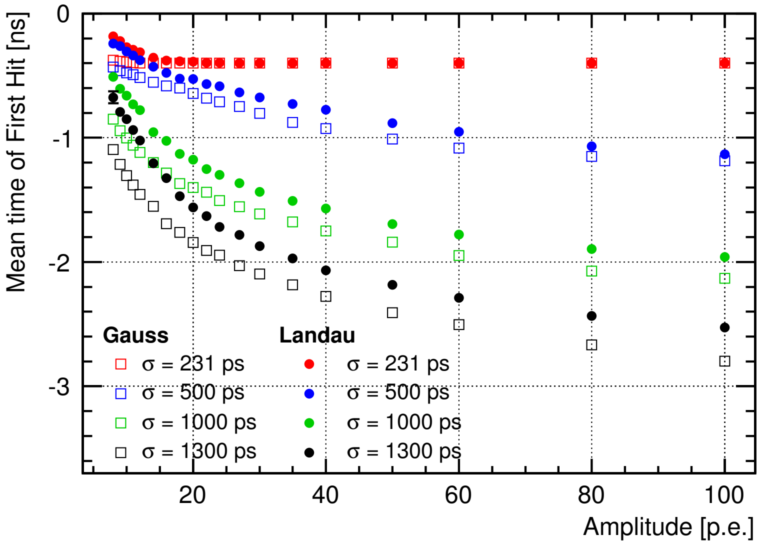

Figure 4.12: Result of a series of Toy MC experiments to estimate the dependence of the mean Time of first Hit on the signal amplitude for Gaussian and Landau shaped time resolutions of width σ. A resolution of $\sigma = 1\,\mathrm{ns}$ is expected to be close to the actual value of the T3B setup.

level it does not contribute, as the trigger only sets the time when the event is acquired but has no influence on the arrival time of individual photons.

4.3 Simulation

4.3.1 GEANT4: Hadronic Shower Development Simulation

The simulation of the interaction of the incident particles with the detector matter was performed with GEANT4 (cf. subsection 3.6.2).

Geometry

For that a detailed model of the CALICE W-AHCal geometry as it was at the testbeam was put into GEANT4. The dimensions and the material budget for a single layer of the CALICE W-AHCal and the T3B experiment are shown in Figure 4.13. These plots show the used materials and their corresponding width plotted against their nuclear interaction length (full line) and their radiation length (dashed line). A single CALICE W-AHCal layer sums up to a total of 24.5 mm, which corresponds to $0.13\,\lambda_I$ or $2.97\,X_0$. Thus the entire detector of 38 layers has a depth of 931 mm, $4.9\,\lambda_I$ or $112.9\,X_0$. The material budget of the T3B layer on the other hand is negligible with a depth of 13 mm and a corresponding $0.02\,\lambda_I$ and $0.06\,X_0$. Between the CALICE W-AHCal and the T3B layer was a gap filled with air of 34.5 mm, corresponding to an empty slot (without

W-absorber or W-AHCal cassette) and the missing absorber of the T3B layer. At the testbeam a steel/scintillator tailcatcher was installed downstream of the T3B layer. Albeit very seldom, it can cause neutrons to back scatter to the T3B layer. Thus in the simulation a steel block with a depth of 50 cm was installed after an air gap of 9 cm.

The geometry alongside with an example event originating from the interaction of a 60 GeV pion is shown in Figure 4.14. The pion is incident from the left, first interacting with the 38 sandwich layers of the CALICE W-AHCal (absorber in gray, scintillator in cyan) and forming a hadronic shower before passing through the T3B layer (blue) and finally the tailcatcher steel block (orange). The tracks of the individual particles are shown as well, with the pions shown in red, the protons in magenta and the electromagnetic component (photons, electrons) in blue. The neutrons tracks are drawn in green. One can see that the first hard interaction starts about 10 layers in the W-AHCal, which corresponds to $1.3\,\lambda_{\mathrm{I}}$ or $1.1\,\lambda_{\pi}$. The resulting low energetic neutrons perform a random walk and do in fact also back scatter from the tailcatcher towards the T3B layer.

Shower Start Definition

The shower starting point is defined as the first hard interaction of the incident particle with the detector material. As we have full information on all steps, it is defined as the position where the particle is destroyed and converted into any kind of daughter particles.

This definition provides a more accurate shower starting position than the one from the Primary Track Finder in the CALICE W-AHCal (cf. subsection 3.5.6). However, as the former one is not available for data for obvious reasons, the different accuracies in the shower starting point identification can lead to undesired systematic errors in the analysis when comparing data with simulation. The obvious solution would be to use the Primary Track Finder both for simulation and for data. However, for technical reasons this was not possible. Instead the resolution of the Primary Track Finder was successfully reproduced by smearing the exact shower starting position with a Gaussian of $\sigma = 2.0$ layers.

Physics lists

As it was already discussed in subsection 3.6.2, there are different models describing the possible physics processes responsible for the shower development. However, in Geant4 version 9.4*p*03, which was used for the simulation, only two physics lists provide the high precision neutron tracking (HP). This high precision neutron tracking is expected to be of importance for the proper description of the late neutron component in tungsten absorber. The two physics lists that include it are `QBBC` and `QGSP_BERT_HP`.

`QGSP_BERT` is a version of the latter without the high precision neutron tracking. It was used for a long time for the mass production at the LHC experiments CMS and ATLAS. It, too, was used for the six benchmark processes of the CLIC Conceptional Design Report, one of which is presented in chapter 5. Thus `QGSP_BERT` is included here to see the effect of the high precision neutron tracking code.

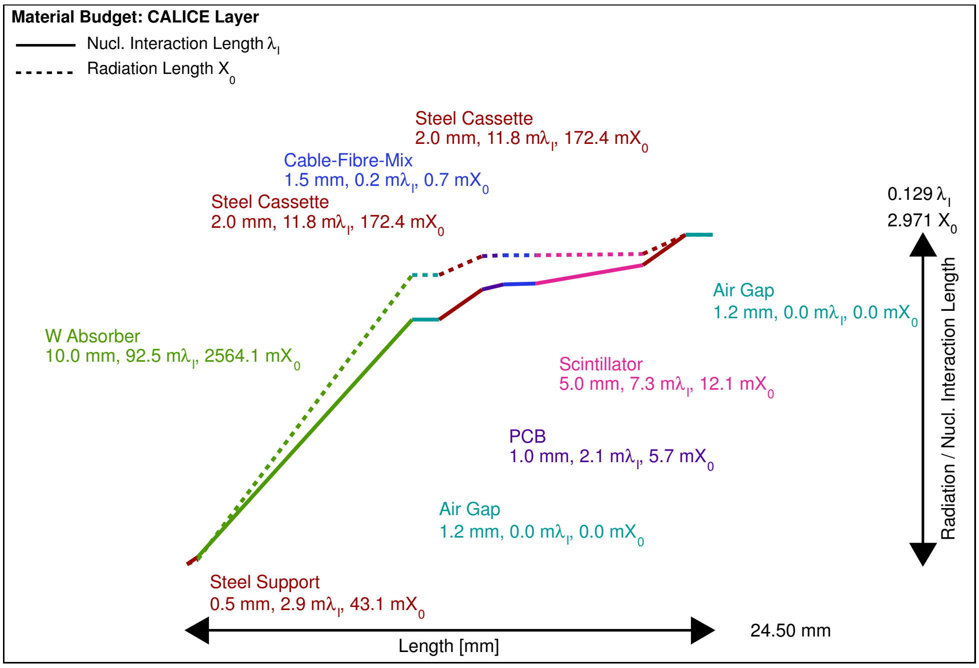

(a) CALICE

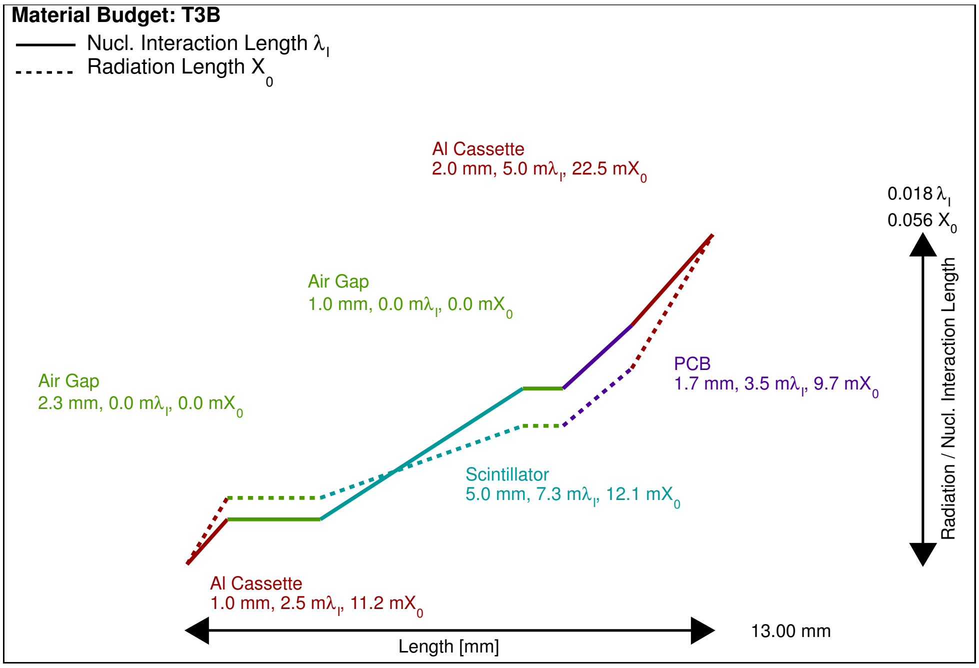

(b) T3B

Figure 4.13: The material budget of a single layer of the CALICE W-AHCal and the T3B layer as implemented into the GEANT4 simulation.

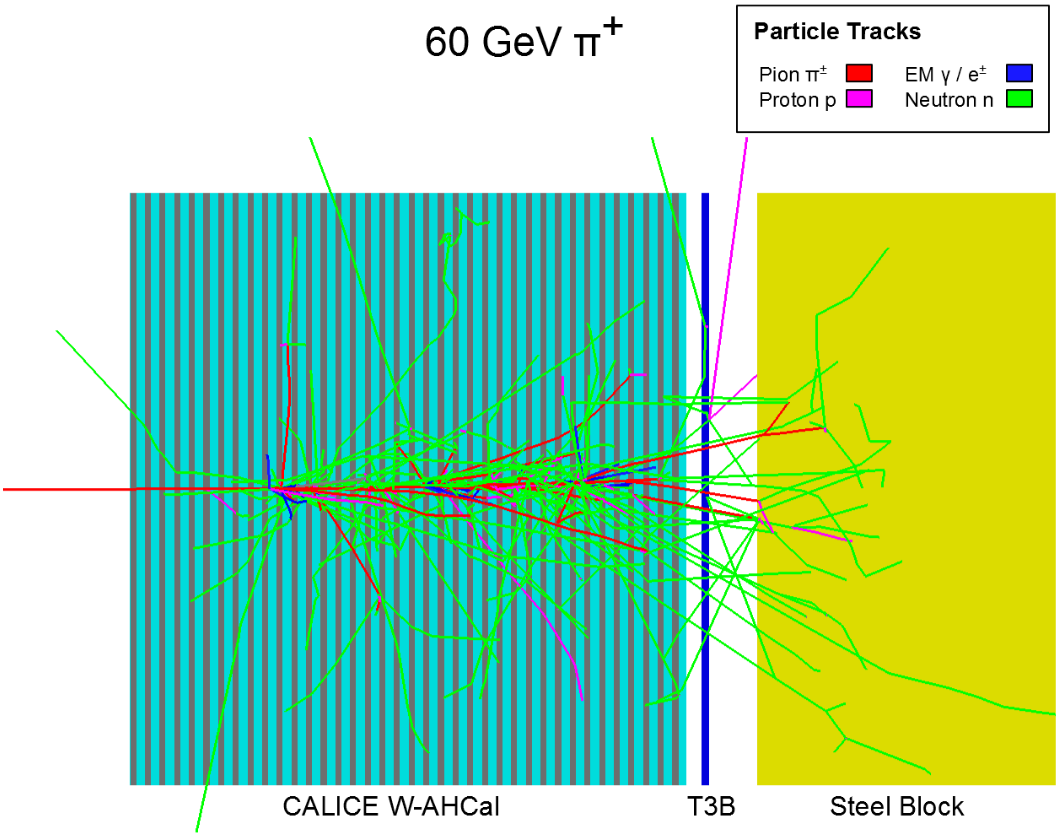

Figure 4.14: An example of a simulated 60 GeV pion event. The particle is incident from the left. The geometry consists of first the 38 CALICE W-AHCal layers, of which the cassette which includes the scintillator is shown in cyan and the tungsten absorber is shown in grey. After that the single T3B layer is shown in blue before the steel block simulating the tailcatcher is shown in orange. Particle tracks are shown in red (pion), magenta (proton), green (neutron) and blue (electron, photon).

Simulation Detail and Storage

Geant4 simulates the interaction of particles with matter as a series of single steps, each of which is a simulation of a certain physical process. The time and the amount of deposited energy are available for each these steps. In the present case this information was saved into a ROOT tree for all steps that occurred within the T3B layer. Conversion into photons or other detector and electronic specific effects are not considered in this phase. However, Birks' Law [71], which describes the non linearity in photon conversion in scintillators, is already included at this point by artificially modifying the amplitude of the deposited energy of the step.

4.3.2 Digitization: Detector Response Simulation

The raw information on energy deposition obtained from the GEANT4 simulation is digitized to include detector and electronic effects in several stages. This includes the conversion of the deposited energy to photon equivalents while taking the photon statistics of the scintillator with the attached SiPM into account. Another effect considered during the digitization is the correct modelling of the time distribution of the photon equivalents. However, the first step is the spatial conversion into T3B like tiles, together with the time partitioning into bins of 800 ps, modeling the accuracy of the used oscilloscopes.

Spatial and Time Partitioning

In the simulation the T3B layer is not divided into several tiles, but instead consists of a complete layer of scintillator material. Using the geometry information of the actual T3B layer with respect to the CALICE AHCAL, each simulation step is - based on its position - matched to one of the 15 $30 \times 30 \times 5\,\mathrm{mm}^3$ scintillator tiles. If the hit was outside the T3B strip it is discarded.

The oscilloscopes used for the data acquisition have a sampling frequency of 1.25 GS/s corresponding to 800 ps. Hence, the simulation has to use the same binning. This is done by creating an array of hits similar to a histogram with a bin size of 800 ps for each tile position. Using the timestamp of the hit the correct bin of the histogram is identified, and the hit is added to it under consideration of its energy.

Scintillator Photon Conversion

The energy deposition of the simulation has to be converted into the same unit as the one used by the actual data, which is provided in terms of detected photons equivalents (p.e.).

As Birks' Law was already applied in the GEANT4 simulation, the number of created photons scales linearly with the energy deposition and can be described by a single conversion coefficient $c_{\mathrm{GeV,p.e.}}$.

However, the value of the conversion factor depends among other effects on the number of photons created in the scintillator, the distribution of these photons in the scintillator as well as the fill factor and quantum efficiency of the SiPM. Thus its determination is tedious and error prone. Instead the conversion is done by using the MIP energy scale as intermediate step. For this scale, both the number of detected photons and the deposited energy is known, as described in the following

The conversion factor $c_{\mathrm{GeV,MIP}}$ responsible for the conversion of the deposited energy to the MIP scale, where 1 MIP is once more defined as the most probable value of the energy deposition distribution of a minimum ionizing particle, is determined by the simulation of muons. The fit on the resulting Landau distribution yields a value of $c_{\mathrm{GeV,MIP}} = 805\,\mathrm{keV/MIP}$.

The second conversion factor for converting from the MIP scale to photon equivalents $c_{\mathrm{MIP,p.e.}}$, can be extracted from testbeam data and lab measurements. Again the most probable value of the resulting Landau distribution defines the MIP scale and results in a conversion factor of $c_{\text{p.e.,MIP}} = 25\,\text{p.e./MIP}$. Note that this value is higher than the 17.8 p.e./MIP of the Time of first Hit which were presented in subsection 4.2.3, as the Time of first Hit is not defined over the entire time but over the shorter time window of 9.6 ns.

Following both steps, the energy conversion of the amplitude A in a single T3B tile is done by:

$$A[\text{p.e.}] = A[\text{GeV}]\frac{c_{\text{p.e.,MIP}}\left[\frac{\text{p.e.}}{\text{MIP}}\right]}{c_{\text{GeV,MIP}}\left[\frac{\text{GeV}}{\text{MIP}}\right]}$$

Photon Statistics

A minimal ionizing particle passing through a T3B scintillator tile will create a few thousand photons. However, as stated in the previous section the average number of photons actually detected by the SiPM is only around 20. Consequently, the probability of detecting a photon is small and one cannot predict the exact number of photons that will be detected, even if the amount of created photons is known. This is a typical example for a Poissonian distribution.

During the digitization, the original amplitude A_{raw} is corrected for this photon statistic process. As the amplitude is given in units of photons equivalents, the first step is to round its value to the nearest integer. In the next step a Poissonian distribution with the resulting amplitude A_{raw} as mean is created. By using this distribution as a probability density function, one single random integer number is generated. This number is the new amplitude A_{digi}.

Trigger Jitter and SiPM Afterpulsing

Within the simulation the time scale is well defined. The particle is created at the same location with the same momentum at the exact same point in time. At the testbeam, however, are a set of different contributions that have negative impact on the detector resolution. Most of these effects were already discussed in the context of the Time of first Hit in subsection 4.2.6. With the exception of the time slewing due to different amplitudes, a feature unique to the Time of first Hit and thus not affecting the resolution of single p.e., all these effects have to be applied on the simulation, as well. This is true for SiPM specific features, especially the afterpulsing, as well.

Both the time smearing and the afterpulsing effects can be seen in Figure 4.15, which shows the sum of 1 p.e. hit histograms of a 180 GeV muon run. As muons should deposit their energy instantaneously without any late components, the tail of the distribution shows the effect of afterpulsing. Around the peak the distribution is shaped like a Gaussian, which is the time jitter of the detector.

In order to correctly mimic these effects in the digitization, each photon equivalent is smeared according to this muon distribution. The result is a 1 p.e. hit histogram which is very close to the one originating from real testbeam data.

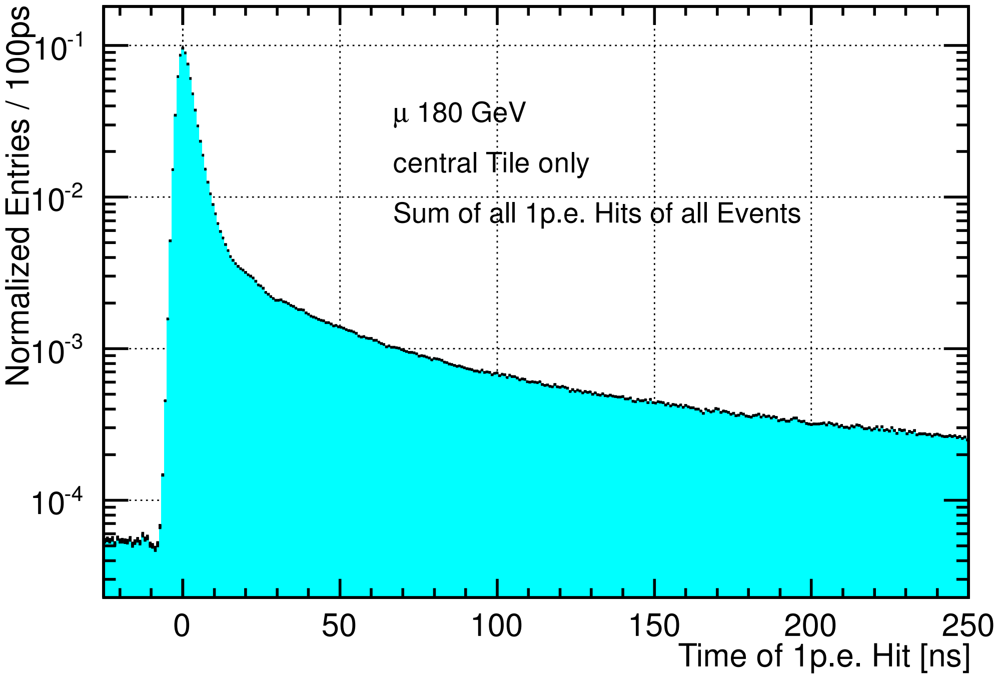

Figure 4.15: Sum of all 1p.e. hit histograms for a muon. Histogram is normalized to number of entries = 1.

4.4 Results

This section presents the results of the analysis of the reconstructed Time of first Hit data, which was obtained at the testbeam, with a focus on the deposited energy over time and the shower profiles. Note that the lateral shower properties are already discussed in detail in [70]. Therefore the presented analysis will focus on the longitudinal shower properties which is only possible with the synchronisation of W-AHCal and T3B events. In all cases a comparison to simulated data is performed in order to validate the underlying physics lists. Finally a comparison between the pion and proton response will be performed.

The results presented here are obtained from datasets of 2 million events in case of simulation and 1.3 million pion events for 60 GeV, 883 000 for 80 GeV and only about 50 000 for 180 GeV. The proton dataset contained 808 000 triggered events of 60 GeV.

4.4.1 Energy Dependence

The energy of the incident beam particle typically has significant influence on the shower shape, especially on its size and the number of secondary particles. A hadronic shower, however, consists of several components, each with a different time scale. These originate from the different processes that happen at each cascade step. With increasing

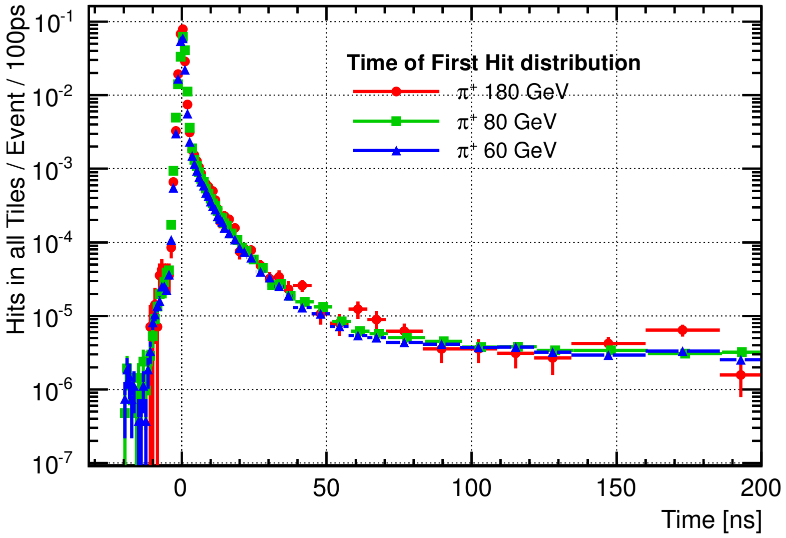

Figure 4.16: The Time of first Hit distribution for different energies, normalized to the number of events. Hits in all T3B tiles contribute.

energy the number of cascade steps increases, but the individual components at each step stay roughly the same. Therefore no dependence of the time evolution of the shower on the energy is expected.

This can be seen by studying the distribution of Time of first Hit for different energies, which is shown in Figure 4.16. It contains the histograms normalized to the number of contributing events for all T3B tiles and thus over the entire shower width. It shows that there is no statistical significant difference in the shape of the three different energies of 60, 80 and 180 GeV.

A similar picture presents itself when one examines the transverse development of the mean Time of first Hit, which is shown in Figure 4.17. While one can clearly see a trend to later hit times for a greater shower radius with the outer shower part being approximately $10 - 12$ ns later with respect to the shower center, no clear dependence on the beam energy is visible.

For that reason we will concentrate on 60 GeV pions in the following.

4.4.2 Energy Deposition over Time

When designing a hadronic calorimeter the integration time, i.e. the time in which the detector is sensitive and accumulating signal, has to be tuned according to the time structure of hadronic showers. In theory the integration time would ideally cover the entire energy deposition time of hadronic showers in order to reduce statistical errors on the measurement. In potential real world applications such as the ILD detector at CLIC where bunch crossings occur every 0.5 ns, however, the overlap with subsequent events significantly limits the integration time window. A study on which fraction of

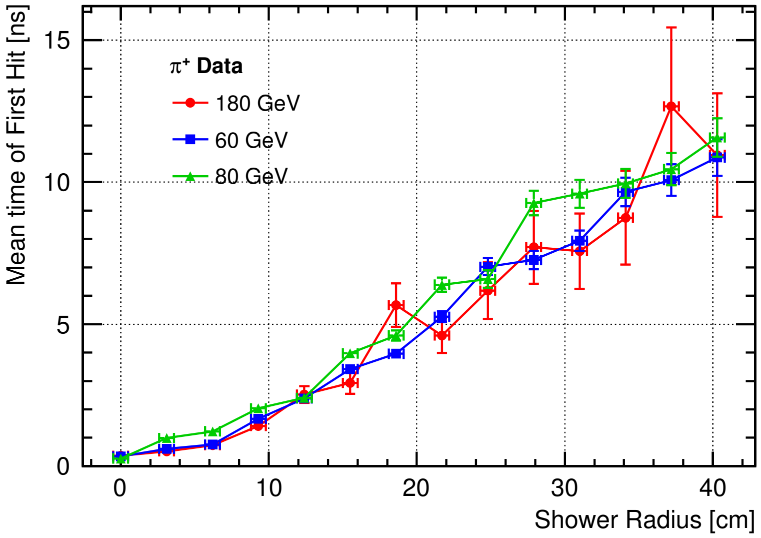

Figure 4.17: The mean Time of first Hit at different shower radii.

the total energy is deposited after what time helps to find a good compromise on the integration time.

This quantity can be obtained by first creating a histogram filled with all Time of first Hits, weighted with their respective amplitude. This gives the average energy deposition of hadron showers for every point in time. Thus the second step is the integration of this histogram.

However, as T3B is only a single strip, some correction factors need to be included in order to correctly represent the energy deposition fraction of an actual calorimeter. As discussed in subsection 4.2.2, the amplitudes are normalized to the sensitive geometric area of the respective tile. Furthermore, differences in the frequency of the shower starting positions are taken into account by normalizing the amplitude with the number of events with shower starts in the different W-AHCal layers.

Integrating over several μs is infeasible in a real detector and typically also not necessary to achieve a good energy reconstruction. The shaping time of the W-AHCal prototype, for example, was in the order of $100 - 150\,$ns. Thus a maximum integration time of $200\,$ns was assumed for the present study, so that the energy deposited at a certain time is considered relative to the total deposition in $200\,$ns. Depositions at later times were not included in this analysis.

Before the results obtained from the simulation of different physics lists can be compared to the data acquired at the testbeam, the method used to reconstruct the time distribution of the energy deposition fraction is validated. Studying the changes to the distribution due to the analysis is done by comparing the raw simulation output of Geant4 with the fully digitized and reconstructed simulation of the same physics lists. Figure 4.18 shows the resulting energy deposition fraction curves of a $60\,$GeV π^+ simulated with the `QBBC` physics list. Once the distribution is created with Time

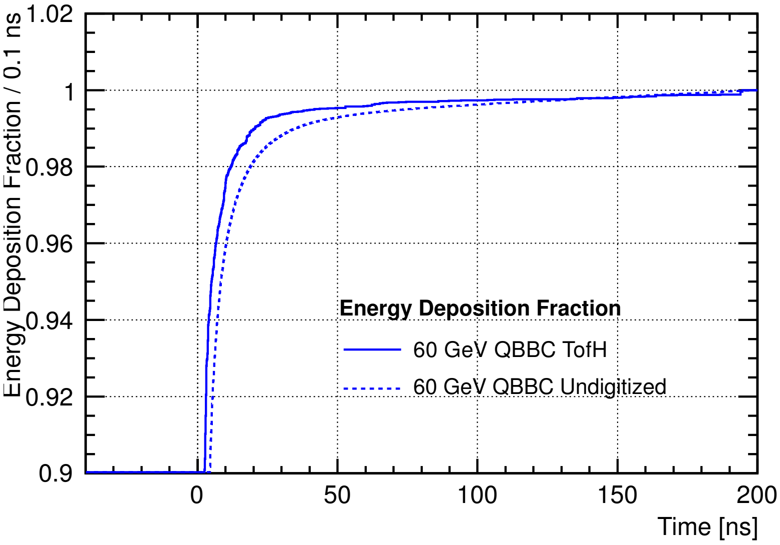

Figure 4.18: Comparison of the fraction of deposited energy over time. One set was generated from data of the T3B strip obtained from a full detector simulation including digitization and reconstruction using Time of First Hit. The other set is the pure Geant4 output of the entire detector without digitization or reconstruction.

of first Hit (TofH) data (including all mentioned corrections) of a simulated and fully digitized T3B strip, and it is once obtained from pure Geant4 data of the entire detector without digitization (undigitized).

Clearly the reconstructed, Time of first Hit based data from the T3B strip overestimates the response speed, as it reached 98% already after about 10 ns, while the undigitized, actual energy deposition reaches that value only after 20 ns. This effect can be explained mainly with the time definition of the Time of first Hit, which uses the arrival time of the second photon which is obviously earlier than the average arrival time of all photons. This definition of the Time of first Hit intended to compensate the delaying effects such as the photon travel time in the scintillator and the decay constant of the scintillator, both of which were implemented in the digitization. Obviously the comparison to the raw simulation data reveals that this definition overcompensates the delaying effects, shifting the Time of first Hit based energy deposition fraction curve to earlier times.

However, it is expected that calorimeters such as the one within the ILD concept mimic the behaviour of the Time of first Hit definition, as the read out electronics will only assign a single timestamp to a hit in contrast to the full waveform of the oscilloscopes used at T3B.

A comparison of the energy deposition fraction between the different physics lists and testbeam data is shown in Figure 4.19. As before the results are obtained from the 60 GeV π^+ dataset. One can clearly see that the high precision physics lists `QGSP_BERT_HP` and `QBBC` do a better job of describing the behaviour of late energy

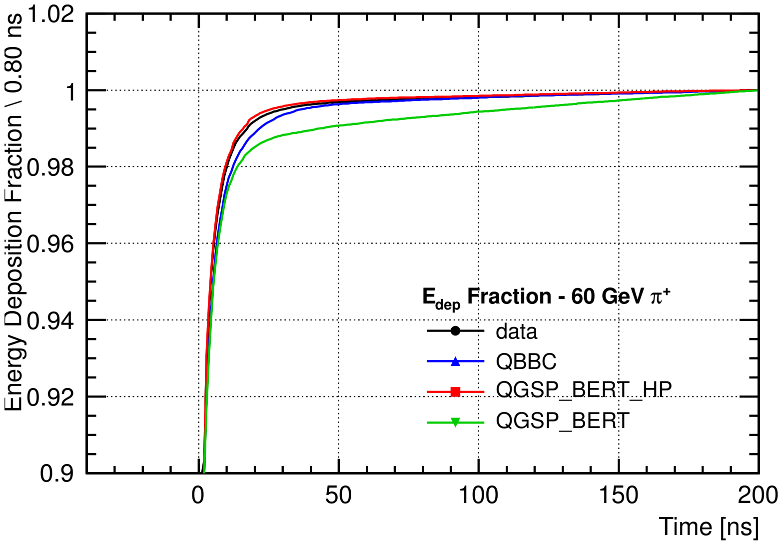

Figure 4.19: Comparison of the fraction of deposited energy over time between data and simulation with different physics lists.

depositions than the `QGSP_BERT` physics list. However, the deviation of the latter is only in the order of 1%. Furthermore the plot shows that over 90% over the energy are deposited almost instantaneously, and all simulations as well as the testbeam data reach a fraction of 98% after about 10 ns when using the Time of first Hit definition. According to Figure 4.18 at the 98% level a 10 ns delay in the Time of first Hit based energy deposition fraction is consistent with a 20 ns delay in the undigitized case, thus limiting the need for longer integration times in calorimeters, also when tungsten is used as absorber.

4.4.3 Mean Time of first Hit: Longitudinal Shower Development

This section focuses on the development of the shower after its first hard interaction, the shower start, with a stronger focus towards the longitudinal development. This is done by using the shower start finder algorithm which was described in subsection 3.5.6 and section 4.3.1. Based on this information, the events recorded by the T3B layer can be classified by their distance to the shower starting position. Note that all events independent on their shower starting point have been triggered by the $10 \times 10\,\mathrm{cm}^2$ scintillator coincidence, which was placed at a constant distance with respect to the T3B layer. Thus unlike in a complete hadronic calorimeter the direct time of flight of the particles does not contribute. Instead all longitudinal time differences presented here originate purely from the underlying physical shower processes.

Lateral differences in the behaviour are evaluated by splitting the shower radially into three regions: a shower core (two central tiles, −1.5 cm to 4.6 cm), an intermediate

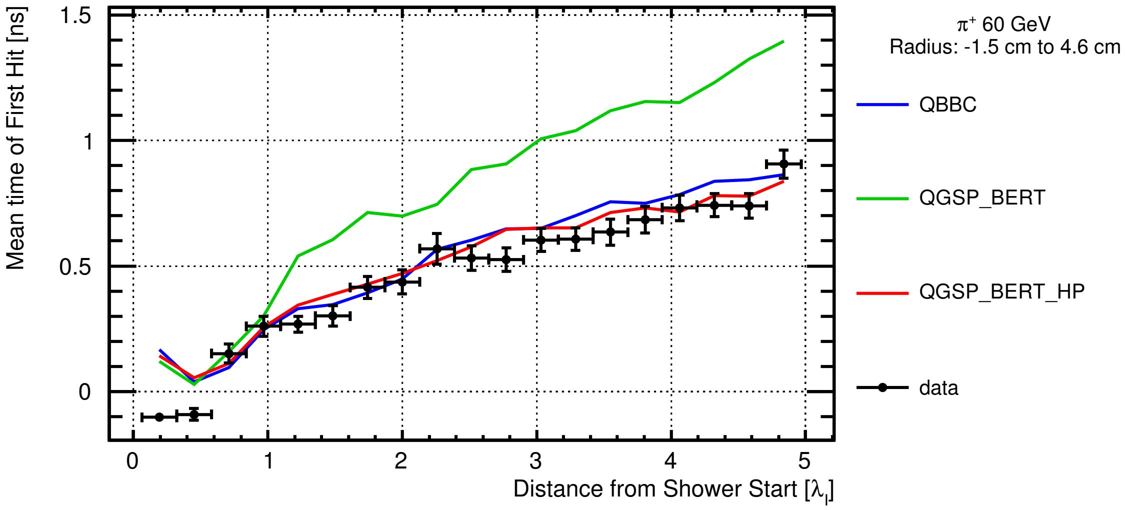

Figure 4.20: Changes of the Mean Time of first Hit over the distance from the shower starting position for the central part of the shower.

region (tiles 3 to 7, 4.7 cm to 20.1 cm) and the outer region (tiles 8 to 14, 20.2 cm to 38.7 cm).

For all these subsets the mean Time of first Hit, based on the range of -40 to 200 ns, is evaluated for testbeam data and for the simulation data obtained using the three different physics lists `QGSP_BERT`, `QGSP_BERT_HP` and `QBBC`. The results for the shower center are shown in Figure 4.20, the intermediate region is shown in Figure 4.21(a) and the outer region is shown in Figure 4.21(b). For the sake of readability statistical errors are only shown for data but are omitted for simulation. However, as the number of simulated and testbeam events is the same order of magnitude, the errors are of similar size.

Central Shower Region

As the nuclear interaction length is significantly larger than the radiation length, electromagnetic (sub-)showers are more dense since they deposit their energy over a shorter distance. Most of their energy is deposited within the first 10 to 15 X_0 and close to the shower axis (cf. [30]). Thus while electromagnetic sub-showers can occur at any stage during the hadronic cascade, the ones that are most visible in this central region (radius below 4.6 cm) are the ones that were induced at or shortly after the overall shower start.

As a single W-AHCal layer has about 2.97 X_0, the typical electromagnetic shower range of 10 to 15 X_0 correspond to about 4 to 5 layers, which is exactly the range were the behaviour of the mean Time of first Hit differs in Figure 4.20. Note that in this figure two W-AHCal layers are combined into a single data point in order to be less prone to statistical fluctuations.

The hadronic part, dominating after a distance of 1 λ_I from the shower start, on the other hand, leads to a steady rise of the mean time with higher distances. The two high precision physics lists, `QBBC` and `QGSP_BERT_HP`, reproduce the behaviour well within the statistical errors. `QGSP_BERT`, on the other hand, only reproduces the electromagnetic part, but overestimates the mean Time of first Hit in the hadronic part.

Note that with increasing distance to the shower starting position the mean Time of first Hits changes only very little in this central shower region. Over the entire distance of 4.9 λ_I the change in the mean Time of first Hit is in the order of 1 ns, which is quite close to the expected resolution 0.8 ns (cf. subsection 4.2.6).

Intermediate and Outer Shower Radius

Both for the intermediate and outer radius region the electromagnetic component is expected to be substantially less pronounced, but instead these regions are expected to be dominated by hadronic interactions. Figure 4.21 shows the mean Time of first Hit for different distances from the shower starting position for both regions.

In this region the data is not so well reproduced by the simulation. While `QGSP_BERT` is again significantly overestimating the mean Time of first Hit by at least a factor of 2, the two high precision physics lists are closer to the data, but still overestimating the development by about 1 ns in the intermediate region and about 2 ns in the outer region.

Within their statistical errors, both regions do not show a specific form of the distribution, with the exception that closer to the shower starting point the hits tend to come earlier.

4.4.4 Longitudinal Shower Profile

Assuming a radial symmetry of the hadronic cascades, the development of the average hadronic shower can be reconstructed by combining the shower start information with the T3B measurements. Hence, the time evolution of complete calorimeter profiles can be reconstructed. Here we focus on the comparison of the shower profiles of the instantaneous energy depositions with the intermediate and late depositions, as well as their reproduction by the simulation with various physics lists.

Reconstruction of the Calorimeter Profile

The longitudinal *calorimeter* profile gives the typical energy deposition in the different layers of the calorimeter, obtained by repeatedly measuring the response to a certain particle type at the same energy.

Contrary to that a longitudinal *shower* profile gives the typical response of the same calorimeter to the same particles, but measured with respect to the shower starting point. Assuming that all particles would start their shower in the first layer of the calorimeter, the shower profile and the calorimeter profile would be identical. However, hadronic interactions and as such the first hard interaction are statistical processes, and therefore the shower profile can only be measured if the shower starting point is known.

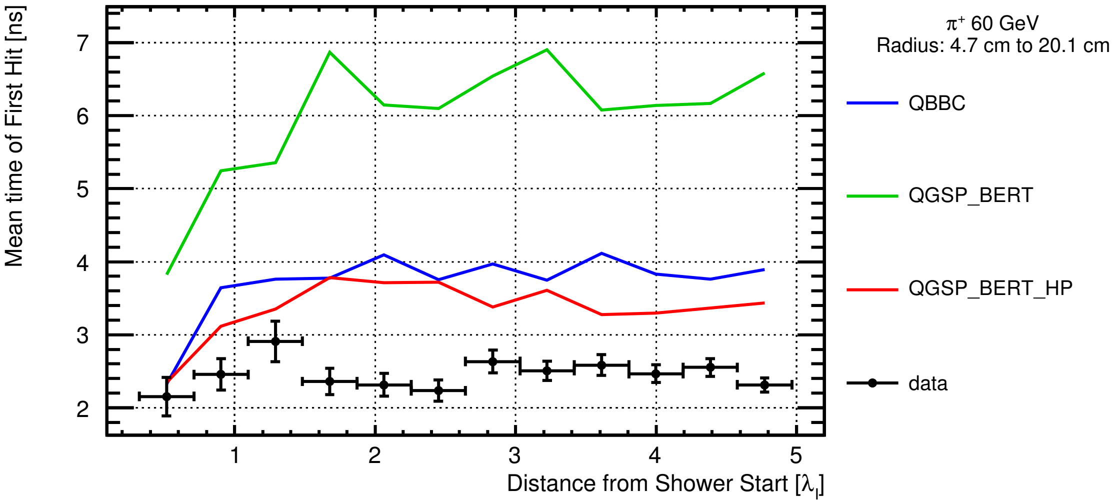

(a) Intermediate Shower Region

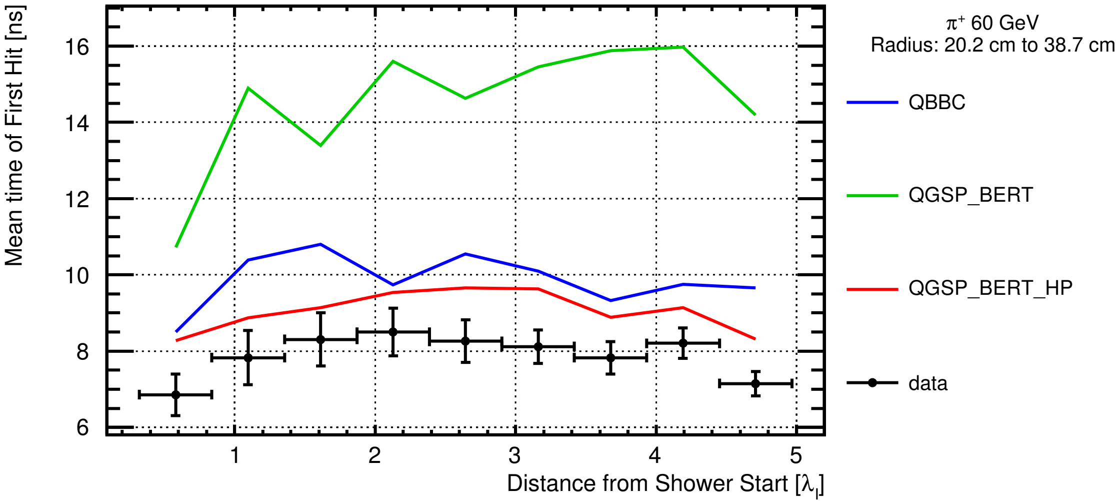

(b) Outer Shower Region

Figure 4.21: Changes of the Mean Time of first Hit over the distance from the shower starting position for the intermediate (upper plot) and the outer region (lower plot) of the shower radius.

With the help of the shower start finder algorithms the shower profile can even be reconstructed with only the T3B layer at hand. This is done by first filling a histogram with the distance between the shower starting layer in the CALICE W-AHCal and the T3B layer, weighted with the amplitude of the deposited energy in T3B. In this step the geometry of the single T3B strip is taken into account by scaling the energy deposition of the Time of first Hits according to geometrical coverage, as explained in subsection 4.2.5. As the shower starting position changes from event to event, the T3B layer samples the entire shower layer by layer. However, this implicitly assumes that the shower start is equally distributed over all W-AHCal layers, which it is not. Instead it falls exponentially with higher layer numbers, i.e. deeper shower starting positions. Therefore each layer of the histogram needs to be reweighted with the number of events having a shower start in that layer.

The shower profile and the shower start profile can be used to reconstruct the calorimeter profile. This is possible as the calorimeter profile is essentially just an overlay of several shower profiles which start in different depth of the calorimeter, each at a different rate.

The principle is explained with an imaginary 10 layer calorimeter in Figure 4.22. The upper plot (Figure 4.22(a)) shows the resulting shower start profile where each layer is assigned its unique color. As one can see, the shower start distribution falls with an exponential with negative exponent. The shower profile, as it can be reconstructed with the T3B layer, is shown in dark red in Figure 4.22(b), already weighted with the rate of a shower start in layer 1. Subsequently the green histogram again is the shower profile, but with a shower start not in layer 1, but in layer 2, once more weighted with the rate of shower starts in layer 2 and stacked on top of the distribution for layer 1. By adding up the shower profiles weighted with the rate of shower starts, the resulting overall shape gives the calorimeter profile.

Smearing of the Calorimeter Profile by the Limited Shower Start Identification Resolution

When reconstructing the calorimeter profile, the shower start profile is essential to correctly weight the individual shower profiles to the correct number of events. The shower start identification algorithms, however, have a limited resolution in the order of $\sigma = 2$ layers. To study the effect on the resulting calorimeter profile of such a smearing, a simulation of a 60 GeV π^+ was created using the `QBBC` physics list. To be independent of detector effects, the pure undigitized data as it is created by GEANT4 is used as a input.

Figure 4.23 shows the calorimeter profiles. The one in red is obtained from the full information of all active detector layers and acts as a reference here. Below that there are three versions of a reconstructed calorimeter profile, obtained with the technique discussed above.

The difference between the three profiles, shown here in blue, green and black, is the resolution of the used shower start finder. The blue version has a resolution of $\sigma = 0$ layers, which is identical to knowing the exact shower start position. Thus the shape is identical to the real shower profile obtained from the full detector information.

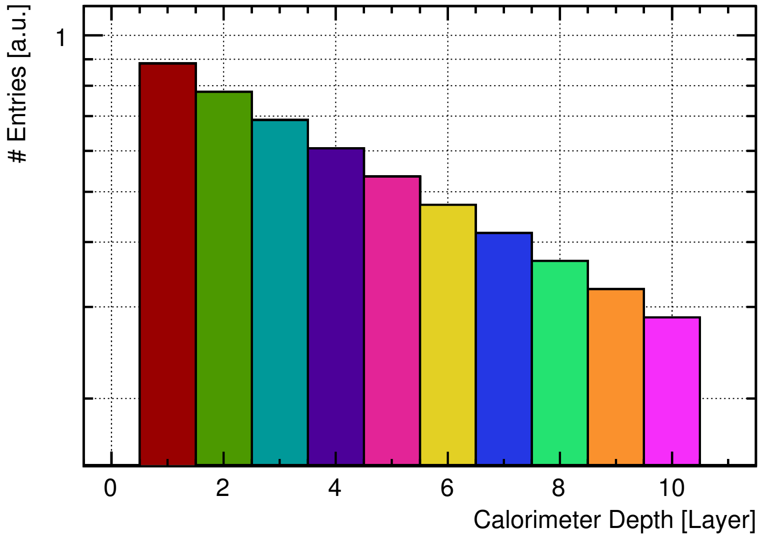

(a) Shower Start Profile

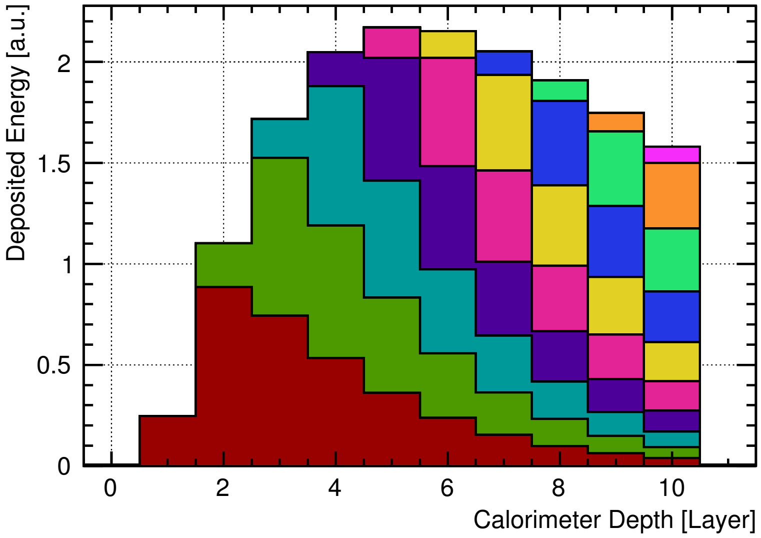

(b) Calorimeter Profile as a Set of Stacked Shower Profiles

Figure 4.22: The principle on how the calorimeter profile (overall shape, lower picture) can be built from the shower profile (dark red, lower picture) and the shower start profile (upper picture). For details please refer to the text.

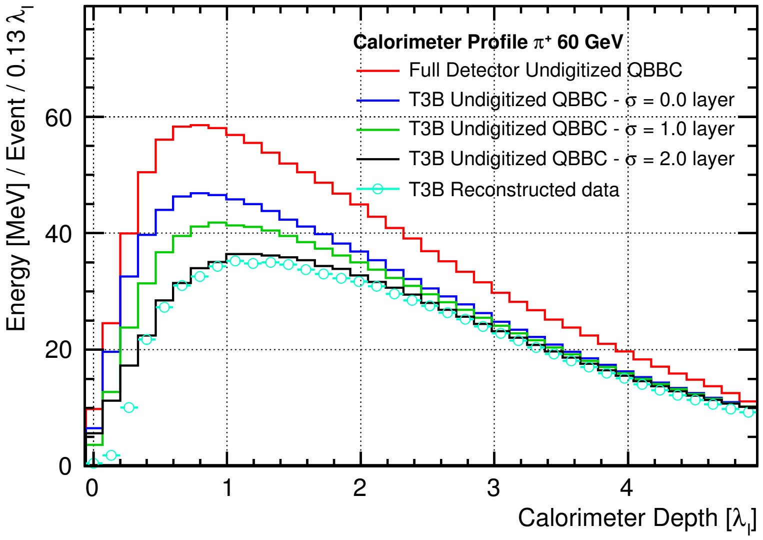

Figure 4.23: The calorimeter profile for a CALICE W-AHCal like detector, obtained from pure simulation without digitization of 60 GeV π^+. The calorimeter profile is once taken from all active layers, and three times reconstructed from the last layer using the shower start profile for reconstruction. The shower start profile has been smeared by Gaussian with a σ of 0, 1 or 2 detector layers.

The differences in the amount of deposited energy originates most likely from the different sensitivity of T3B and W-AHCal calorimeter layers, caused by differences in the geometrical structure and used materials in the cassettes. For green and black profiles the shower start finder has a Gaussian resolution of $\sigma = 1$ layer and $\sigma = 2$ layers respectively. One can see that the deterioration in the shower start identification resolution leads to a shift of the calorimeter profile peak towards the back of the calorimeter. Furthermore it leads to a downshift of the peak height.

Both effects can easily be explained when considering the effect of the smearing on the shower start distribution. Through the smearing an event with a shower start in layer N might be shifted downwards or upwards at the same probability. However, the shower start distribution itself is described by a falling exponential, i.e. the number of events with an early shower start is higher than the number of events with a late shower start. Hence by the smearing the average starting position is shifted downwards to the end of the calorimeter, and thus overestimating the number of events with an shower start there. As the peak of the real calorimeter profile is not at the beginning of the calorimeter, but after about $0.8\,\lambda_\mathrm{I}$, the number of events with a shower start at that position is overestimated by the smearing, and thus weighted down.

For comparison Figure 4.23 also includes the fully reconstructed TofH-based T3B test-beam data in cyan. Its calorimeter profile is quite close to the black curve of undigitized simulated data with a Gaussian shower start resolution of $\sigma = 2$ layers. Therefore for all analysis presented in this thesis an Gaussian resolution of $\sigma = 2$ layers is assumed for the shower start in simulated data (cf. section 4.3.1).

In the following, however, we will concentrate on the overall shape of the profiles. Thus the reduced height of the profile has no influence. Only the shift of the peak towards the end of the calorimeter introduces a systematic offset of about $0.3\,\lambda_{\mathrm{I}}$.

The Longitudinal Shower Profile

Using the technique described above, the shower profile of a 60 GeV π^+ was generated for different time ranges. These were chosen to be sensitive to the three different contributions to the time structure of hadronic showers.

- $0 - 2.4$ ns: The near instantaneous part caused by electromagnetic subshowers, strong hadronic interactions and intra-nuclear cascades.
- $2.4 - 16$ ns: Intermediate part, caused mainly by neutron elastic scattering.
- $16 - 250$ ns: Slow component. After the neutrons lost their energy through elastic scattering, they might be captured by a nucleus. The binding energy released by this neutron capture excites the nucleus, which then in turn emits detectable photons.

The resulting shower profile is shown twice in Figure 4.24. In the upper plot the profiles of the individual time ranges are stacked on top of each other, such that the overall shape is the sum of all time regions and as such the profile as seen by a real calorimeter. The profiles are displayed with their absolute energy deposition in terms of MIP per calorimeter layer. The lower plot is a copy of the one above, but the plots of the time ranges are normalized to individually give their relative energy deposition fraction per calorimeter layer, in order to be able to better compare their shape.

One thing that immediately stands out is the domination of the energy depositions within the first 2.4 ns, which is almost exclusively responsible for the overall shower shape. This is in agreement with the time development of the total energy deposition fraction, discussed in subsection 4.4.2.

In addition, the shape of the instantaneous part is characterized by a faster rise, with a peak after already around $0.3\,\lambda_{\mathrm{I}}$, whereas the intermediate and the slow component both have their peak only at around $0.6\,\lambda_{\mathrm{I}}$. This behaviour is caused by the dense but range limited electromagnetic part of the shower, which mainly contributes to the instantaneous shower component.

Based on the shower profiles, the calorimeter profile can be constructed. In this process the statistical fluctuations seen in the shower profiles are washed out by their repeated overlay.

Differences with respect to the shower radius are shown by splitting the longitudinal calorimeter profile into three regions:

- The central part consisting of the two inner most tiles, covering $-1.5 - 4.6$ cm.
- An intermediate part of the tiles 3 to 7, covering $4.7 - 20.1$ cm.

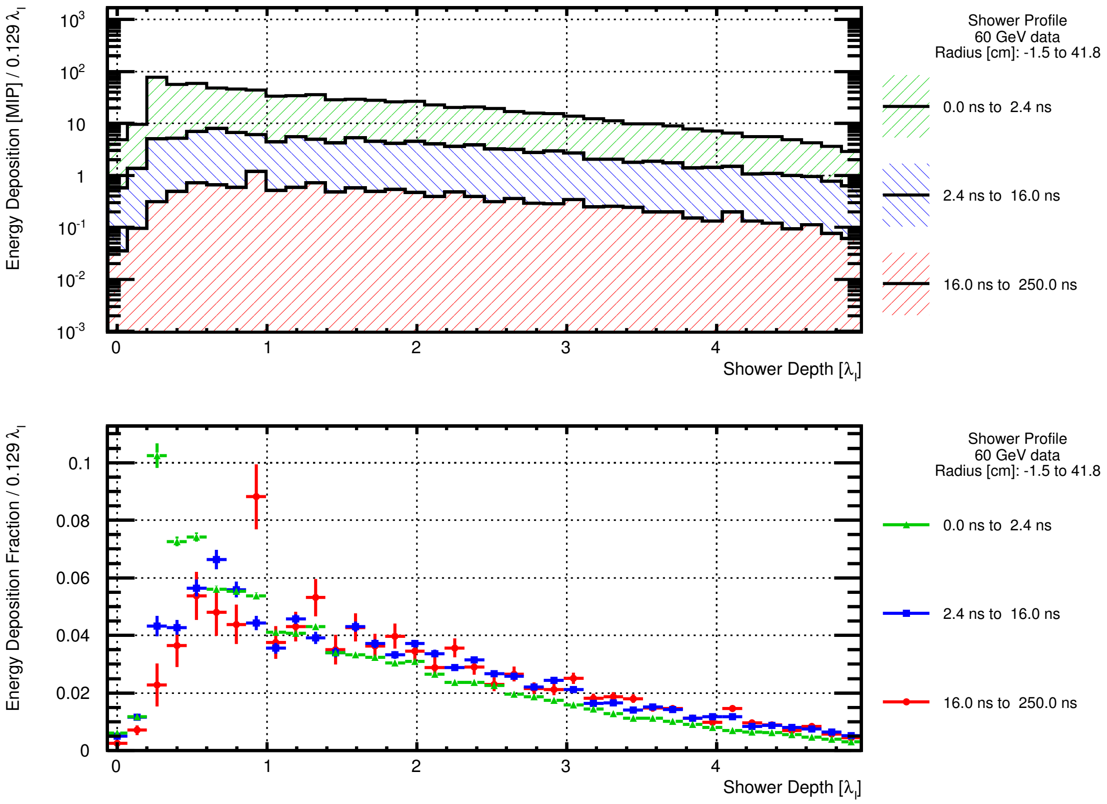

Figure 4.24: The shower profile for 60 GeVπ^+ data, split into different times. In the upper plot the three parts are shown in terms of their total energy deposition of MIP per layer, stacked on top of each other to get the total shower profile. In the lower plot the same distributions are shown, but scaled to the relative energy deposition fraction per layer, acting as a shape comparison.

- The outer part with the tiles 8 to 15, covering $20.2 - 41.8$ cm.

The distribution of the three radial regions ranges again split into the same three time ranges introduced above are shown in Figure 4.25. The normalization is again that each profile sums up to 1, i.e. it shows the relative energy deposition per layer within the specific time and radial range.

For high shower radii, there are no statistically significant differences in the calorimeter profile for the three different time ranges. They all tend to peak around 1.7 λ_I. For the intermediate and the slow time region there is a slight tendency for the peak to wander to the back of the calorimeter when moving from the outer shower radius to the center. However, there is a significant change in the shape of the instantaneous part, where the peak moves forward to be at around 1 λ_I for the central part. This is a clear sign of the electromagnetic sub-showers fraction, as electromagnetic showers tend to be very dense in the W-AHCal, as one calorimeter layer already has almost 3 X_0. Thus their range is limited, with only small impact in the intermediate shower radius

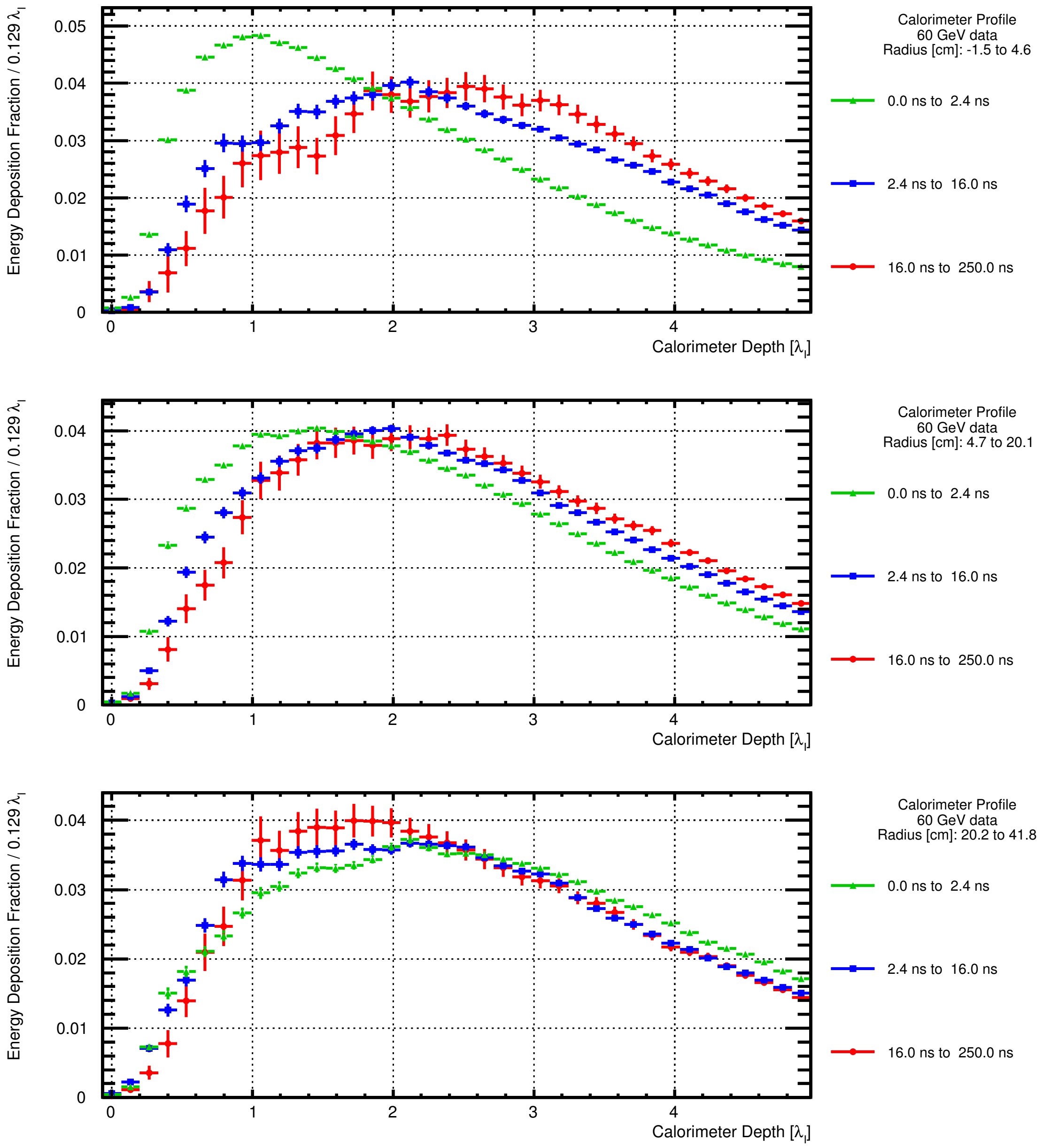

Figure 4.25: Shape comparison of the longitudinal calorimeter profile for 60 GeVπ^+ data split into different time ranges. The three plots show different segments of the shower radius.

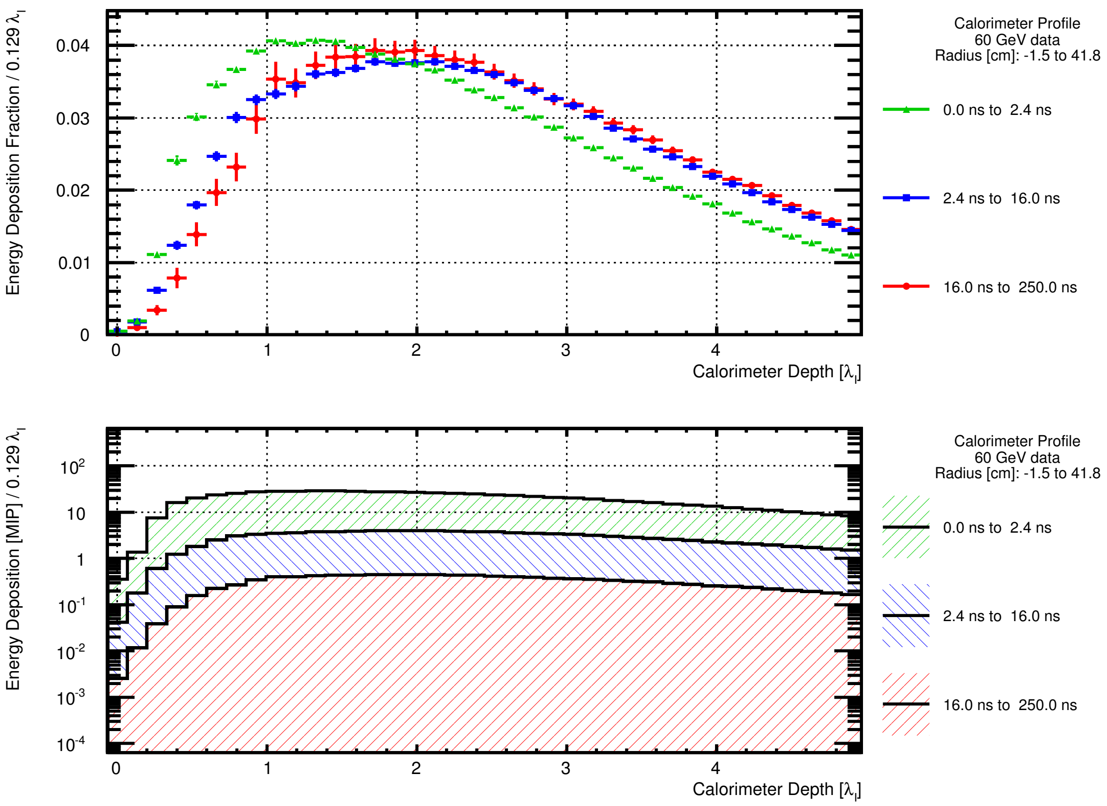

Figure 4.26: Longitudinal calorimeter profile for 60 GeVπ^+ data split into different time ranges. The upper plot shows the shapes for the different time ranges, while the lower plot shows the total calorimeter profiles, stacked with the individual time contributions.

range and not seen for large radii, where the shape is dominated by pure hadronic interactions.

Putting all three shower radii into a single plot gives the overall longitudinal shower profile, shown again twice in Figure 4.26. As before, the upper plot shows the calorimeter profile, normalized for the individual time ranges, while the lower plot is the result of stacking the three time components on top of each other.

One can see that the peak of the instantaneous part is slightly shifted to the calorimeter front with respect to the other two time ranges due to the electromagnetic subshower part.

Comparison to Simulation

A comparison of the calorimeter profile obtained from data with the ones from the simulation, based on the three different physics lists `QGSP_BERT`, `QGSP_BERT_HP` and `QBBC`, is shown in Figure 4.27 for the entire radial extend of the shower. As before the statistical fluctuations of the shower profile are smeared out by its repeated overlay in the construction of the calorimeter profile and are thus only visible in the statistical

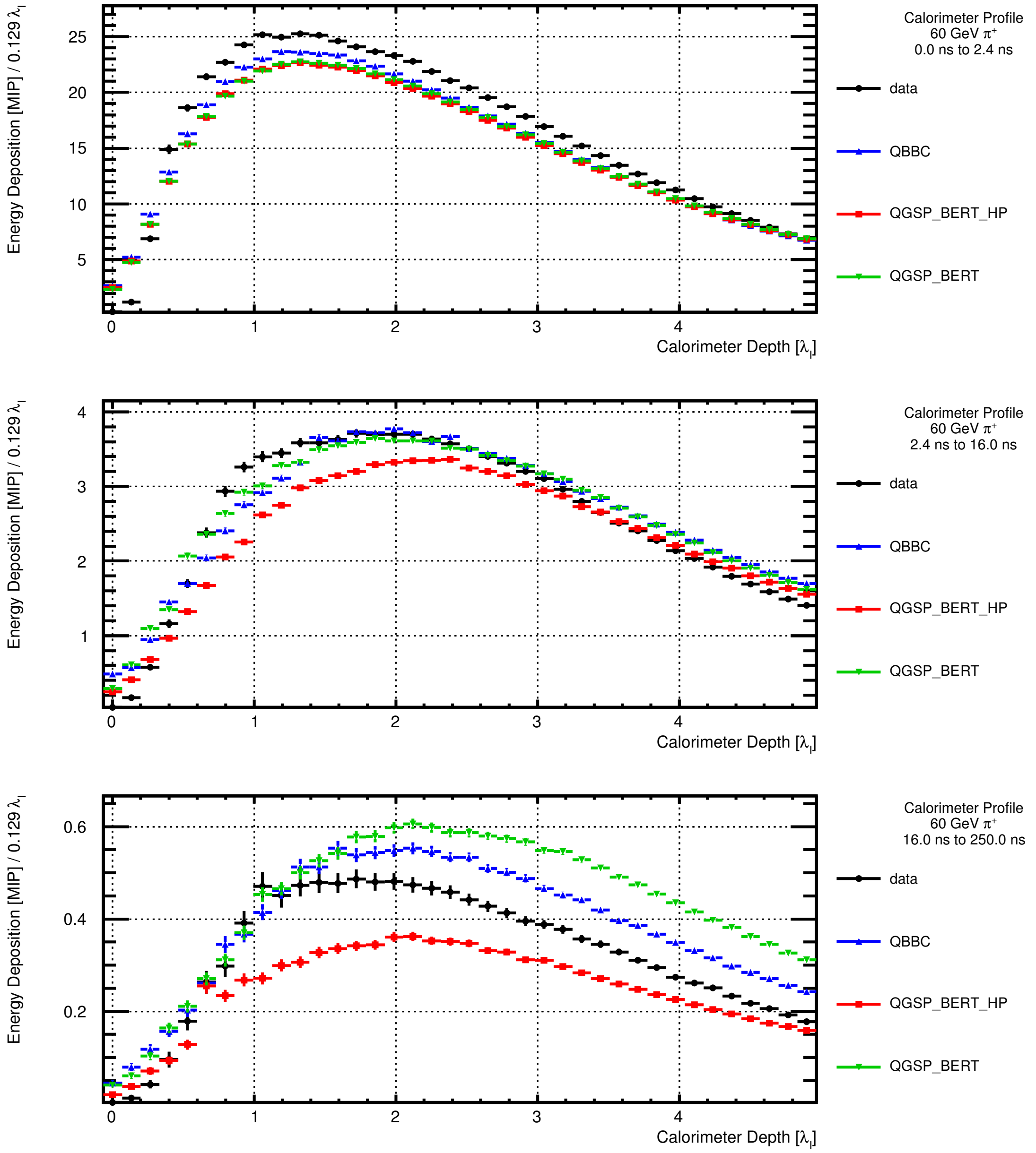

Figure 4.27: Shape comparison of the longitudinal calorimeter profile for 60 GeVπ^+ data split into different time ranges. The three plots show simulation with different physics lists for the three time ranges.

errors.

In the early time range of 0 ns to 2.4 ns, shown in the upper of the three plots in Figure 4.27, the agreement between the two physics simulations of `QGSP_BERT` and `QGSP_BERT_HP` is clearly within statistical limits while `QBBC` deposits about 3% more energy in the central region of $1-2\,\lambda_\mathrm{I}$. Except for the first layers, the calorimeter profile of the testbeam data lies above the simulation, depositing about 10% more energy than the two `QGSP` based simulations around the peak of the profile. However, the overall shape of the calorimeter response is in good agreement for all four data sets.

In the central plot, showing the intermediate time range of 2.4 ns to 16 ns, the change of the peak towards the calorimeter rear is reproduced well by all physics list. However, small differences between the physics lists and the testbeam data start to occur in the shape, as the profile of the testbeam data has a steeper rise towards the peak around $2\,\lambda_\mathrm{I}$ as well as a faster drop towards the end than all of the physics lists. However, the total amount of deposited energy is well described by `QGSP_BERT_HP` in the first $\approx 0.5\,\lambda_\mathrm{I}$ and around 3 to $4\,\lambda_\mathrm{I}$, while the peak around 1.5 to $3\,\lambda_\mathrm{I}$ is best described by `QGSP_BERT` and `QBBC`.

For the late components of 16 ns to 250 ns, shown in the lower plot, the differences between all four data sets are most significant. While the rise in the deposited energy per layer up to $1\,\lambda_\mathrm{I}$ is reproduced well by all physics lists, for the profile above $1\,\lambda_\mathrm{I}$ `QGSP_BERT` and `QBBC` overestimate the detector response by about 0.12 MIP/layer and 0.07 MIP/layer respectively. At the same time their profile peaks at $2.3\,\lambda_\mathrm{I}$ (`QGSP_BERT`) and $2.0\,\lambda_\mathrm{I}$ (`QBBC`) respectively, which is considerably after the one of the testbeam data, which peaks at $1.8\,\lambda_\mathrm{I}$. `QGSP_BERT_HP`, on the other hand, constantly underestimates the detector response by up to 0.15 MIP/layer in the region around $1.5\,\lambda_\mathrm{I}$. However, towards the calorimeter rear the overestimation falls and is less pronounced, such that it is almost within statistical limits around $4.9\,\lambda_\mathrm{I}$. As the other physics lists, the position of the peak of the profile of `QGSP_BERT_HP` is shifted towards the calorimeter end ($2.1\,\lambda_\mathrm{I}$).

4.4.5 Comparison of Pion with Proton Response

The results presented so far all were based solely on pion data, as they represent the main content of hadronic showers. Other hadrons, however, might result in a different time structure. This assumption is especially true for baryons. For example their showers tend to have a lower electromagnetic fraction as opposed to showers created by mesons, as the baryon number conservation limits the pion production in general and the π^0-production in particular, which are the main cause of the electromagnetic sub-showers. Therefore this section compares the pion response with the one from protons.

A big advantage for this comparison is that they originate from the same data sample, since the secondary beam at CERN SPS was an admixture of both particles. Using the Cherenkov system both particle species can be selected with high efficiency. The obligatory calibration of the $t = 0$ ns by fitting the peak of the Time of first Hit distribution of the central tile was performed prior to the particle selection and is thus identical in both cases, reducing systematic uncertainties to a minimum. Therefore the

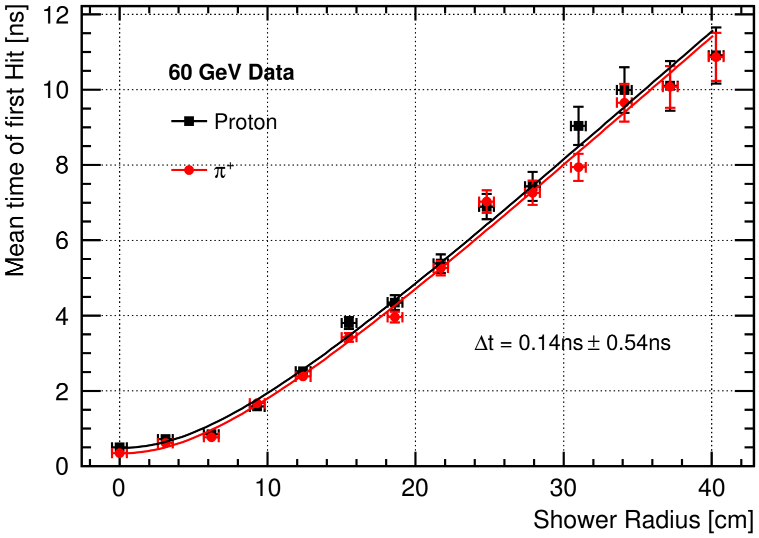

Figure 4.28: The mean Time of first Hit for different shower radii, once for pions and once for protons, extracted from the same 60 GeV testbeam run.

comparison between pion and proton response has a better relative time resolution than the global one discussed in subsection 4.2.6.

A comparison of the Time of first Hit distribution was already shown in Figure 4.9 and revealed no significant differences between the pion and proton responses.

Here a more detailed investigation is performed by studying the development of the mean Time of first Hit as a function of the shower radius. The resulting profiles for both pions and protons are shown in Figure 4.28. Within statistical limits no obvious difference can be seen in the two profiles. Instead their overall shape seems to be identical. Thus in order to extract an overall time difference, both distributions are fitted. The function describing the distribution has two components. For higher radii it seems to rise linearly for both particle types. However, in the central part this linear dependence is broken, and was described by a falling exponential. The resulting function thus is:

$$f(x) = e^{ax+b} + cx + d, \tag{4.1}$$

where a is negative and d denotes the constant offset in ns. In order to extract the constant offset between both sets, both the pion and the proton dataset were fitted at the same time with the same fit parameters a, b and c, but with individual constants d_π and d_p. The resulting time difference is

$$\begin{aligned} \Delta t &= \left| d_\pi - d_\mathrm{p} \right| \\ &= 0.14\,\mathrm{ns} \pm 0.54\,\mathrm{ns}, \end{aligned}$$

and thus not statistical significant. Therefore no difference in the time response between pions and protons could be identified in the radial profile.

4.5 Conclusion

In order to reach the desired instantaneous luminosity, the bunch crossing rate at the Compact Linear Collider (CLIC) is very high with a bunch spacing of only 0.5 ns. At the same time a significant amount of beam induced background is produced, leading to pile-up. To identify the measurements of a single real physics event it is therefore crucial that the detector, one of which is the International Large Detector (ILD), has accurate time stamping capabilities which are used to cut away pile-up contributions. This includes the energy measurement of the calorimetric system. However, during a hadronic cascade low energetic neutrons are created which cause non-instantaneous energy depositions of several ten ns up to μs after the start of the cascade. These late energy depositions can therefore lead to incorrect energy measurements. This is especially true in the barrel calorimeter of the ILD, which uses tungsten as absorber and thus produces a significant higher amount of neutrons than steel absorbers. The influence of these late energy depositions on the overall detector performance is thus studied in detailed full detector simulations, which in turn rely on correct models for the hadronic cascades.

In order to verify the hadronic cascade models underlying to this detector simulation, a small testbeam experiment, called Tungsten Timing Testbeam (T3B), was developed. It consists of a single strip of 15 $3 \times 3 \times 0.5\,\mathrm{cm}^3$ scintillator cells read out with Silicon Photomultipliers, the same technology principle used in the CALICE W-AHCal hadron calorimeter which is a prototype for the ILD. These were placed transverse to the shower axis, starting from the shower center outwards and thus covering a total radial range of 46.5 cm (including gaps between cells) of the hadronic shower. Assuming radial symmetry, the data recorded by this strip can be used to measure the average response of hadronic showers. A special feature of these cells is that they were read out with USB oscilloscopes with sub-ns sampling, thus enabling the measurement of the time structure of the hadronic showers.

T3B was parasitic to the testbeam campaign of the CALICE analog hadron calorimeter (W-AHCal) prototype which was using tungsten absorber plates. The beam tests took place at the Proton Synchrotron and the Super Proton Synchrotron at CERN in 2010 and 2011. The T3B experiment was specifically designed for this campaign, including the development of a dedicated data acquisition software that allowed for a constant monitoring of the SiPM gain in addition to recording the beam data taken with the cells.

With this information it was possible to perform a decomposition of the SiPM waveforms to individual single pixel contributions, and thus significantly reducing the dependency on environmental changes influencing the SiPM response. Single energy depositions were reconstructed using the Time of first Hit, i.e. the first energy deposition of 8 pixels in 9.6 ns, corresponding to 0.45 MIP.

The testbeam setup was reproduced in GEANT4 for a detailed simulation. This included the subsequent digitization of the simulated data to account for known detector effects such as afterpulsing and photon traveling time in the scintillator, which were implemented based on muon data taken at the testbeam.

By comparing the time stamps and the number of events recorded per spill, it was possible to synchronize the T3B data stream with the one from the CALICE W-AHCal and thus gaining information on the complete shower development in the calorimeter. This was used to extract information on the shower starting layer by using the Primary Track Finder algorithm of the CALICE collaboration. Thus it was possible to classify the detector response along the longitudinal shower axis, and reconstruct the time structure of the shower profile. With this it was possible to construct the calorimeter profiles as well as get the mean Time of first Hit along the shower axis and the fraction of deposited energy over time.

Based on these observables a comparison to the GEANT4 simulation showed a good agreement of the high precision physics lists `QGSP_BERT_HP` and `QBBC`, whereas `QGSP_BERT`, a version of the former physics list without high precision neutron tracking, substantially overestimates the amount of late energy depositions. However, within the total energy deposition fraction the differences are below 1%, and especially over 98% of the energy is deposited within the first 20 ns, thus limiting the influence of late energy depositions on the hadron calorimeter energy resolution in detectors with state-of-the-art readout electronics and with the use of timing cuts in the reconstruction.

Last but not least a comparison in time between the response of pions and protons was performed. Within the statistical error, no dependency on the primary particle type could be found.

Chapter 5

Measurement of the Mass and Cross Section of Right-handed Scalar Quarks with the Compact Linear Collider

As already described in detail in section 3.2, the Compact LInear Collider (CLIC) is a concept of an electron-positron linear collider with a center of mass energy of 3 TeV. Its purpose is a precise measurement of the properties of known particles as well as the discovery of yet unknown particles beyond the standard model. The detector systems developed for CLIC are introduced in detail in the physics and detector volume of the CLIC conceptional design report (CDR) [10]. A particular challenge at CLIC is the high rate of beam induced background of $\gamma\gamma \rightarrow$ hadrons and its influence on the particle flow algorithm which is used for the event reconstruction. In order to evaluate the physics performance and study the impact of this background, six benchmark processes [72] were introduced. These processes were specifically selected to test specific aspects of the detector systems and the event reconstruction efficiency. One of these benchmarks focuses on the reconstruction performance with the particle flow algorithm at events with two high energetic jets and missing energy. This was done via the measurement of the mass and the cross section of super symmetric right-handed scalar quarks for an integrated luminosity of $\int \mathrm{d}t\mathcal{L} = 2000\,\mathrm{fb}^{-1}$, corresponding to a runtime of 5 years at full design luminosity. This chapter will discuss the details of this measurement, most of which were already published in [73].

5.1 The CDR SUSY Model Type I

For the purpose of the CDR benchmark processes dedicated supersymmetric models were created using a set of different tools. For this analysis the CDR SUSY Model Type I was used [72]. Its parameters can be seen in Table 5.1 and the resulting mass spectrum for the squarks, gluinos and the three lightest neutralinos can be found in Table 5.2. The cross section for the different particle production processes in dependence of the

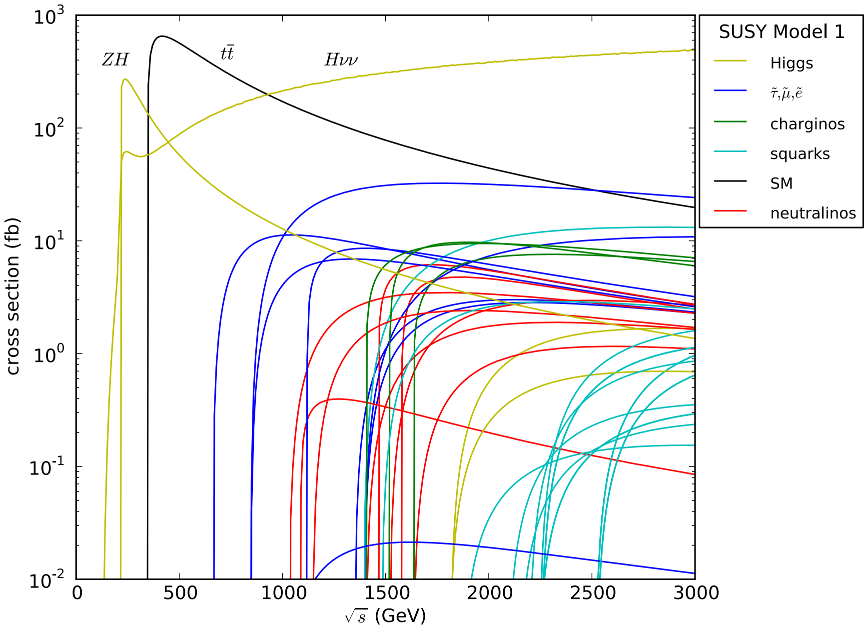

Figure 5.1: SUSY Production cross section for different particles as a function of $\sqrt{s}$.

parameter	value
M_1	750 GeV
M_2	940 GeV
M_3	540 GeV
A_0	-750 GeV
m_0	303 GeV

parameter	value
$\tan\beta$	24
μ	> 0
m_t	173.3 GeV
$M_b(M_b)$	4.25 GeV
$\alpha_S(M_Z)$	0.118

Table 5.1: The SUSY parameters for the model used in the presented analysis [10, 72].

center of mass energy $\sqrt{s}$ are shown in Figure 5.1.

Note that the SUSY Model Type I is not a constraint Minimal Super Symmetric Model (cMSSM) as it does not have unified gaugino masses. It was explicitly designed for another CLIC CDR benchmark process, in which pair produced heavy supersymmetric Higgs bosons are reconstructed. However, for the purpose of the detector and reconstruction benchmark the exact nature of the model is not important. Note, however, that the model is not excluded by latest LHC results based on the 2012 data.

One of the model's relevant features is the decay chain of the squarks. As R-parity is conserved, the squarks will decay to the lightest supersymmetric particle (LSP), the neutralino $\tilde{\chi}^0_1$, along with standard model particles. The first step in this decay chain will be the gluino $\tilde{g}$ in most models, as its coupling to the squark has QCD strength. This is of course only possible, if the squark is heavier than the gluino. The gluino will then decay further, predominantly to lighter squarks, which ultimately decay then into

particle	mass [GeV]
$\widetilde{\mathrm{g}}$	1239.7
$\widetilde{\chi}_1^0$	328.3
$\widetilde{\chi}_2^0$	701.8
$\widetilde{\chi}_3^0$	760.2

particle	mass [GeV]
$\widetilde{\mathrm{u}}_\mathrm{r}$, $\widetilde{\mathrm{c}}_\mathrm{r}$	1125.7
$\widetilde{\mathrm{d}}_\mathrm{r}$, $\widetilde{\mathrm{s}}_\mathrm{r}$	1116.1
$\widetilde{\mathrm{t}}_1$	739.4
$\widetilde{\mathrm{b}}_1$	1043.3

particle	mass [GeV]
$\widetilde{\mathrm{u}}_\mathrm{l}$, $\widetilde{\mathrm{c}}_\mathrm{l}$	1125.7
$\widetilde{\mathrm{d}}_\mathrm{l}$, $\widetilde{\mathrm{s}}_\mathrm{l}$	1116.1
$\widetilde{\mathrm{t}}_2$	1121.8
$\widetilde{\mathrm{b}}_2$	1096.0

Table 5.2: Masses of the most important particles of the used SUSY model [10, 72].

at least one neutralino:

$$\begin{aligned} \widetilde{q} &\to \widetilde{\mathrm{g}} + q \qquad\qquad \text{for } m_{\widetilde{\mathrm{g}}} < m_{\widetilde{q}_r} \\ &\quad \hookrightarrow \widetilde{\chi}_1^0 + X(+\ldots) \end{aligned} \tag{5.1}$$

But in the SUSY Model I the gluino is heavier than the squark. Hence this decay channel is kinematically not allowed. As the squarks couple to the weak gauginos, they can decay into either a chargino, which will decay further to the LSP, the neutralino, or directly to the neutralino. The exact decay, however, is subject to the mixing of the charginos. As it was discussed in subsection 2.2.5, the mass eigenstates of the neutralinos and the charginos are an admixture of their gauge eigenstates. However, in most SUSY models the mixing for the lightest neutralino $\widetilde{\chi}_1^0$ is small and its component is almost completely bino $\widetilde{\mathrm{B}}$. The second lightest neutralino $\widetilde{\chi}_2^0$ on the other hand is mostly wino $\widetilde{\mathrm{W}}$. In contrast to the left handed squarks, which do carry weak isospin and consequently couple strongly to the winos, the right handed squarks have no isospin. As a consequence they only couple to the bino. As the lightest neutralino is mostly bino, right handed squarks will mostly decay to their SM partner and the lightest neutralino. Left handed squarks, however, will favour the decay into heavier neutralinos or charginos due to the stronger coupling of squark-quark-wino, before they ultimately, too, create at least one neutralino:

$$\widetilde{q}_r \to \widetilde{\chi}_1^0 + q \tag{5.2}$$

$$\begin{aligned} \widetilde{q}_l &\to \widetilde{\chi}_2^0 + q \\ &\quad \hookrightarrow \widetilde{\chi}_1^0 + X(+\ldots) \\ &\to \widetilde{\chi}^{\pm} + q' \\ &\quad \hookrightarrow \widetilde{\chi}_1^0 + Y(+\ldots) \end{aligned} \tag{5.3}$$

5.2 The light-flavoured Squarks Benchmark Process

The purpose of this benchmark process is to test jet and missing energy reconstruction for high energy jets in a simple topology. The high energetic jets are a stress test for the particle flow algorithm and the calorimetric system, as it is crucial to separate clusters of the individual jet particles. Due to the missing energy it is not possible to use the knowledge of the initial state to compensate for lack of accuracy in the jet reconstruction. With the CDR SUSY Model I at hand, the necessary event topology is created by right handed squarks. This excludes the stop and the sbottom, as their mass eigenstates are an admixture of both left and right handed squarks, resulting in more complicated decay patterns.

5.2.1 The Signal Process

In this analysis we will focus on the production of the right-handed super partners of the four lightest quarks: $\widetilde{\mathrm{u}}_\mathrm{r}$, $\widetilde{\mathrm{d}}_\mathrm{r}$, $\widetilde{\mathrm{s}}_\mathrm{r}$ and $\widetilde{\mathrm{c}}_\mathrm{r}$. At a lepton collider the squarks are produced in pairs via the s-channel process:

$$\mathrm{e}^-\mathrm{e}^+ \to \gamma/\mathrm{Z}^0 \to \widetilde{q}_r\overline{\widetilde{q}_r}$$

As we have discussed before, in the current SUSY model I the right handed squarks prefer a decay through the weak interaction to the lightest neutralino along with the corresponding SM quark. The decay has a branching fraction of 99.7%:

$$\widetilde{q}_r \to q + \widetilde{\chi}_1^0 \qquad\qquad \mathcal{B} = 99.7\%$$

The neutralino $\widetilde{\chi}_1^0$ will not interact with the detector matter and consequently will escape direct detection and show up as missing energy E_miss. The quark on the other hand will start fragmentation and create a high energetic jet. Hence, the total process for the creation and decay of right handed squarks looks like:

$$\begin{aligned}\mathrm{e}^- + \mathrm{e}^+ \to \gamma/\mathrm{Z}^0 &\to \widetilde{q}_r\overline{\widetilde{q}_r} \\ &\xrightarrow{(99.7\%)^2} q\overline{q} + 2\widetilde{\chi}_1^0 \\ &\qquad = 2 \text{ jets} + E_\mathrm{miss}\end{aligned}$$

The corresponding Feynman diagram is shown in Figure 5.2. Up- and down-type squarks differ in mass by 9.6 GeV, and the production of up-type squarks is favoured:

$$\frac{\sigma_{\widetilde{\mathrm{u}}}}{\sigma_{\widetilde{\mathrm{d}}}} = 3.82$$

The combined cross section for the production of all four squarks at CLIC including effects from the beam-energy spectrum is 1.47 fb.

The signature of this process is missing energy and two high energetic jets. With energies up to 1 TeV and more, the jets are a very dense structure of high momentum particles.

5.2.2 Background Processes

The event signature of the signal process with two jets and missing energy is very generic and can be generated by a couple of standard model and SUSY processes as well. In the following a list of these processes and their relevance to the benchmark process will be discussed. The list of the processes along with their respective cross sections can also be seen in Table 5.3.

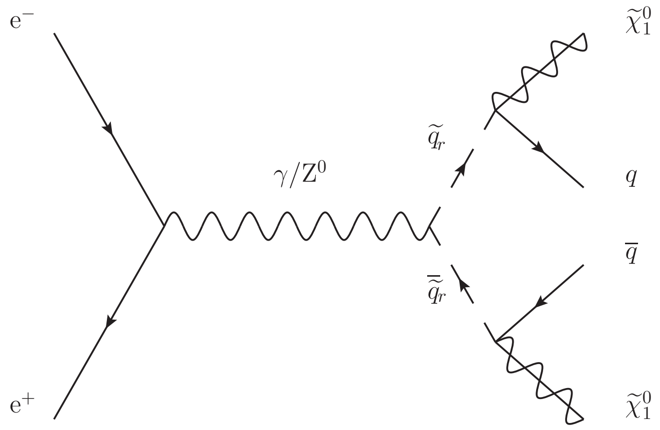

Figure 5.2: Feynman diagram for the production and the predominant decay of two right handed scalar quarks at the compact linear collider. Here, $\tilde{q}_r$ denotes first and second generation squarks, but not the stop $\tilde{\mathrm{t}}$ and sbottom $\tilde{\mathrm{b}}$ as their mass eigenstates is an admixture of left and right handed squarks.

	process	cross section σ[fb]	$\sigma/\sigma_{\mathrm{signal}}$
signal	$e^+e^- \to \tilde{q}_r\bar{\tilde{q}}_r \to q\bar{q}\tilde{\chi}_1^0\tilde{\chi}_1^0 \quad (q = udsc)$	1.47	1
SM, E_{miss}	$e^+e^- \to q\bar{q}\nu\bar{\nu}$	~ 1500	$\sim 1.0 \cdot 10^3$
	$e^+e^- \to q\bar{q}e^\pm\nu$	~ 5300	$\sim 3.6 \cdot 10^3$
	$e^+e^- \to \tau^-\tau^+\nu\bar{\nu}$	~ 130	$\sim 8.8 \cdot 10^2$
SM, no E_{miss}	$e^+e^- \to q\bar{q}$	~ 3000	$\sim 2.0 \cdot 10^3$
	$e^+e^- \to q\bar{q}e^+e^-$	~ 3300	$\sim 2.2 \cdot 10^3$
SUSY	$e^+e^- \to q\bar{q}\nu\bar{\nu}\tilde{\chi}_1^0\tilde{\chi}_1^0$	~ 1.0	~ 0.7
	$e^+e^- \to q\bar{q}\ell^\pm\nu\tilde{\chi}_1^0\tilde{\chi}_1^0$	~ 8.5	~ 5.8
	$e^+e^- \to \ell^+\ell^-\nu\bar{\nu}\tilde{\chi}_1^0\tilde{\chi}_1^0$	~ 0.6	~ 0.4

Table 5.3: List of signal and background processes with their corresponding cross section at the compact linear collider at 3 TeV. The signal process only includes right handed squarks of the first and second generation.

Standard Model Processes with Missing Energy

Within the standard model missing energy is created only through neutrinos. The number of processes with neutrinos and an event signature of two jets is limited. Jets are typically created by high energetic quarks. So the processes to look at creates a q-$\bar{q}$ pair alongside with at least one neutrino. Due to lepton number conservation the neutrino is created together with another lepton.

A neutrino as second lepton is closest to the event signature in question. This results in the first considered background process: $e^+e^- \to q\bar{q}\nu\bar{\nu}$, where q can be any of the six quarks and ν can be any of the three neutrinos, with $\bar{q}$ and $\bar{\nu}$ being the corresponding anti particles.

A second choice for the remaining lepton is to be an electron (positron). If this electron is hidden in one of the jets, this process, too, has the required event shape. This results in our second background process $\mathrm{e}^+\mathrm{e}^- \to q\overline{q}\mathrm{e}\nu$. This is short hand for the two groups of flavour changing charged current processes $\mathrm{e}^+\mathrm{e}^- \to \mathrm{u}\overline{\mathrm{d}}\mathrm{e}^+\nu_\mathrm{e}$ and $\mathrm{e}^+\mathrm{e}^- \to \overline{\mathrm{u}}\mathrm{d}\mathrm{e}^-\overline{\nu}_\mathrm{e}$, with u standing for all up type quarks (uct), and d representing all down type quarks (dsb).

The case where the second lepton is a muon or tau are not considered here, as they have a significantly lower cross section and thus have negligible impact. In addition, taus create an electromagnetic jet of many particles and thus will not meet the criterion for escaping the interaction point undetected.

Although most jets are created by strong interacting particles there is an exception: The lifetime of taus is short enough for it to decay in flight, creating a number of particles alongside. There are different decay modes, which include both pure leptonic decays and a mix of lepton and hadronic decays, both of which create a mix of particles resembling a jet. Together with two neutrinos accounting for the missing energy, the third considered background process is $\mathrm{e}^+\mathrm{e}^- \to \tau^-\tau^+\nu\overline{\nu}$.

As one can see in the right most column in Table 5.3, the cross section of these processes is significantly above the signal one. Especially the first two processes are three orders of magnitudes higher. This requires a sophisticated and reliable background rejection.

Standard Model Processes without Real Missing Energy

Events with missing energy can be created by processes without real missing energy. This can be due to insensitive detector regions, inefficiencies in the reconstruction or the creation of neutrinos at some point within the event.

The first background process considered here is the pair production of two quarks in a s-channel process $\mathrm{e}^+\mathrm{e}^- \to q\overline{q}$. This will create two high energetic jets with an $1 + \cos^2\theta$ distributed flight direction. Thus part of the particles may hit the insensitive detector regions such as the beam pipe and fake missing energy.

The second background process is a scattering process in which two quarks are generated in addition to the electron and the positron: $\mathrm{e}^+\mathrm{e}^- \to q\overline{q}\mathrm{e}^+\mathrm{e}^-$. There are several possible Feynman diagrams generating these final state particles, but the dominating contribution is a t-channel scattering process in which both the electron and the positron will only emit a single photon which is used to generate the pair of quarks. In this process the flight direction of the electron (positron) is not altered significantly and peaks in the forward direction ($|\cos\theta| \lesssim 1$). Consequently the electron (positron) has a non negligible chance of escaping detection through the beampipe, faking missing energy E_miss.

Compared to the signal process the cross sections of these two processes are three orders of magnitude higher (see Table 5.3). So although the probability of generating fake missing energy events is low, one could expect that these two processes interfere with the measurement of the signal process. However, as we will see in subsection 5.3.2 their contribution is negligible and consequently these processes were not considered in the analysis.

SUSY Processes with Missing Energy

In supersymmetry in addition to the standard model neutrino, the neutralino creates missing energy. So, the relevant supersymmetric background processes are similar to the standard model ones discussed before, but with an added pair of neutralinos. The process $e^+e^- \to q\overline{q}e^-e^+$ however, is excluded here, as the two electrons in addition to the two jets do not fulfill the required two jets and missing energy event shape.

The result are the three processes $e^+e^- \to q\overline{q}\nu\overline{\nu}\widetilde{\chi}_1^0\widetilde{\chi}_1^0$, $e^+e^- \to q\overline{q}\ell^\pm\nu\widetilde{\chi}_1^0\widetilde{\chi}_1^0$ and $e^+e^- \to \ell^+\ell^-\nu\overline{\nu}\widetilde{\chi}_1^0\widetilde{\chi}_1^0$. They all have a final state of six particles, requiring at least six vertices in the Feynman diagram. Hence, as shown in Table 5.3, their cross section is very small and it is expected that they do not contribute significantly to the background spectrum.

As all these processes have six particles in the final state, the integration and consequently the event generation takes significantly longer than for processes with two or four final state particles. This time was too high for any kind of large scale event generation. Consequently, none of the discussed processes were considered during the analysis as of now, but will be at a later time. However, as the cross section of the processes is low it is expected that they can easily be rejected using the techniques discussed in this thesis.

5.2.3 Beam induced Background

On top of the actual collision process, each event contains particles from beam induced background. At CLIC these do have several sources. For details see [10] and references therein.

One of these processes is the production of coherent and incoherent pairs of e^+ e^- through interaction of beamstrahlung induced photons with either the collective field (coherent) or individual particles (incoherent) of the opposing beam. Most of these e^+ e^- pairs have a low transverse but high overall momentum, and consequently they leave the detector volume close to the electron/positron bunches along the beampipe without being detected. However, some of these pairs are indeed registered by the detector and hence overlay over the actual physics events.

The second and for this analysis more important process is the creation of hadrons via the interaction of virtual or real photons of the colliding beams: $\gamma\gamma \to$ hadrons. These hadrons are mostly boosted in forward direction but also can reach large angles and overlay over the actual event. Within the detector acceptance of $\theta > 8\,^\circ$, a mean of 2.8 hadrons with a center of mass energy greater than 5 GeV are expected per bunch crossing.

One challenge for the detectors at CLIC is the high repetition rate with only 0.5 ns or 15 cm between two bunch crossings. For technical reasons the detector and its read out electronics are not capable to read out at this rate. Instead, some subdetectors such as the time projection chamber integrate over the entire bunch train of 312 bunches. Other subdetectors, such as the calorimetric system, search for actual energy depositions, assign them a ns-precision time stamp and integrate over a few 10 to 100 ns. However, as we have seen in chapter 4, the development of hadronic showers itself takes longer than

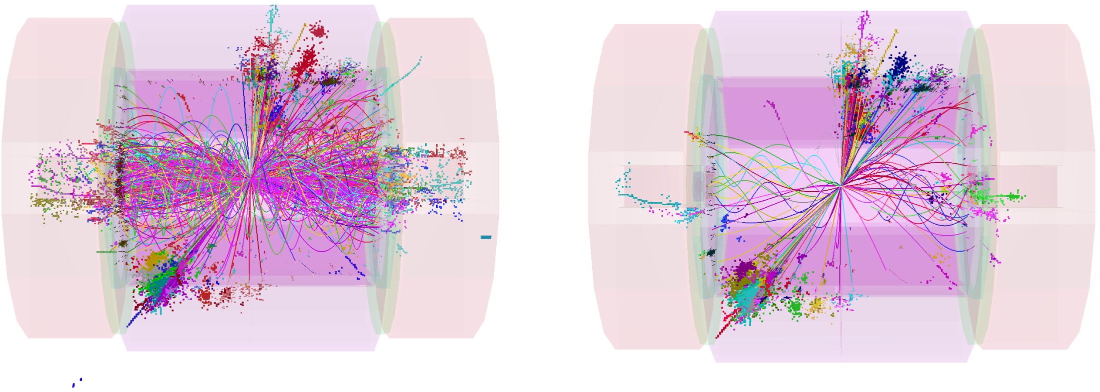
(a) Prior to timing cuts

(b) After timing cuts

Figure 5.3: Reconstructed particles of an example event of $e^+e^- \rightarrow H^+H^- \rightarrow t\bar{b}\bar{t}b$ at 3 TeV with an equivalent of an overlay of background particles corresponding to 60 bunch crossings. The left plot is before, the right plot after timing cuts.

the arrival of the subsequent bunch crossings and their particles. Note that through the beam induced background the total energy deposition per bunch train (312 bunches) sums up to more than 20 TeV in the calorimetric system. Although most of it is focused in the forward region, this requires very sophisticated and stringent cuts on time to minimize the overlay of these beam induced background particles, while integrating long enough to be able to record the real energy depositions of the hadronic shower.

In the presented analysis, the integration time of the different subdetectors was assumed to be 10 ns, with the exception of the HCAL barrel region (100 ns) and the TPC (entire bunch train). The expected background of these approximately 20 bunch crossings (BX) is reduced to 1.2 TeV per event. As this is very high compared to the center of mass energy of 3 TeV, additional cuts based on the transverse momentum p_t of reconstructed particles and on the time of individual hits of a cluster, rejecting hits outside a specified region of the truncated mean of the time were necessary. For this analysis the *Default* cut was chosen, to which details can be found in [10] and in Appendix B. In addition there are the *Tight* and *Loose* cuts, which impose even more (less) stringent cuts. They are only used for comparison of different jet clustering algorithms in subsection 5.3.4.

After the *Default* cuts about 0.5% of the energy of a di-jet event are lost, while the energy of the remaining background is approximately 175 GeV. The effect of these additional timing cuts is shown in Figure 5.3, showing an example event overlayed with background events corresponding to 60 bunch crossings before and after the timing cuts.

5.3 Event Generation, Simulation and Reconstruction

The data used in the analysis has to be simulated in several steps. Except for the last, which is the jet reconstruction, all these steps were performed centrally at CERN for all benchmark processes.

In the first step the actual processes on the partonic level are simulated, resulting in events with sets of elementary particles and partons. These partons undergo a process called fragmentation or hadronization, building hadrons out of these partons. This entire step is called event generation (subsection 5.3.1). In a second step cuts based on this generator level information are applied, to reduce significantly the amount of data that has to be processed (subsection 5.3.2). This step is specific to the squark benchmark process. After that the interaction of the generated particles with the detector are simulated, and the detector response is used to reconstruct the individual particles (subsection 5.3.3). Finally the reconstructed particles are used as input for jet finding (subsection 5.3.4).

5.3.1 Event Generation

The event generation (cf. subsection 3.6.1) is done using WHIZARD 1.95 [53, 54].

It calculates the possible processes within the given model along with their corresponding cross sections under consideration of initial and final state radiation, the luminosity spectrum as well as the kinematics of the resulting particles.

The fragmentation of final state particles into jets is done using PYTHIA 6 [55].

5.3.2 Generator Level Cut

This analysis was performed using an integrated luminosity of $\int \mathrm{d}t\mathcal{L} = 2000\,\mathrm{fb}^{-1}$. This corresponds to a total number of over 26 million events for signal and background. Even with the computing grid available, this number of events was too high to be simulated.

Hence a first cut already on generator level information is necessary to reduce the number of events with full detector simulation. As the event signature of the signal contains missing energy, a cut on missing energy or missing transverse momentum $p_{\mathrm{t,miss}}$ is an obvious choice for the background rejection, which is used in the actual analysis, as well. On the generator level the visible transverse momentum is calculated by adding up all contributions of visible particles in the detector acceptance range:

$$p_{t,\mathrm{vis}} = |\vec{p}_{t,\mathrm{vis}}| = \sqrt{\left(\sum_i^{\mathrm{particles}} p_{x,i}\right)^2 + \left(\sum_i^{\mathrm{particles}} p_{y,i}\right)^2} \tag{5.4}$$

The missing transverse momentum points into the opposite direction as the visible transverse momentum, but has the same value. During the actual analysis, which uses full detector simulated data, a cut on the missing transverse momentum of $p_{\mathrm{t,miss}} > 600\,\mathrm{GeV}$ is performed. A similar cut is necessary at the generation level.

process $e^+e^- \to$	number of events for $\mathcal{L} = 2\,\mathrm{ab}^{-1}$ all	$p_{\mathrm{t,miss}} < 330\,\mathrm{GeV}$	$330\,\mathrm{GeV} < p_{\mathrm{t,miss}} < 530\,\mathrm{GeV}$	$530\,\mathrm{GeV} < p_{\mathrm{t,miss}}$
$q\bar{q}$	$6.073 \cdot 10^6$	$(6.072 \pm 0.011) \cdot 10^6$	1381 ± 167	203 ± 64.2
$q\bar{q}e^-e^+$	$6.68 \cdot 10^6$	$(6.68 \pm 0.012) \cdot 10^6$	20.3 ± 20.3	0 ± 0
$q\bar{q}e\nu$	$10.53 \cdot 10^6$	$(10.01 \pm 0.002) \cdot 10^6$	$(362.2 \pm 2.9) \cdot 10^3$	$(155.5 \pm 1.9) \cdot 10^3$
$q\bar{q}\nu\bar{\nu}$	$3.114 \cdot 10^6$	$(2.911 \pm 0.008) \cdot 10^6$	$(153.4 \pm 1.8) \cdot 10^3$	$(48.9 \pm 1) \cdot 10^3$
$\tau^-\tau^+\nu\bar{\nu}$	$249.3 \cdot 10^3$	$(245.6 \pm 2.2) \cdot 10^3$	2971 ± 244	682 ± 117
signal	2947	518.3 ± 87.6	666.4 ± 99.3	1762 ± 162
sum	$26.6 \cdot 10^6$	$25.9 \cdot 10^6$	$521 \cdot 10^3$	$207 \cdot 10^3$

Table 5.4: Number of events for different regions of missing transverse momentum $p_{\mathrm{t,miss}}$ for the different processes. Values are given for an integrated luminosity of $\int \mathrm{d}t\mathcal{L} = 2\,\mathrm{ab}^{-1}$, extrapolated from $\int \mathrm{d}t\mathcal{L} = 100\,\mathrm{fb}^{-1}$.

However, due to finite jet energy resolution the cut on generator level should be smaller. Hence a value of 530 GeV is chosen.

Based on a generation for an integrated luminosity of $\int \mathrm{d}t\mathcal{L} = 100\,\mathrm{fb}^{-1}$, the number of events for each channel for different $p_{\mathrm{t,miss}}$ regions were extrapolated and three cutting regions were chosen: everything with a transverse momentum below 330 GeV is rejected directly after the generation, while everything above 530 GeV is kept. For the intermediate region of $330\,\mathrm{GeV} < p_{\mathrm{t,miss}} < 530\,\mathrm{GeV}$ only 10% of the events are passed on to simulation for later crosschecks. The number of events for the processes within the different cutting regions can be found in Table 5.4.

This reduces the amount of events that need to be simulated to about 250 kEvts, of which 200 kEvts pass the high cut of $p_{\mathrm{t,miss}} > 530\,\mathrm{GeV}$ and are used directly in the analysis while the other 50 kEvts are from the intermediate cutting region.

One can see that the process $e^+e^- \to q\bar{q}e^-e^+$ has no missing transverse momentum above 530 GeV. Hence it can be neglected and is not simulated at all.

Number of Generated Events per Job

Due to technical restrictions on the resources available for a single grid job, the number of events that can be simulated and reconstructed cannot exceed 10 in one job. This restriction does not apply on the generation, however, and subsequent simulation and reconstruction jobs can ignore any surplus of events in the data file. On the other hand the number of events per job should not be lower than 10. Thus the number of events that are generated by WHIZARD has to be big enough that after the cut on the missing transverse momentum it is close to 10. The expected number of events can be calculated if the cut efficiencies are known, which are easy to obtain from the data in Table 5.4.

However, a priori it is not known how many events will pass the transverse momentum cut on an event by event basis, meaning that there is a difference between the expected N_e and the actual N_a number of events after the cut. Hence the number of generated

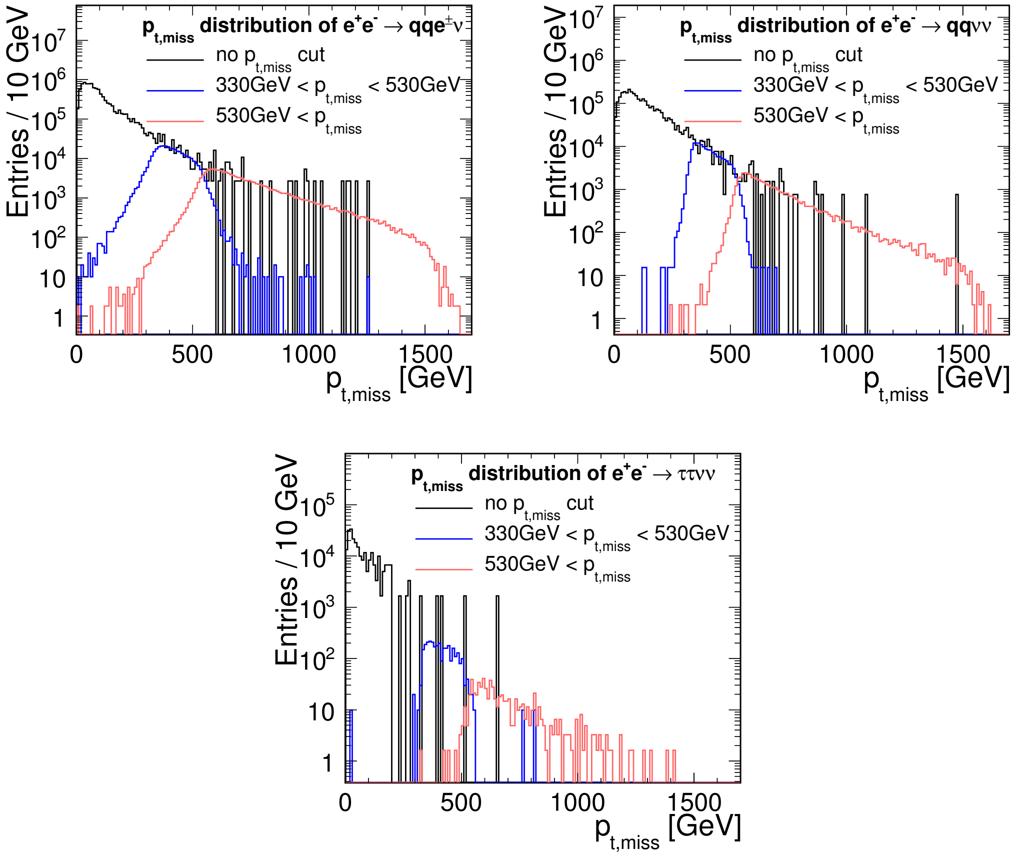

Figure 5.4: The missing p_t distribution after full detector simulation for the background channels $e^+e^- \to q\bar{q}e\nu$ (left), $e^+e^- \to q\bar{q}\nu\nu$ (right) and $e^+e^- \to \tau\tau\nu\nu$ (bottom) scaled to an integrated Luminosity of $\int \mathrm{d}t\mathcal{L} = 2000\,\mathrm{fb}^{-1}$. The black histogram shows the distribution without the generator level cut but with low statistics and high weighting factors. The red and blue distributions were created with a generator level cut of $330\,\mathrm{GeV} < p_t < 530\,\mathrm{GeV}$ (blue) and $530\,\mathrm{GeV} < p_t$ (red) and small weighting factors.

events per job needs to be increased. Assuming a Possionian distribution yields that an increase of the generated events by 80% leads to 99% of all jobs having at least 10 events after the generator level cut.

Applying this requirement to the process $\mathrm{e}^+\mathrm{e}^- \to q\bar{q}$ would mean the generation of more than 500 kEvts per job. This is too much even for generator jobs. However, the contribution of this process to the background is small, as after the initial missing p_t cut already a signal to noise ratio of about 15:1 is achieved, which is far better than for any of the other considered background processes. Any additional background rejection will increase this value significantly. Thus it is save to ignore this background channel.

Crosscheck of Transverse Momentum Cut

The cut on missing transverse momentum was done on generator level using all available information of the particles. This corresponds to assuming a perfect detection and reconstruction of the particles by the detector and the software, which is obviously not the case. Consequently a cut on 530 GeV on generator level can through smearing and other not considered effects still result in events with a higher missing transverse momentum after the reconstruction, or vice versa. This was checked by comparing the missing momentum distribution for the two cut regions with a full detector simulation without cuts. For the latter only a few thousand events for each of the background channels were generated. The $p_{\mathrm{t,miss}}$ distribution for all three cases is created, while it is being scaled to a full luminosity of $\int \mathrm{d}t\mathcal{L} = 2000\,\mathrm{fb}^{-1}$ by applying weight factors to each event when filling the histogram. Figure 5.4 shows the resulting distributions of the (missing) transverse momenta for the three channels $q\overline{q}e\nu$, $q\overline{q}\nu\overline{\nu}$ and $\tau^-\tau^+\nu\overline{\nu}$. The black curve shows the simulation without generator level cut, but with large weighting factors greater than 10^3, while the blue and the red curve show the two regions with generator level cut and significantly smaller weighting factors. The overall $p_{\mathrm{t,miss}}$ distribution can be seen and is smoothly created out of the three components, showing the success of the generator level cut.

As it will be shown in section 5.5, the first step of background rejection is a cut on the transverse momentum of 600 GeV. Thus, the intermediate cut region of $330\,\mathrm{GeV} < p_{\mathrm{t,miss}} < 530\,\mathrm{GeV}$ can be neglected for the analysis, as - with very few exceptions - it does not generate events with a higher missing transverse momentum.

5.3.3 Simulation and Event Reconstruction

Detector Simulation

The second step in the simulation chain is the simulation of the detector response to the created particles. This is done using MOKKA, which is based on the GEANT4 framework (see subsection 3.6.2). The result is a detailed information of the flight path of all particles and the corresponding energy depositions in the different active detector materials, and is written into LCIO [74] files. The geometry model used was the CLIC_ILD model, which is based on the International Large Detector (ILD) [33] and is described in detail in subsection 3.4.4 and [75].

Further on, the detector response itself is simulated by converting the deposited energy into signals of simulated electronics. This step is called digitization and is performed with MARLIN in the ILC software framework [76].

The beam induced background of $\gamma\gamma \to$ hadrons is simulated independently. Background corresponding to a total of 60 bunch crossings is overlayed over each actual physics event in this step, assuming the physics event is in the 10th bunch crossing.

Reconstruction and Particle Flow

The reconstruction, like the digitization, is performed in the MARLIN framework. Its main step consists of pattern recognition and track finding for the TPC and the silicon detectors, as well as merging the resulting tracks were applicable.

This data is used as input for the particle flow algorithm (cf. subsection 3.4.3), which tries to reconstructs all visible particles from the detector response. Here the new version of PandoraPFA is used [77], which is a reimplementation of [37].

5.3.4 Jet Clustering

As it was discussed in subsection 3.4.3, final state quarks and gluons will undergo a process called fragmentation. During this process the final state particle will create a variety of different particles, which altogether are called a jet. Thus, by this process, which is caused by the confinement property of the strong force, the two high energetic quarks in the final state of the signal process $e^+e^- \to q\bar{q}\widetilde{\chi}_1^0\widetilde{\chi}_1^0$, too, will lead to the creation of two high energetic jets.

The tau on the other hand is, unlike the quark and the gluon, a lepton and hence cannot hadronize through the strong interaction. Nevertheless, it has different decay modes, some of which result in final states with one or multiple hadrons. For highly energetic τs this results in low-multiplicity jets.

The identification of jets is done with jet finders. The most important feature of a jet algorithm is that it needs to be both collinear and infrared safe. The former describes the insensitivity of the result of an algorithm to a collinear split (i.e. decay) of a particle, while the latter describes the insensitivity of the algorithm against the addition of extremely low energetic (infrared) particles to the event. If these conditions are not met, the divergent loop corrections of the corresponding Feynman diagrams, which would normally cancel, are not taken properly into account, leading to a disagreement between theory prediction and measurement.

Jet Algorithms

There are several different approaches and algorithms for the jet identification, which can be separated into two main types. The first one is a geometrical (top-down) approach in which cones of a fixed size are set and rotated in the detector in such a way, that they contain a (local) maximum of particles. The other one, a bottom-up approach, is the recursive recombination of the particles into pseudo-particles, based on pair-wise distance between two particles. The distance is based on a algorithm specific function and does not need to be related to the true geometrical particle distance. This recombination of (pseudo-) particles can either be stopped at a certain number of identified pseudo-particles which are then defined as jets, or if the minimal (maximal) distance between two jets is above (below) a prior set threshold. For more details see [78].

In the present study, the FastJet library was used [79], which provides a variety of different collinear and infrared-safe algorithms.

A key challenge of the event reconstruction is the beam induced background of $\gamma\gamma \to$ hadrons. Large parts of the background can be rejected using tight timing and p_t cuts. Still, a significant part of the reconstructed event energy is originating from this background, causing potential systematic effects on the squark mass measurement if this background is picked up by the jet finder. This can be largely avoided by using appropriate exclusive jet finders.

In contrast to the inclusive jet finding algorithms which include every reconstructed particle, exclusive jet algorithms introduce *beam-jets* which are excluded from the reconstruction. These algorithms were originally designed for the use at hadron colliders, where the remnants of the colliding protons fly in the very forward region and do not contribute to the process. As the $\gamma\gamma \to$ hadrons background peaks in the forward region, too, the exclusive jet algorithms are a natural choice for the background rejection. On top of that they offer the possibility to cluster an event into a predefined number of jets, a feature which is useful especially at lepton colliders with a clear event structure.

The k_t Algorithm

The exclusive jet algorithms implemented in the FastJet library are two variants of the k_t-algorithm, which are optimized for electron-positron and for hadron colliders respectively. The k_t algorithm is a recombination algorithm which recursively merges particles pair-wise based on a distance function d_{ij} between two particles. The distance to the beam-jets $d_{i\mathrm{B}}$ of a particle i is taken into account as well. Recursively the distances of each particle to the beam-jet as well as the pair-wise distance between all particles is evaluated. The pair of particles (or the particle and the beam) with the minimal distance are merged into a new pseudo particle. This process is repeated until the number of pseudo particles, i.e. jets, is at a predefined number, which is 2 in our case. The exact definition of the distance d_{ij} and $d_{i\mathrm{B}}$ marks the difference between the two variants and has a strong influence on the susceptibility to the $\gamma\gamma \to$ hadrons background.

The electron-positron variant is called `ee_kt_algorithm`. It uses the energy E and the angle θ between the two particles for its distance definition:

$$d_{ij,\mathrm{ee}} = \min(E_i^2, E_j^2)(1 - \cos\Delta\theta_{ij}) \tag{5.5}$$

$$d_{i\mathrm{B},\mathrm{ee}} = E_i^2 \tag{5.6}$$

Both E and θ are defined in the center-of-mass-system (CMS) of the collision. In hadron collisions, however, the CMS typically is boosted along the z-axis with an unknown magnitude. Hence a different definition of the distance function d_{ij} is used at hadron colliders. The hadron variant of the algorithm, called `kt_algorithm`, relies on for hadron collider typical transverse observables, replacing the energy by k_t, and the angle by the boost-invariant pseudorapidity η and the azimuthal angle ϕ:

$$d_{ij,\mathrm{hadr}} = \min(k_{t,i}^2, k_{t,j}^2)\frac{\Delta\eta_{ij}^2 + \Delta\phi_{ij}^2}{R^2} \tag{5.7}$$

$$d_{i\mathrm{B},\mathrm{hadr}} = k_{t,i}^2 \tag{5.8}$$

The radius R (measured in η, ϕ) is a user adjustable parameter influencing the size of the jets. Especially in the case of forcing an event into a fixed number of jets, this parameter R controls the size and thus the amount of particles included in the jets and, as a consequence, the amount of particles rejected as background. The big advantage

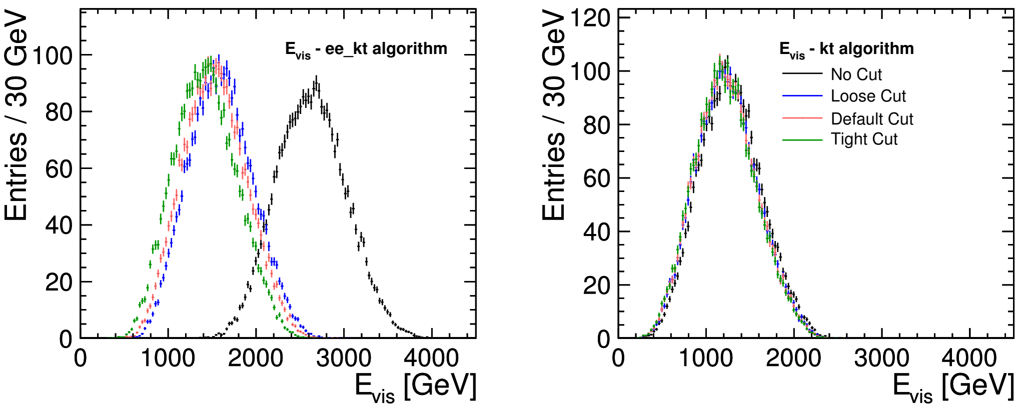

Figure 5.5: The visible energy $E_{\mathrm{vis}} = E_{\mathrm{Jet1}} + E_{\mathrm{Jet2}}$ for the four different timing cuts *Tight*, *Default*, *Loose* and *No Cut*. The electron-positron variant of the k_t - algorithm (left) picks up significantly more of the $\gamma\gamma \to$ hadrons pile up, while the hadron variant of the k_t - algorithm (right) is almost insensitive to this background.

of this metric is the use of the pseudo rapidity, which stretches the distance between particles in the forward region. As the beam induced background peaks in the forward region, the hadron variant of the algorithm can help rejecting this background, making it the optimal choice in the case of the electron positron collider CLIC. Following the studies performed in the scope of this thesis, presented in detail in the following, the k_t-algorithm was adopted as default jet finder for CLIC as well as for the ILC studies when including background.

Performance Comparison

The performance of the `ee_kt_algorithm` and the `kt_algorithm` is evaluated by comparing their susceptibility to beam induced background of $\gamma\gamma \to$ hadrons. As already discussed in subsection 5.2.3, this background is reduced in the event reconstruction by the three increasingly stringent timing cuts *Loose*, *Default* and *Tight*. These cuts are applied on signal data including the usual background from $\gamma\gamma \to$ hadrons equivalent to 60 bunch crossings. Both variants of the k_t algorithm are applied to these three data sets and, in addition, on a set without any timing cut. The latter one is an unrealistic scenario to enhance any effects of the algorithm on the background rejection. Both algorithms are used in exclusive mode, clustering to exactly two jets. The `kt_algorithm` has the radius R set to 0.7, which is the same setting used in the actual analysis.

Figure 5.5 shows the visible energy of the two jets $E_{\mathrm{vis}} = E_{\mathrm{Jet1}} + E_{\mathrm{Jet2}}$ for the four different data sets for both k_t variants. One can see that the `ee_kt_algorithm` is indeed very sensitive to this beam induced background. The distribution of the visible energy E_{vis} shifts clearly for the different cuts, and it includes almost the entire energy of 1.4 TeV caused by the additional 60 bunch crossings in the case without timing cuts. The hadron variant, on the other hand, is much more stable against this overlayed background. While there is almost no difference visible for the three different cut values, even the additional 1.4 TeV for the unrealistic case without any timing cuts do not shift the distribution significantly. Thus, the `kt_algorithm` is used throughout this analysis.

Jet Clustering in the Analysis and other Jet Algorithms

In the present analysis the exclusive mode k_t algorithm `kt_algorithm` of the FASTJET library with $R = 0.7$ is used. The exclusive mode of the `kt_algorithm` supports two clustering termination conditions:

1. The maximum pair-wise distance $d_{i,j}$ between all particles is higher than a previously set distance $d_{cut} > \max(d_{i,j})$.
2. The number of pseudo-particles (jets) $N_{\text{jets,evt}}$ reaches a previously set value $N_{\text{jets,cut}} = N_{\text{jets,evt}}$. Events with a higher number of jets are identified after the clustering via the distance $d_{n,n+1} = d_{2,3}$ at which the transition from a two jet event to a three jet event takes place. The value of $d_{2,3}$ is larger for real 3-jet events than for real 2-jet events.

In the present case the signal process contains two quarks in the final state. Hence, the jet clustering should result in events with two jets for the signal. For a cut based analysis of such a case the two termination conditions described above are equivalent. For the first approach all events with more than two jets for a given d_{cut} are rejected, while the second approach will first cluster all events to two jets before rejecting higher multiplicity jet events by comparing $d_{2,3}$ with d_{cut}. The fine tuning of the correct d_{cut} value is an essential step for such an analysis. The first approach has the disadvantage that it requires the entire dataset to be reprocessed for each new value of d_{cut}. This is not necessary in the second approach, as $d_{2,3}$ has already been calculated for all events. Additionally the latter can be used for a multi-variate based background rejection using $d_{2,3}$ as one amongst many other input variables, as well, whereas the former can only be used in a cut-based analysis.

Other algorithms, like the inclusive anti-k_t or the SISCone [80] algorithm, which are both available in FASTJET, were tested as well. They, too, make use of the pseudo rapidity in their metric and consequently outperform the `ee_kt_algorithm`. But as they are inclusive, they do include the particles from the beam induced background, creating additional jets. Thus the number of created jets cannot be fixed and the parameters have to be found to get the correct number of jets for the majority of the events. Taking only the two most energetic jets as signal and rejecting the remaining, lower energetic jets proved to be a viable solution. Their initial performance, however, was not as good as the one of the `kt_algorithm`. It is expected to get similar results for the anti-k_t and the SISCone algorithm as for the hadronic k_t by intensive tuning of the jet algorithm parameters, especially the d_{cut} value. However, this would require several iterations of jet clustering and assessing the quality of the result. Despite the other algorithms being expected to perform equally well, the hadron k_t jet clustering algorithm had several additional advantages:

- The exclusive mode directly rejects beam induced $\gamma\gamma \rightarrow$ hadrons background through beam jets.
- The number of jets can be fixed to be always exactly 2. Consequently no events are dropped during the clustering, thus increasing the statistics.
- Identification of non-squark background events with more than 2 jets can be done after the clustering using the $d_{2,3}$ parameter, getting rid of the time consuming reclustering after a change of the parameters. This can be done by:
  - cutting on the $d_{2,3}$ value, which is identical to clustering the events with a previously set d_{cut} value and rejecting events with more than 2 jets.
  - using the $d_{2,3}$ parameter as one of many input observables to a multi variate classifier to identify background events. In this approach background events are not solely classified by their number of jets, but by including the full event information, allowing a more effective and finer distinction between signal and background.

Because of these points the exclusive hadron k_t algorithm (`kt_algorithm`) in FASTJET was used with a radius of $R = 0.7$. The background rejection was done by using the $d_{2,3}$ value as one of the inputs to the Boosted Decision Trees and will be explained in detail in section 5.5.

5.4 Squark Mass Measurement Techniques

After the reconstruction of the signal events, the actual squark masses have to be reconstructed from the data. Specifically for the present analysis with two squarks decaying to two jets and two neutralinos several methods were investigated in [81].

One of these is the distribution of jet energies which in its original form has a rectangular shape with a minimal and maximal entry of jet energies. By identifying the edges of this so called box distribution both the squark mass and the neutralino mass can be extracted. However, the shape of the box is distorted by initial state radiation, the luminosity spectrum and smearing through detector resolution. Hence the borders of the box distribution are not well defined. Furthermore standard model background especially in the low energy region makes the edge identification even harder, rendering precision measurements impossible in the squark channel.

Instead one can assume that the lightest neutralino $\widetilde{\chi}_1^0$ can be measured with better accuracy in other channels such as the production and decay of sleptons as it was shown in another CDR benchmark process [82], where the usage of the box distribution was indeed possible. As a consequence the estimation of a single edge instead of two is sufficient for the squark mass extraction.

Due to the initial state radiation and the luminosity spectrum the center of mass energy at CLIC has a tail to low energies, which directly influences the maximum energy of the jets and hence the edge and with it the squark mass measurement. This situation is even more extreme at hadron colliders where the center of mass energy

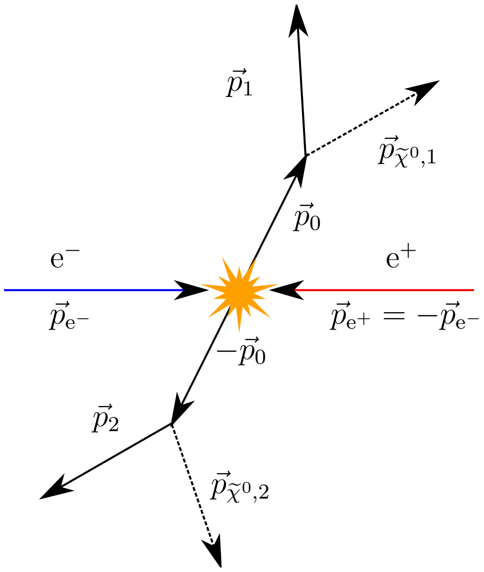

Figure 5.6: Diagram of the momenta of two particles which are created back-to-back in the reference frame of the collision, before they each decay into an invisible neutralino and a visible jet.

of a collision is not well defined. One of the variables developed for such conditions is called M_C [83]. It is intended for the mass measurement of heavy particles which are produced in pairs back-to-back in the center-of-mass system of the collision. Both particles decay into a visible and an invisible particle (cf. Figure 5.6). In its original form M_C was constructed purely from transverse information as M_{CT}, as it is common for hadron colliders. As the events at a lepton collider provide additional information, the observable was slightly adjusted.

M_C is the invariant mass constructed by the four vector of one quark (jet) $p_1 = (E_1, \vec{p}_1)$, and the parity transformed four vector of the other quark (jet) $\mathcal{P}(p_2)$. The big advantage of this observable is that it is insensitive to contra linear boosts of equal magnitude of the two squarks. As these are always created in pairs flying back to back in their reference frame, M_C is independent of the center of mass energy.

Neglecting the mass of standard model quarks, M_C is defined as:

$$\begin{aligned} M_C^2 &= (E_1 + E_2)^2 - (\vec{p}_1 - \vec{p}_2)^2 \\ &= 2(E_1 E_2 + \vec{p}_1 \vec{p}_2) \end{aligned} \tag{5.9}$$

Its distribution is bound from above by:

$$M_C^{max} = \frac{m_{\tilde{q}_r}^2 - m_{\tilde{\chi}_1^0}^2}{m_{\tilde{q}_r}} \tag{5.10}$$

If the mass of the neutralino $m_{\tilde{\chi}_1^0}$ is known, the squark mass $m_{\tilde{q}_r}$ can be calculated:

$$m_{\tilde{q}_r} = \frac{1}{2}\left(M_C^{max} + \sqrt{(M_C^{max})^2 + 4m_{\tilde{\chi}_1^0}^2}\right) \tag{5.11}$$

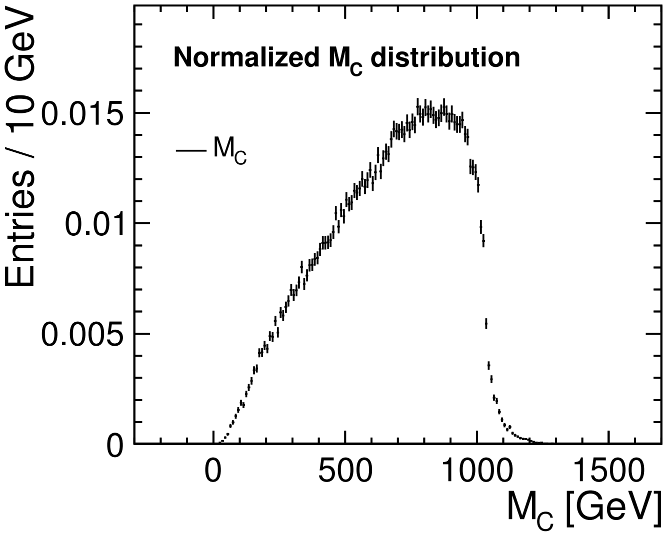

Figure 5.7: The M_C distribution including effects by the luminosity spectrum.

The triangle shaped distribution of M_C including effects due to the luminosity spectrum but without the simulation of the detector response can be seen in Figure 5.7. Here as well as for the distribution of the jet energies (box distribution) the upper edge M_C^{max} is not well defined. The smearing of the edge is caused partly by a finite detector resolution on the one hand. On the other hand initial state radiation and the luminosity spectrum of the machine spoil the implicit assumption that the center-of-mass frame is at rest in the laboratory frame. However, the boost of the center-of-mass frame with respect to the laboratory frame is small in most cases. Hence, still the full information as opposed to just the transverse information of the event is used.

Instead of having to find a reliable definition on how to extract M_C^{max} from the smeared distribution, in this analysis a different approach was followed. For the squark mass estimation a template method was chosen, creating several M_C distributions each for different known values of the squark masses and comparing these to the measurement. This technique has the advantage that the entire distribution contributes to the measurement instead of just the upper edge. Hence a higher sensitivity is expected for the template method, of which details will be discussed in section 5.6.

5.5 Background Rejection

Before the squark mass can actually be extracted from the data, the large number of physics background events has to be rejected. This is the most challenging part of the presented analysis, because as shown in subsection 5.2.2, the combined cross section of the three main background processes, $q\bar{q}\nu\bar{\nu}$, $q\bar{q}e\nu$ and $\tau^-\tau^+\nu\bar{\nu}$ is more than three orders of magnitude higher than the one of right handed squarks. As the squark mass

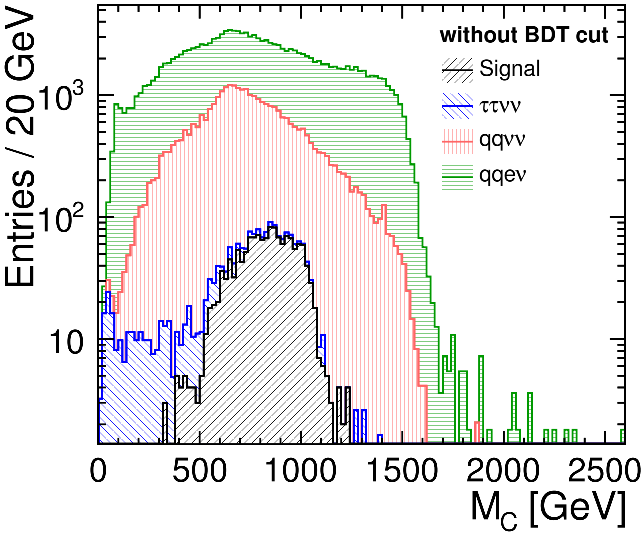

Figure 5.8: The M_C distribution stacked with all considered backgrounds after a simple $p_t > 600\,\mathrm{GeV}$ cut is applied.

extraction requires a high signal purity, especially in the region of the kinematic edge, it is crucial to obtain a background rejection of about four orders of magnitude, while preserving a substantial amount fraction of the signal events.

Due to the high amount of missing energy, a first cut on the missing transverse momentum of $p_{\mathrm{t,miss}} > 600\,\mathrm{GeV}$ is performed, reducing the number of events of the dominating background channels to 10^{-2}, in the case of the $\tau^-\tau^+\nu\overline{\nu}$ final state even to 10^{-3} of their original values. The signal is reduced by the cut to 48.5%.

This cut on missing transverse momentum was chosen because of its efficiency on the one hand. On the other hand it was necessary in order to keep the analysis consistent with the generator level cut, which was necessary as technical reasons limited the maximum number of simulated events. As shown in subsection 5.3.2, the generator level cut, too, works on the missing transverse momentum. However, due to finite detector and reconstruction resolution the cut performed on the fully simulated and reconstructed data has to be stronger than the one on generator level. In the present case the generator level cut requires a missing transverse momentum of $p_{\mathrm{t,miss,gen}} > 530\,\mathrm{GeV}$, while in the analysis a stronger cut on the missing transverse momentum of $p_{\mathrm{t,miss,reco}} > 600\,\mathrm{GeV}$ is used.

The effect of this cut on the M_C distribution is shown in Figure 5.8. Clearly additional background rejection is necessary, which is performed by using Boosted Decision Trees.

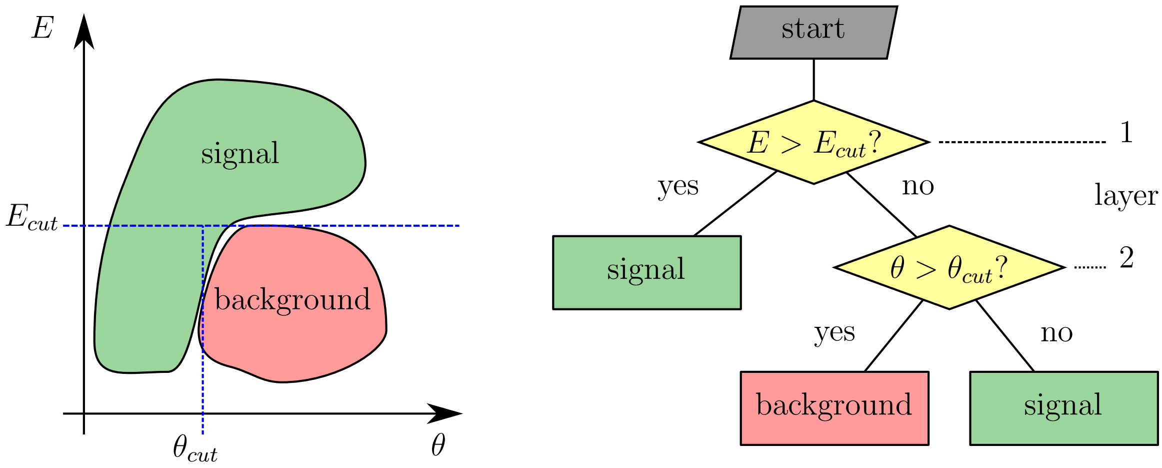

Figure 5.9: An example of a decision tree with a depth of two layers to separate signal from background for a case with two observable E and θ.

5.5.1 Boosted Decision Trees

Decision trees are a well established classification tool and a part of the Toolkit for Multi Variate Analysis TMVA [84], which was used in this analysis.

A decision tree is a binary tree of nodes, i.e. starting with a single node in the first layer each node may either contain the desired classification response (either signal or background), or have exactly two daughter nodes in the subsequent layer. In the latter case each node "decides" which of its two daughters is the correct one for the given event based on an internal threshold of a single event variable. This means that each node splits the phase space into two regions based on that threshold using rectangular cuts, and the complete tree can select hypercubes from the phase space and classify them as either signal or background.

An example of a decision tree is shown in Figure 5.9. It shows a case with two observables E and θ in which signal and background are distributed as shown in the left side of the plot. Such a case cannot be solved with simple rectangular cuts without losing a significant amount of signal. The corresponding decision tree shown on the right side, however, is able to classify a given event into signal and background with very high efficiency.

Before a decision tree can be used it first needs to be build up, or "grown". As with most multi-variate analysis techniques this is done with training data, i.e. data for which the distinction between signal and background is already known. The growing is done node-by-node. At each node creation step the best cut for discriminating signal from background from all available observables is chosen. In case of TMVA this is achieved by creating `nCuts` cut values for each observable choosing the one with the lowest misclassification error, which is defined as

$$\text{missclassification error} = 1 - \max(p, 1-p) \tag{5.12}$$

$$p = \frac{\#\text{ signal events}}{\#\text{ total events}}$$

with p being the purity of the sample for the given cut. This cut selection is equivalent to choosing the cut with the highest or lowest signal purity. Using the cut the node divides the given data into two branches of leaf nodes for both of which this step is repeated and further nodes are grown. The splitting of a leaf node stops if either the number of events at the node is lower than the TMVA parameter `nEventsMin` or the maximum number of layers `MaxDepth` is reached. In that case the leaf node is classified based on its signal purity as either signal (+1) or background (-1).

The classification power of a single tree is of course limited. Already in the artificial example of Figure 5.9 not the entire signal could be separated from the background. Hence a decision tree is called a weak learner which by itself has only limited discrimination power. This restriction is overcome by boosting.

Boosting

Boosting is the process of converting a weak learner like a decision tree into a strong learner with higher discrimination power by creating a set of weak learners and use their majority vote.

For this analysis the AdaBoost algorithm [85], which is short for adaptive boosting, was used through TMVA. A good description can also be found in [86].

The basic principle is that a total of T decision trees are built over several rounds $t = 1 \ldots T$. A weighting factor $D_t(x_i)$ is assigned to each individual event $x_i \in \{x_1, \ldots, x_N\}$. These weights are considered when building the variable distributions which are used as input for the cut evaluation when creating a node. The idea is that the weighting factor is increased (decreased) for wrongly (correctly) classified events, such that the tree which is build in the subsequent round focuses on the misclassified events.

For the first round all events start with the same event weight, which is always normalized in such a way that the sum all weights is 1:

$$D_1(x_i) = \frac{1}{N} \; \forall \, x_i. \tag{5.13}$$

In each round t a single decision tree is built under consideration of the event weight. Typically some events are wrongly classified by this decision tree. The classification error ϵ_t of this tree (which is not to be confused with the misclassification error from above) is then the sum of all weights of all misclassified events:

$$\epsilon_t = \sum_{\text{misclassified } x_i} D_t x_i. \tag{5.14}$$

Based on this classification error a boosting parameter α_t is calculated, which is used to adapt the weighting factors for the next round:

$$\alpha_t = \frac{1}{2}\ln(\frac{1-\epsilon_t}{\epsilon_t}) \tag{5.15}$$

$$D_{t+1}(x_i) = \frac{D_t(x_i)}{Z_t} \times \begin{cases} e^{-\alpha_t} & \text{if } x_i \text{ correctly classified} \\ e^{\alpha_t} & \text{if } x_i \text{ incorrectly classified} \end{cases} \tag{5.16}$$

where Z_t is a normalization factor. The event weighting factors are increased for misclassified events, giving them a stronger consideration when building the next tree.

This boosting step is repeated until a forest of T trees is created. Each tree assigns $+1$ or -1 for signal and background respectively and is weighted by its classification error ϵ_t. The classification response of the forest of Boosted Decision Trees to an event is the weighted mean ("majority vote") of all trees. This response is called BDT.

Boosted decision trees have the advantage that they rely on simple cuts and yet are able to perform cuts in higher dimensions, giving a significant improvement of the classification performance over simple rectangular cuts. In addition they are not sensitive when including observables with small or no relevance to the rejection, as during growing the most significant observable is chosen every time. However, statistical fluctuations of the training sample can lead to the growing of decision nodes specific to these fluctuations. This is called overfitting or overtraining and has a negative influence on the classification performance. This can be checked by applying the Boosted Decision Trees on a statistical independent testing sample, for which the classification in signal and background is already known as well. If the distribution of the response for the training sample differs from the one for the testing sample, the trees were indeed overtrained.

5.5.2 Application to the Squark Benchmark

Boosted Decision Tree Construction

The Boosted Decision Trees were used for the background rejection in the squark Benchmark. The exact list of parameters used for the training of the Boosted Decision Trees can be seen in Appendix C.1.

In order not to introduce a bias, the data sample used for the analysis needs to be statistically independent from the one used for the training and validation of the Boosted Decision Trees. Hence the available dataset was splitted into two groups of equal size: One analysis sample and one training and testing sample. As the Boosted Decision Trees need to be validated after their training, the training and testing sample was again divided into two equal parts. The first one was used for the training, i.e. growing of the trees, the second part for the tests, such as checking against overtraining.

As a consequence of having these statistical independent samples for analysis and test and training, the total amount of needed events is doubled to an equivalent of $\int \mathrm{d}t\mathcal{L} = 4000\,\mathrm{fb}^{-1}$. However, this amount of data was not available at the time of the analysis for all processes. Instead the available data was divided and event weighting

process	# simulated events	# events for $\mathcal{L} = 2\,\mathrm{ab}^{-1}$	weight
$\mathrm{e}^+\mathrm{e}^- \rightarrow q\overline{q}\mathrm{e}\nu$	62267	112434.3	1.81
$\mathrm{e}^+\mathrm{e}^- \rightarrow q\overline{q}\nu\overline{\nu}$	14989	31021.8	2.07
$\mathrm{e}^+\mathrm{e}^- \rightarrow \tau^-\tau^+\nu\overline{\nu}$	278	451.4	1.62
$\mathrm{e}^+\mathrm{e}^- \rightarrow \widetilde{q}_r\overline{\widetilde{q}}_r$	1461	1460.9	1.00

Table 5.5: The number of events that were simulated, the number of events which are needed for a Luminosity of $\mathcal{L} = 2\,\mathrm{ab}^{-1}$ (both after the cut $p_t > 600\,\mathrm{GeV}$) and the corresponding weighting factors. These numbers are taken from the training and testing sample (see text for details). The analysis sample has very similar numbers.

was used, based on the available statistics for the corresponding channel. The resulting weights are shown in Table 5.5.

The events were classified using a total of 18 different observables. A short list is in Table 5.6. It includes observables of the two jets, like their angle towards the beam axis, which differed for signal and background as unlike the signal some of the physics background processes are produced via a t-channel which tend to peak in forward (backward) region. Another powerful discriminator is the energy and the ID of the leading (i.e. most energetic) particle in the jets. This is extremely dependent on the Particle Flow Algorithm performance. The list includes the jet distances in the form of $y_{n,n+1} = d_{n,n+1}/E^2_{vis}$, as well, to identify events which differ from the expected 2-jet shape. Some jet independent variables like the energy of the highest energetic lepton are included, too. The distributions of all variables can be found in Appendix C.1.

Cut Value Estimation and Overtraining Cross Check

Possible overtraining was checked by comparing the BDT distributions obtained for the training and the testing sample with a Kolmogorov-Smirnoff test, which gives the probability that two sets of events originate from the same underlying distribution. For the signal (background) the result of the comparison is 41.2% (75.8%), giving a slight, but negligible indication of overtraining.

The response of the Boosted Decision Trees to the four processes $q\overline{q}\mathrm{e}\nu$ (green), $q\overline{q}\nu\overline{\nu}$ (red), $\tau^-\tau^+\nu\overline{\nu}$ (blue) and the signal (black) of the test sample are shown as a stacked histogram in Figure 5.10(a). Clearly the signal can be separated to a large extend from the background. The optimal cut value on the response of the Boosted Decision Trees is determined based on the signal significance $S/\sqrt{S+B}$, all of which are displayed in Figure 5.10(b). The highest significance is achieved for a cut of BDT > -0.066, which is indicated as a dashed line in both figures. The corresponding significance for the training sample is $S/\sqrt{S+B} = 25.9$ and $S/\sqrt{S+B} = 25.7$ for testing sample. The good agreement of these two values shows that potential overtraining effects are negligible.

Variable	Description
`Accoplan_jet12`	The accoplanarity between the two jets
`E_max_lepton`	The energy of the Lepton with the highest energy
`E1`	The energy of the jet with the higher energy
`E2`	The energy of the jet with the lower energy
`M_inv_jet1`	The invariant mass of the jet with the higher energy
`M_inv_jet2`	The invariant mass of the jet with the lower energy
`NParJet12Ratio`	The ratio of the number of particles between the two jets
`pt_miss`	Missing p_t in the event after jet clustering
`N_lepton`	Number of leptons
`N_par`	Number of particles
`cosTheta1`	$\cos\theta$ for the jet with the higher energy
`cosTheta2`	$\cos\theta$ for the jet with the lower energy
`leadParE1`	Energy of the leading particle for the jet with the higher energy
`leadParE2`	Energy of the leading particle for the jet with the lower energy
`leadParID1`	ID of the leading particle for the jet with the higher energy
`leadParID2`	ID of the leading particle for the jet with the lower energy
`y_cut_high`	Distance at which the jet finder would find 3 instead of 2 jets
`y_cut_low`	Distance at which the jet finder would find 1 instead of 2 jets

Table 5.6: List of input variables used for the training and the classification of the events with the Boosted Decision Trees.

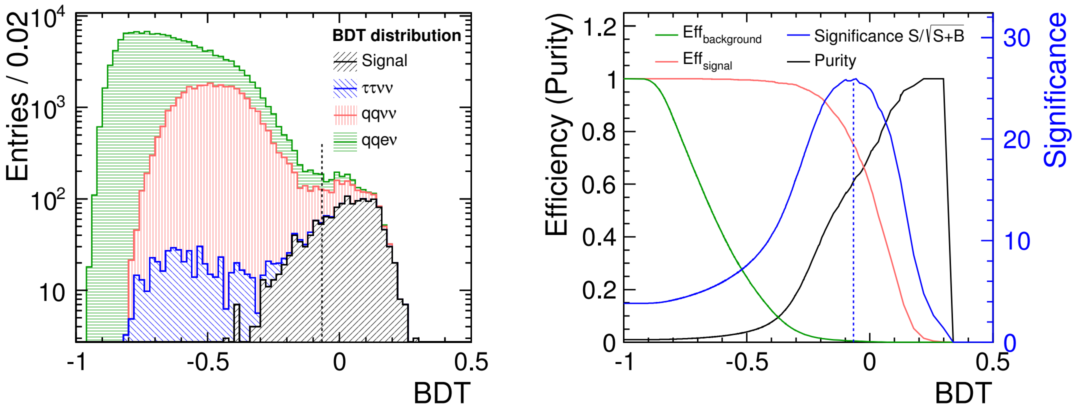

(a) Stacked BDT Distribution

(b) BDT Significance and Efficencies

Figure 5.10: The left plot shows the stacked output of the Boosted Decision Trees BDT for signal and background. The cut value of BDT > -0.066 providing maximal significance is indicated with the dashed black line. The right histogram shows the efficiencies for signal and background as well as the significance for different cut values.

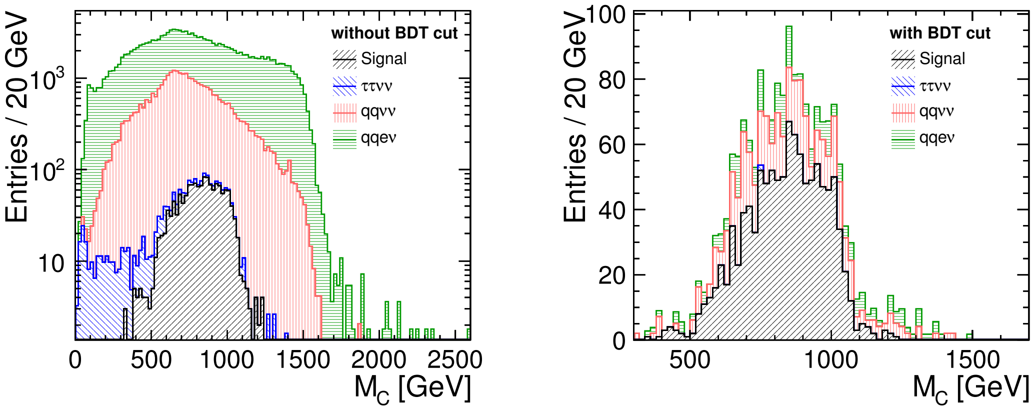

(a) $p_t > 600$ GeV

(b) $p_t > 600$ GeV and BDT Cut

Figure 5.11: The M_C distribution stacked with all considered backgrounds. In the left plot only a simple $p_t > 600\,\mathrm{GeV}$ cut is applied, while the right plot shows the distribution after an additional cut on the output of the Boosted Decision Trees of $BDT > -0.066$.

Background Rejection and Cut Efficiency

The effect of the application of the background rejection with the Boosted Decision Trees and a cut value of BDT > -0.066 is illustrated in Figure 5.11, showing the M_C distribution once after the cut on the transverse momentum, and once after the $p_{\mathrm{t,miss}}$ and the BDT cut.

The overall cut efficiency of the transverse momentum cut and Boosted Decision Tree selection needs to be known for the cross section measurement. It was obtained from an independent high statistics sample with a corresponding integrated luminosity of $\int \mathrm{d}t\mathcal{L} = 19\,\mathrm{ab}^{-1}$. The result is $\epsilon = 0.362$, which is in good agreement with the cut efficiency of the BDT as shown in Figure 5.10 combined with the extrapolated cut efficiency for the transverse momentum cut from Table 5.4.

Figure 5.12 shows the effect on the pure signal M_C distribution. While the upper edge of the distribution is not altered, the tail towards lower energies is significantly reduced. This originates primarily from the cut on $p_{\mathrm{t,miss}}$, which precludes low M_C values.

5.5.3 Purity and Background Fit

The combination of the cut on the transverse momentum and the Boosted Decision Trees very effectively rejected the standard model background considered in this analysis. Still a non-negligible background contribution remained as illustrated in Figure 5.13, showing the stacked M_C distribution with signal and remaining background. The overall purity of the distribution is 0.613.

Both for the squark mass extraction and especially for the cross section measurement

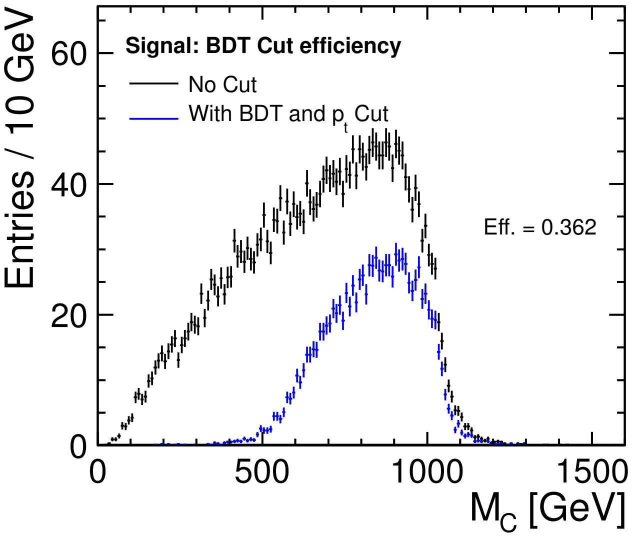

Figure 5.12: The M_C distribution before and after the background rejection cuts for pure Squark events.

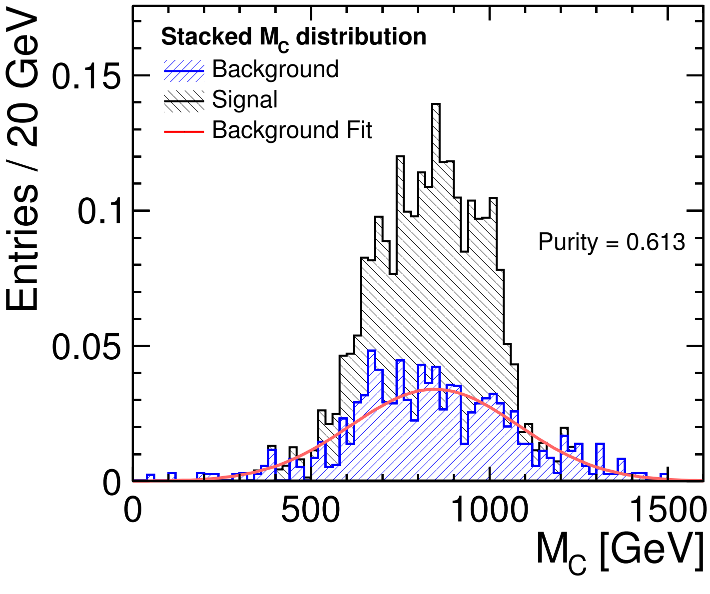

Figure 5.13: The M_C distribution after background rejection cuts divided into the signal and background parts. The background was fitted with a simple Gaussian.

the removal of this remaining background contribution is essential. Consequently this background was parametrized with a simple Gaussian from the testing sample as indicated in red in Figure 5.13. This parametrization was subtracted from the M_C distribution of the analysis sample prior to the squark mass and cross section estimation.

5.6 Squark Mass Measurement

As already discussed in section 5.4, one way to extract the squark masses from the M_C distribution is to use its upper bound M_C^{max} and calculate the squark mass according to Equation 5.11. However, the M_C distribution is smeared through jet energy resolution, luminosity spectrum and initial state radiation leading to an ill-defined upper edge.

Instead a template fit method was chosen, in which a set of M_C distributions are generated, each for a different squark mass. These distributions are compared to the M_C distribution obtained from the analysis. This template fit has the advantage that during the generation of the templates all of the effects mentioned above can easily be included. Furthermore instead of just using the upper edge, as it would be the case for the M_C^{max} technique, the entire M_C distribution is used during the template fit, although here, too, the upper edge is the driving factor. As a consequence it is to be expected to provide smaller statistical errors and higher stability against remaining background contributions and statistical fluctuations than the M_C^{max} technique.

5.6.1 Template Generation

In the SUSY model used for the present analysis, the mass $m_{\widetilde{\mathrm{u}}}$ of the up- ($\widetilde{\mathrm{u}}_\mathrm{r}, \widetilde{\mathrm{c}}_\mathrm{r}$) and the mass $m_{\widetilde{\mathrm{d}}}$ of the down-type ($\widetilde{\mathrm{d}}_\mathrm{r}, \widetilde{\mathrm{s}}_\mathrm{r}$) right handed squarks differ by approximately 10 GeV:

$$m_{\widetilde{\mathrm{u}}} = m_{\widetilde{\mathrm{d}}} + 9.6\,\mathrm{GeV} \tag{5.17}$$

As this difference is small compared to the total mass and the production cross section of the up type squarks is almost four times higher than the one for down type squarks, the present analysis is unable to distinguish between these two squarks families. Instead the template fit will result in an average of their masses, weighted with their respective cross sections:

$$\frac{\sigma_{\widetilde{\mathrm{u}}}}{\sigma_{\widetilde{\mathrm{d}}}} = 3.82 \tag{5.18}$$

$$m_{\widetilde{q}} = \frac{\sigma_{\widetilde{\mathrm{u}}} m_{\widetilde{\mathrm{u}}} + \sigma_{\widetilde{\mathrm{d}}} m_{\widetilde{\mathrm{d}}}}{\sigma_{\widetilde{\mathrm{u}}} + \sigma_{\widetilde{\mathrm{d}}}} \tag{5.19}$$

For the template generation a similar mass splitting between up- and down-type squarks of exactly 10 GeV was used. The templates were generated in steps of 3 GeV for the range of 1050 GeV to 1250 GeV, assuming that the approximate mass region of the squarks is already known from another source like the M_C^{max} method or an independent experiment like the LHC:

$$m_{\tilde{\mathrm{u}}} = m_{\tilde{\mathrm{d}}} + 10\,\mathrm{GeV} = \{1050, 1053, \ldots, 1248\}\,\mathrm{GeV}. \tag{5.20}$$

To minimize influences on the final result through statistical fluctuations of the template distributions, each of these templates was generated with 50000 events which corresponds to an integrated luminosity of $\int \mathrm{d}t\mathcal{L} = 33.6\,\mathrm{ab}^{-1}$. As computation power was limited, these 3.3 million events could not go through the entire processing chain. The full detector simulation and reconstruction were omitted and replaced by including detector effects on generator level.

This included the rejection of particles in the very forward region $|\cos\theta| > 0.995$ and low momentum particles $p < 100\,\mathrm{MeV}$ to account for the detector acceptance region. As a second step jet clustering was performed using the same algorithm as for the fully simulated data earlier in this analysis (`kt_algorithm` with $R = 0.7$). Detector effects were included by smearing the energy of the resulting jets with a Gaussian. The width of this Gaussian is the assumed jet energy resolution σ_{Jet} and was obtained by comparing the fully simulated M_C distribution with a single template close to the actual squark masses using a Kolmogorov-Smirnoff test, after smearing the jet energies of the template with different resolutions of:

$$\sigma_{\mathrm{Jet}} = \{0, 1, 2, 3, 3.5, 4, 4.5, 5, 7.5, 10\}\,\%. \tag{5.21}$$

These results are shown in Figure 5.14. For better readability only the extreme (no smearing, smearing of 10%) and the optimal cases are shown. The result closest to the full simulated data was the template with a smearing of $\sigma_{\mathrm{Jet}} = 4.5\%$. This is compatible with the expected resolution of PandoraPFA of 3.5% to 4.0% RMS_{90} for TeV scale jets. A few examples of the templates are shown in Figure 5.15.

The templates do not include any kind of background, as the remaining background contribution after the rejection with transverse momentum cut, Boosted Decision Trees and subtraction of the remaining background with a parametrized fit is expected to be negligible in the case of fully simulated data. In addition the smearing only included the jet energies, which is sufficient for the correct reproduction of the M_C distribution with detector effects. But the smearing misses the influence on other observables like the number of particles or the correct particle ID. This information, however, is used by the Boosted Decision Trees for the event classification, and as a consequence the classification performance on the templates is worse than for full simulation.

Hence the selection based on the Boosted Decision Trees and the subtraction of the remaining, Gaussian shaped, background events as described in subsection 5.5.3 are not performed for the generation of the templates. However, as the cut on the transverse momentum of $p_{\mathrm{t,miss}} < 600\,\mathrm{GeV}$ has a significant influence on the shape of the M_C distribution, it is included in the template generation.

The templates do not include overlayed events of $\gamma\gamma \to$ hadrons from beam induced background, since with the usage of the `kt_algorithm` as jet finder their influence is assumed to be negligible.

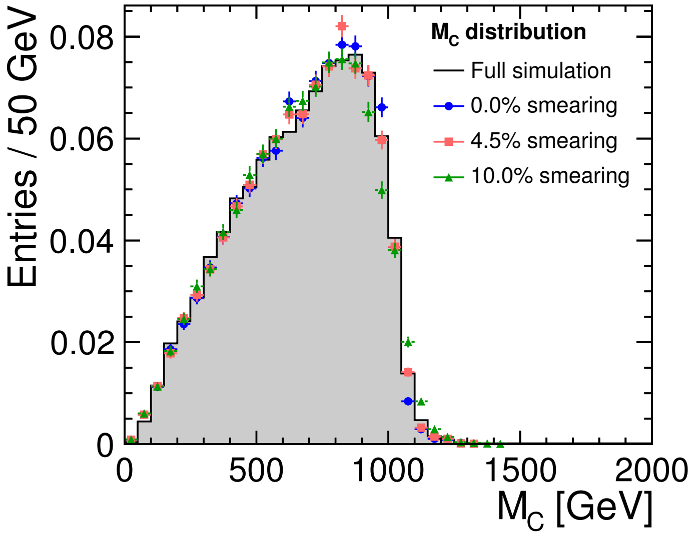

Figure 5.14: The M_C distribution obtained from generator level information without full detector simulation, but with smeared jet energy assuming a Gaussian jet energy resolution of 0, 4.5 and 10 per cent. For comparison a fully simulated sample is shown in black.

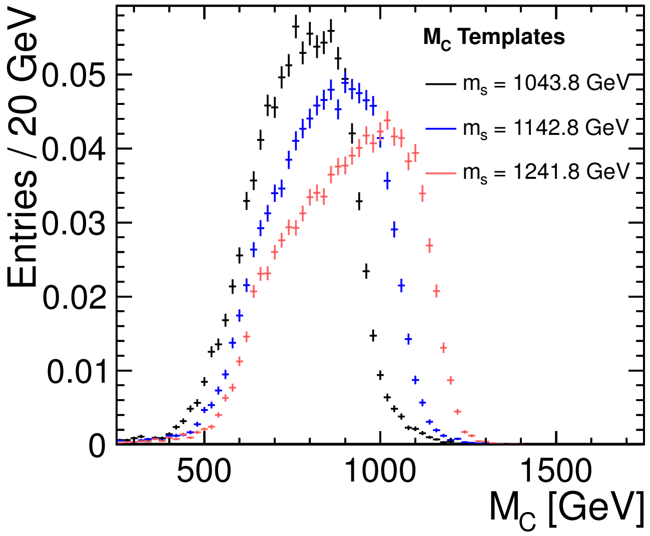

Figure 5.15: The M_C distribution of 3 example templates, with their respective integral normalized to unity. For better readability the error bars are omitted.

The template construction method might introduce a bias towards the final result. To correct for this bias, the templates need to be calibrated. This is done by applying the entire squark extraction method as described in the following section to an independent, high statistics sample of fully simulated signal data without Standard Model background, but including the beam induced background of $\gamma\gamma \to$ hadrons. The result obtained is:

$$m_{\tilde{q}} = 1127.9\,\mathrm{GeV} \pm 1.35\,\mathrm{GeV} \tag{5.22}$$

This value is slightly higher than the input of $m_{\tilde{q},\mathrm{in}} = 1123.7\,\mathrm{GeV}$. This bias was removed by recalibrating each template to a new squark mass which is 4.2 GeV smaller than its respective original value.

5.6.2 Template Fit

The template fit is performed in two steps. In the first step the M_C distribution for each template is compared with the one of the measurement using a binned χ^2:

$$\chi^2 = \sum_{n}^{\mathrm{bins}} \frac{\Delta_n^2}{\sigma_{\mathrm{meas},n}^2 + \sigma_{\mathrm{templ},n}^2} \tag{5.23}$$

Here Δ_n^2 denotes the difference between template and data of the M_C distributions histogram in bin n while $\sigma_{\mathrm{meas},n}$ and $\sigma_{\mathrm{templ},n}$ are the statistical errors of bin n for the measurement and the template respectively. Since Δ_n and hence χ^2 is dependent on the normalization of the two histograms, the χ^2 is minimized for each individual template, using the normalization factor of the template as free parameter. As shown in Figure 5.16 the M_C distributions for the measurement after background subtraction and the template with the lowest χ^2 match very well.

An improvement of the result over the template's mass spacing of 3 GeV can be obtained in the second step: The χ^2 value from the comparison to the measurement is entered as function of its squark mass into Figure 5.17 for each template. As the χ^2 is quadratic, the resulting function $f(x)$ is a parabola with three parameters: The parameter a, the minimum χ^2_{min} and the actual squark mass $m_{\tilde{q}}$:

$$f(x) = a(x - m_{\tilde{q}})^2 + \chi^2_{min} \tag{5.24}$$

The errors for each χ^2 point were set to $\sigma_{\chi^2} = \sqrt{\chi^2} = \chi$, increasing the weight of the points around the minimum of the function. The extracted squark mass from the fit is:

$$m_{\tilde{q}} = 1125.5\,\mathrm{GeV} \tag{5.25}$$

5.6.3 Statistical Error and Final Result

The statistical error of the squark mass measurement is obtained by performing Toy-MC experiments. Each experiment takes the histogram of the M_C distribution for the measurement as input and randomly shifts the value of each bin of the histogram according to a Gaussian with a σ corresponding to the statistical error of this bin.

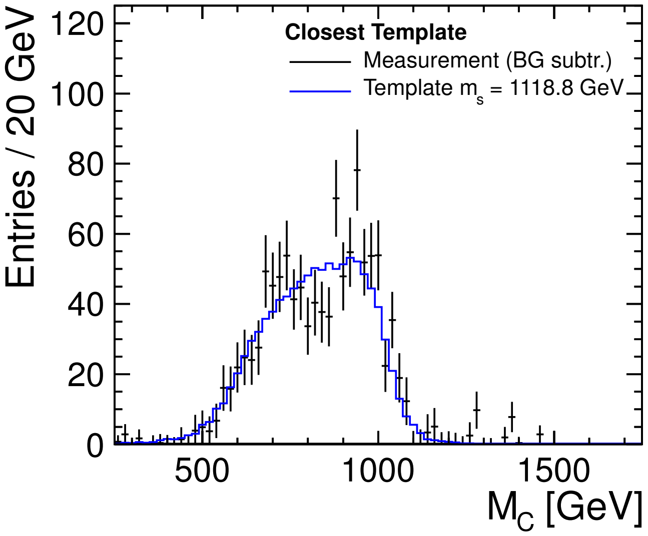

Figure 5.16: The M_C distribution for the measurement (background subtracted) and the template with the lowest χ^2.

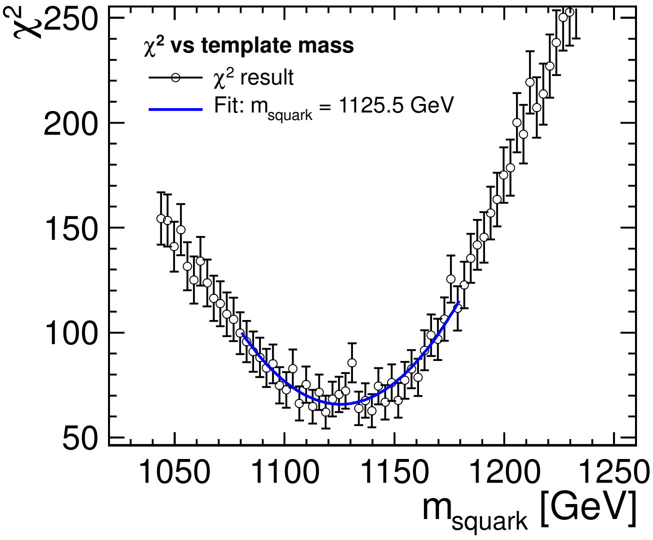

Figure 5.17: The χ^2 between the measurement and the template for the masses of the templates.

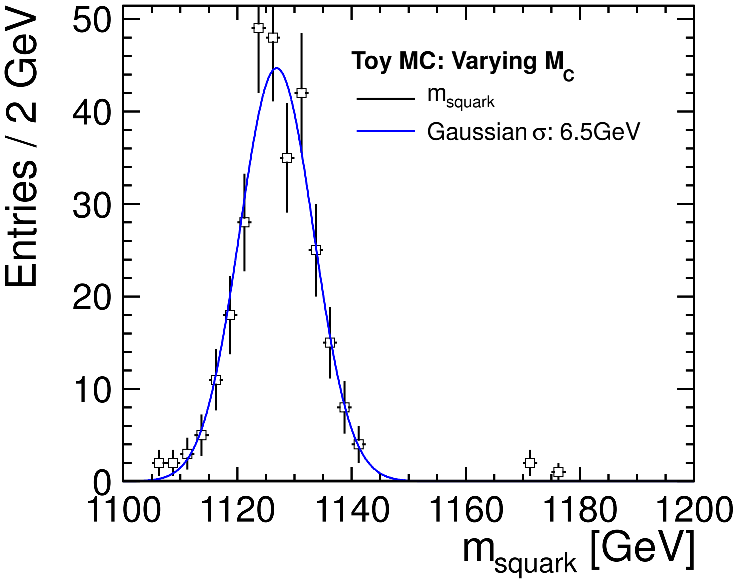

Figure 5.18: The results of 500 repetitions of a Toy-MC experiment to determine the squark mass. The width of this distribution gives the statistical error on the squark mass.

Then the squark mass extraction as described above is repeated. The resulting squark masses of the 500 Toy-MC experiments are shown in Figure 5.18. This width σ of this distribution is the resulting statistical error and was obtained from a Gaussian fit. Its value was determined to be 6.5 GeV, leading to a final result of the squark mass to be:

$$m_{\tilde{q}} = 1125.5\,\text{GeV} \pm 6.5\,\text{GeV(stat)} \tag{5.26}$$

This result corresponds to a relative error of 0.58% and is in good agreement with the input value of

$$m_{\tilde{q},\text{in}} = 1123.7\,\text{GeV} \tag{5.27}$$

As the measurement at hand uses the mass of the lightest neutralino $\tilde{\chi}^0_1$ as input assuming its measurement to be performed in a different, more suitable process, its statistical uncertainty has to be considered, too. The neutralino mass enters into the calculation of the M_C distribution, shifting the upper edge M_C^{max} and as a consequence the squark mass. For the particle masses considered here, an uncertainty of 1 GeV on the neutralino mass translates into an uncertainty of 0.54 GeV of the squark mass. Using the uncertainty of $\sigma_{\tilde{\chi}^0_1} = 3.4\,\text{GeV}$ obtained in [82], this results in an additional uncertainty of 1.8 GeV on the squark mass.

5.7 Cross Section

The cross section of a process is defined as the total number of events N_{tot} per integrated luminosity $\int \mathrm{d}t\mathcal{L}$. The number of events can easily be obtained from the total integral of the background subtracted M_C distribution, giving the number of events after the background rejection N_{cut} and the efficiency of the background rejection ϵ.

$$\sigma_{\widetilde{q}} = \frac{N_{tot}}{\int \mathrm{d}t\mathcal{L}} = \frac{N_{cut}}{\epsilon \int \mathrm{d}t\mathcal{L}} = \frac{1120.7}{0.362 \cdot 2000\,\mathrm{fb}^{-1}} \tag{5.28}$$

$$= 1.55\,\mathrm{fb} \pm 0.07\,\mathrm{fb}(\mathrm{stat}) \tag{5.29}$$

which is in good agreement with the input value of

$$\sigma_{\widetilde{q},\mathrm{in}} = 1.47\,\mathrm{fb} \tag{5.30}$$

Here the statistical error is taken from the number of events after the background rejection N_{cut}, which was obtained from the quadratic sum of the statistical errors of the histogram of the M_C distribution for the measurement.

5.8 Systematic Errors

The measurement of the squark mass yields a certain value, which is dependent on the available data sample and the method used. The dependence on statistical fluctuations were given with the statistical error, which was discussed in subsection 5.6.3.

However, independent on the available statistics of the data sample, systematic effects can have significant influences on the measurement. Here two main topics will be discussed: First, if the training of the Boosted Decision Trees with signal samples of correct squark masses introduces a bias into the background rejection, favouring the input value (subsection 5.8.1). In subsection 5.8.2, we will investigate the influence of the luminosity spectrum of the collider on the measurement.

5.8.1 Training of Boosted Decision Trees

For the squark mass measurement the background rejection is an essential step for which Boosted Decision Trees are used. These were grown using training data samples, both for the signal and background. It is likely that in the analysis the Boosted Decision Trees will predominantly classify those events as signal that contribute to that value of the squark mass which was used for their training, hence introducing a bias towards that value in the squark mass measurement.

In the analysis presented in this thesis, the Boosted Decision Trees were trained with the correct value of the squark mass as it was specified in the underlying CDR SUSY model I. This value is of course not known a priori in a real experiment. In this section this potential systematic bias will be studied by extracting the squark mass in the same way from the same data set as before, but using Boosted Decision Trees that were trained with values for the squark mass that differ from the value of the CDR SUSY model I.

o[GeV]	-20	-10	± 0	$+10$	$+20$
BDT cut	-0.109	-0.079	-0.066	-0.050	-0.081
$m^o_{\tilde{q}}$[GeV]	1123.5	1121.3	1125.5	1126.3	1125.1
stat. err. [GeV]	6.6	6.8	6.5	6.4	6.7

Table 5.7: The effect on the measurement of the squark mass $m_{\tilde{q}}$ of different mass assumptions in the training of the event selection.

Boosted Decision Tree Growing with Wrong Squark Masses

Signal samples were created in which the squark masses $m^o_{\tilde{q},\mathrm{in}}$ were artificially shifted up and down by an offset o of ±10 and ±20 GeV,

$$m^o_{\tilde{q},\mathrm{in}} = m_{\tilde{q},\mathrm{in}} + o, \tag{5.31}$$

resulting in additional four data sets of $m^{-20}_{\tilde{q},\mathrm{in}}$, $m^{-10}_{\tilde{q},\mathrm{in}}$, $m^{+10}_{\tilde{q},\mathrm{in}}$ and $m^{+20}_{\tilde{q},\mathrm{in}}$. In this nomenclature the original squark mass is $m^0_{\tilde{q},\mathrm{in}} \equiv m_{\tilde{q},\mathrm{in}}$. No other changes to the SUSY models were made, in particular the decay modes and the cross sections of all particles were kept. Then, the complete chain of event generation, simulation, reconstruction and jet finding as described in detail in the previous sections is applied.

Each of these four sets was used to replace the original signal set during the growing of the Boosted Decision Trees, while the standard model background set was kept. There was no individual tuning of the boosting parameters. Instead all four sets were created with the identical settings as in the original analysis. Cross checks revealed that there were no overtraining effects for the ±10 GeV sample. However, the Kolmogorov-Smirnoff comparison of the BDT distribution between the training and the testing sample reveals a slight overtraining (0.69) for the +20 GeV sample. For the −20 GeV sample, however, the Kolmogorov-Smirnoff test results in an even smaller value (0.05). This is an indication for strong overtraining which could be reduced by tuning the boosting parameters. In favor of the comparability between the five (one original and four trained with offset to the squark mass) forests of Boosted Decision Trees, no tuning of the parameters was performed.

As in the analysis before, the cut value on the BDT response with the highest significance was extracted from their respective testing samples, which, too, were generated with the same squark mass offset.

Results

The forests of Boosted Decision Trees were used to measure the squark mass $m^o_{\tilde{q}}$ as already described in previous sections with their individual BDT cut values. This includes calibration of the templates and fitting of the remaining background events with a Gaussian. Note that although these Boosted Decision Trees were trained using a signal sample with an offset o, the measurement was performed on the original sample without offset.

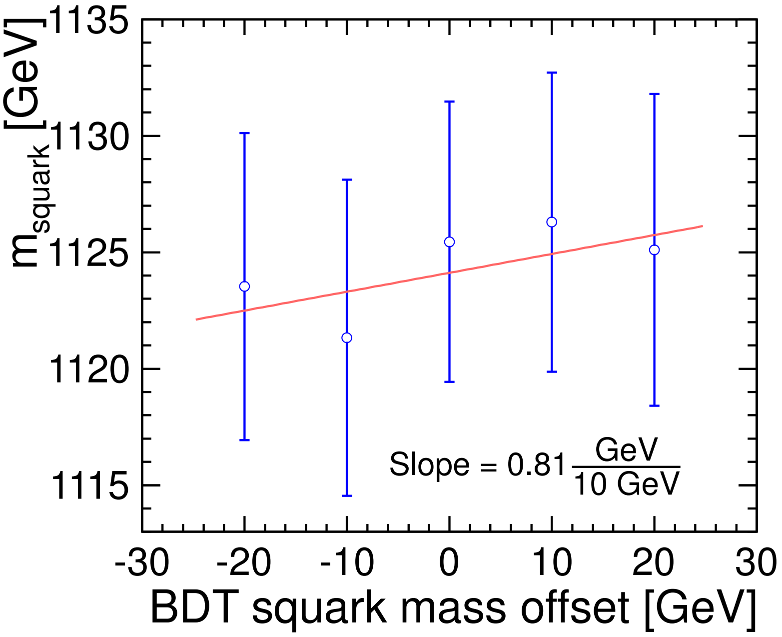

Figure 5.19: The effect on the measurement of the squark mass $m_{\tilde{q}}$ of different mass assumptions in the training of the event selection. As the same data sample is used, the statistical errors of the different points are highly correlated. The linear fit excludes the central point which is the original measurement without an offset.

The result of the squark mass measurement for the different mass assumptions in the training of the event selection are shown in Table 5.7 and Figure 5.19. In both cases the original measurement with no offset ($o = 0\,\text{GeV}$) is included for comparison. Note that the statistical errors given here are strongly correlated, as the input data sample is identical and only different background rejection was used.

To get the dependence of the final measurement on the offset o, a linear function was fitted to the result excluding the original measurement without offset. This shows that a change of 10 GeV on Boosted Decision Tree input squark mass results in a change of 0.81 GeV in the final squark mass measurement.

This systematic influence can be avoided at a real experiment by iteratively redoing the analysis, changing the value of the squark mass used to train the Boosted Decision Trees until it is identical to the result of the measurement.

5.8.2 Luminosity Spectrum

The Compact Linear Collider has a nominal center-of-mass-energy $\sqrt{s}$ of approximately 3 TeV. However, there are a few effects that influence the actual center-of-mass-energy of the collision $\sqrt{s'}$. On the one hand there are beam induced uncertainties, such as an energy spread of 0.1% by the accelerator. On the other hand highly energetic photons

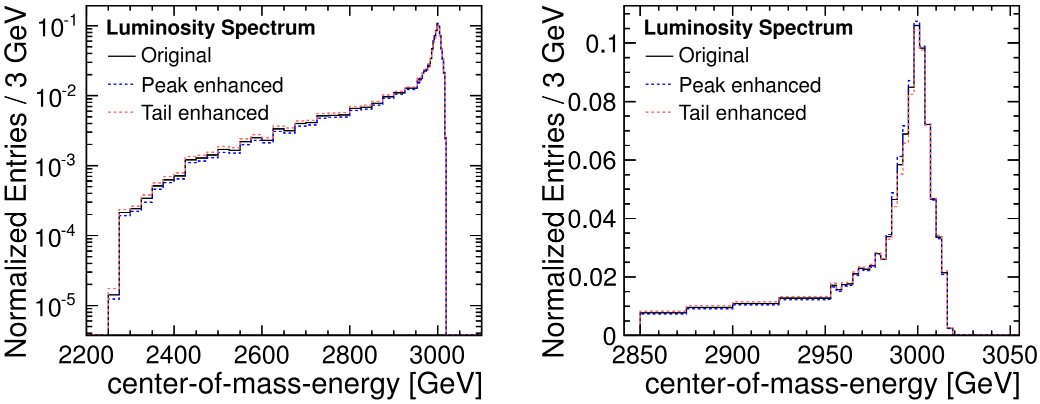

(a) Unzoomed (b) Zoomed

Figure 5.20: The CLIC luminosity spectrum for the squark production process. The left plot shows the complete range, while the right plot is zoomed to the peak region. In black the original luminosity spectrum is shown, while blue and red show the modified versions with 5% of the events moved to the peak (blue) respectively to the tail (red).

can be emitted by the electron or positron prior to the collision, caused either by initial state radiation or likewise by beam-beam interactions, called beamstrahlung. As a consequence the actual center-of-mass-energy $\sqrt{s'}$ follows a distribution which is called luminosity spectrum. This spectrum peaks at the nominal value $\sqrt{s}$ with long tails towards lower energies. At CLIC, only 35% of the effective luminosity is within 1% of the nominal center-of-mass-energy [10]. An example of the luminosity spectrum for the squark production process is shown in Figure 5.20.

For a precision measurement it is essential that the luminosity spectrum is taken into account. In the present analysis this was done by including the effect in the generation of the squark mass templates as well as the training (and analysis) data for the Boosted Decision Trees.

However, at a real machine the luminosity spectrum needs to be measured with high precision. This section will discuss how a measurement error on the luminosity spectrum influence the squark mass result. The measurement error is simulated by an ad-hoc variation of shifting 5% of the events from the tail of the luminosity spectrum into its peak (and vice versa), which is a conservative error assumption. In order not to introduce dependencies on statistical fluctuations, the same data sample is used, but each signal event is reweighted according to the different energy spectrum.

Luminosity Spectrum Generation

The luminosity spectrum is specific to a process, as the available energy directly influences the cross section. It is built from the initial-state-radiation (ISR) spectrum and the beamstrahlungs spectrum. The ISR spectrum is extracted from the files of the squark simulation, while the beamstrahlungs spectrum is generated using GuineaPig[87]. The cross section for the squark production is calculated independently in steps of 10 GeV. Both spectra contain individual information on each of the two beams (electron and positron).

The actual generation of the luminosity spectrum is done as a series of 250 million ToyMC experiments. Each experiment randomly picks values for the beamstrahlung and the initial state radiation for both the electron and the positron. As the beamstrahlungs (BS) spectrum gives the energy of the electron (positron) *after* the energy loss through beamstrahlung, the energy of the beams is: $E_e = E_{\mathrm{BS},b} - E_{\mathrm{ISR},b}$, with e denoting either the electron or the positron beam. With the new values for the energy of the two beams, the new center-of-mass-energy $\sqrt{s'} = \sqrt{4E_{\mathrm{e}^-}E_{\mathrm{e}^+}}$ is calculated. The corresponding cross section σ' for this energy is extracted from the available list through a linear interpolation between the data points. This cross section is used to create a two dimensional lookup table, which will give you the cross section for the two beam energies E_{e^-} and E_{e^+}. It is implemented by a two dimensional histogram with the beam energies E_{e^-} and E_{e^+} as x- and y-axis, in which each Toy-MC-event is filled using the cross section as weighting factor.

This procedure is repeated for a beamstrahlungs spectrum where 5% of the events where artificially moved from the peak to the tail, artificially broadening the spectrum. This will be called tail-enhanced spectrum . A third luminosity spectrum with a focus on the peak is generated, too. Here, 5% of the events are moved from the tail to the peak, generating a peak-enhanced spectrum.

By dividing the cross section histogram of the original luminosity spectrum by the one for the altered luminosity spectrum, one gets the cross section ratio between these two spectra for each energy of the two beams. The cross section ratio can be used as an event weight, as the available data was generated using the original luminosity spectrum, and the ratio will give you by how much an event with the specified beam energies needs to be scaled to match the cross section in the altered luminosity spectrum. Hence this cross section ratio histogram will be called weight histogram.

Impact on the Squark Mass Measurement

When building the M_C distribution, the energy of the two beams for a given signal event is taken to look up the corresponding weight factor in the generated weight histogram. This weight is considered when filling the M_C histogram.

In total three M_C histograms are created, all from the total available data set for the squarks with an integrated luminosity of $\int \mathrm{d}t\mathcal{L} = 21\,\mathrm{ab}^{-1}$: One each for the tail-enhanced and the peak-enhanced luminosity spectrum, and one unmodified for comparison. Then the squark mass is extracted using the template fit as described in subsection 5.6.2, including the application of the Boosted Decision Trees but without any background consideration. The result is shown in Table 5.8. Note that as the entire available signal data set and no background was used in this study, the resulting squark mass differs slightly from the results in Equation 5.26. Clearly the effect on the squark mass measurement is negligible, as the ad-hoc variation of 5% of the events in the luminosiy spectrum yields in a squark mass change of about 0.07 GeV. This shows

luminosity spectrum	tail-enhanced	no change	peak-enhanced
$m_{\tilde{q}}$ [GeV]	1120.15	1120.08	1120.00

Table 5.8: The result of the squark mass extraction with the template fit method on the full available signal-only dataset of $\int \mathrm{d}t\mathcal{L} = 21\,\mathrm{ab}^{-1}$ for the three different luminosity spectra.

the strong point of the M_C observable, which is invariant under contra-linear boosts.

5.9 Conclusions

As part of one of the six benchmark processes for the CLIC Conceptual Design Report, the mass and cross section measurement of super symmetric right-handed scalar quarks in a dedicated SUSY model was performed. Due to the higher mass of the gluino, the right handed squarks almost exclusively decay into their Standard Model partner and the lightest neutralino, allowing to test the detector and the particle flow based reconstruction of missing energy and two high energetic jets in a simple topology. Using a combination of missing transverse energy cuts and multivariate classifiers it was possible to achieve a high signal significance despite standard-model background processes that exceed the signal production cross section by almost four orders of magnitude. The beam induced background from $\gamma\gamma \to$ hadrons processes could be controlled by timing cuts in the reconstruction and by a suitable choice of the jet finder. For full detector simulations of the CLIC CDR SUSY benchmark model with light-flavored right-squark masses of around 1125.5 GeV, a statistical precision of 6.5 GeV, corresponding to 0.58%, was achieved for combined up- and down-type squarks with an integrated luminosity of $2\,\mathrm{ab}^{-1}$ using a template fit with generator-level templates. For the same data sample, a statistical precision of 5% was achieved for the total production cross section. A systematic bias due to mass of the squarks in the training sample used for the multivariate background rejection was studied and found to be small, with less than 1 GeV per 10 GeV offset of the squark mass from the correct value. Systematic changes in the luminosity spectrum have a negligible effect on the measurement, demonstrating that precision measurements of the properties of new, strongly interacting particles are possible at CLIC.

Chapter 6

Conclusion

This thesis presented measurements of the time structure of hadronic showers in tungsten performed with a dedicated testbeam experiment. Furthermore, an analysis to measure the mass and cross-section of supersymmetric right-handed scalar quarks at a future e^+ e^- collider was discussed.

The Standard Model is a quantum field theory describing three of the four known forces of nature: the strong nuclear force, the weak nuclear force and the electromagnetic force. It is often claimed to be the most successful theory in particle physics, as it was able to predict the existence of particles such as the weak gauge bosons $W^\pm$ and Z^0 or the top quark which were indeed discovered at collider experiments. The latest and at the same time last open successful prediction was the existence of the Higgs boson which was discovered by the experiments ATLAS and CMS at the Large Hadron Collider (LHC) at CERN in 2012. However, despite the Standard Model's high accuracy and successful predictions it cannot be the ultimate theory describing our universe, as it does not provide answers to several fundamental open questions. One of these is the hierarchy problem which addresses the discrepancy between the fundamental coupling constants of the theory and the observed masses of the particles. This affects for example the Higgs mass, which receives large divergent correction factors. These need to be compensated by a careful renormalization, thus artificially fine tuning the theoretical value to the observed one without any physical motivation. Extensions to the Standard Model such as Supersymmetry (SUSY) provide a more elegant solution by imposing a new particle symmetry. In this theory each particle has a superpartner with the same quantum numbers except for the spin, which differs by $\frac{1}{2}$. Thus each boson has a fermion as superpartner and vice versa, which add loop corrections to the Standard Model Lagrangian and thereby intrinsically cancel the divergences. As SUSY is spontaneously broken, the masses of the new particles are higher than their corresponding Standard Model superpartners. Depending on the exact model, the new particles have masses of $\mathcal{O}\,(1\,\mathrm{TeV})$.

Particle accelerator experiments such as the LHC search for these new particles while they continue to perform precision tests on the Standard Model. A new concept of such an accelerator is the Compact Linear Collider (CLIC). As it collides electrons with positrons, it both has a higher sensitivity in the electroweak sector and, due to its clean environment, allows for measurements at a higher precision than hadron colliders such as the LHC. One of the two detector concepts for CLIC is the International Large Detector (CLIC_ILD). It is optimized for the usage of the Particle Flow Algorithm (PFA), which improves the jet energy resolution by geometrically tracking each particle throughout the detector and use the energy measurements of all subdetectors. In order to be able to geometrically separate the clusters caused by individual particles, the calorimeters are thus very granular. The tungsten analog hadron calorimeter (W-AHCal) is a prototype of such a calorimeter which was built by the CALICE (CALorimeter for a LInear Collider Experiment) collaboration. One of the challenges of CLIC is the high bunch crossing rate of 0.5 ns and the beam induced background which in combination leads to pile-up. Therefore the detectors use time cuts to reduce this pile-up background. However, neutrons created in hadronic cascades lead to a non-instantaneous energy deposition in the calorimeter in the order of $\mathcal{O}\,(10\,\mathrm{ns})$ up to $\mathcal{O}\,(1\,\mu\mathrm{s})$. This is especially true for the barrel calorimeters of CLIC_ILD as they use tungsten as absorber material and thus create a higher number of neutrons than calorimeters using steel absorber. Therefore detailed studies on the correct timing cuts have been made to verify the detector performance of CLIC_ILD by using full detector simulations based on GEANT4. The GEANT4 toolkit simulates interactions of particles with matter. In particular it includes different models for hadronic cascades, called physics lists. Thus the accuracy of the detector performance validation depends on the accuracy of these physics lists.

The time structure of the physics lists of GEANT4 has never been validated for hadronic calorimeters with tungsten absorbers. Thus the development of the Tungsten Timing Testbeam (T3B) experiment is the focus of the first part of this thesis. It is dedicated to the measurement of the time structure of hadronic showers and thus performing the necessary validation of the physics lists. T3B is a parasitic experiment to the CALICE W-AHCal, which is the prototype of the barrel hadronic calorimeter of the CLIC_ILD and thus has a tungsten absorber structure. During beam tests at the CERN Proton Synchrotron and Super Proton Synchrotron, T3B recorded the response of a strip of 15 $30 \times 30 \times 5\,\mathrm{mm}^3$ scintillator tiles which were placed perpendicular to the beam axis, starting in the center of the calorimeter and thus covering hadronic showers with a radius of up to 45 cm. The tiles were read out with directly coupled SiPMs which in turn were monitored by USB oscilloscopes with a sampling rate of 1.25 GS/s. A data acquisition software was developed within this thesis to control the four oscilloscopes, optimized for the CERN spill cycles of the CALICE W-AHCal testbeam. By requiring a minimal energy deposition of 0.45 MIP in 9.6 ns within a tile, the time of first hit was reconstructed. The T3B experiment was triggered by the W-AHCal, thus allowing a offline synchronization of the two otherwise independent data streams. By applying the Primary Track Finder, a shower start finding algorithm developed for the AHCal by the CALICE collaboration, on the W-AHCal data, it is possible to correlate the average response of T3B and the hadronic shower starting position. Assuming radial symmetry, it is thus possible to reconstruct the average development of hadronic showers over time. The testbeam data was compared to the result of simulations using the `QGSP_BERT`, `QGSP_BERT_HP` and the `QBBC` physics lists. The comparison shows that the high precision tracking of low energetic neutrons, which is only included in the latter two physics lists, is necessary for a correct reproduction of the detector response to hadronic cascades in tungsten. Both physics lists provide a good description of the testbeam data, with some small deviations in the reconstructed calorimeter profile at times above 16 ns as well as slightly overestimating the mean time of first hits for shower radii above 4.7 cm. The `QGSP_BERT` physics list only correctly reproduces the relativistic and electromagnetic part of hadronic cascades. The amount of late energy depositions, however, is overestimated which was also visible in an increase in the mean time of first hits. Nevertheless despite this overestimation of the late neutron component, 98% of the total recorded energy is deposited within 10 ns by the testbeam data and all physics lists including `QGSP_BERT`. Thus the effect on the detector performance is small, with `QGSP_BERT` producing conservative results.

The physics performance of the CLIC_ILD concept in the environment of the CLIC accelerator was studied in the second part of this thesis. This was done on the basis of one of the six benchmark processes which were specifically selected for this purpose in the context of the CLIC Conceptional Design Report (CDR). For these benchmark studies a specific SUSY scenario with TeV-scale light-flavoured right-handed scalar quarks was created, which almost exclusively decay into their standard model superpartner and the lightest neutralino. Hence, the pair production at CLIC of right-handed squarks leads to exactly two high energetic jets and missing energy, a very generic event topology not limited to this SUSY scenario. Thus, the measurement of the mass and the production cross-section of the squarks, which were studied in a full detector simulation using the `QGSP_BERT` physics list, is a stress test on the particle separation and energy measurement performance of the Particle Flow Algorithm based event reconstruction. This is especially true as background from beam induced pile-up events originating from $\gamma\gamma \rightarrow$ hadrons needed to be rejected by strict timing and transverse momentum cuts. The remaining pile-up particles, which are mostly located in the forward direction, were rejected by using the hadron variant of the exclusive mode k_t jet finder algorithm of the FastJet library. The rejection of Standard Model background with missing energy was done by a combination of missing transverse energy cuts and multivariate classifiers, achieving a significance of $S/\sqrt{S+B}$ of 25.7 after a reduction of the background by almost four orders of magnitude. The squark mass was extracted with a χ^2-based template fit using generator-level templates of known squark masses. These were compared with the full detector simulation measurement using the M_C distribution, which is a mass-sensitive variable constructed from the jet energies. For the CLIC CDR SUSY benchmark model with the right-handed light-flavoured squark mass of around 1125.5 GeV, a statistical precision of 6.5 GeV corresponding to 0.58% was achieved for an integrated luminosity of $\int \mathrm{d}t\mathcal{L} = 2\,\mathrm{ab}^{-1}$. For the same data sample, a statistical precision of 5% was achieved for the total production cross-section. Systematic studies indicate a small bias on the value of the squark mass in the training sample of the multivariate classifier of less than 1 GeV per 10 GeV offset of the squark mass from the correct value. Systematic changes in the luminosity spectrum have a negligible effect on the measurement, demonstrating that precision measurements of the properties of new, strongly interacting particles are possible at CLIC.

Acknowledgements

This thesis would not have been possible without the support and help of many people over the past years.

First of all I want to thank my adviser **Dr. Frank Simon** who was always a great help and never ran out of valuable tips, hints and ideas whenever it came to analyzing results or facing obstacles. Your support and guidance was invaluable.

My supervisor **Prof. Dr. Christian Kiesling** who gave me the possibility to do research in such an interesting field like particle physics. I want to thank you for your guide and your enthusiasm which always inspired me.

My colleague **Christian Soldner**. Together we designed the T3B experiment, wrote the software, took the data and had a lot of fun controlling the entire H8 beam line in the North Hall of CERN for a single night.

My colleagues **Katja Seidel**, **Marco Szalay** and **Michal Tesař** along with the members of the MPI Belle group for the interesting physical and non physical discussions. Especially **Martin Ritter**, who also proved to be an invaluable source of solutions to any kind of computer related problems. Working with all of you was always fun.

The whole CERN LCD group, especially **Erik van der Kraaij**, **Angela-Isabela Lucaci-Timoce** and **Stephane Poss** for their support at the testbeam and their help on CALICE-software and Dirac related questions.

And last but not least my parents, **Ingrid** and **Reinhard**, my sisters **Ina** and **Britta** and especially my girlfriend **Anna-Maria Hahn** for their support.

Appendix A

UML Diagram of the Software DAQ Core

The UML class diagram of the most important classes and their functions is given in Figure A.1. Classes that run in their own thread and the corresponding functions running in this thread are marked with `<<Thread>>`.

The central part is the class `DataReadOut`, which is instantiated once in the main graphical user interface.

Each `Oscilloscope` owns an instance of `OsciSettings`, which contains the `Setting`s that are necessary for its configuration. These oscilloscope settings are specialized through inheritance to meet the specific PS6000 and PS2000 oscilloscope requirements represented by `OsciSettingsPS6000` and `OsciSettingsPS2000`. As the number of `Setting`s necessary for the configuration is large, only a few examples are included in the UML diagram. The same is true for the `Setting`s used by the `RunMode`.

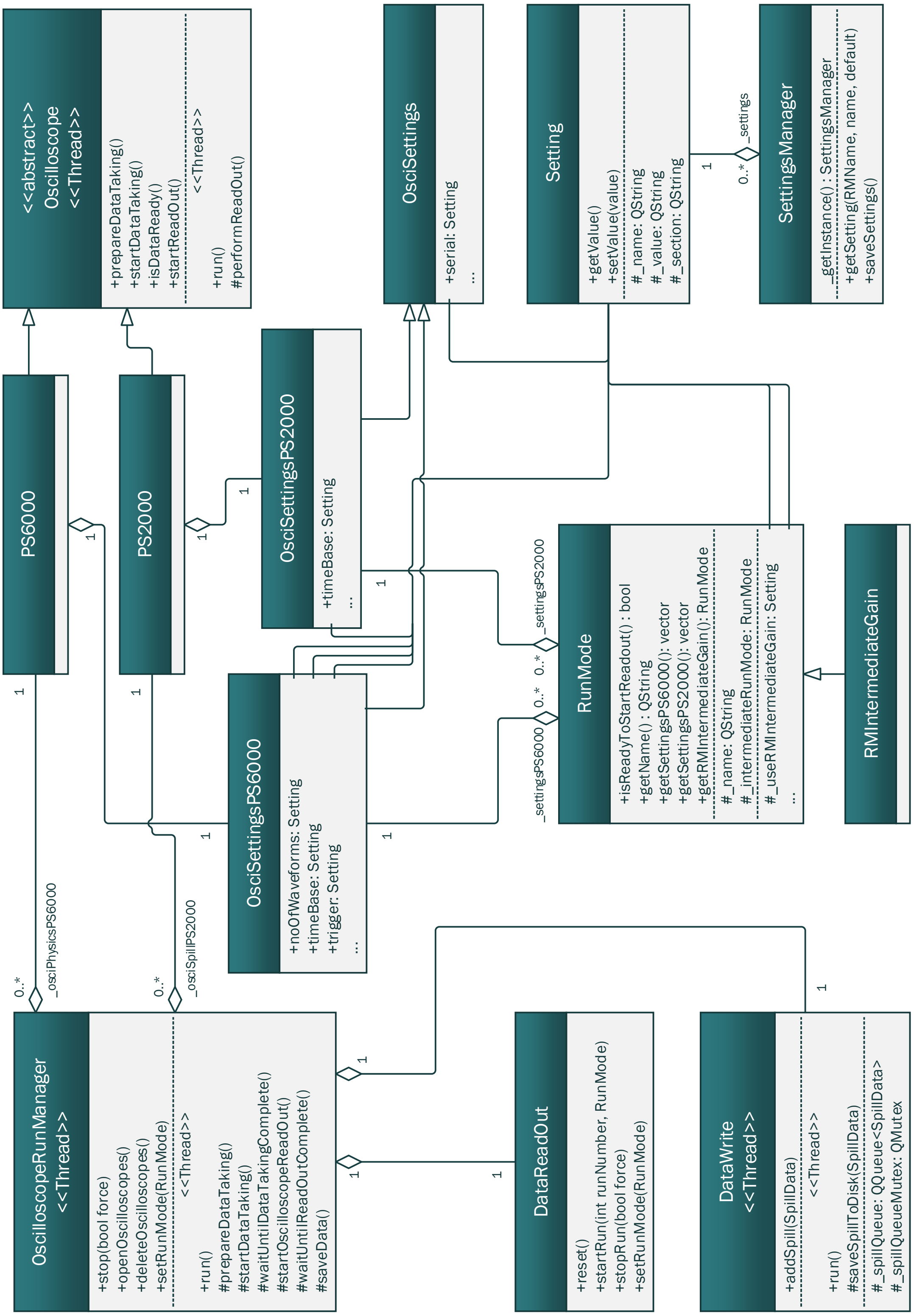

Figure A.1: UML diagram of the core of the T3B data acquisition software.

Appendix B

Timing Cuts for the Reduction of overlay Background

For the background rejection of overlayed particles from $\gamma\gamma \to$ hadrons the timing information of clusters in the electromagnetic and hadronic calorimeters is used. Each cell with energy deposition has the time information on the time of first hit. Out of a calorimetric cluster the mean of this time is taken, and cells with a distance higher than the ones listed in Table B.1 are neglected for the reconstruction.

particle	region	p_t range	time cut
photons	all	$0.75\,\mathrm{GeV} \leq p_t < 4\,\mathrm{GeV}$	$t < 2.0\,\mathrm{ns}$
		$0\,\mathrm{GeV} \leq p_t < 0.75\,\mathrm{GeV}$	$t < 1.0\,\mathrm{ns}$
neutral hadrons	central $\cos\theta \leq 0.975$	$0.75\,\mathrm{GeV} \leq p_t < 8\,\mathrm{GeV}$	$t < 2.5\,\mathrm{ns}$
		$0\,\mathrm{GeV} \leq p_t < 0.75\,\mathrm{GeV}$	$t < 1.5\,\mathrm{ns}$
	forward $\cos\theta > 0.975$	$0.75\,\mathrm{GeV} \leq p_t < 8\,\mathrm{GeV}$	$t < 2.0\,\mathrm{ns}$
		$0\,\mathrm{GeV} \leq p_t < 0.75\,\mathrm{GeV}$	$t < 1.0\,\mathrm{ns}$
charged particles	all	$0.75\,\mathrm{GeV} \leq p_t < 4\,\mathrm{GeV}$	$t < 3.0\,\mathrm{ns}$
		$0\,\mathrm{GeV} \leq p_t < 0.75\,\mathrm{GeV}$	$t < 1.5\,\mathrm{ns}$

Table B.1: Cuts on the time and the transverse momentum to reject overlayed background particles from $\gamma\gamma \to$ hadrons.

Appendix C

TMVA BDT Training Parameters and Observables

C.1 Training Parameters

The list of parameters and their corresponding values that were used for the training of the Boosted Decision Trees with TMVA for the squark mass benchmark are listed in Table C.1.

TMVA Parameter	Value
`NTrees`	150
`nEventsMin`	3500
`MaxDepth`	3
`BoostType`	AdaBoost
`AdaBoostBeta`	0.3
`SeparationType`	MisClassificationError
`nCuts`	14
`PruneMethod`	NoPruning

Table C.1: List of TMVA settings used to grow the Boosted Decision Trees.

C.2 List of TMVA Observables

This section contains the distribution of all input observables to the Boosted Decision Trees used during the squark mass benchmark analysis. The distributions show their respective signal contribution in black and their background contribution in blue stacked on top of each other. Here the jets are ordered by their energy, i.e. Jet 1 has a higher energy than Jet 2.

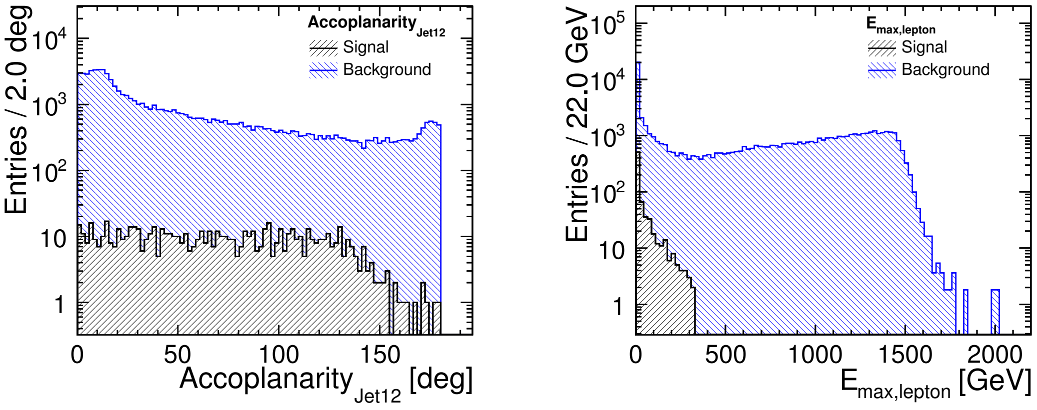

(a) Acoplanarity Jets (b) $E_{\text{max,Lepton}}$

Figure C.1: Stacked Histogram showing two of the input variables of the Boosted Decision Trees.

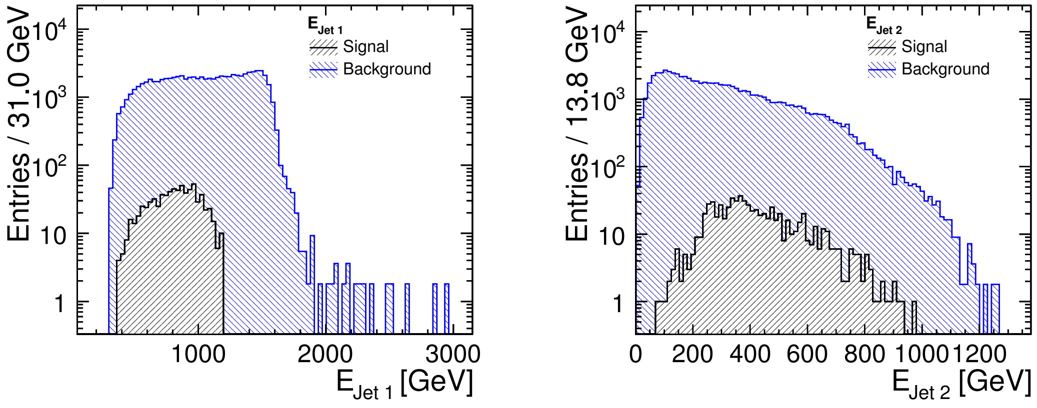

(a) E_{Jet1} (b) E_{Jet2}

Figure C.2: Stacked Histogram showing two of the input variables of the Boosted Decision Trees.

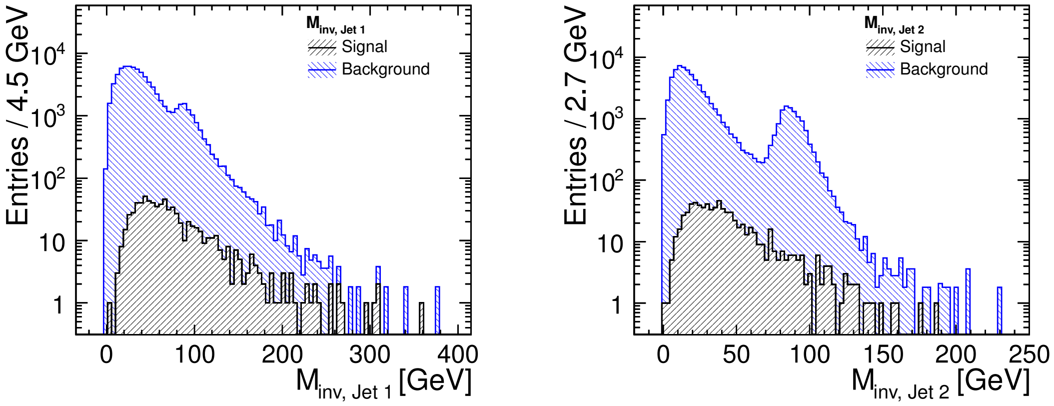

(a) $M_{\mathrm{inv.,Jet1}}$ (b) $M_{\mathrm{inv.,Jet2}}$

Figure C.3: Stacked Histogram showing two of the input variables of the Boosted Decision Trees.

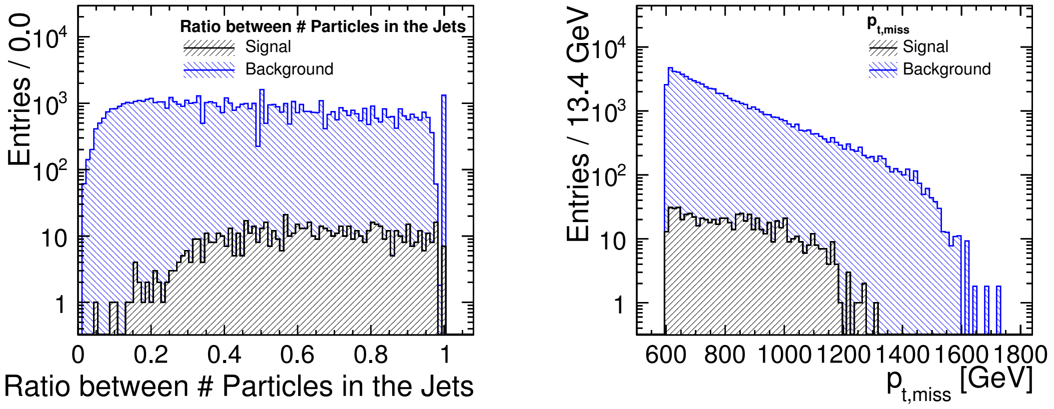

(a) Number of particles in the jet with less particles divided by the jet with more particles.

(b) $p_{t,\mathrm{miss}}$

Figure C.4: Stacked Histogram showing two of the input variables of the Boosted Decision Trees.

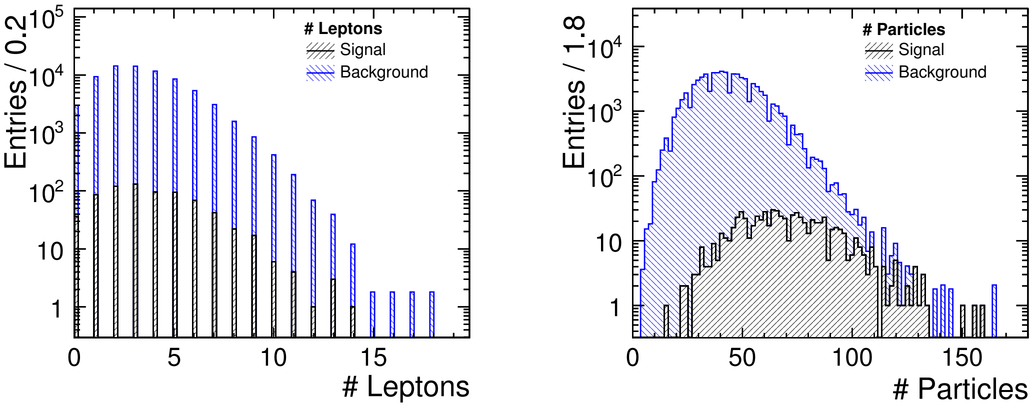

(a) N_{Lepton} (b) $N_{\mathrm{reconstructedParticles}}$

Figure C.5: Stacked Histogram showing two of the input variables of the Boosted Decision Trees.

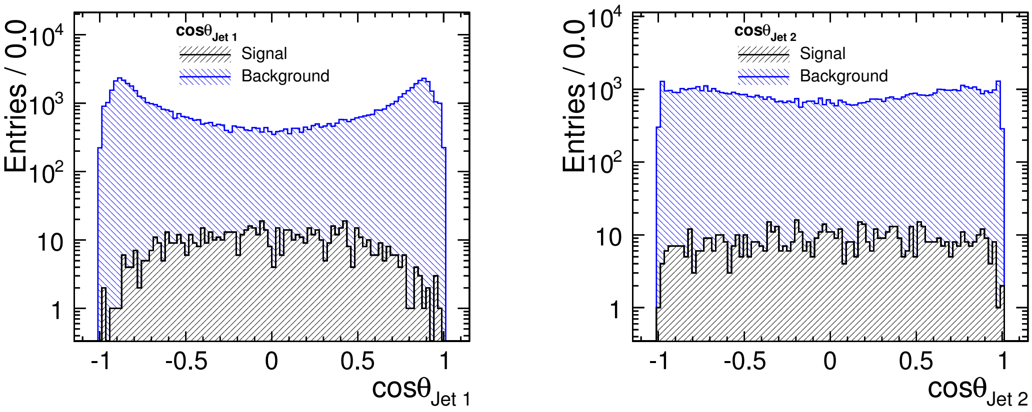

(a) $\cos\Theta_{\mathrm{Jet1}}$ (b) $\cos\theta_{\mathrm{Jet2}}$

Figure C.6: Histogram showing two of the input variables of the Boosted Decision Trees.

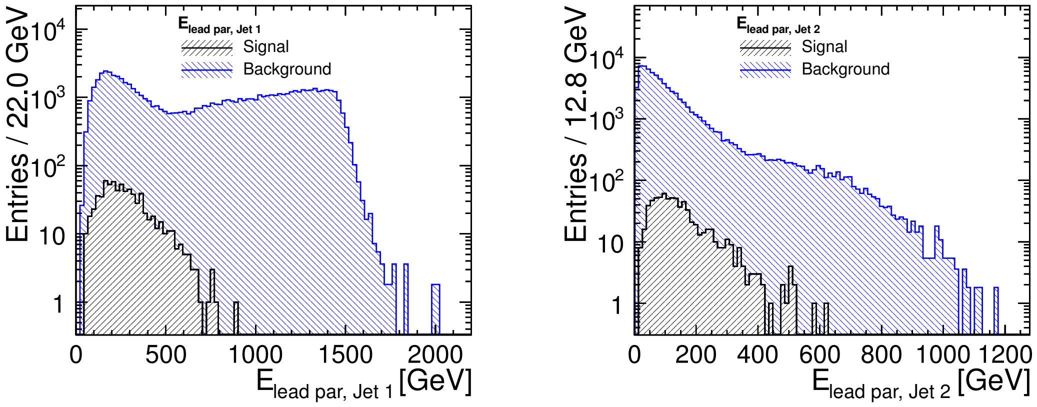

(a) Energy of leading particle in Jet 1 (b) Energy of leading particle in Jet 2

Figure C.7: Stacked Histogram showing two of the input variables of the Boosted Decision Trees.

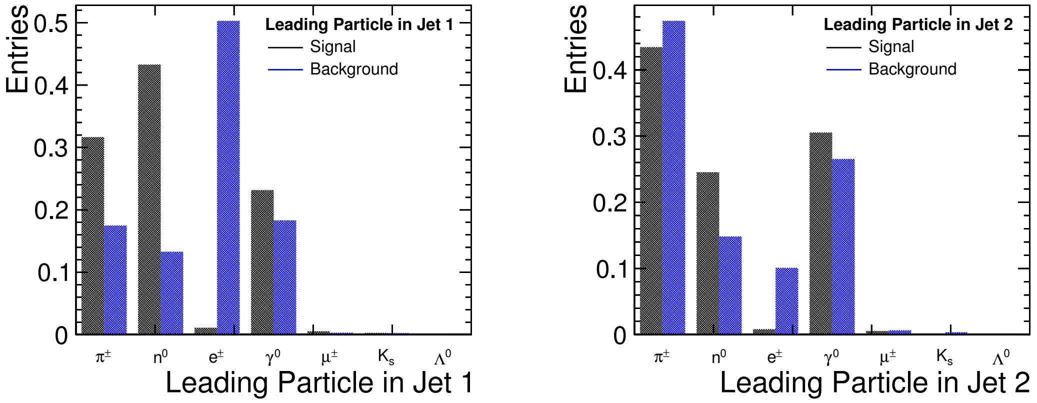

(a) Particle Type of leading particle in Jet 1 (b) Particle Type of leading particle in Jet 2

Figure C.8: Leading particle type, as identified by PandoraPFA for signal and background for both jets. This information is used as input for the boosted decision trees.

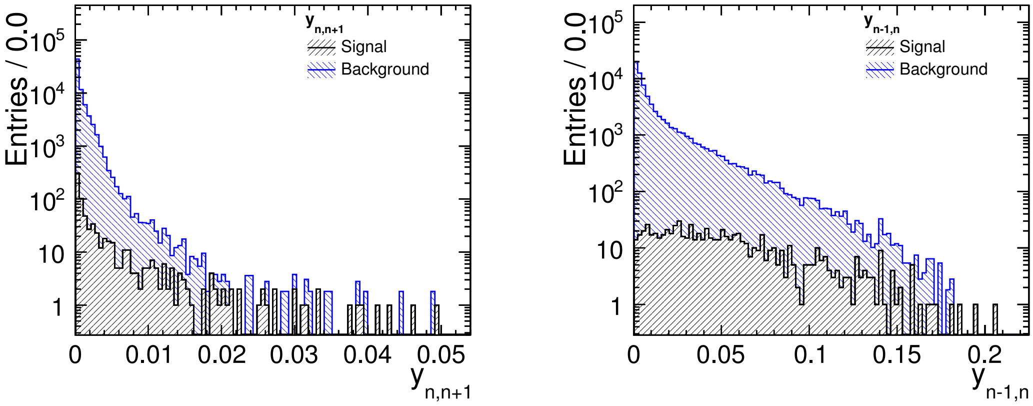

(a) Distance at which the Event would turn from a 2 to a 3 jet event

(b) Distance at which the Event would turn from a 1 to a 2 jet event

Figure C.9: Stacked Histogram showing two of the input variables of the Boosted Decision Trees.

Bibliography

[1] J. J. Thomson. “XL. Cathode Rays”. In: *Philosophical Magazine Series 5* 44.269 (1897), pp. 293–316. DOI: `10.1080/14786449708621070`.

[2] J.J. Thomson. “XXIV. On the structure of the atom: an investigation of the stability and periods of oscillation of a number of corpuscles arranged at equal intervals around the circumference of a circle; with application of the results to the theory of atomic structure”. In: *Philosophical Magazine Series 6* 7.39 (1904), pp. 237–265. DOI: `10.1080/14786440409463107`.

[3] Sir Ernest. Rutherford. “The Scattering of α and β Particles by Matter and the Structure of the Atom”. In: *Philosophical Magazine.* 6th ser. 21 (May 1911), pp. 669–688.

[4] Sheldon L. Glashow. “Partial-symmetries of weak interactions”. In: *Nuclear Physics* 22.4 (1961), pp. 579 –588. ISSN: 0029-5582. DOI: `10.1016/0029-5582(61)90469-2`. URL: `http://www.sciencedirect.com/science/article/pii/0029558261904692`.

[5] A. Salam and J.C. Ward. “Electromagnetic and weak interactions”. In: *Physics Letters* 13.2 (1964), pp. 168 –171. ISSN: 0031-9163. DOI: `10.1016/0031-9163(64)90711-5`. URL: `http://www.sciencedirect.com/science/article/pii/0031916364907115`.

[6] Steven Weinberg. “A Model of Leptons”. In: *Phys. Rev. Lett.* 19 (21 Nov. 1967), pp. 1264–1266. DOI: `10.1103/PhysRevLett.19.1264`. URL: `http://link.aps.org/doi/10.1103/PhysRevLett.19.1264`.

[7] *Organisation européenne pour la recherche nucléaire - European Organization for Nuclear Research.* URL: `http://www.cern.ch`.

[8] Georges Aad et al., ATLAS Collaboration. “Observation of a new particle in the search for the Standard Model Higgs boson with the ATLAS detector at the LHC”. In: *Phys.Lett.* B716 (2012), pp. 1–29. DOI: `10.1016/j.physletb.2012.08.020`. arXiv:`1207.7214 [hep-ex]`.

[9] Serguei Chatrchyan et al., CMS collaboration. “Observation of a new boson at a mass of 125 GeV with the CMS experiment at the LHC”. In: *Phys.Lett.* B716 (2012), pp. 30–61. DOI: `10.1016/j.physletb.2012.08.021`. arXiv:`1207.7235 [hep-ex]`.

[10] Lucie Linssen et al., eds. *Physics and Detectors at CLIC: CLIC Conceptual Design Report.* 2012. arXiv:`1202.5940 [physics.ins-det]`.

[11] Wolfgang Hollik. *Quantum field theory and the Standard Model.* 2010. arXiv:`0708.4233 [hep-ph]`.

[12] Stephen P. Martin. *A Supersymmetry primer.* 1997. arXiv:`hep-ph/9709356 [hep-ph]`.

[13] Peter W. Higgs. "Broken symmetries, massless particles and gauge fields". In: *Phys.Lett.* 12 (1964), pp. 132–133. DOI: `10.1016/0031-9163(64)91136-9`.

[14] J. Beringer et al. "The Review of Particle Physics". In: *Phys. Rev. D* 86 (2012).

[15] Steven Weinberg. "Implications of Dynamical Symmetry Breaking". In: *Phys.Rev.* D13 (1976), pp. 974–996. DOI: `10.1103/PhysRevD.13.974`.

[16] J. Wess and B. Zumino. "Supergauge Transformations in Four-Dimensions". In: *Nucl.Phys.* B70 (1974), pp. 39–50. DOI: `10.1016/0550-3213(74)90355-1`.

[17] C. Regis et al. "Search for Proton Decay via $p \to \mu^+ K^0$ in Super-Kamiokande I, II, and III". In: *Phys.Rev.* D86 (2012), p. 012006. DOI: `10.1103/PhysRevD.86.012006`. arXiv:`1205.6538 [hep-ex]`.

[18] Savas Dimopoulos and David W. Sutter. "The Supersymmetric flavor problem". In: *Nucl.Phys.* B452 (1995), pp. 496–512. DOI: `10.1016/0550-3213(95)00421-N`. arXiv:`hep-ph/9504415 [hep-ph]`.

[19] Serguei Chatrchyan et al., CMS collaboration. *Search for new physics in events with same-sign dileptons and b jets in pp collisions at $\sqrt{s} = 8$ TeV.* 2012. arXiv:`1212.6194 [hep-ex]`.

[20] G. Arnison et al. "Experimental observation of isolated large transverse energy electrons with associated missing energy at s=540 GeV". In: *Physics Letters B* 122.1 (1983), pp. 103 –116. ISSN: 0370-2693. DOI: `10.1016/0370-2693(83)91177-2`.

[21] G. Arnison et al. "Experimental observation of lepton pairs of invariant mass around 95 GeV/c2 at the CERN SPS collider". In: *Physics Letters B* 126.5 (1983), pp. 398 –410. ISSN: 0370-2693. DOI: `10.1016/0370-2693(83)90188-0`.

[22] S. Schael et al. "Precision electroweak measurements on the Z resonance". In: *Phys.Rept.* 427 (2006), pp. 257–454. DOI: `10.1016/j.physrep.2005.12.006`. arXiv:`hep-ex/0509008 [hep-ex]`.

[23] Burton Richter. "From the psi to Charm: The Experiments of 1975 and 1976". In: *Rev.Mod.Phys.* 49 (1977), p. 251. DOI: `10.1103/RevModPhys.49.251`.

[24] Eric Hand. "Muon collider gains momentum". In: *Nature* 462 (2009), pp. 260–261. DOI: `10.1038/462260a`.

[25] M. Aicheler et al., eds. *A Multi-TeV Linear Collider based on CLIC Technology: CLIC Conceptual Design Report.* Oct. 12, 2012. URL: `https://edms.cern.ch/document/1234244/6`.

[26] P. Lebrun et al., eds. *The CLIC Programme: Towards a Staged e+e- Linear Collider Exploring the Terascale : CLIC Conceptual Design Report.* Aug. 8, 2012. arXiv:`1209.2543 [physics.ins-det]`.

[27] H. Bethe. "Zur Theorie des Durchgangs schneller Korpuskularstrahlen durch Materie". In: *Annalen der Physik* 397.3 (1930), pp. 325–400. ISSN: 1521-3889. DOI: `10.1002/andp.19303970303`.

[28] William R. Leo. *Techniques for Nuclear and Particle Physics Experiments: A How-to Approach.* Springer, Feb. 25, 1994. ISBN: 3-540-57280-5.

[29] L. Landau. "On the energy loss of fast particles by ionization". In: *J.Phys.(USSR)* 8 (1944), pp. 201–205.

[30] Richard Wigmans. *Calorimetry: Energy Measurement in Particle Physics (International Series of Monographs on Physics).* Oxford University Press, USA, Dec. 2000. ISBN: 9780198502968.

[31] Christian Wolfgang Fabjan. "Calorimetry in high-energy physics; 1985 ed." In: CERN-EP-85-54 (Apr. 1985), 57 p.

[32] Claus Grupen. *Particle Detectors.* Cambridge Monographs on Particle Physics, Nuclear Physics and Cosmology. Ed. by T. Ericson. Ed. by P. V. Landshoff. Vol. 5. Cambridge: Cambridge University Press, 1996. ISBN: 978-0-521-55216-5.

[33] Toshinori Abe et al., ILD Concept Group - Linear Collider Collaboration. *The International Large Detector: Letter of Intent.* Tech. rep. 2010. arXiv:`1006.3396 [hep-ex]`.

[34] Gerald Aarons et al., ILC collaboration. *International Linear Collider Reference Design Report Volume 2: PHYSICS AT THE ILC.* Tech. rep. 2007. arXiv:`0709.1893 [hep-ph]`.

[35] Lars Weuste. "A Study of Track Segments within Hadronic Showers with a Highly Granular Hadronic Calorimeter". Diploma Thesis. Ludwig-Maximilians-Universität and Max Planck Institut für Physik, Sept. 7, 2009.

[36] Nils Feege. "Silicon photomultipliers: Properties and application in a highly granular calorimeter". Diploma Thesis. 2008. DOI: `10.3204/DESY-THESIS-2008-050`.

[37] M. A. Thomson. "Particle Flow Calorimetry and the PandoraPFA Algorithm". In: *Nucl. Instrum. Meth.* A611 (2009), pp. 25–40. DOI: `10.1016/j.nima.2009.09.009`. arXiv:`0907.3577 [physics.ins-det]`.

[38] C. Adloff et al., CALICE collaboration. "Construction and Commissioning of the CALICE Analog Hadron Calorimeter Prototype". In: *JINST* 5 (2010), P05004. arXiv:`1003.2662 [physics.ins-det]`.

[39] G. Bondarenko et al. "Limited Geiger-mode microcell silicon photodiode: New results". In: *Nucl.Instrum.Meth.* A442 (2000), pp. 187–192. DOI: `10.1016/S0168-9002(99)01219-X`.

[40] P. Buzhan et al. “Silicon photomultiplier and its possible applications”. In: *Nucl.Instrum.Meth.* A504 (2003), pp. 48–52. DOI: `10.1016/S0168-9002(03)00749-6`.

[41] Simon Pfau. “A Study of Silicon Photomultiplier Properties in the Context of Highly Granular Calorimeters”. Diploma Thesis. Technische Universität München, Mar. 2012.

[42] Kolja Prothmann. “Comparative Measurements of Silicon Photomultipliers for the Readout of a Highly Granular Hadronic Calorimeter”. Diploma Thesis. Ludwig-Maximilians-Universität, Oct. 17, 2008.

[43] Christian Soldner. “Scintillator Tile Uniformity Studies for a Highly Granular Hadron Calorimeter”. Diploma Thesis. Ludwig-Maximilians-Universität and Max-Planck-Institut für Physik, Sept. 17, 2009.

[44] F. Simon and C. Soldner. “Uniformity Studies of Scintillator Tiles directly coupled to SiPMs for Imaging Calorimetry”. In: *Nucl.Instrum.Meth.* A620 (2010), pp. 196–201. DOI: `10.1016/j.nima.2010.03.142`. arXiv:`1001.4665 [physics.ins-det]`.

[45] Dominik Dannheim, Wolfgang Klempt, and Erik van der Kraaij. *Beam tests with the CALICE tungsten analog hadronic calorimeter prototype.* Tech. rep. LCD-2012-002. CERN, Apr. 2012. URL: `https://edms.cern.ch/document/1211436`.

[46] J. Repond et al., CALICE Collaboration. “Design and Electronics Commissioning of the Physics Prototype of a Si-W Electromagnetic Calorimeter for the International Linear Collider”. In: *JINST* 3 (2008), P08001. DOI: `10.1088/1748-0221/3/08/P08001`. arXiv:`0805.4833 [physics.ins-det]`.

[47] C. Adloff et al., CALICE collaboration. “Response of the CALICE Si-W Electromagnetic Calorimeter Physics Prototype to Electrons”. In: *J.Phys.Conf.Ser.* 160 (2009), p. 012065. DOI: `10.1088/1742-6596/160/1/012065`. arXiv:`0811.2354 [physics.ins-det]`.

[48] C. Adloff et al., CALICE collaboration. “Study of the interactions of pions in the CALICE silicon-tungsten calorimeter prototype”. In: *JINST* 5 (2010), P05007. DOI: `10.1088/1748-0221/5/05/P05007`. arXiv:`1004.4996 [physics.ins-det]`.

[49] CALICE Collaboration. *Calorimetry for Lepton Collider Experiments - CALICE results and activities.* Tech. rep. 2012. arXiv:`1212.5127 [physics.ins-det]`.

[50] CALICE Collaboration. “Construction and performance of a silicon photomultiplier/extruded scintillator tail-catcher and muon-tracker”. In: *JINST* 7 (2012), P04015. DOI: `10.1088/1748-0221/7/04/P04015`. arXiv:`1201.1653 [physics.ins-det]`.

[51] C. Adloff et al., CALICE collaboration. “Tests of a particle flow algorithm with CALICE test beam data”. In: *JINST* 6 (2011), P07005. DOI: `10.1088/1748-0221/6/07/P07005`. arXiv:`1105.3417 [physics.ins-det]`.

[52] C. Adloff et al., CALICE collaboration. “Hadronic energy resolution of a highly granular scintillator-steel hadron calorimeter using software compensation techniques”. In: *JINST* 7 (2012), P09017. DOI: `10.1088/1748-0221/7/09/P09017`. arXiv:`1207.4210 [physics.ins-det]`.

[53] Wolfgang Kilian, Thorsten Ohl, and Jurgen Reuter. “WHIZARD: Simulating Multi-Particle Processes at LHC and ILC”. In: *Eur.Phys.J.* C71 (2011), p. 1742. DOI: `10.1140/epjc/s10052-011-1742-y`. arXiv:`0708.4233 [hep-ph]`.

[54] Mauro Moretti, Thorsten Ohl, and Jurgen Reuter. *O'Mega: An Optimizing matrix element generator.* 2001. arXiv:`hep-ph/0102195 [hep-ph]`.

[55] Torbjorn Sjostrand, Stephen Mrenna, and Peter Z. Skands. “PYTHIA 6.4 Physics and Manual”. In: *JHEP* 0605 (2006), p. 026. DOI: `10.1088/1126-6708/2006/05/026`. arXiv:`hep-ph/0603175 [hep-ph]`.

[56] S. Agostinelli et al., GEANT4 collaboration. “GEANT4: A Simulation toolkit”. In: *Nucl.Instrum.Meth.* A506 (2003), pp. 250–303.

[57] John Allison et al. “Geant4 developments and applications”. In: *IEEE Trans.Nucl.Sci.* 53 (2006), p. 270. DOI: `10.1109/TNS.2006.869826`.

[58] A. Ribon et al. “Status of Geant4 hadronic physics for the simulation of LHC experiments at the start of LHC physics program”. In: *CERN-LCGAPP-2010-02* (2010).

[59] A. Dotti et al. “Recent improvements on the description of hadronic interactions in Geant4”. In: *J.Phys.Conf.Ser.* 293 (2011), p. 012022. DOI: `10.1088/1742-6596/293/1/012022`.

[60] Nils Feege. “Imaging Pion Showers with the CALICE Analogue Hadron Calorimeter”. PhD thesis. University of Hamburg, 2011. arXiv:`1109.1982 [hep-ex]`.

[61] H. Fesefeldt. “The simulation of hadronic showers: physics and applications”. In: *PITHA-85-02* (1985).

[62] G. Folger and J.P. Wellisch. “String parton models in GEANT4”. In: *eConf* C0303241 (2003), MOMT007. arXiv:`nucl-th/0306007 [nucl-th]`.

[63] Bo Nilsson-Almqvist and Evert Stenlund. “Interactions Between Hadrons and Nuclei: The Lund Monte Carlo, Fritiof Version 1.6”. In: *Comput.Phys.Commun.* 43 (1987), p. 387. DOI: `10.1016/0010-4655(87)90056-7`.

[64] Aatos Heikkinen, Nikita Stepanov, and Johannes Peter Wellisch. “Bertini intranuclear cascade implementation in GEANT4”. In: *eConf* C0303241 (2003), MOMT008. arXiv:`nucl-th/0306008 [nucl-th]`.

[65] G. Folger, V. N. Ivanchenko, and J. P. Wellisch. “The Binary Cascade”. In: *Eur. Phys. J* A21 (3 2004), p. 407. ISSN: 1434-6001.

[66] *MPPC Multi-Pixel Photon Counter Technical Information Pamphlet.* Hamamatsu Photonics. URL: `http://sales.hamamatsu.com/`.

[67] *Radiant Mirror Foil.* URL: `http://solutions.3m.com`.

[68] PicoTech Inc. 2012. URL: `http://www.picotech.com/`.

[69] C. Adloff et al. “Recent results of Micromegas sDHCAL with a new readout chip”. In: *Linear Collider Workshop 2011*. Ed. by M. Chefdeville. 2012. arXiv:`1202.0624 [physics.ins-det]`.

[70] Christian Soldner. “The Time Development of Hadronic Showers and the T3B Experiment”. PhD thesis. Max-Planck-Institut für Physik and Ludwigs Maximilian Universität, 2012.

[71] John B. Birks. *The Theory and practice of scintillation counting*. 1964.

[72] M. Thomson et al. *The physics benchmark processes for the detector performance studies of the CLIC CDR*. Tech. rep. LCD-2011-016. CERN, 2011. URL: `https://edms.cern.ch/document/1155831`.

[73] Lars Weuste and Frank Simon. *Mass and Cross Section Measurements of light-flavored Squarks at CLIC*. Tech. rep. LCD-2011-027. CERN, 2011. URL: `https://edms.cern.ch/document/1158627`.

[74] Frank Gaede et al. “LCIO: A Persistency framework for linear collider simulation studies”. In: *eConf* C0303241 (2003), TUKT001. arXiv:`physics/0306114 [physics]`.

[75] A. Münnich and A. Sailer. *The CLIC ILD CDR Geometry for the CDR Monte Carlo Mass Production*. Tech. rep. LCD-2011-002. CERN, 2011.

[76] URL: `http://ilcsoft.desy.de/portal`.

[77] J.S. Marshall. “Redesign of PandoraPFA”. In: *IWLC*. Oct. 2010.

[78] Gavin P. Salam. “Towards Jetography”. In: *Eur.Phys.J.* C67 (2010), pp. 637–686. DOI: `10.1140/epjc/s10052-010-1314-6`. arXiv:`0906.1833 [hep-ph]`.

[79] Matteo Cacciari and Gavin P. Salam. “Dispelling the N^3 myth for the k_t jet-finder”. In: *Phys.Lett.* B641 (2006), pp. 57–61. DOI: `10.1016/j.physletb.2006.08.037`. arXiv:`hep-ph/0512210 [hep-ph]`.

[80] Gavin P. Salam and Gregory Soyez. “A practical seedless infrared-safe cone jet algorithm”. In: *Journal of High Energy Physics* 2007.05 (2007), p. 086. URL: `http://stacks.iop.org/1126-6708/2007/i=05/a=086`.

[81] F. Simon. *Techniques and Prospects for light-flavored sQuark Mass Measurements at a Multi-TeV e+e- Collider*. Tech. rep. LCD-2010-012. CERN, 2010. URL: `https://edms.cern.ch/document/1098599`.

[82] Marco Battaglia et al. *Physics performance for Scalar Electrons, Scalar Muons and Scalar Neutrinos searches at CLIC*. Tech. rep. LCD-2011-018. CERN, 2011. URL: `https://edms.cern.ch/document/1157230`.

[83] Daniel R. Tovey. “On measuring the masses of pair-produced semi-invisibly decaying particles at hadron colliders”. In: *JHEP* 04 (2008), p. 034. DOI: `10.1088/1126-6708/2008/04/034`. arXiv:`0802.2879 [hep-ph]`.

[84] Andreas Hoecker et al. "TMVA: Toolkit for Multivariate Data Analysis". In: *PoS* ACAT (2007), p. 040. arXiv:`physics/0703039`.

[85] Yoav Freund and Robert E. Schapire. "A Decision-Theoretic Generalization of on-Line Learning and an Application to Boosting". In: *Journal of Computer and System Sciences* 55 (1997), pp. 119–139.

[86] Yoav Freund and Robert E. Schapire. *A Short Introduction to Boosting*. 1999.

[87] D. Schulte. *Beam-beam simulations with GUINEA-PIG*. Tech. rep. CERN-PS-99-014-LP. CERN, 1999.

List of Figures

List of Tables